University of Southampton

Faculty of Engineering and Physical Sciences

School of Chemistry

INVESTIGATING NANOSCALE CATALYSTS FROM PRIMARY GROWTH TO CATALYTIC ACTIVITY

by

George Frederick Tierney

ORCID: 0000-0002-7409-6362

Thesis for the degree of Doctor of Philosophy

July 2021

University of Southampton

Abstract

Faculty of Engineering and Physical Sciences

School of Chemistry

Doctor of Philosophy

Investigating Nanoscale Catalysts from Primary Growth to Catalytic Activity

by

George Frederick Tierney

The ability to mass produce tailored nanoparticles, e.g. uniform sizes and surface site types, and accessibilities, has wide reaching implications for both academic and industrial research. Sol-immobilisation is proven to offer an easy to control route for the preparation of metallic nanoparticles, where a colloidal solution of nanoparticles is preformed (stabilised using polyvinyl alcohol) and anchored to a support material. However, as yet, there is limited understanding of how systematic variations to the synthesis parameters influence the fundamental nucleation and growth steps in nanoparticle formation.

Systematic changes to the solvent of synthesis, through the addition of C_1-C_4 linear and branched chain alcohols, were employed in the preparation of metallic Pd colloids. It was discovered using spectroscopic techniques (UV-Vis, IR and XAFS) and TEM imaging that the greatest control of nanoparticle growth was achieved in solutions of equal MeOH and H_2O parts per volume. Additionally, Pd colloids prepared in solutions of > 50 vol. % MeOH saw a drastic decrease in their achieved metal loading. This issue was remedied by removing the acidification step during immobilisation. The resultant influence of this updated procedure on Pd nanoparticle properties was characterised using the previously listed techniques along with thermal decomposition methods (TGA, TPR, TPD). From this, it was established that the synthesis of Pd nanoparticles in MeOH caused increased layering of the stabiliser around the nanoparticle and support surfaces, suppressing the spillover of H_2. The performance of these non-acidified PVA-capped Pd nanoparticles were investigated for furfural hydrogenation. The limiting of H_2 spillover was shown to be highly effective in switching off the acid-catalysation pathway to acetals over the TiO_2 support surface, making it selective for the desired hydrogenation products.

In addition, the mechanisms of colloidal Au nucleation and growth were investigated *via* novel XAFS experiments. A proof of concept study for *in situ* XAFS measurements was first approached by measuring solutions of preformed Au colloids prepared under varied

synthesis parameters: synthesis temperature = 1, 25, 50 and 75 °C, and [Au] = 50, 100 and 1000 μM. The established relationship between synthesis temperature and nanoparticle size was found to be consistent in colloidal and supported Au NP systems. The influence of the [Au] on XAFS nanoparticle size, however, was only observed after immobilisation of the colloid, something which has not previously been reported. Building on the successful acquisition of colloidal XAFS, a continuous microfluidic system was designed and implemented to measure the *in situ* reduction of $HAuCl_4$ ([Au] = 100 μM) to Au^0 nanoparticles. Issues concerning the flow regime of the cell, metal deposition on the reactor walls, and X-ray compatibility were all considered prior to *in situ* measurements. XAFS data acquired during reduction showed that under mild reducing conditions nanoparticle nucleation occurs on a 10^2 ms time scale, and that complete reduction of the Au species occurs over the course of 3.5 seconds. Furthermore, this novel work proves that time-resolved studies of colloidal nanoparticle nucleation and growth are feasible.

Table of Contents

Table of Tables

Table of Figures

List of Accompanying Materials

Research Thesis: Declaration of Authorship

Print name: George Frederick Tierney

Title of thesis: Investigating Nanoscale Catalysts from Primary Growth to Catalytic Activity

I declare that this thesis and the work presented in it are my own and has been generated by me as the result of my own original research.

I confirm that:

1. This work was done wholly or mainly while in candidature for a research degree at this University;
2. Where any part of this thesis has previously been submitted for a degree or any other qualification at this University or any other institution, this has been clearly stated;
3. Where I have consulted the published work of others, this is always clearly attributed;
4. Where I have quoted from the work of others, the source is always given. With the exception of such quotations, this thesis is entirely my own work;
5. I have acknowledged all main sources of help;
6. Where the thesis is based on work done by myself jointly with others, I have made clear exactly what was done by others and what I have contributed myself;
7. Parts of this work have been published as:

G. F. Tierney, S. Alijani, M. Panchal, D. Decarolis, M. de Briceno de Gutierrez, K. M. H. Mohammed, J. Callison, E. K. Gibson, P. B. J. Thompson, P. Collier, N. Dimitratos, E. C. Corbos, F. Pelletier, A. Villa and P. P. Wells, "Controlling the production of acid catalyzed products of furfural hydrogenation by Pd/TiO_2", *ChemCatChem*, 2021, DOI: 10.1002/cctc.202101036R1.

G. F. Tierney, D. Decarolis, N. Abdullah, S. M. Rogers, S. Hayama, M. Briceno de Gutierrez, A. Villa, C. R. A. Catlow, P. Collier, N. Dimitratos and P. P. Wells, "Extracting Structural Information of Au Colloids at Ultra-Dilute Concentrations: Identification of Growth During Nanoparticle Immobilization", *Nanoscale Advances*, 2019, **1**, 2546-2552.

Conferences

Oral Presentations: UK Catalysis Conference 2020, Loughborough; Johnson Matthey Academic Conference 2021, virtual.

Poster Presentations: Johnson Matthey Academic Conference 2018, 2019, 2020, Warwick/Loughborough; 17th International Congress on X-ray Absorption Spectroscopy 2018, Krakow, Poland.

Signature: .....Date: 30/07/2021

Acknowledgements

Firstly, I would like to thank my academic supervisor, Dr. Peter Wells, for giving me the opportunity to embark on this research project. I will be forever grateful for all of the support and guidance he has given me over the course of my research, even when I did not believe in my own scientific ability. Moreover, I would also like to express further gratitude to past and present members of the Wells research group; in particular, Scott, Rachel, Pip, Ellie, Norli, Donato and Evan are thanked for their support both during my PhD and beamtime experiments. Further appreciation is given to Dr. Khaled M. H. Mohammed, Dr. June Callison and Monik Panchal for their help in preparing and characterising samples when I was recovering from surgery. In addition, Dr. Shahram Alijani is thanked for his help in performing catalytic testing at the Università degli Studi di Milano, and I would like to thank Dr. Alberto Villa for giving me the opportunity to work in his laboratory in Milan during periods in 2018 and 2019. Dr. Nikolaos Dimitratos is also thanked for sharing his scientific knowledge throughout my PhD.

I would also like to thank Johnson Matthey for part funding of the project. Dr. Frédéric Pelletier and Dr. Elena Crina Corbos are both thanked for being my industrial supervisors during the project. Their support and knowledge has allowed me to conceptualise the impact of this research outside of academia. The electron microscopy department of JM is also thanked for taking me on as an intern during summer 2018; in particular, Dr. Martha Briceno de Gutierrez, who also performed the bulk of STEM imaging present in this body of work, and Dr. Trung Dung Tran, who performed STEM-EELS.

Beamtime staff at various synchrotron facilities are thanked for sharing their knowledge in writing successful experimental proposals, as well as their advice during XAFS experiments; Paul B. J. Thompson (BM28/XMaS, ESRF), Dr. Shusaku Hayama (I20-Scanning, DLS). Dr. Emma K. Gibson, Dr. Veronica Celorrio, Dr. Nitya Ramanan and Dr. Martin Wilding are thanked for organising and running the UK CatHub BAG allocation XAFS measurements on B18 (DLS) across the previous 4 years. Dr. Giannantonio Cibin and Dr. Diego Gianolio are thanked for their work as B18 beamline staff during the BAG experiments.

I am grateful that I was able to work in a multidisciplinary research facility and am also especially thankful to all of the support staff of the Research Complex at Harwell, in particular Alec and Andy who were always on hand to help with troubleshooting equipment issues. I am appreciative for the opportunities presented to myself to socialise with other

members of the catalytic community during the numerous conferences and events organised by Corinne Anyika and other CatHub staff. Gratitude is also extended to the students of the CatHub who were always on hand for lengthy debates and discussions, particularly Stefan, Dan, Monik, Andrea, Emma and Alex.

I am grateful for the support and encouragement of my friends, siblings and parents over the course of my PhD, helping me to keep going on this journey. Finally to my partner Daniela, who I cannot thank enough for her continued motivation and patience during the writing up of this work.

Abbreviations

NP	Nanoparticle
[…]	Brackets signify component concentration
PVA	Polyvinyl alcohol
pI	Isoelectric point
MeOH	Methanol
EtOH	Ethanol
PrOH	1-Propanol
IsOH	*Iso*propyl alcohol
*t*BuOH	*Tert*-Butyl alcohol
DMAB	Dimethylamine borane
UV-Vis	Ultraviolet-Visible spectroscopy
MP-AES	Microwave Plasma – Atomic Emission Spectroscopy
ppm	Parts Per Million
TEM	Transmission Electron Microscopy
STEM	Scanning Transmission Electron Microscopy
HAADF	High Angle Annular Dark Field
DF	Dark Field
BF	Bright Field
HRTEM	High Resolution Transmission Electron Microscopy
EDX	Energy Dispersive X-ray analysis
EELS	Electron Energy Loss Spectroscopy
XAFS	X-ray Absorption Fine Structure
XANES	X-ray Absorption Near-Edge Structure
EXAFS	Extended X-ray Absorption Fine Structure
FTIR	Fourier Transform Infrared
DRIFTS	Diffuse Reflectance IR Fourier Transform Spectroscopy
TPD	Temperature Programmed Desorption
TPR	Temperature Programmed Reduction
TGA	Thermogravimetric Analysis
XRF	X-ray Fluorescence
GC	Gas Chromatography
MS	Mass Spectroscopy

TOF	Turnover Frequency
TCD	Thermal Conductivity Detector
FID	Flame Ionisation Detector
FA	Furfuryl Alcohol
THFA	Tetrahydrofurfyl Alcohol
THF-ME	Tetrahydrofurfuryl-methyl ether
THFIE	*Iso*propyl tetrahydrofurfyl-ether
FIE	*Iso*propyl furfuryl-ether
2-MF	2-methylfuran
2-MTHF	2-methyltetrahydrofuran
PFD	Octadecafluorodecahydronaphthalene
PO	Perfluoro-1-octanol
PTFE	Polytetrafluoroethylene
PEEK	Polyether ether ketone
DLS	Diamond Light Source
ESRF	European Synchrotron Research Facility
JMTC	Johnson Matthey Technology Centre
ID	Internal Diameter
OD	Outer Diameter

Chapter 1 Introduction

1.1 Introduction to Catalysis

1.1.1 Catalysis

The use of catalytic processes is ubiquitous in the chemical industry, with an estimated 90 % of industrial chemical processes employing at least one catalytic step.[1] The increasing worldwide demand for energy, the production of petro-, fine-, commodity- and pharmaceutical chemical products, as well as a global drive to reduce greenhouse gas emissions, all make catalysis an important area of research.[1–4] Catalytic processes were first described by Berzelius in 1836 as: "*…many substances, simple and compound, solid and in a state of solution, possess the power of exercising upon chemical bodies an influence essentially distinct from chemical affinity, an influence which consists in the production of a displacement, and a new arrangement of their elements, without directly and necessarily participating in it"*.[5] In 1895, Ostwald provided a revised definition for catalysis in which he incorporated the kinetic nature of the process and further refined this in 1902, when he described a catalyst as "*any substance which alters the velocity of a chemical reaction without appearing in the final product"*.[6,7] To summarise, a catalyst provides an alternative pathway by which the reaction can proceed, lowering the activation energy and increasing the rate at which the reaction reaches equilibrium without itself altering the position. The lower activation energies afforded not only improve selectivities to desired products, but a greater atomic efficiency in the process can also be observed, in turn enhancing the economic and environmental impacts of industrial reactions.[8,9]

Depending on the physical state of the catalyst and substrate/reactant, it is possible to group catalysts into two categories: (1) homogenous catalysts, where the catalyst and substrate are in the same phase of matter, i.e. liquid or gaseous, and (2) heterogeneous catalysts, where the catalyst and reactant are present in different phases, i.e. solid/liquid, solid/gas or liquid/gas. For many industrial reactions, the ease at which a catalyst can be separated from the products (or remnant reactants) and, therefore, be readily recycled, makes heterogeneous catalysis a much more advantageous process.

1.1.2 Heterogeneous Catalysis

Heterogeneous catalysis can be thought of as a cyclic process: reactants adsorb to the catalyst surface, form intermediate structures and the products then desorb whilst the surface returns to its initial state.[1,9] A hypothetical energy level diagram for a reaction with and without the presence of a catalyst is given in *Figure 1-1*. The reaction pathway without a catalyst occurs as a single step process with a high-energy activation barrier, E_G. Conversely, the catalysed pathway occurs *via* several steps which have lower activation barriers than the non-catalysed reaction, causing the reaction to reach equilibrium at a much faster rate.

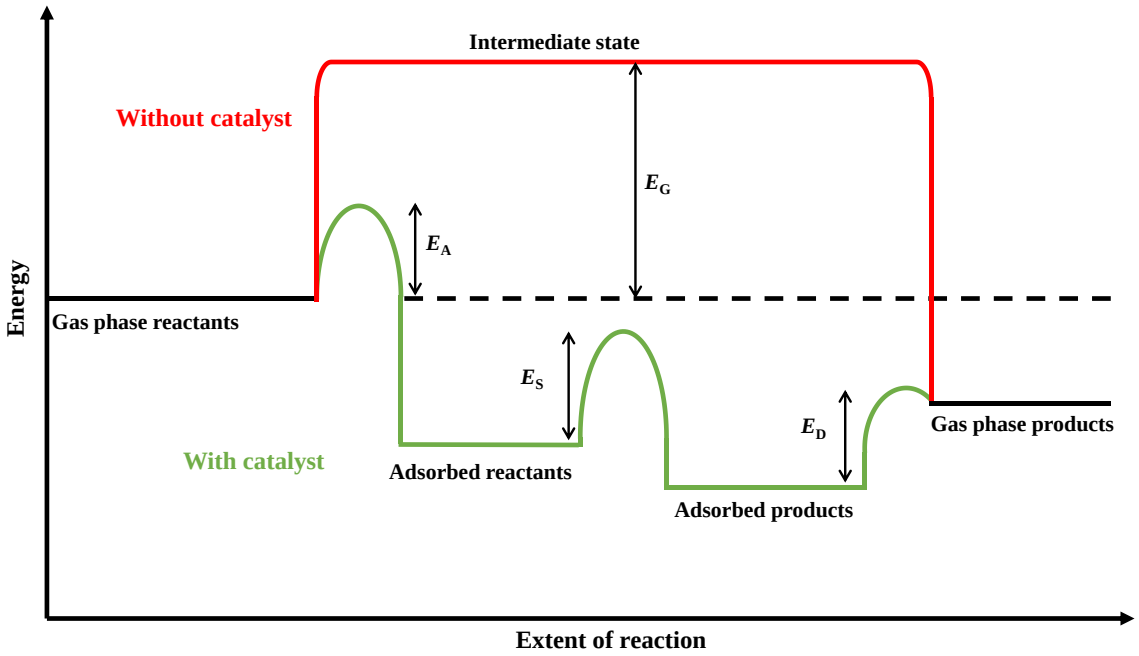

Figure 1-1. *Schematic of the effect a heterogeneous catalyst has on the activation energies of a gas phase reaction, where E_A is the energy of adsorption, E_S is the energy for the surface reaction, E_D is the energy of desorption and E_G is the energy for the gas phase reaction in the absence of a catalyst; image is adapted from J. C. Védrine, in Metal Oxides in Heterogeneous Catalysis, ed. J. C. Védrine, Elsevier Inc., 1st edn., 2018, pp. 1–41.*[1]

When gaseous reactants are passed over a catalyst, adsorption of the reactants to the catalyst surface initiates the reaction, thus making the surface (or available active sites) of a heterogeneous catalyst of great importance.[9] Once adsorbed, the reaction of interest can then proceed *via* three mechanisms: (1) the Eley-Rideal mechanism, where a gaseous reactant reacts with an adsorbed reactant, (2) the Langmuir-Hinshelwood mechanism, in which two adsorbed reactants interact on the surface to form the desired product, or (3) the Mars-van Krevelen mechanism, which is mainly used to describe the kinetics of selective oxidation

reactions, predominantly over metal oxides, carbides and sulphides. Here, the surface plays an active role in the reaction by forming a chemical bond between the surface and one reactant. Much like Eley-Rideal, the second reactant reacts from the gas phase and leaves a vacancy on the surface once the reaction product has desorbed. This vacancy is then filled through the migration of atoms from the bulk to the surface.[10] In both mechanisms (1) and (2), the reaction product is fully desorbed once formed (*Figure 1-2*). For the purpose of this review, only the first two mechanisms will be considered further.

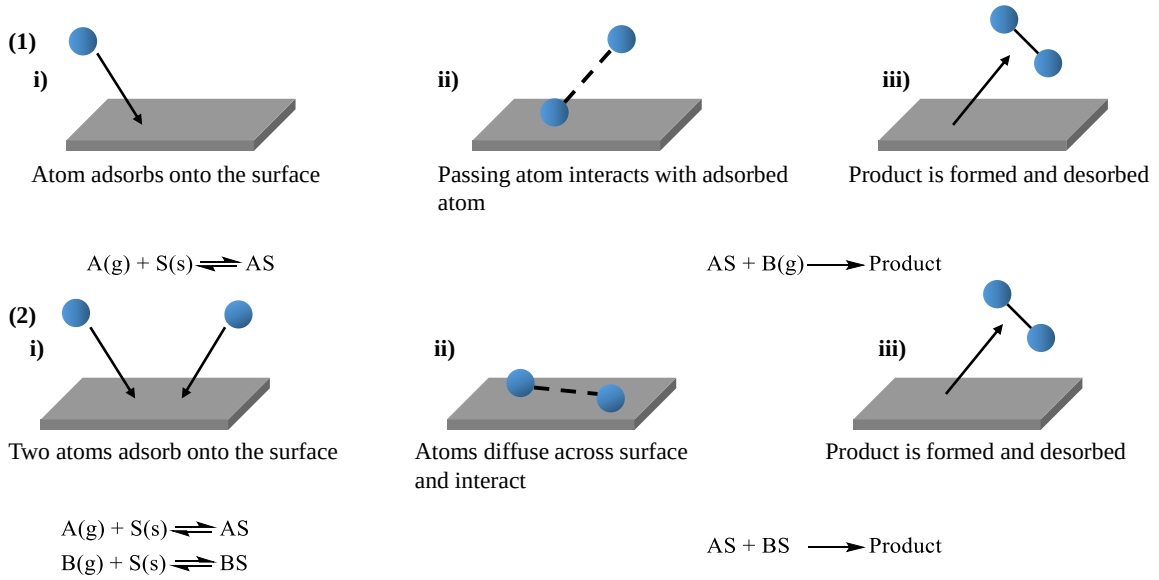

Figure 1-2. *Simplified reaction schemes for (1) the Eley-Rideal and (2) the Langmuir-Hinshelwood mechanisms; below each of the mechanisms are simplified equations describing their respective reaction processes, denoted i)-iii).*

For a catalyst to be successful, not only does it require an abundance of active surface sites (steps, edges and terraces), the properties of these sites must also be taken into consideration as they have a great influence on the activity of heterogeneous catalysts.[11] In recent decades, the development and engineering of heterogeneous catalysts on the nanoscale has been a major focus as this optimises the number of surface sites per unit volume. One such area is the use of nanoparticles (NPs), defined as materials that are between 1-100 nm in size.[11] A major benefit of using metallic NPs is the improved reactivity of the resultant catalyst in comparison to the bulk metal. One method in which the reactivity can be improved is *via* the deposition of NPs onto a support, this aids in increasing the surface area of the metal, and so creates as many available active sites as possible.[12] The dispersion of the nanoparticles (*Equation 1-1*) is defined as the percentage of atoms on the surface, N_S, relative to the total number of atoms in a particle (the bulk), N_T. By using the surface area and volume occupied by an atom (in an FCC structure), the dispersion of a spherical Pd particle and the impact of

particle size on dispersion have been calculated (*Figure 1-3*). The correlation between particle size and the number of available surface sites is evident and, interestingly, when preparing Pd nanoparticle catalysts with sizes < 2 nm, the dispersion and number of surface atom sites are greatly increased. Furthermore, it is more economically viable to prepare nanoparticles of precious metals than use bulk quantities.[13] By thrifting these expensive metals (e.g. Au, Pt, Pd) and supporting them as nanoparticles, highly active catalysts can be produced that are both cost-effective and environmentally friendly.[14–17] However, there is a delicate balance to consider when preparing NPs with reduced sizes (< 5 nm), as the activity can potentially be negatively impacted by decreasing access to the available surface sites, e.g. with smaller size, a decrease in NP planes is observed.[18]

$$D = \frac{N_S}{N_T}$$

Equation 1-1. *Dispersion of nanoparticles, where N_S is the percentage of atoms on the surface and N_T is the total number of atoms in a particle.*

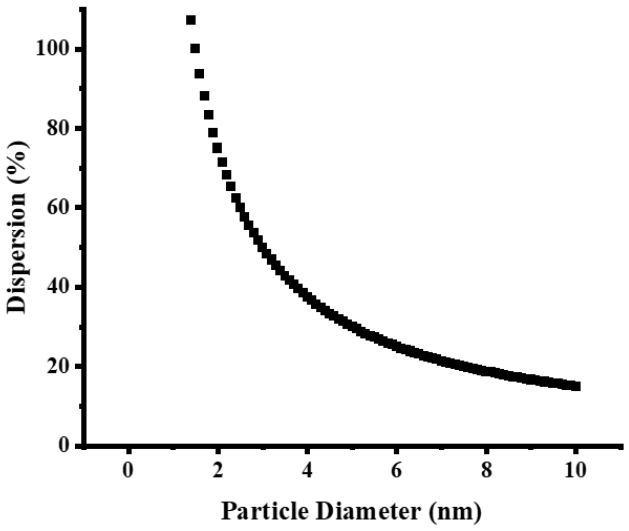

Figure 1-3. *Pd particle dispersion as a function of increasing particle diameter, calculated using* ***Equation 1-1****.*

To summarise, the use of NP catalysts is very beneficial for a multitude of modern processes as the use of small quantities of precious metals affords highly active catalysts whilst keeping the economic aspects of synthesis low.[19–21] The anchoring of NPs onto support materials also allows for their stabilisation with high NP dispersion.[22] This is particularly useful for the reforming of feedstock chemicals.[23] In this work, NPs were supported onto a metal oxide, in this case titanium dioxide (TiO_2). TiO_2 was chosen as the support due to its low cost and non-toxic nature, as well as its chemical and thermal stabilities.[24,25,26]

1.2 Synthesis of Metal Nanoparticles

Nanoparticle catalysts have, for many years, been extensively studied for a wide range of chemical processes, including for the synthesis of fine chemicals and for green chemistry applications.[27–29] Catalysts composed of metallic NPs with controlled shape, size and structure have reportedly been prepared through a myriad of synthetic routes.[30–32] The production of these metal NPs can be categorized into two separate processes: "top-down" and "bottom-up" (*Figure 1-4*). The former synthesis route utilises mechanochemical methods, such as ball milling, to physically grind bulk metals into macro- or nanoscale units.[33,34] However, this route has limitations in forming NP catalysts with desirable properties due to the low degrees of control. Top-down methods also require large quantities of starting materials which are high in cost, making the process less lucrative.[34] Contrastingly, bottom-up approaches offer a more economically viable route for building NP catalysts. Synthetic methods used in this approach involve the reduction of precursor metals to atoms and/or ions. Subsequent to this, a growth stage causes the monomer/ionic units to coalesce, forming metallic clusters and/or NPs.[35] In essence, nanoparticle formation can be described as the following generalised process: reaction initiation by physical or chemical activation, nucleation, particle growth and larger particle formation.[36]

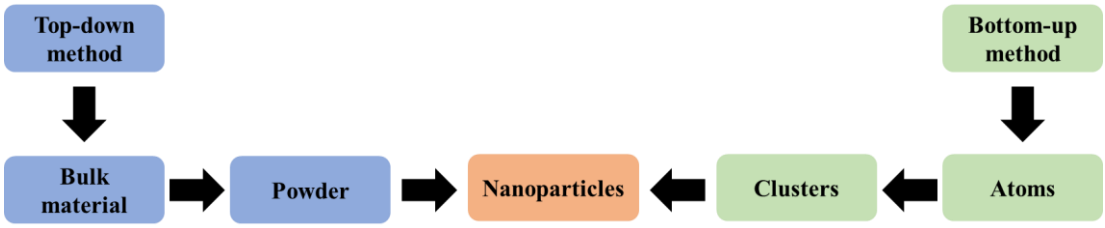

Figure 1-4. *Synthetic processes involved in the formation of nanoparticles; image is adapted from Ealias and Saravanakumar, IOP Conf. Ser. Mater. Sci. Eng., 2017,* ***263****, 1-15.*[37]

Of the many available bottom-up synthesis procedures, impregnation,[38] co-precipitation,[39] and sol-immobilisation[40] all yield NPs with desirable features (< 10 nm). Therefore, the choice of an appropriate synthesis solvent is paramount in preparing ultra-small NPs (1-5 nm) with maximal dispersion and greater surface site availability.

1.2.1 Impregnation

Impregnation is a widely used synthesis method in both academic and industrial research. This is due to its ease of use and its capability to form supported metal NP catalysts with

high surface-to-volume ratios and thermal stabilities, affording catalysts with up to 30 wt. % metal loadings.[41] During impregnation, the pores of a support material are wetted using a metal salt precursor solution, the loading of which is dependent on the metal concentration and solubility in solution. Synthesis through incipient wetness impregnation occurs when the volume of the metal solution is equal to the total pore volume of the support. Through this, a paste is produced that requires removal of the excess solvent *via* heat treatment.

A major drawback to impregnation is the use of thermal treatments. Removal of excess solvent can be performed by either heating the solvent to its boiling point or by using more gentle drying conditions with or without the flow of gases such as He, H_2, or N_2.[42] However, the drying temperature must be carefully controlled as it can influence the dispersion of NPs within the final catalyst; for an impregnated sample, the concentration of NPs can assemble either homogenously, around the edge or in the centre of the support's pore structure.[43,44] Typically, high temperature thermal treatments are necessary to ensure complete removal of any precursor salt residues, e.g. chlorine, as it is a poison that can detrimentally impact catalyst activity.[42,45] Interestingly, Sankar *et al*. described a modified impregnation method for Au-Pd NPs, wherein an excess of Cl^- anions was used to help increase NP dispersion *in lieu* of a stabilising agent; here, heat treatment in strong reducing conditions (5 % H_2/Ar atmosphere) was employed to fully remove the residual Cl and prevent NP sintering.[46] Dann *et al.* also reported the influence of the precursor salt on the nucleation and growth of Pd NPs supported on γ-Al_2O_3.[47] In their study, Pd NPs were prepared using two precursor salts, palladium nitrate ($Pd(NO_3)_2$) and tetraamminepalladium (II) hydroxide in NH_4OH solution ($Pd(NH_3)_4(OH)_2$), which formed Pd NPs with average sizes of 4.4 and 3.1 nm respectively. Utilising combined X-ray absorption fine structure (XAFS) and diffuse reflectance infrared Fourier transform (DRIFTS) spectroscopies, the nitrate precursor was observed to facilitate the pre-assembly of monomer units over the alumina surface through the mono-, bi-, and tridentate binding modes of NO_2. Conversely, the ammine based precursor displayed an earlier onset of ligand decomposition during calcination, forming nitrosyl moieties that adsorb onto Al_2O_3, limiting the movement of Pd across the surface.[47] The findings of this study displayed how simplistic alterations to the choice of precursor salt played a significant role on the final NP size; however, it did not afford narrower particle size distributions. Whilst the impregnation preparation of NPs were readily optimised, the growth processes of NPs could not be strictly controlled, e.g. as a result from the thermal treatment[42] or the choice of precursor salt.[47] Hence, monitoring of the fundamental NP formation processes during impregnation would be a difficult endeavour.

1.2.2 Coprecipitation

Preparation of nanoparticle catalysts *via* coprecipitation is a relatively simple technique; not only does it yield catalysts with high metal loadings (~ 60-80 wt %), it also allows for the active phase (NPs) and the support material to be prepared in a single step.[48] This protocol has therefore been employed in industrial settings for the preparation of a large number of commercial catalysts.[49] Here, the one-pot method involves the controlled dosing and mixing of the precursor components (metal salt solution and precipitating agent) to initiate precipitation of the desired product whose characteristics, e.g. chemical phases, dispersion, and surface area of the active phase, can be fine-tuned by manipulating the solution pH and [metal salt].[8,49] The kinetics of nucleation and particle growth have been shown to be adjustable in homogenous solutions by the controlled release of anions and cations which can result in monodisperse nanoparticles.[50] However, further work is required to obtain the final catalyst; the gel formed through coprecipitation is aged (left to undergo chemical and physical changes), washed (to remove any remnant precursor ions, e.g. Na or Cl, that could negatively impact reactivity or selectivity), dried and then calcined.

This method is well researched in the literature, with many exploring how changes to the synthesis parameters affect NP size. Al-Sayari *et al*. reported the preparation of Au/ZnO catalysts with high Au NP dispersions and NP sizes < 5 nm, through a one-step coprecipitation synthesis.[51] The metal loading of the Au NPs was found to be dependent on the pH of the precipitation solution (Au loading: 6.5 wt. % at pH = 5, 1.9 wt. % at pH = 10). The acidic and basic nature of the precipitation solution is therefore an important factor in controlling NP size but can also lead to leaching of Au. Another drawback to this method is the large quantities of waste produced as the salt solution and the precipitation product have to be separated by filtration prior to drying.[49] When trying to measure the fundamental processes of NP formation in coprecipitation methods, issues arise due to the high supersaturation levels and low stability of the precursor salt solution, making it troublesome to monitor particle growth during sample aging.[48,49] Furthermore, the introduction of heat treatments to remove residues can be detrimental when preparing NP catalysts (< 5 nm).

1.2.3 Colloids

Colloidal solutions are liquid mixtures consisting of one substance of ultra-small and insoluble particles dispersed homogeneously throughout a second solvent. An example of this is sol-immobilisation (*Figure 1-5*) which can be split into three important steps:

(1) Reduction of the metal salt solution in the presence of a stabilising agent.

(2) Addition of a solid support (conventionally a metal oxide) and acidification of the slurry.

(3) Washing, filtering and drying (at room temperature) of the catalyst slurry.

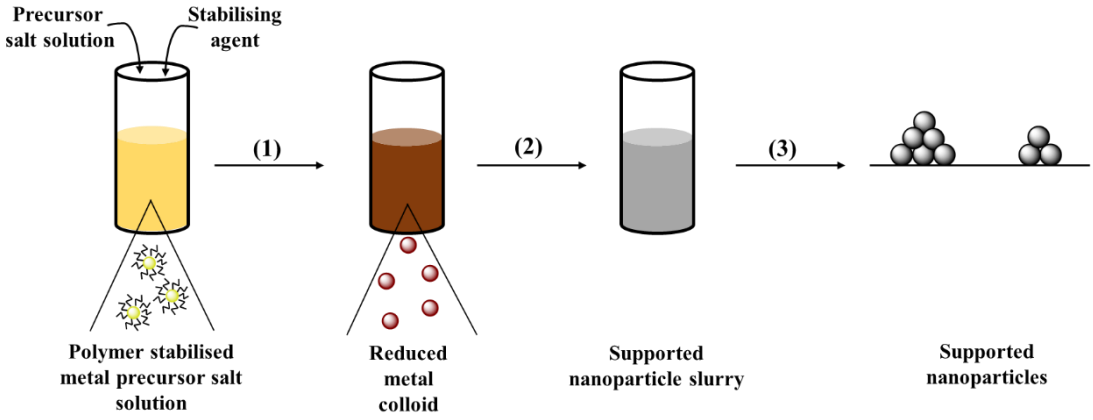

***Figure 1-5**. Schematic illustrating NP synthesis via sol-immobilisation. Step (1) chemical reduction of a metal salt solution (e.g. $HAuCl_4$) in the presence of a stabilising agent (e.g. PVA) using a reducing agent. Step (2) the support material is added to the formed colloid and is acidified. Step (3) Catalyst slurry is washed using deionised water, filtered under vacuum and dried at room temperature for > 12 hrs.*

Pre-forming of the metal colloid is required during NP synthesis and is achieved *via* reduction of the metal precursor to its zero valent state using a strong reducing agent, e.g. $NaBH_4$ (step (1)). This is performed in the presence of a stabilising agent, such as polyvinyl alcohol (PVA), to limit coalescence of the colloidal NPs through steric or electrostatic effects.[52,53] Acidification of the colloidal slurry in step (2) is required to immobilise the colloidal NPs on the support surface. The required pH for this step corresponds to the isoelectric point (pI), a state where the colloid or catalyst slurry carries no overall electric charge. Furthermore, the pI is dependent on the support material used[41]; for TiO_2 (P25, a mixture of anatase and rutile phases of TiO_2 ~ 80:20), the pI is equal to 5.8, therefore the pH is adjusted to 1-2 to enable the metal to be supported *via* charge interaction.

Unlike synthesis through impregnation and co-precipitation, sol-immobilisation can be performed without the use of thermal treatments post-synthesis, limiting the likelihood of the supported NPs agglomerating *via* external influences. Advantageously, the parameters used in colloidal synthesis can also be easily altered to afford greater control of NP properties, e.g. the temperature of synthesis[54] and the stabilising[55] and reducing agents,[56] to

produce ultra-small NPs < 5 nm.[40,57] Furthermore, sol-immobilisation synthesis has been utilised in the formation of bimetallic NPs with narrow size distributions.[58,59] Dimitratos *et al.* described the capability of sol-immobilisation in the preparation of Au-Pd bimetallic NPs, particularly in the synthesis of core-shell (Au@Pd and Pd@Au) NPs with controlled NP sizes of 3-5 nm.[60] The catalysts prepared in this study showed much improved activity when compared to those prepared through impregnation, whilst using much lower concentrations of the metal salt. Synthesis *via* sol-immobilisation procedures is therefore highly favourable for the preparation of tailored NP catalysts.

1.3 Colloidal Nanoparticle Synthesis: Batch *vs.* Microflow

1.3.1 Synthesis in Batch Conditions

Conventionally, the synthesis of metal NPs in laboratory procedures has revolved around beaker sized reaction vessels (batch), where catalysts are produced on a gram scale. Sol-immobilisation on batch scales has been described thoroughly in the literature, where research in the control of NP properties has focussed on manipulating the temperature of synthesis,[61] the concentrations of reagents,[62] the rates of reagent addition,[63] the type of reducing[56] or stabilising[64] agents used, and the composition of the synthesis solvent.[65.] These studies have been concerned with how changes to these parameters affect NP size; however, this is not the sole property that impacts NP activity.[66,67] Medlin *et al.* reported a method of directing selectivity by using self-assembled monolayers (SAMs) of different thiols over Pd NP surfaces, altering the availability of terrace and edge sites in the hydrogenation of furfural.[68] The introduction of alcohols into the synthesis solvent is another beneficial method to influence NP properties; Teranishi and Miyake described the use of incremental volumes of short chain linear alcohols (C_1-C_3) added to the synthesis solvent in place of a reducing agent for Pd NP formation.[65] Here, Pd NP size was better controlled after refluxing H_2PdCl_4 in 40 vol. % ethanol for 3 hrs. More recently, Rogers *et al*. investigated the influence of EtOH on NP properties when prepared with a strong reducing agent ($NaBH_4$); not only did this form Pd NPs with sizes < 3 nm, they were also able to tailor surface site speciation.[54] Adjustments to the synthesis parameters therefore allow for tailoring of NP properties which provides an increase in product homogeneity as a function of narrowed NP size distributions, as well as surface site availability.[54,69] A less commonly reported step in the formation of sol-immobilised catalysts is the impact of residual Cl and S species remnant from the precursor salt and acidification process, respectively. Ineffective removal of these

elements (Cl and S) from the surface is detrimental for NP catalysts as they both act as poisons in various reaction processes.[70,71] However, scaling up synthesis protocols from the laboratory to industrial production creates additional issues; the number of process steps and the need for vast parameter control make sol-immobilisation a laborious task, with optimisation of the procedure through removal of specific steps highly sought after. Additionally, a small change to the size of the reactor used can impact the reactant contact time and the energy efficiency of the synthesis (temperature and mass transport phenomena). This can then impact the control of NP nucleation and growth and, subsequently, reduce NP homogeneity.[72] It is therefore imperative to consider the effect of the synthesis procedure on the homogeneous nature of the colloid when increasing the production of NPs.

1.3.2 Synthesis in Microflow Systems

In the pursuit of preparing "designer" nanoparticles continuously on an industrial scale, the use and scale-up of microscale systems over macroscale (batch) production has yielded both beneficial synthetic results and reductions to the overall cost of the process.[72–74.] Importantly, the use of microscale devices improves the potential of elucidating the principle nucleation and growth steps in NP formation.[75,76] This favourable synthesis method offers the user a host of advantages over batch processes (*Table 1-1*).

Table 1-1. *Advantages and disadvantages of microfluidic systems used for the synthesis of nanoparticles.*[77]

Advantages	Disadvantages
• Low solution/reagent consumption • Excellent control of reagents and other experimental parameters (concentrations, residence times) • High reproducibility of synthesis • Increased mixing • Reduced synthesis time	• Fouling/ deposition of nanoparticles is a risk • Limited integration with online characterisation techniques • Labour intensive set-up • Complex device design • Can be expensive to manufacture microfluidic device/cell

The downsizing of reactor vessels from litre glass beakers to millimetre devices has led to improvements in many areas of synthesis. One example of this is the optimisation of reaction completion time; where synthesis through batch processes required multiple hrs of reaction

time, the same process in flow can now be completed within a 10 minute time frame.[78] This is attributed to changes in the transfer of heat and mass through reaction mixtures (transport phenomena).[79,80] Here, mass transfer refers to the concentration at which a reaction occurs.

By decreasing the size of the reactor vessel, the surface area-to-volume ratio rises allowing for greater heat transfer and interaction of precursors and reducing agents inside microflow systems; thus the transport phenomena produce a reaction mixture vastly higher in homogeneity than batch analogues.[81] Similar to this, a rise in atomic and environmental efficiency is observable due to limited chemical waste formation, and a reduction in external solvent used in purification steps.[82] The microscale also improves the safety of reaction processes where the chemicals used are harmful or toxic and aids in limiting the use of expensive chemicals, such as precious metal salts.[83] Synthesis of metallic nanoparticles on microfluidic scales is therefore a useful method to employ for *in situ* studies of nanoparticle nucleation and growth and has been reported widely.[76,84–86]

1.4 Nanoparticle Nucleation and Growth

Controlled synthesis of NPs with tailored sizes, shapes and surface site availability is well established and proven to be reproducible through colloidal preparations.[54,65,66] However, definitive understanding of the fundamental steps involved in NP formation is not yet reported. Elucidating the mechanisms of nucleation and growth will allow for more successful engineering of nanomaterials with specific and desirable sizes, shapes, structures and dispersions, overall offering optimised routes to reproducible NP synthesis.

The process of formation consists of a primary nucleation step that is followed by nanoparticle growth. The majority of the literature in this research area is based on classical nucleation theory developed by Becker and Döring; they describe the process of nucleation proceeding if a supersaturation condition is met, as well as stating that the rate of nucleation decreases as the precursor is depleted.[87,88] Nucleation, in a homogenous fashion, is the spontaneous and random formation of nuclei once supersaturation of the precursor at a critical concentration has been achieved; it is described thermodynamically in *Equation 1-2* for a spherical nucleus. Terms within this expression correspond to the favourable bonding between two monomers decreasing the Gibbs bulk free energy (the negative term), and the unfavourable nature of this bonding due to increases in Gibbs free surface energy (the positive term). The relationship between the Gibbs free energy and the nuclei radius can be plotted graphically as a NP cluster's free energy as a function of its size (*Figure 1-6*).

Continuous nucleation of monomers occurs until the critical radius, r_c, is reached and its corresponding energy is the activation energy, ΔG_c. Therefore, growth of the formed particles does not begin until the activation energy has been met by clusters with sufficient radius; if these criteria are not matched, dissolution of the cluster becomes a more feasible process.[88,89]

$$\Delta G = -\frac{4}{3}\pi r^3 |\Delta G_v| + 4\pi r^2 \gamma$$

Equation 1-2. *Thermodynamic expression for the homogenous nucleation process; where ΔG is the total free energy of a nanoparticle (the sum of the surface free energy and the bulk free energy), r is the radius of a spherical particle, γ is the surface energy and $|\Delta G_v|$ is the difference in Gibbs bulk free energy per unit volume.*[89]

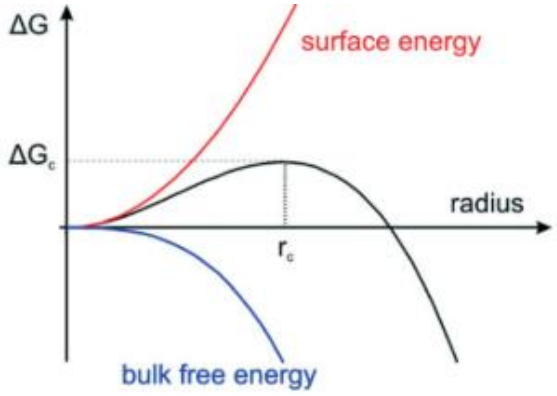

Figure 1-6. *Graphical depiction of the dependence of the cluster free energy on the radical cluster size according to classical nucleation theory, ΔG is the cluster free energy, ΔG_c is the maximum free energy and r_c is the critical radial size; image taken from J. Polte, CrystEngComm, 2015, **17**, 6809–6830.*[89]

Classical nucleation theory acted as the foundation for the particle nucleation theory developed by LaMer and Dinegar in 1950.[90] LaMer and Dinegar described burst nucleation: a process dependent on the concentration of nuclei/monomer within the solution. Over a short period of time, the concentration of the precursor solute, C, increases towards the critical concentration for nucleation, C_{crit}, and once over this threshold, enters the nucleation phase marked as I (*Figure 1-7*). This reaches a maximum when the precursor supply rate, consumption rate for nucleation and nuclei growth are balanced (II). In stage (III), consumption of the solute is proportional to the growth of the produced nuclei, in turn decreasing the concentration below the critical level. Therefore, without a new nucleation event occurring, the concentration of the solute decreases further until equilibrium is

achieved.[90–92] This process is thus determined by the supply rate of the solute and the subsequent growth rate of generated nuclei. However, this approach only gives a generalised view of the subsequent particle growth of stable nuclei.

In the immediate years after the theory of burst nucleation was published, Turkevich proposed an alternative mechanism for Au^0 particle formation.[93,94] He described the formation of Au particles kinetically *via* an organiser pathway; here, Au^0 formation occurred according to the following assumptions:

(1) Au nuclei within a solution formed with the same diameter,

(2) The subsequent growth processes were consistent for nuclei and larger particles,

(3) The complete end of the reaction occurred upon addition of hydroxylamine hydrochloride.

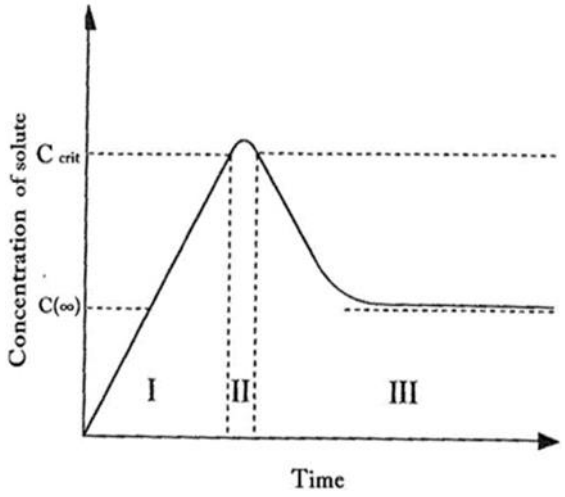

Figure 1-7. *LaMer nucleation and growth schematic. I and II represent rapid increased concentration of free monomers and burst nucleation respectively. III shows decrease in concentration due to monomer diffusion through solution. C_∞ is the equilibrium concentration of the solute with the bulk solid and C_{rit} denotes the critical concentration as the minimum concentration for nucleation; image taken from T. Sugimoto, J. Colloid Interface Sci., 2007,* ***309****, 106–118.*[92]

Turkevich's organiser pathway describing the reduction of $HAuCl_4$ using sodium citrate therefore occurred in four distinct steps:

(1) Induction period, this is a chemical process, where the removal of the inhibitor for reduction occurs. Inhibition of this process was found to be dependent on the oxidation of citrate to acetone dicarboxylate ions. Nucleation was initiated once a sufficient concentration of the oxidation product had been formed,

(2) Autoaccelerating portion, this is where the rate of oxidation was much higher than the usage of acetone dicarboxylate ions in chloroauric acid reduction,

(3) Linear portion, here nucleation occurs at a constant rate and is limited by the rate of precursor reduction to nuclei,

(4) Decay portion, in this step, nucleation begins to decrease and the system shifts toward particle growth, where the precursor was utilised on the surface of already formed nuclei instead of undergoing independent reduction.

The general growth mechanism that followed this preparatory method was validated by Polte *et al*. using combined small angle X-ray scattering (SAXS) and X-ray absorption near-edge structure (XANES) analysis.[89] In an ideal colloidal system nucleation would follow a homogeneous regime, where spherical nuclei form at the same instance within the liquid phase.[95] In reality homogenous nucleation is rarely observed due to impurities in reaction solutions and the walls of the mixing channel offering alternative and higher energy surfaces for instantaneous nucleation, leading to heterogeneous nucleation at varied rates.[89,96]

Growth mechanisms of nanoparticles have been postulated for nearly a century across varying publications and reviews; however, it is still an area of colloidal science without definitive understanding.[16,88,90,91,96–98] LaMer and Dinegar provided an assessment of growth following burst nucleation, where diffusion of monomer units through solution toward one another gives rise to particle coalescence and cluster formation (*Figure 1-8*).[90] Ostwald, however, detailed a conflicting theory whereby "ripening" of particles in solution was a factor of NP solubility.[99] Instead, it was proposed that growth occurred as a consequence of smaller particles in solution, where particle size is inversely proportional to the chemical potential of the particle. As the particle gets smaller in size, its surface free energy increases as does the particle instability, causing the smaller particles to emit atoms (adatoms). These emitted atoms then interact with larger, more stable particles and amalgamate with them (*Figure 1-8*).

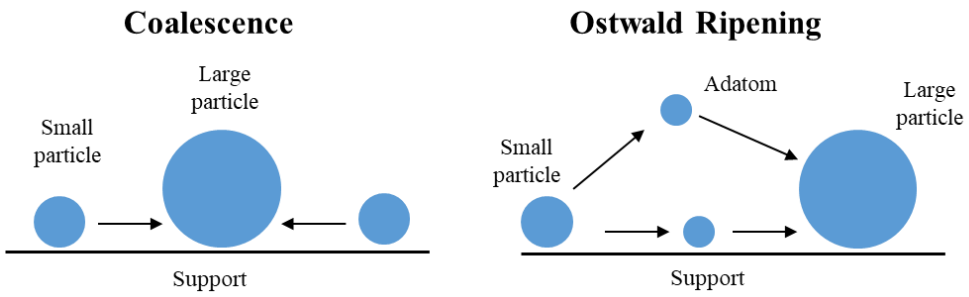

Figure 1-8. *Illustration of the differences between the two particle growth mechanisms, (left) Ostwald ripening and (right) coalescence.*

1.5 *In situ* Investigations of Nanoparticle Formation.

The literature concerning real time measurements of nanoparticle formation is limited at present, with studies offered using lab based techniques such as UV-Vis,[100,101] TEM[88] as well as more advanced synchrotron techniques, i.e. SAXS and XAFS.[76,89,102] Successful pairing of these X-ray spectroscopic techniques with microfluidic systems has aided in furthering the understanding of colloidal nucleation and growth *via in situ* studies; particularly due to the reaction time post reagent mixing being proportional to the distance travelled along the mixing channel.[98] XAFS investigations of colloidal formation have focussed on the determination of the average oxidation state and local geometry of the colloids by examining colloidal solutions using XANES.[103–105] Notably, initial characterisation of the nucleation step has been published in recent years where the rapid (< 300 ms)[84] reduction of the Au metal salt precursor to its atomic species[106] ($Au^{3+} \rightarrow Au^{0}$) was followed *in situ*. However, determining NP size or nature of the adjacent atoms to the X-ray absorbing atom is a harder task using XAFS, where extended X-ray absorption fine structure (EXAFS) measurements of colloidal NP formation, to the best of the author's knowledge, have not been successfully reported. Instead, NP size and the growth process have been measured by *in situ* SAXS.[76,89,107,108] Where calculation of NP growth is made through fitting of experimentally acquired data, however, the lower limit of the method is far larger than those of monomer units, a consequence of larger particles dampening the scattering of smaller particles and monomers that can be present in the colloid. Other issues arise from the fixing of particle sizes and shapes in calcualtions.[109,110] Further discussion of *in situ* XAFS in the literature is presented in section 6.1.5.

1.6 Aims and Objectives

The principle aim of this body of work is to explore and elucidate how systematic changes to the synthesis conditions applied within the sol-immobilisation procedure influence the properties of nanoparticles. Furthermore, optimisation of the synthetic controls will be examined for the preparation of catalysts with enhanced activities. This thesis will:

(1) Determine the effect of alcohols as solvents for sol-immobilisation of Pd nanoparticle catalysts, as well as describe the influence of incremental alcohol concentration within an optimised colloidal procedure,

(2) Ascertain how interactions between the solvent system and the stabilising agent influence product selectivity in the hydrogenation of furfural at low temperatures,

(3) Assess the impact of the reduction temperature (1-75 °C) and precursor salt concentration ([Au] < 1000 μM) on the formation of colloidal Au nanoparticles, pre- and post-immobilisation using *ex situ* XAFS experiments, and

(4) Elucidate the initial colloidal nucleation phase of Au nanoparticles by developing and implementing a microfluidic cell for novel *in situ* XAFS measurements.

1.7 References

1 J. C. Védrine, in *Metal Oxides in Heterogeneous Catalysis*, ed. J. C. Védrine, Elsevier Inc., 1st edn., 2018, pp. 1–41.

2 N. Subramanian, in *Modern Developments in Catalysis*, eds. G. J. Hutchings, M. Davidson, C. R. A. Catlow, C. Hardacre, N. Turner and P. Collier, World Scientific Publishing, 1st edn., 2017, pp. 1–2.

3 C. R. Catlow, M. Davidson, C. Hardacre and G. J. Hutchings, *Phil. Trans. R. Soc. A*, 2016, **374**, 20150089–20150090.

4 C. Morgan, *Johnson Matthey Technol. Rev.*, 2014, **58**, 217–220.

5 J. J. Berzelius, *Edinburgh New Philos. J.*, 1836, **21**, 223–228.

6 W. Ostwald, *Zeitschrift für Phys. Chemie1*, 1894, **15**, 705–706.

7 W. Ostwald, *Nature*, 1902, **6**, 522–526.

8 M. Bowker, *The Basis and Applications of Heterogeneous Catalysis*, Oxford University Press, Oxford, 1998.

9 J. Hagen, in *Industrial Catalysis A Practical Approach*, ed. J. Hagen, Wiley-VCH Verlag GmbH & Co., Weinheim, 2nd edn., 2006, pp. 99–222.

10 P. Mars and D. W. van Krevelen, *Chem. Eng. Sci.*, 1954, **3**, 41–59.

11 G. A. Dorofeev, A. N. Streletskii, I. V. Povstugar, A. V. Protasov and E. P. Elsukov, *Colloid J.*, 2012, **74**, 675–685.

12 G. Schmid and L. F. Chi, *Adv. Mater.*, 1998, **10**, 515–526.

13 W. Zang, G. Li, L. Wang and X. Zhang, *Catal. Sci. Technol.*, 2015, **5**, 2532–2553.

14 I. Saldan, Y. Semenyuk, I. Marchuk and O. Reshetnyak, *J. Mater. Sci.*, 2015, **50**, 2337–2354.

15 B. R. Cuenya, *Thin Solid Films*, 2010, **518**, 3127–3150.

16 J. Polte, T. T. Ahner, F. Delissen, S. Sokolov, F. Emmerling, A. F. Thünemann and R. Kraehnert, *J. Am. Chem. Soc.*, 2010, **132**, 1296–1301.

17 C. E. Chan-Thaw, A. Villa and L. Prati, in *Gold Catalysis: Preparation, Characterization, and Applications*, eds. L. Prati and A. Villa, Pan Stanford, 1st edn., 2015, pp. 59–63.

18 K. Kinoshita, *J. Electrochem. Soc.*, 1990, **137**, 845–848.

19 H. Tsunoyama, H. Sakurai, N. Ichikuni, Y. Negishi and T. Tsukuda, *Langmuir*, 2004, **20**, 11293–11296.

20 D. Astruc, *Inorg. Chem.*, 2007, **46**, 1884–1894.

21 L. S. Sarma, C. H. Chen, S. M. S. Kumar, G. R. Wang, S. C. Yen, D. G. Liu, H. S. Sheu, K. L. Yu, M. T. Tang, J. F. Lee, C. Bock, K. H. Chen and B. J. Hwang,

Langmuir, 2007, **23**, 5802–5809.

22 A. A. Shutilov, G. A. Zenkovets, I. Y. Pakharukov and I. P. Prosvirin, *Kinet. Catal.*, 2014, **55**, 111–116.

23 J. P. Lange, E. van der Heide, J. van Buijtenen and R. Price, *ChemSusChem*, 2012, **5**, 150–166.

24 D. K. L. Chan, P. L. Cheung and J. C. Yu, *Beilstein J. Nanotechnol.*, 2014, **5**, 689–695.

25 L. C. Sim, K. H. Leong, S. Ibrahim and P. Saravanan, *J. Mater. Chem. A*, 2014, **2**, 5315–5322.

26 S. Fodor, G. Kovacs, K. Hernadi, V. Danciu, L. Baia and Z. Pap, *Catal. Today*, 2017, **284**, 137–145.

27 C. Zhang, Y. Li, Y. Wang and H. He, *Environ. Sci. Technol.*, 2014, **48**, 5816–5822.

28 A. Banerjee and S. H. Mushrif, *J. Phys. Chem. C*, 2018, **122**, 18383–18394.

29 S. Horikoshi and N. Serpone, in *Microwaves in Nanoparticle Synthesis: Fundamentals and Applications*, 2013, pp. 1–24.

30 L. Yang, H. Cheng, Y. Jiang, T. Huang, J. Bao, Z. Sun, Z. Jiang, J. Ma, F. Sun, Q. Liu, T. Yao, H. Deng, S. Wang, M. Zhu and S. Wei, *Nanoscale*, 2015, **7**, 14452–14459.

31 I. Ijaz, E. Gilani, A. Nazir and A. Bukhari, *Green Chem. Lett. Rev.*, 2020, **13**, 59–81.

32 V. S. Cabeza, in *Advances in Microfluidics - New Applications in Biology, Energy, and Materials Sciences*, ed. X.-Y. Yu, IntechOpen, 1st edn., 2016, pp. 385–410.

33 C.-J. Jia and F. Schüth, *Phys.Chem.Chem.Phys*, 2011, **13**, 2457–2487.

34 T. Tsuzuki and P. G. M. C. Cormick, *Mechanochemistry Mech. Alloy. 2003*, 2004, **9**, 5143–5146.

35 M. Takagi, T. Maki, M. Miyahara and K. Mae, *Chem. Eng. J.*, 2004, **101**, 269–276.

36 R. Karnik, F. Gu, P. Basto, C. Cannizzaro, L. Dean, W. Kyei-Manu, R. Langer and O. C. Farokhzad, *Nano Lett.*, 2008, **8**, 2906–2912.

37 A. M. Ealias and M. P. Saravanakumar, *IOP Conf. Ser. Mater. Sci. Eng.*, 2017, **263**, 1–15.

38 F. A. Deorsola and D. Vallauri, *J. Mater. Sci.*, 2011, **46**, 781–786.

39 C. Pereira, A. M. Pereira, C. Fernandes, M. Rocha, R. Mendes, M. P. Fernandez-Garcia, A. Guedes, P. B. Tavares, J.-M. Greneche, J. P. Araujo and C. Freire, *Chem. Mater.*, 2012, **24**, 1496–1504.

40 M. Sankar, N. Dimitratos, D. W. Knight, A. F. Carley, R. Tiruvalam, C. J. Kiely, D. Thomas and G. J. Hutchings, *ChemSusChem*, 2009, **2**, 1145–1151.

41 M. Schmal, in *Heterogeneous Catalysis and its Industrial Applications*, ed. M. Schmal, Springer International Publishing, Sao Paulo, 1st edn., 2016, pp. 161–188.

42 E. Marceau, X. Carrier and M. Che, in *Synthesis of Solid Catalysts*, ed. K. P. de Jong, Wiley-VCH Verlag GmbH & Co., Weinheim, 1st edn., 2009, pp. 59–82.

43 P. Munnik, P. E. de Jongh and K. P. de Jong, *Chem. Rev*, 2015, **115**, 6687–6718.

44 X. Liu, J. G. Khinast and B. J. Glasser, *Chermical Eng. Sci.*, 2008, **63**, 4517–4530.

45 L. Espinosa-Alonso, K. P. de Jong and B. M. Weckhuysen, *Phys. Chem. Chem. Phys.*, 2010, **12**, 97–107.

46 M. Sankar, Q. He, M. Morad, J. Pritchard, S. J. Freakley, J. K. Edwards, S. H. Taylor, D. J. Morgan, A. F. Carley, D. W. Knight, C. J. Kiely and G. J. Hutchings, *ACS Nano*, 2012, **6**, 6600–6613.

47 E. K. Dann, E. K. Gibson, C. R. A. Catlow, P. Collier, T. E. Erden, D. Gianolio, C. Hardacre, A. Kroner, A. Raj, A. Goguet and P. P. Wells, *Chem. Mater.*, 2017, **29**, 7515–7523.

48 C. Louis, in *Synthesis of Solid Catalysts*, ed. K. P. de Jong, Wiley-VCH Verlag GmbH & Co., 1st edn., 2009, pp. 369–391.

49 M. Lok, in *Synthesis of Solid Catalysts*, ed. K. P. de Jong, Wiley-VCH Verlag GmbH & Co., Weinheim, 1st edn., 2009, pp. 135–152.

50 C. Burda, X. Chen, R. Narayanan and M. A. El-Sayed, *Chemistry and properties of nanocrystals of different shapes*, 2005, vol. 105.

51 S. Al-Sayari, A. F. Carley, S. H. Taylor and G. J. Hutchings, *Top. Catal.*, 2007, **44**, 123–128.

52 S. Campisi, M. Schiavoni, C. E. Chan-Thaw and A. Villa, *Catalysts*, 2016, **6**, 1–21.

53 S. Campisi, D. Ferri, A. Villa, W. Wang, D. Wang, O. Kro and L. Prati, *J. Phys. Chem. C*, 2016, **120**, 14027–14033.

54 S. M. Rogers, C. R. A. Catlow, C. E. Chan-Thaw, A. Chutia, N. Jian, R. E. Palmer, M. Perdjon, A. Thetford, N. Dimitratos, A. Villa and P. P. Wells, *ACS Catal.*, 2017, **7**, 2266–2274.

55 L. Prati and A. Villa, *Catalysts*, 2012, **2**, 24–37.

56 P. K. Khanna, P. V. More, J. P. Jawalkar and B. G. Bharate, *Mater. Lett.*, 2009, **63**, 1384–1386.

57 A. Villa, D. Wang, G. M. Veith, F. Vindigni and L. Prati, *Catal. Sci. Technol.*, 2013, **3**, 3036–3041.

58 J. A. Lopez-Sanchez, N. Dimitratos, P. Miedziak, E. Ntainjua, J. K. Edwards, D. Morgan, A. F. Carley, R. Tiruvalam, C. J. Kiely and G. J. Hutchings, *Phys. Chem.*

Chem. Phys., 2008, **10**, 1921–1930.

59 S. Cattaneo, S. J. Freakley, D. J. Morgan, M. Sankar, N. Dimitratos and G. J. Hutchings, *Catal. Sci. Technol.*, 2018, **8**, 1677–1685.

60 N. Dimitratos, J. A. Lopez-Sanchez, D. Morgan, A. F. Carley, R. Tiruvalam, C. J. Kiely, D. Bethell and G. J. Hutchings, *Phys. Chem. Chem. Phys.*, 2009, **11**, 5142–5153.

61 G. Mountrichas, S. Pispas and E. I. Kamitsos, *J. Phys. Chem. C*, 2014, **118**, 22754–22759.

62 N. Moloto, N. Revaprasadu, P. L. Musetha and M. J. Moloto, *J. Nanosci. Nanotechnol.*, 2009, **9**, 4760–4766.

63 G. Muralidharan, L. Subramanian, S. K. Nallamuthu, V. Santhanam and S. Kumar, *Ind. Eng. Chem. Res.*, 2011, **50**, 8786–8791.

64 O. Rac, P. Suchorska-Woźniak, M. Fiedot and H. Teterycz, *Beilstein J. Nanotechnol.*, 2014, **5**, 2192–2201.

65 T. Teranishi and M. Miyake, *Chem. Mater.*, 1998, **4756**, 594–600.

66 Z. S. Pillai and P. V. Kamat, *J. Phys. Chem. B*, 2004, **108**, 945–951.

67 J. Piella, N. G. Bastús and V. Puntes, *Chem. Mater.*, 2016, **28**, 1066–1075.

68 S. H. Pang, C. A. Schoenbaum, D. K. Schwartz and J. W. Medlin, *Nat. Commun.*, 2013, **4**, 1–6.

69 S. M. Rogers, C. R. A. Catlow, C. E. Chan-Thaw, D. Gianolio, E. K. Gibson, A. L. Gould, N. Jian, A. J. Logsdail, R. E. Palmer, L. Prati, N. Dimitratos, A. Villa and P. P. Wells, *ACS Catal.*, 2015, **5**, 4377–4384.

70 L. J. Hoyos, M. Primet, H. Praliaud, I. U. Claude, B. Lyon and A. A. Einstein, *J. Chem. Soc. Faraday. Trans.*, 1992, **88**, 3367–3373.

71 S. wei Liu, R. Guo, X. Sun, J. Liu, W. Pan, Z. Xin, X. Shi, Z. Wang, X. Liu and H. Qin, *J. Energy Inst.*, 2019, **92**, 1610–1617.

72 O. Długosz and M. Banach, *React. Chem. Eng.*, 2020, **5**, 1619–1641.

73 K.-J. Wu, G. M. de Varine Bohan and L. Torrente-Murciano, *React. Chem. Eng.*, 2017, **2**, 116–128.

74 C. Jiménez-González, P. Poechlauer, Q. B. Broxterman, B.-S. Yang, D. am Ende, J. Baird, C. Bertsch, R. E. Hannah, P. Dell'Orco, H. Noorman, S. Yee, R. Reintjens, A. Wells, V. Massonneau and J. Manley, *Org. Process Res. Dev.*, 2011, **15**, 900–911.

75 T. Hendel, M. Wuithschick, F. Kettemann, A. Birnbaum, K. Rademann and J. Polte, *Anal. Chem.*, 2014, **86**, 11115–11124.

76 J. Polte, R. Erler, A. F. Thünemann, S. Sokolov, T. T. Ahner, K. Rademann, F. Emmerling and R. Kraehnert, *ACS Nano*, 2010, **4**, 1076–1082.

77 J. Ma, S. M.-Y. Lee, C. Yi and C.-W. Li, *Lab Chip*, 2017, **17**, 209–226.

78 M. J. Nieves-Remacha, A. A. Kulkarni and K. F. Jensen, *Ind. Eng. Chem. Res.*, 2013, **52**, 8996–9010.

79 H. Löwe, V. Hessel, P. Löb and S. Hubbard, *Org. Process Res. Dev.*, 2006, **10**, 1144–1152.

80 J. Wegner, S. Ceylan and A. Kirschning, *Adv. Synth. Catal.*, 2012, **354**, 17–57.

81 V. Hessel, *Chem. Eng. Technol.*, 2009, **32**, 1655–1681.

82 M. I. Burguete, H. Erythropel, E. Garcia-Verdugo, S. V. Luis and V. Sans, *Green Chem.*, 2008, **10**, 401.

83 E. Shahbazali, V. Hessel, T. Noël and Q. Wang, *Phys. Sci. Rev.*, 2019, **1**, 1–21.

84 G. Hofmann, G. Tofighi, G. Rinke, S. Baier, A. Ewinger, A. Urban, A. Wenka, S. Heideker, A. Jahn, R. Dittmeyer and J.-D. D. Grunwaldt, *J. Phys. Conf. Ser.*, 2016, **712**, 012072.

85 X. Y. Bingwen and L. Li, *Microfluid. Nanofluid*, , DOI:10.1007/s10404-013-1199-4.

86 A. Ghazal, J. P. Lafleur, K. Mortensen, J. P. Kutter, L. Arleth and G. V. Jensen, *Lab Chip*, 2016, **16**, 4263–4295.

87 R. Becker and W. Döring, *Ann. Phys.*, 1935, 719–752.

88 T. J. Woehl, J. E. Evans, I. Arslan, W. D. Ristenpart and N. D. Browning, *ACS Nano*, 2012, **6**, 8599–8610.

89 J. Polte, *CrystEngComm*, 2015, **17**, 6809–6830.

90 V. K. LaMer and R. H. Dineger, *J. Am. Chem. Soc.*, 1950, **72**, 4847–4854.

91 C. B. Whitehead, S. Özkar and R. G. Finke, *Mater. Adv.*, 2021, **2**, 186–235.

92 T. Sugimoto, *J. Colloid Interface Sci.*, 2007, **309**, 106–118.

93 J. Turkevich, P. C. Stevenson and J. Hillier, *Discuss. Faraday Soc.*, 1951, **11**, 55–75.

94 J. Turkevich, P. C. Stevenson, B. J. Turkevich and P. C. Stevenson, *J. Phys. Chem.*, 1953, **57**, 670–673.

95 S. G. Kwon and T. Hyeon, *Small*, 2011, **7**, 2685–2702.

96 N. T. K. Thanh, N. Maclean and S. Mahiddine, *Chem. Rev.*, 2014, **114**, 7610–7630.

97 H. Zheng, R. K. Smith, Y. Jun, C. Kisielowski, U. Dahmen and A. P. Alivisatos, *Science*, 2009, **324**, 1309–1313.

98 E. M. Chan, M. A. Marcus, S. Fakra, M. ElNaggar, R. A. Mathies and A. P.

Alivisatos, *J. Phys. Chem. A*, 2007, **111**, 12210–12215.

99 W. Z. Ostwald, *Zeitschrift für Phys. Chemie*, 1900, **34**, 495–503.

100 B. L. Caetano, C. V. Santilli, S. H. Pulcinelli and V. Briois, *Phase Transitions*, 2011, **84**, 714–725.

101 M. S. Affandi, N. Bidin, M. Abdullah, M. S. A. Aziz, M. Al-Azawi and W. Nugroho, *J. Nanophotonics*, 2015, **9**, 093089.

102 N. Steinfeldt, *Langmuir*, 2012, **28**, 13072–13079.

103 M. Herbst, E. Hofmann and S. Förster, *Langmuir*, 2019, **35**, 11702–11709.

104 A. M. Karim, N. Al Hasan, S. Ivanov, S. Siefert, R. T. Kelly, N. G. Hallfors, A. Benavidez, L. Kovarik, A. Jenkins, R. E. Winans and A. K. Datye, *J. Phys. Chem. C*, 2015, **119**, 13257–13267.

105 I. J. Godfrey, A. J. Dent, I. P. Parkin, S. Maenosono and G. Sankar, *ACS Omega*, 2020, **5**, 13664–13671.

106 R. Becker and W. Doring, *Ann. Phys.*, 1935, **24**, 719–752.

107 P. R. A. F. Garcia, O. Prymak, V. Grasmik, K. Pappert, W. Wlysses, L. Otubo, M. Epple and C. L. P. Oliveira, *Nanoscale Adv.*, 2020, **2**, 225–238.

108 A. Kabelitz, A. Guilherme, M. Joester, U. Reinholz, M. Radtke, R. Bienert, K. Schulz, R. Schmack, R. Kraehnert and F. Emmerling, *CrystEngComm*, 2015, **17**, 8463–8470.

109 M. Harada and Y. Inada, *Langmuir*, 2009, **25**, 6049–6061.

110 M. Harada and H. Einaga, *Langmuir*, 2007, **23**, 6536–6543.

Chapter 2 Materials and Methods

The sol-immobilisation synthesis protocol used for the work presented in this thesis, and the characterisation and testing methods employed to interrogate the subsequently prepared Pd and Au nanoparticle catalysts, are detailed in this chapter. Across all work, the prepared colloidal and TiO_2 supported metal NPs have been characterised by ultraviolet-visible spectroscopy (UV-Vis), transmission electron microscopy (TEM), scanning TEM (STEM) coupled with energy dispersive X-ray (EDX) and electron energy loss (EELs) spectroscopies, as well as Fourier transform infrared (FTIR) and diffuse reflectance infrared Fourier transform spectroscopy (DRIFTS). Metal loadings for the prepared catalysts were measured *via* microwave plasma atomic emission spectroscopy (MP-AES) and both the nature of their chemical oxidation states, and their physical properties, were analysed on a per atom average using X-ray absorption fine structure (XAFS) spectroscopy. For the activity tested Pd catalysts (Chapter 3), the nature and strength of the acidic surface sites on the Pd surfaces were measured *via* temperature programmed desorption/reduction (TPD/TPR) using NH_3 and H_2 as probe molecules, respectively. Decomposition products of the Pd nanoparticles catalysts, PVA and TiO_2 were also measured using thermogravimetric analysis (TGA). Lastly, the fouling of Au NPs on the microfluidic cell channel's walls (Chapter 6) was examined using X-ray fluorescence (XRF).

2.1 Reagents and Materials

The suppliers of all chemical reagents and assorted materials used for catalytic synthesis and for beamline studies are detailed in *Table 2-1*, *Table 2-2* and *Table 2-3*.

Table 2-1. *Chemical reagents used in the synthesis of colloidal Pd nanoparticles and for furfural hydrogenation testing in Chapters 3 and 4, respectively.*

Reagent	Supplier	Chapter
Potassium tetrachloropalladate (K_2PdCl_4, ≥ 99.99 %, trace metal basis)	Merck	3
Sodium tetrachloropalladate (Na_2PdCl_4, ≥ 99.99 %, trace metal basis)	Merck	3 & 4
Sodium borohydride ($NaBH_4$)	Merck	3 & 4
Polyvinyl alcohol (PVA, M_w = 9000-10,000 g mol^{-1} 80 % hydrolysed)	Merck	3 & 4
Concentrated sulfuric acid (H_2SO_4, 95-97 %)	Merck	3 & 4
Methanol (MeOH, ≥ 99.99 %)	Merck	3 & 4
Ethanol (EtOH, ≥ 99.99 %)	Merck	3
1-Propanol (PrOH, ≥ 99.99 %)	Merck	3
*Iso*propyl alcohol (IPA, ≥ 99.99 %)	Merck	3 & 4
tert-Butyl alcohol (*t*BuOH, ≥ 99.99 %)	Merck	3
Furfural (99 %)	Merck	4
Dodecanol (98 %)	Merck	4

Table 2-2. *Chemical reagents used for the synthesis and measurement of Au/TiO_2 and Au colloidal nanoparticle formation as presented in Chapters 5 and 6, respectively.*

Reagent	Supplier	Chapter
Hydrogen tetrachloroaurate (III) hydrate ($HAuCl_4 \cdot xH_2O$, ≥ 99.9 % trace metal basis)	Merck	5 & 6
$NaBH_4$	Merck	5 & 6
Dimethylamine borane (DMAB)	Merck	6
PVA (M_w = 9000-10,000 g mol^{-1} 80 % hydrolysed)	Merck	5 & 6
TiO_2 (P25)	Degussa	5
Sodium hydroxide (NaOH, pellets)	Supelco	6
Sulfuric acid (H_2SO_4, 37 %)	Merck	5
Octadecafluorodecahydronaphthalene (PFD, 95 %)	Merck	6
1*H*,1*H*,2*H*,2*H*-Perfluoro-1-octanol (PO, 97 %)	Merck	6

Table 2-3. *Materials and equipment used in the development of a microfluidic device for the measurement of colloidal Au NP formation as presented in Chapter 6.*

Material / Equipment	Supplier	Chapter
PTFE tubing (varying inner diameters)	Cole-Parmer	6
PEEK fittings	Col-Parmer	6
Masterflex® C/L® Peristaltic pump	Cole-Parmer	6
Aladdin *AL1000HP* syringe pump	World Precision Instruments	6
Aladdin *AL4000* double syringe pump	World Precision Instruments	6

2.2 Sol-Immobilisation Synthesis of Metal Nanoparticles

All metal nanoparticles were prepared following a variation of a standard sol-immobilisation method; systematic changes were made to the pre- and post-immobilisation steps, depending on the chapter of interest, to investigate their resulting influence on NP formation.[1–5] For the work presented in this thesis, colloidal synthesis has been performed by reducing a metal salt solution, prepared using either K_2PdCl_4, Na_2PdCl_4 or $HAuCl_4{\cdot}xH_2O$, in the presence of a stabilising agent, for example PVA, to limit unwanted coalescence and collapse of NPs *via* steric and/or electrostatic effects, and form small NPs with narrow size distributions.[6–8] The following reducing agents were used in this work: for Chapters 3-5, supported Pd/TiO_2 and Au/TiO_2 catalysts were prepared using $NaBH_4$ to ensure rapid and complete reduction of the aqueous metal precursor to colloidal monomer units.[9] However, the rapid decomposition of $NaBH_4$ in water releases large quantities of $H_{2(g)}$, which is an issue when measuring *in situ* colloidal Au formation. The colloids prepared in Chapter 6 were therefore reduced using dimethylamine borane (DMAB), a milder reducing agent, to suppress the evolution of $H_{2(g)}$.[10] Synthesised NPs in this work were all supported on TiO_2 (P25) allowing improvements in catalytic properties to be compared against prior work in the group;[5,11] the low toxicity and high physical and chemical stabilities of TiO_2 affords strong metal-support interactions during acidification and loading of the active component, however, this is not a key facet of the work. Systematic variations made during metal NP synthesis in each chapter are outlined in their respective sections. Briefly, the employed parameters explore the influence of the composition of the synthesis solvent,[11,12] the nature of the stabilising and reducing agents,[8,13] the reduction temperature (1-75 °C),[5] and the concentration of the metal precursor salt on NP properties.[6]

2.3 Ultraviolet-Visible Spectroscopy

Ultraviolet-visible spectroscopy describes the absorbance and reflectance of light in the 200-800 nm region of the electromagnetic spectrum. Chromophoric materials can be irradiated using a UV light source causing promotion of ground state electrons to higher unoccupied molecular orbitals; these transitions allow for the excitation of π-, non-bonding or *d*-band electrons. This is calculated using the Beer-Lambert law, which describes how the molar extinction coefficient, ε, the concentration of the absorbing species, c, and the path length, l, all contribute towards the absorbance of a solution, A.

Changes in chromophoric properties are easily observed in this work during reduction of the metallic precursor salt solutions from the Pd^{2+}/Au^{3+} oxidation state(s) to the zero-valent colloids, which is exceptionally useful when studying the initial formation of NPs. For the Pd catalysts, removal of ligand-to-metal charge transfer (LMCT) and *d-d* transitional absorption bands across the UV-Vis spectrum, as well as formation of a broad and continuous absorption band, highlighted that chemical reduction had taken place and that the colloidal Pd had been formed.[14,15] The metal of the precursor salt has influence on the features measured in the UV-Vis spectrum during reduction; for Ag-, Cu- and Au-based colloidal solutions, the evolution of a broad absorption band does not appear. Instead, a surface plasmon resonance (SPR) band is observed upon reduction.[16,17] On exposure to light, the oscillating electromagnetic field of the light induces a collective coherent oscillation of electrons in the metal conduction band of the metal NP. Oscillations around the particle surface lead to charge separation, and subsequent dipole oscillations along the direction of the light's electric field occur which are deemed as SPR when the amplitude of the oscillation reaches a specific frequency (*Figure 2-1*).[18] Strong absorption of the incident light results from the SPR, and can therefore be measured using UV-Vis spectrometers. SPR band intensity and wavelength have been shown to be dependent on NP properties that affect the electron charge density on the particle surface, such as: metal type, particle size, shape, structure and composition.[3,19,20] This technique is known to be very useful in quantifying NPs < 20 nm; however, when NP size is < 10 nm, the SPR band of Au NPs is dampened due to phase changes resulting from the increased rate of electron-surface oscillations compared to larger particles.[21]

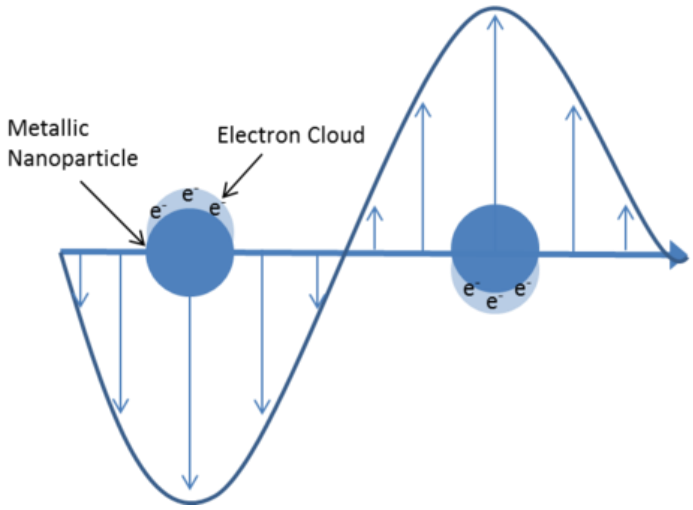

Figure 2-1. *Illustration of the surface plasmon resonance for a metallic sphere; image taken from www.Nanohybrids.net/pages/plasmonics.*[22]

UV-Vis data of the different Pd and Au solutions and colloids were acquired by placing 4 mL of the solution into a quartz cuvette which were run against a blank of the corresponding solvent solution, this acted as the background reference. Measurements were made using a Shimadzu UV-1800 UV-Vis spectrophotometer.

2.4 Microscopy and Sample Imaging

2.4.1 Transmission Electron Microscopy

Transmission electron microscopy allows for the morphologies of catalyst surfaces to be observed on nanometre scales, enabling surface NP particle sizes and distributions to be measured and calculated, respectively. Synthesis of metal NPs through a sol-immobilisation procedure yields particles with average sizes ranging from < 1 to 100 nm, pushing the limit of what light microscopes can effectively image. Instead, electron microscopes are used to achieve higher magnification, by treating electrons as both waves and particles, described by the *de Broglie* equation (*Equation 2-1*).[23] Adjusting the velocity of the electrons can yield the desired wavelength for use during TEM imaging.

$$\lambda = \frac{h}{\rho}$$

Equation 2-1. *The de Broglie equation, where λ is the wavelength of light, h is Planck's constant (6.626 × 10^{-34} J s) and ρ is the momentum of light (velocity × mass).*[23]

In a conventional electron microscope (*Figure 2-2*), an electron beam is generated through the emission of electrons from a tungsten filament located at the top of the microscope under an atmosphere of ~10^{-5} mbar. The generated electron beam is then focussed by a series of condenser lenses whilst travelling toward the sample inside of a vacuum chamber, only allowing electrons within a small energy range to pass through, giving the electron beam a well-defined energy.[24] Interaction of the beam and the sample is dependent on sample thickness and atomic number of the sample, the electron beam can therefore be absorbed or scattered by differing degrees. Post-sample interaction, the electron beam is spread by projection lenses onto a phosphorescent screen allowing for observations to be made by eye. Finally, the electron beam is converted into a digital image by a charged couple device (CCD) fitted to the microscope.

TEM measurements were performed at the Research Complex at Harwell (RCaH), Didcot, U.K. using the Gatan Microscopy suite software to view and acquire NP images. Catalyst

samples were first prepared by adding < 10 mg of the solid sample in high purity ethanol and sonicated for 15 minutes to ensure complete dispersion. 40 µL of the suspension was then pipetted onto a holey carbon film supported on a 300 mesh Cu TEM grid. The grids were then left at room temperature to allow for any remaining solvent to evaporate before insertion of the grid into the microscope. The microscope used was a JEOL JEM 2100 EM with an acceleration voltage of 200 KeV. ImageJ software was used to display the NP images and calculate the average NP diameter for each catalyst with a sample population of between 200–300 NPs.[25]

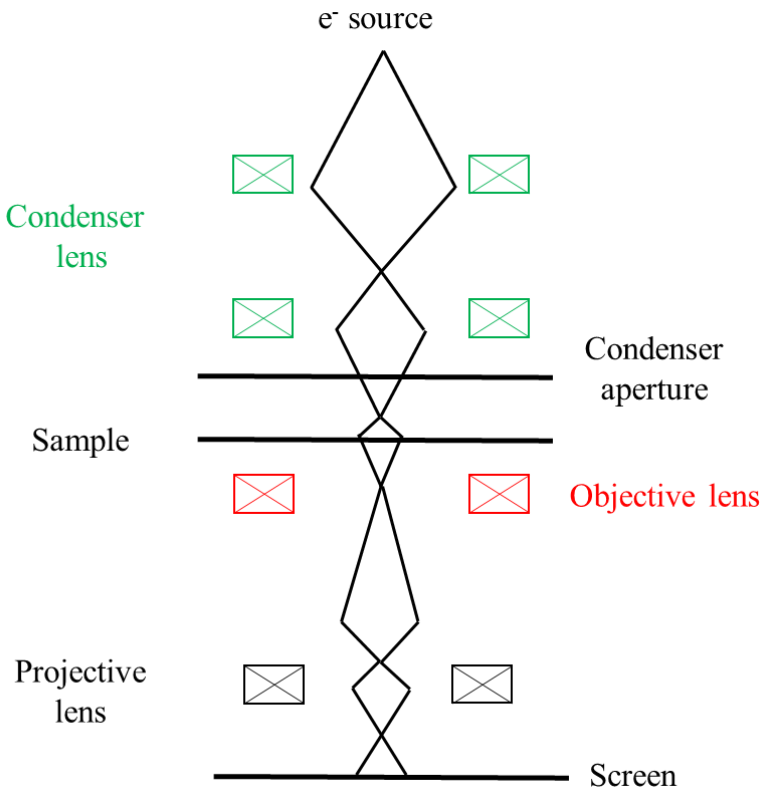

Figure 2-2. *Simplistic schematic of a transmission electron microscope. The path of the electron beam is shown from the electron source toward the viewing screen; image is adapted from Atomic World, http://www.hk-phy.org/atomic_world/tem/tem02_e.html.*[24]

2.4.2 Scanning TEM and High Angle Annular Dark Field and Bright Field Imaging Modes

Scanning TEM was used to acquire images at higher magnification and resolution than is capable with a conventional electron microscope. STEM imaging is performed in the same way as with TEM; however, once the electron source beam is accelerated to high energy, it

is passed through a high quality magnetic lens, projecting a highly demagnified image of the electron source on the sample, producing a focussed probe that is scanned to generate the images.[26] Three main imaging modes are utilised in STEM that are based on the path of electrons scattering from the sample (*Figure 2-3*):

(1) High angle annular dark field imaging (HAADF), where scattered electrons are collected by the HAADF-STEM detector in greater quantities than can pass through objective apertures of the microscope. Detection at a high angle means that electrons are scattered from the nucleus of sample atoms, making the technique highly sensitive to changes in the atomic number of the sample.

(2) Dark field (DF): much like HAADF, dark field electrons are collected by the detector after they have been scattered away from the incident direction. Here, the atomic number of the scattered atoms influences the image. Heavier atoms such as Au and Pd can therefore give brighter regions against dark backgrounds due to the higher number of electrons applicable for scattering.

(3) Bright field (BF): Due to the electron source beam not travelling close to the sample atom centres, the electrons suffer limited change in their angular coordinates after interaction and subsequent scattering, they are then collected by the detector, with heavier atoms giving a darker response against lighter backgrounds.

Samples imaged using STEM were prepared in the same way as samples for standard electron microscope, however, the solution was pipetted onto a 300 mesh holey carbon Cu grid instead. BF and HAADF STEM analysis was performed at the electron Physical Science Imaging Centre (ePSIC) facility on the I14 beamline at Diamond Light Source (DLS), Didcot, U.K. using a JEOL-ARM 2000 Aberration-Corrected Transmission Electron Microscope and at Johnson Matthey Tech Centre (JMTC), Sonning Common, Reading, U.K. using a JEOL JEM 2800 STEM; both microscopes were run at an accelerating voltage of 200 KeV.

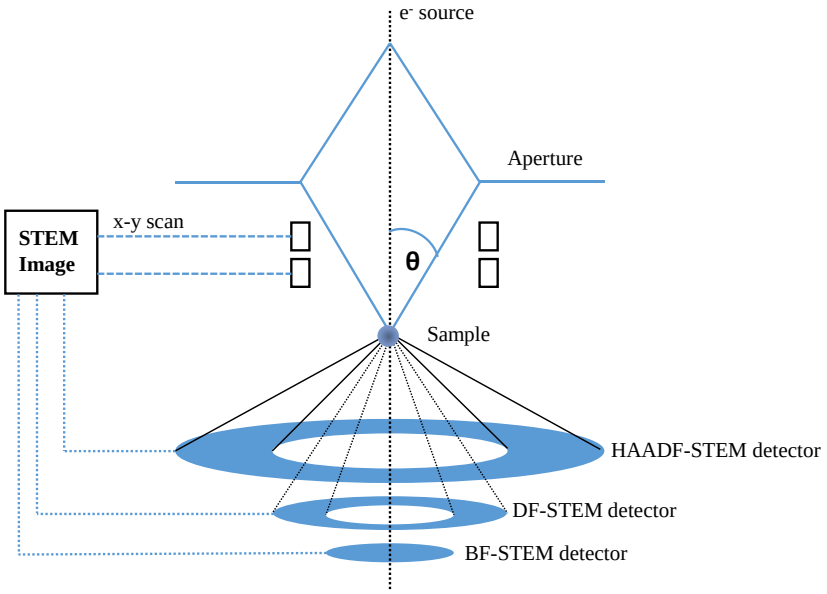

Figure 2-3. *Schematic diagram of the possible scanning transmission electron microscopy (STEM) imaging modes. The position of the detectors used in High Angle Annular (HAAFD), Dark Field (DF) and Bright Field (BF) modes are shown; image adapted* Z. Li, *Scanning transmission electron microscopy studies of mono- and bimetallic nanoclusters, Elsevier Ltd, 1st edn.,* ***2012****, vol. 3.*[26]

2.4.3 Energy Dispersive X-ray Analysis

Energy dispersive X-ray analysis is an element specific characterisation X-ray technique commonly coupled with electron microscopy to give an overall mapping of the sample surface. EDX analysis works on a similar principle to X-ray fluorescence (section 2.10); briefly, an electron beam with energy of 10-20 KeV strikes the sample, resulting in the ionisation of a core-level electron and the formation a core-hole in its place. An electron from a higher valence drops to fill the vacancy, and the difference in energy between the higher and lower orbitals is the element specific X-ray fluorescence that is detected by the EDX detector. Movement of the electron beam across the surface yields a combined image of the different elements in the sample, however, the X-ray intensity of the device is low and so to build up a complete map scan can take long periods of acquisition time.[27] The measured fluorescence line is named after the origin of the core shell, e.g. K-edge is the electron excitation from the 1*s* orbital, the origins of X-ray nomenclature can be found in section 2.8.

EDX analysis was performed simultaneously with STEM imaging, using JEOL EDX detectors attached to the microscope at JMTC (JEOL JEM 2800 STEM, 200 kV) and performed by Dr. Briceno de Gutierrez of JMTC, Sonning Common, Reading, UK.

2.4.4 Electron Energy Loss Spectroscopy

Electron energy loss spectroscopy can also be used to determine the elemental information of the sample, however, the process of analysis for EELS is different to EDX. In EELS, electron spectrometers record the energy lost by the primary electron beam as a result of inelastic interactions with the specimen atoms, ranging from plasmon interactions to ionisation processes. From these processes, structural and electronic information of specific elements in the sample can be acquired.[28] Inelastic scattering of the electron beam on interaction with the sample leads to a loss in energy, it is the distribution of these scattered electrons that provides element specific information. Interaction of the source beam and the sample is however limited to thin atomic layering and use of a low energy electron source beam (100-1000 eV).[29] The valence region (energy loss is < 50 eV) contains information concerning the band structure of the sample atoms. In this region intense features arise from the dielectric properties, surface plasmon resonance or transitions from the valence to conduction bands of the sample.[28] At higher energy loss (> 50 eV), the characteristic features (ionisation edges) are prominent due to the lower proportion of inelastically scattered electrons, where a core-level electron absorbs enough energy from the source beam to be excited toward the continuum.[30] It should be noted that the most intense peak is recorded at 0 eV, corresponding to the zero-loss peak, a peak where electrons are not scattered in the specimen but have been scattered elastically by interaction with the atomic nuclei (*Figure 2-4*).[28,31]

EELS was performed at the ePSIC facility on the I14 beamline at the same time the STEM images were acquired at DLS, Didcot, U.K. using a JEOL-ARM 2000 Aberration-Corrected Transmission Electron Microscope by Dr. Dung Tang of JMTC, Sonning Common, Reading, U.K.

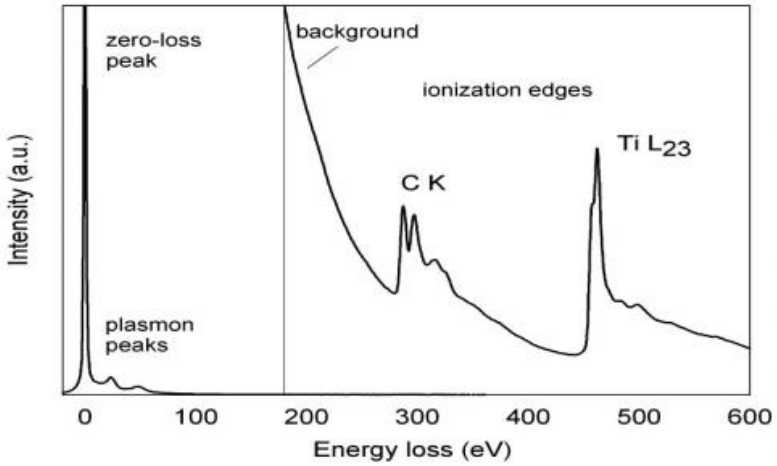

Figure 2-4. *EELS spectrum showing the ionisation edges and zero loss peaks over a sample spectrum; image taken from Hofer et al., IOP Conf. Ser.: Mat. Sci. Eng., 2016,* ***109****, 1-9.*[28]

2.5 Infrared Spectroscopy

Infrared spectroscopy is a commonly employed laboratory-based technique, used to detect molecular vibrations within the infrared region of the electromagnetic spectrum (400-4000 cm^{-1}). Structural information, e.g. functional groups, are described by these molecular vibrations. Of these functional groups, the vibrations can be separated by two types of stretching modes, symmetric and antisymmetric, and four types of bending vibrations, scissoring, rocking, wagging and twisting.[32] For functional groups to be IR active, the electric dipole of the sample molecule must change during vibration and therefore, must obey the vibrational selection rule (*Equation 2-2*).

$$\Delta v = \pm 1$$

Equation 2-2. *Vibrational selection rule for harmonic oscillation transition, where v is the vibrational quantum number.*

The ability to characterise the association of liquid and gas phase probe molecules to solid surfaces has made the technique especially useful in catalyst characterisation. The strength of the acidity (e.g. Brønsted –OH surface groups and Lewis cationic sites) and basic nature of surface sites on the metal oxide supports can be quantified using probe molecules coupled with IR absorption spectroscopies (e.g. FTIR, DRIFTS). For these acidic sites, basic probe molecules such as pyridine, acetonitrile, NH_3 and other amines are generally used.[33,34] The use of compounds containing NH functionalities are best suited to elucidate the strength of surface acid sites, whereby the binding of the NH containing compounds displays IR bands

at ~ 1475 and 1689 cm^{-1}, suggest the adsorption of NH_x onto Brønsted acid sites, whilst adsorption bands observed at ~ 1140, 1450 and 1580 cm^{-1} infer the association of the probe molecule with Lewis acid sites.[35–38]

Basic surface sites, e.g. free oxygen atoms on a metal oxide surface, however are identified using probe molecules with underlying acidic natures, i.e. CO_2 and MeOH.[39] Association of the probe molecule with the surface gives rise to different binding modes, e.g. the adsorption of CO_2 yields mono- and bidentate carbonate species; bridge coordinated HCO_3^-, and linearly coordinated CO_2, are utilised to measure the basic strength of a surface site.[33]

It is also possible to use an IR active substance to characterise available metal nanoparticle surface sites through shifts in their band intensities, and their characteristic wavelengths.[32] CO is a commonly used probe molecule and can be identified by IR bands between 1800 and 2200 cm^{-1}, corresponding to both linear and bridged surface sites (*Figure 2-5*). By using CO as a probe molecule, variations to NP surface availability can be identified *via* shifts in the frequency of adsorption bands, resultant from changes to the electron density of the occupied π* CO molecule bonding orbital.[40]

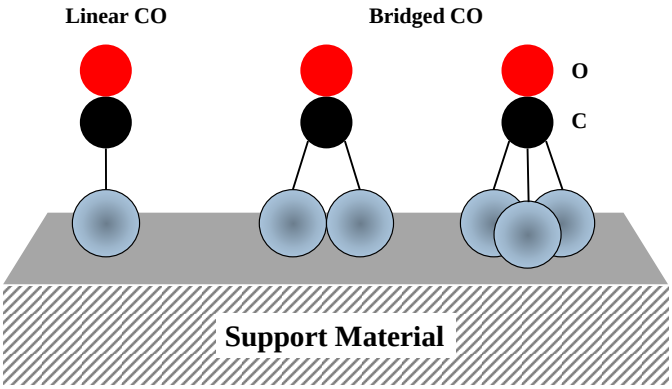

Figure 2-5. *Simplistic diagram showing the types of linear and bridged Pd NP surface sites available for CO adsorption studies.*

For the purposes of this body of work, the acid surface sites were probed using NH_3 (Chapter 4), and the available surface sites of metal NPs were measured using CO (Chapters 3 and 4).

2.5.1 Transmission Infrared

The highly absorbent nature of solids makes transmission IR measurements quiet difficult. To circumvent this issue, samples for transmission IR can be prepared as thin, self-supporting pellets made from ≤ 30 mg of sample. As a known mass of the catalyst is used,

the surface coverage of the probe molecule can be determined quantitatively. During transmission IR measurements, a collimated IR beam is split into two paths, one is directed towards a stationary mirror, and the other moves towards a moving mirror. The constant movement of one mirror back and forth creates a changing path difference between the reflected beams, known as a sinusoidal signal, or more commonly, an interferogram. The interferogram contains information on the absorption intensities at each wavelength in the specified IR region, and is translated into the IR spectrum by Fourier transform.[41]

Transmission IR spectra of the supported NP were acquired by first preparing a thin pellet (13 mm in diameter) from ~ 30 mg of the fresh powder catalyst. After being placed into an air-tight transmission cell, pure $He_{(g)}$ (30 mL min^{-1}) was used to purge the sample and sample surface for 30 minutes. After this purging period, the He flow rate was reduced (20 mL min^{-1}), and 1 minute pulses of 10 % CO/He (10 mL min^{-1}) were introduced over the sample. Once the surface became saturated with CO, excess gaseous CO, physisorbed to the surface and remaining in the transmission cell chamber, was removed by purging the chamber with He (30 mL min^{-1}) for 30 minutes. Background spectra were obtained following this and were subtracted to give IR spectra detailing the available NP surface sites. IR spectra were obtained using a Nicolet iS10 spectrometer at a spectral resolution of 4 cm^{-1} accumulating 64 scans. Data processing was performed using the OMNIC software package.

2.5.2 Diffuse Reflectance Infrared Fourier Transform Spectroscopy

Characterisation of IR active species within samples that are too absorbing for transmission experiments can be achieved by measuring the diffuse reflectance of the incidence beam from the sample surface. For DRIFTS measurements, minimal quantities of sample are required (< 10 mg), and, so, can be loaded directly in the DRIFTS cell, with minimal sample preparation. Interaction of the IR source beam with the sample surface leads to different processes occurring: absorption, specular reflection, internal reflection and diffuse reflection. In DRIFTS studies, it is the diffusely scattered IR radiation that is considered. As the sample is irradiated, the IR beam is not only reflected from the surface, it also penetrates the sample, causing multiple reflective events beneath the surface. The resultant IR radiation is scattered in every direction from the sample and is focussed and directed to the detector *via* mirrors in specific positions surrounding the sample cell (*Figure 2-6*). Due to the increasing signal loss as the IR radiation bounces off of each subsequent mirror, a highly sensitive detector is necessary; a mercury cadmium telluride (MCT) detector is frequently used for measurements of this kind.[43]

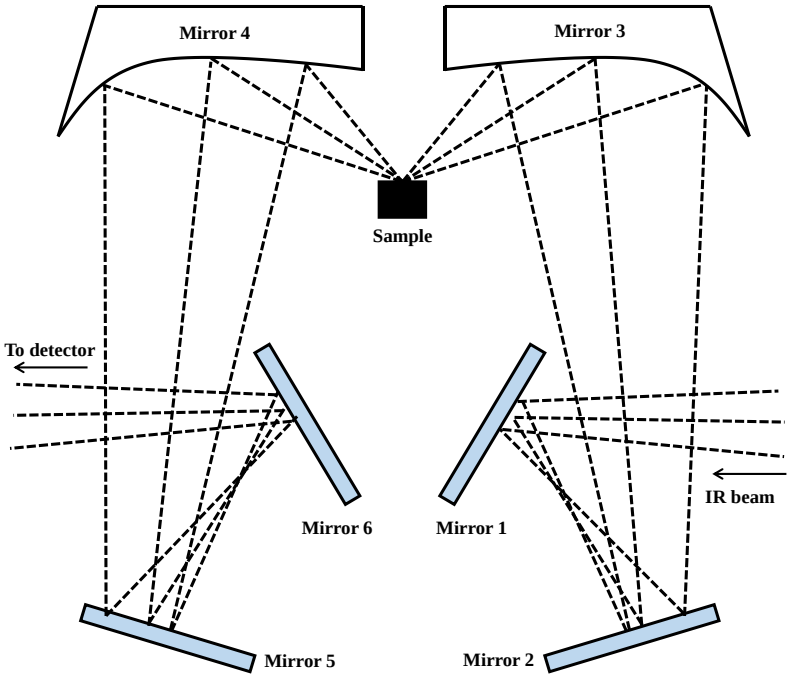

Figure 2-6. *Schematic of the DRIFT optical pathway from start point to detector in a praying mantis cell; image adapted from A. M. McCullagh et al., Top. Catal., 2021, DOI:10.1007/s11244-021-01435-y.*[42]

In this body of work, DRIFTS measurements were collected in conjunction with temperature programmed desorption studies of NH_3 over Pd-based catalysts (Chapter 4). DRIFTS datasets were acquired using a Harrick praying mantis DRIFTS cell integrated with an Agilent Carey 680 Fourier-transform infrared spectrometer. Data was recorded taking 64 scans at 4 cm^{-1} resolution using a high-sensitivity liquid nitrogen cooled MCT detector. Two experimental procedures were used; (1) pre-reduction of the sample surface performed in 4 % H_2/He (40 mL min^{-1}) for 30 minutes at 150 °C and (2) pre-treatment in He (40 mL min^{-1}) at 150 °C for 30 minutes. The cell was then cooled to 25 °C in He (40 mL min^{-1}). The sample was then heated to 100 °C, once at temperature, 5 % NH_3/He (40 mL min^{-1}) was introduced until the surface was adequately saturated. Once saturated, the gaseous mixture was switched to He (40 mL min^{-1}) and heated to 450 °C (10 °C min^{-1}). Background DRIFTS spectra were recorded in flowing He (40 mL min^{-1}) at 100 °C and subtracted from each sample spectrum.

2.6 Thermoanalytical Characterisation Techniques

Thermal analysis covers a range of characterisation techniques where the physical properties of a substance are measured as a function of temperature.[44] Typically a linear heating profile

is applied, with heating rates specified depending on the process under investigation and the capabilities of the instrument's furnace/sensor.

2.6.1 Temperature Programmed Desorption

Temperature programmed desorption is a thermoanalytical technique which enables the structure and quantity of an adsorbed species to be determined by subjecting the sample of interest to a temperature ramp. The use of various substrates during TPD measurements allows for the acidic or basic nature of the sample surface to be realised and elucidates the method of decomposition of the adsorbed species at specific temperatures.[45]

TPD experiments typically consist of three main steps:

(1) Pre-treatment of the sample. During this step, the sample is purged with an inert gas (He, N_2, Ar) at a temperature high enough to adequately clean the sample surface without altering the sample morphology, i.e. preventing artificial NP agglomeration.

(2) Adsorption of the probe molecule (acidic surfaces: NH_3, pyridine etc., basic surfaces: CO_2, methanol) at room temperature.[33,46] The adsorption process occurs until either a specific surface coverage or complete saturation is achieved.

(3) Desorption of the adsorbed species occurs *via* linear heating of the sample whilst the sample is exposed to a constant flow of an inert gas, which carries the desorbed species towards the detector. Observation of decomposition products at increased temperature is a common occurrence in a vast number of TPD experiments.

TPD measurements were acquired as described in section ***2.5.2***; briefly, samples were analysed as close to operating conditions as feasible, therefore, the common catalyst heat pre-treatment to remove surface species was not performed. Instead, the sample was purged with NH_3 and a heating ramp from 25 to 450 °C was set. The adsorption and desorption of NH_3 was monitored using a mass spectrometer (Hiden QGA) ($m/z = 17$), as well as monitoring the outlet for H_2 ($m/z = 2$), N_2 (m/z = 14), H_2O ($m/z = 16$) and the carrier gas He ($m/z = 4$).

2.6.2 Temperature Programmed Reduction

Temperature programmed reduction using H_2 (H_2-TPR) is a useful technique to determine the optimum reducing conditions for both supported and unsupported metal oxide catalysts.[47,48] Further to this, the consumption and production of H_2 on the sample surface can be identified.[49,50] TPR reactions are monitored using a thermal conductivity detector

(TCD) (section 2.11.2), whereby the consumption, and production, of the reducing gas is measured, generating a spectrum where the maximum reduction temperature, T_m, can be found. The parameters required for successful TPR measurements with improved sensitivity were initially investigated by Monti and Baiker who defined the characteristic figure, *K (Equation 2-3)*.[51]

$$K = \frac{S_0}{F\,C_0}$$

Equation 2-3. *Definition of the characteristic number K discovered by Monti and Baiker, where S_0 is the quantity of reducible species (µmol), F is the reducing gas flow rate (mL min^{-1}) and C_0 is the $[H_2]$ in the gas feed (µmol mL).*[51]

The use of a heating rate between 6 and 18 K min^{-1} must be employed to yield a *K* value within the desired limit, $0.9 < K < 2.3$ min; in cases of $K < 0.9$ min, the sensitivity of the instrument becomes too low for adequate or reliable reduction profiles to be acquired, when $K > 2.3$ min, the consumption of H_2 becomes greater than the ideal $\frac{2}{3}$ H_2 consumption proposed for acceptable sample reduction.[51] Reduction of the investigated species is assumed to occur *via* first-order kinetics with respect to the sample and the reducing gas.[52] Further work by Malet and Caballero adapted the above equation to include the heating rate, *β*, allowing for a new parameter to be described: *P* (*Equation 2-4*).[53]

$$P = \frac{\beta\,S_0}{F\,C_0}$$

Equation 2-4. *Definition of the characteristic parameter P as described by Malet and Caballero, where β is the heating ramp rate (K min^{-1}), S_0 is the quantity of reducible species (µmol), F is the reducing gas flow rate (mL min^{-1}) and C_0 is the $[H_2]$ in the gas feed (µmol ml^{-1}).*[53]

In their work, Malet and Caballero demonstrated that the value of this new parameter, *P*, describes the resolution of the reduction profile and can be used to show multi-step reduction mechanisms, whereby $P < 20$ K to achieve a usable resolution.[53] Whilst changes to the ratio of the heating rate and initial concentration of the reducing gas feed are important in displacing the position of the T_m, the profile shape is dependent on the mass of the catalyst, i.e. the initial quantity of reducible surface sites.[53] If the sample size is too large, the resolution will be lost due to mass-transfer limitations giving non-homogeneous reduction across the catalyst.[54]

The ability of Pd to readily activate hydrogen at sub ambient temperatures has been known for many years.[55,56] Resultant from this is the formation of Pd hydride, whereby hydrogen atoms occupy interstitial sites within the Pd lattice.[56] As the temperature of reduction increases reaches between 50-80 °C the hydride decomposes reforming metallic Pd, this temperature has also been found to be linked to increases in crystallite size.[57–60] This causes the decomposition process to result in more H_2 to be observed within the eluent gas, producing a negative peak in the TPR spectrum.

2.6.3 Thermogravimetric Analysis

Thermogravimetric analysis is a widely utilised technique for determining decomposition and combustion products, coke formation and phase transitions by monitoring a sample's weight loss or weight gain during a temperature program. The methodology developed by Honda in 1915 measured the weight loss of a sample using a thermo-balance, typically 0.1 µg precision, and compared to an empty crucible reference.[61,62] Between 10-20 mg of sample is placed into a crucible and subjected to increasing temperature under an inert or reactant gas stream.

2.7 Microwave Plasma-Atomic Emission Spectroscopy

Microwave plasma–atomic emission spectroscopy is used for calculating the metal wt. % loading of the fresh Pd catalysts. This method was chosen due to its greater accuracy (ppm) when compared to elemental quantification using energy dispersive X-ray analysis (0.1 wt. % sensitivity). Analysis involves an initial step of digesting the samples, three 100 mg samples of each powdered catalyst, by separating the metallic species from the support material using aqua regia (1:3 HNO_3:HCl, both analytical grade). The sample and aqua regia solutions are transferred into PTFE tubes, sealed, and placed into an Atom Paar Microwave 3000 centrifuge, along with an aqua regia blank. The samples are then heated to 200 °C and held for 40 minutes before cooling to room temperature. Post digestion these samples are then diluted to 10 vol. % solutions using deionised water (18.2 MΩ cm). Support particulates are removed from the solutions before analysis by filtering through PTFE syringe filters (Cole-Parmer, 0.22 µm pore size, and 50 mm diameter). Standard solutions prepared at Pd concentrations ranging from 1-20 ppm were prepared using a 1000 ppm Pd stock solution (10 % HCl, VWR) and a 10 % aqua regia solution. These standards were loaded for analysis along with samples of 10 % aqua regia and used to calibrate the spectrometer. Calibration curves at the four wavelengths were measured using

standards prepared at 1, 2, 5, 10, 12.5, 15, and 20 ppm Pd in 10 vol. % aqua regia from a 1000 ppm Pd stock solution (10 % HCl, VWR), with an associated error in the calibration standards of 10 %. A test sample was always prepared at 7 ppm to validate the reliability of the standards (*Figure 2-7*). All standards, blanks and samples are vaporised and passed through a microwave induced plasma, exciting electrons in the sample to higher energy states. On the return of the electrons to their initial ground state, a specific and characteristic emission is detected using an Agilent Technologies 4100 MP-AES at four wavelengths of light corresponding to atomic transitions of the sample material.

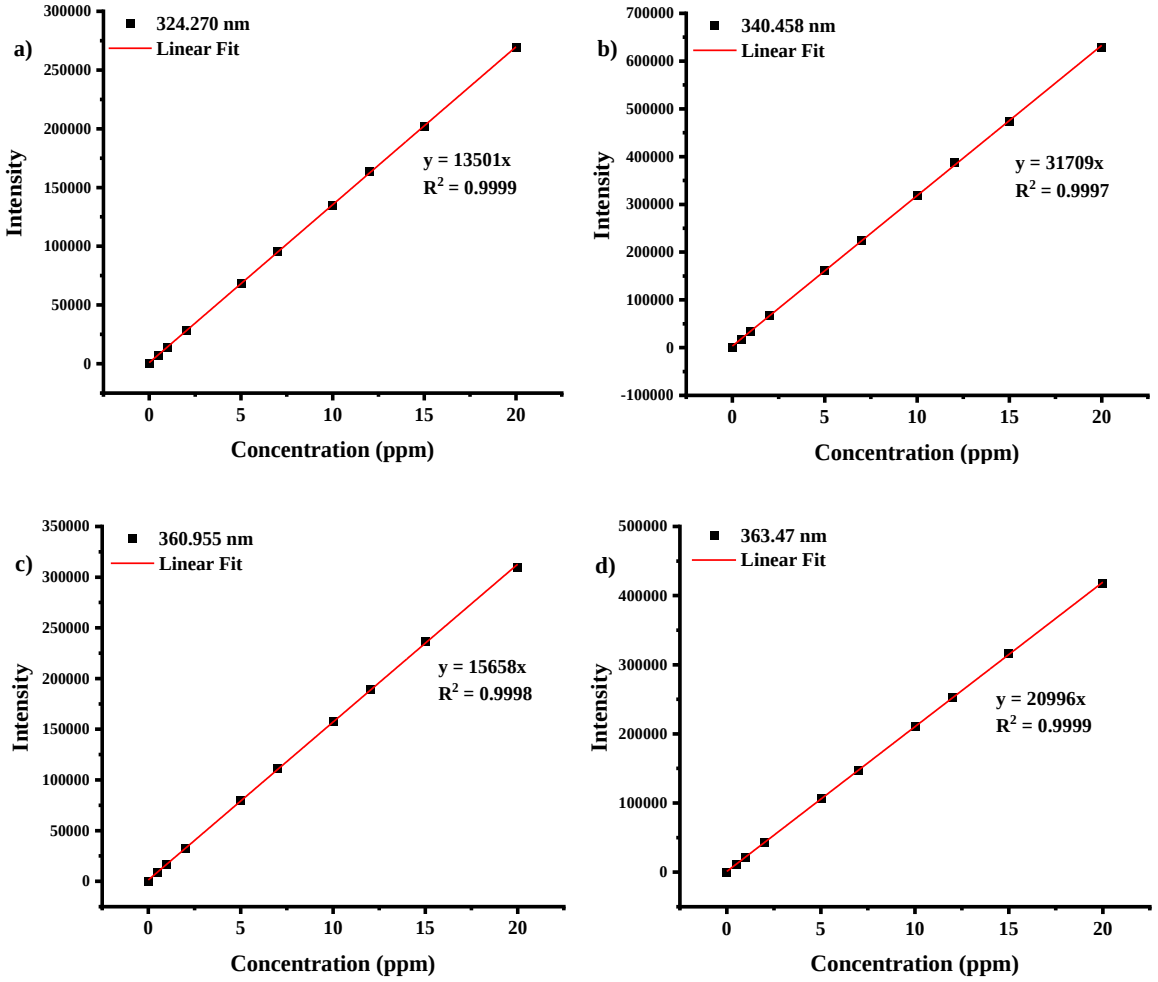

Figure 2-7. *Calibration curves for microwave plasma – atomic emission spectroscopy used to analyse the wt. % Pd loading of all catalysts in this thesis. Four different wavelengths of Pd were measured, a) 324.270 nm, b) 340.458 nm, c) 360.955 nm and d) 363.47 nm. A test sample was plotted against each curve to examine the accuracy of the Pd standards, this was at Pd concentration of 7 ppm.*

2.8 X-ray Absorption Fine Structure

X-ray absorption fine structure is an element specific technique that describes the chemical and physical properties of materials through the absorption of X-rays. Interaction of a sample at energies near and above the core-level binding energies of the electron result in the excitation of an electron from a core orbital in a photoelectric effect. This affords sensitivity to the formal oxidation state, coordination geometry, bond distances and coordination number of the absorbing atom. Importantly, crystallinity is not a necessity for XAFS experiments, making it uniquely placed as an X-ray technique capable of measuring non-crystalline and disordered materials, such as solutions.[30] Furthermore, the highly penetrating nature of X-rays means that elements of trace abundance within the sample can be readily measured.[63,64]

Promotion of an electron from the core level toward the continuum yields an element specific absorption edge, shown by an abrupt increase in the absorption cross-section at a specific energy.[65] XAFS spectra can be divided into two regions, pre- and post- this absorption edge. Prior and inclusive of the edge jump is the X-ray absorption near-edge structure (XANES) region, which probes the photoelectron excitation toward the continuum, yielding information concerning the chemical nature of the absorber, i.e. elemental oxidation state (edge) and local geometry (pre-edge). In XANES spectra, where the absorption edge leads to an intense peak can be referred to as the white line peak. This is a term which dates from the early near-edge measurements performed on photographic film, wherein the intense absorption peaks and over exposure, burned white lines on to the developed film. After the edge jump, physical characteristics can be elucidated *via* assessment and computational fitting of the higher energy region, this is the extended X-ray absorption fine structure (EXAFS), and details the coordination number and radial distances from the absorbing atom to its nearest neighbours.[66]

2.8.1 XAFS Theory

Analysis of materials by XAFS allows for element specific characterisation through the energy-dependent absorption coefficient: $\mu(E)$. The probability the X-rays will be absorbed is described by the Beer law for transmission (*Equation 2-5*), where the absorption coefficient is given in *Equation 2-6*.

$$I_t = I_0 \, e^{-\mu(E)t}$$

Equation 2-5. *Beer law for transmission, where I_0 is the incidence X-ray intensity, I_t is the transmitted X-ray intensity, t is the sample thickness and $\mu(E)$ is the energy-dependent absorption coefficient.*

$$\mu \approx \frac{\rho \, Z^4}{m \, E^3}$$

Equation 2-6. *Relationship of the absorption coefficient, where ρ is the sample density, Z is the atomic number, m is the atomic mass and E is the X-ray incidence energy.*

XAFS is a technique that measures the intensity of the absorption coefficient as a function of energy.[64] Irradiation of the sample by the incident X-ray at an energy equal to that of the binding energy of a core-level is excited to the continuum, forming the absorption edge, this is the photoelectron effect.[64] The position of the absorption edge and its nomenclature are dependent on the origin of the promoted photoelectron, e.g. primary orbital and principle quantum number (*Figure 2-8*).[63] Excitation of the core level during this process ejects the photoelectron with kinetic energy, E_k.

$$E_k = h\upsilon - E_B$$

Equation 2-7. *Determination of core level excitation events through the detected kinetic energy, E_k, where E_B is the binding energy, $h\upsilon$ is the energy of the incident beam: h represents Planck's constant and υ is the frequency of the incidence beam.*

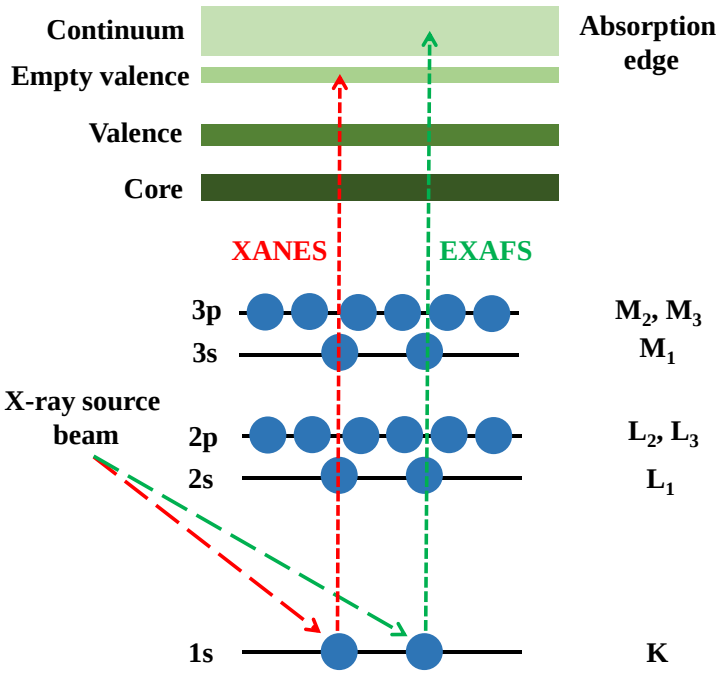

Figure 2-8. *Origin of X-ray absorption edge states corresponding to electron absorption from the ground orbital states and the transitions involved in the XANES and EXAFS spectrum; image adapted from J. Evans, in X-ray Absorption Spectroscopy for the Chemical and Material Sciences, ed. J. Evans, Wiley, 1st edn., 2018, pp. 117-162.*[67]

On excitation of the photoelectron into the continuum, description of the electron in terms of the wave behaviour allows for understanding oscillatory nature of the EXAFS region. The excited photoelectron, with wavelength, λ, is thus related to its momentum, ρ, by the de Broglie equation (*Equation 2-1*, $\lambda = h/\rho$).[23] The momentum is also related to the photo-electron wave vector, k, by $\rho = \hbar k$, with $\hbar = h / 2\pi$. Furthermore, the kinetic energy and momentum are defined as $E = \frac{1}{2} m_e v^2$ and $\rho = m_e v$, respectively. Therefore, when electron has a mass of m_e, the following relationship can be found (*Equation 2-8*).[66,67]

$$\text{(i)} \qquad 2Em_e = \rho^2$$

$$\text{(ii)} \qquad \hbar k = \sqrt{2Em_e}$$

Equation 2-8. *(i) Relationship of the momentum of a photoelectron to its mass, and (ii) reorganising of part i with $p = \hbar k$, where $\hbar$ is the Planck's constant.*

EXAFS is best understood in terms of the wave behaviour of the photoelectron, therefore, the X-ray energy is converted to k, the wavenumber of the photoelectron, with dimensions of 1/distance (*Equation 2-9*).[64]

$$k = \frac{\sqrt{2m_e(E\text{-}E_0)}}{\hbar^2}$$

Equation 2-9. *Mathematical description of the ejected photoelectron as a spherical wave function with a vector of k. E_0 is the absorption edge energy, also referred to as the binding energy of the photoelectron.*

Describing the photoelectron as a spherical wave function allows any potential backscattering phenomena that occurs on interaction of the photoelectron with neighbouring atoms to be quantified (*Figure 2-9*). The summation of both outgoing and backscattered photoelectrons can be taken into account when determining the final state wave function (*Equation 2-10*).

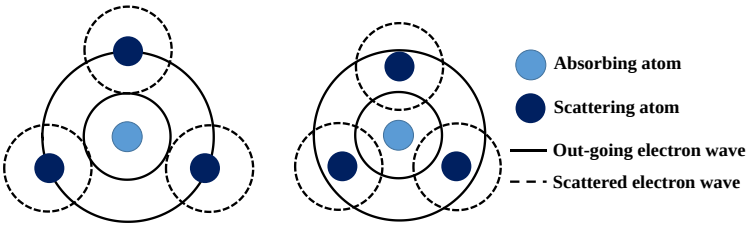

Figure 2-9. *Interference between ejected photoelectron and backscattered off neighbouring atoms, forming the oscillations in the EXAFS region; image adapted from Koningsberger et al., Top. Catal., 2000,* ***10****, 143-155.*[68]

$$\varphi_{\text{final}} = \varphi_{\text{outgoing}} + \varphi_{\text{backscattered}}$$

Equation 2-10. *Description of the final state wave function in EXAFS, determined by the summation of outgoing and backscattered photoelectrons from the absorbing atom.*

Interference of the resultant wave function determines the variation in the total absorption coefficient, μ, giving rise to the EXAFS phenomenon.[63] This higher energy EXAFS region extends up to 1000 eV past the absorption edge and is characterised by the oscillatory modulation in the absorption coefficient (*Figure 2-10*).

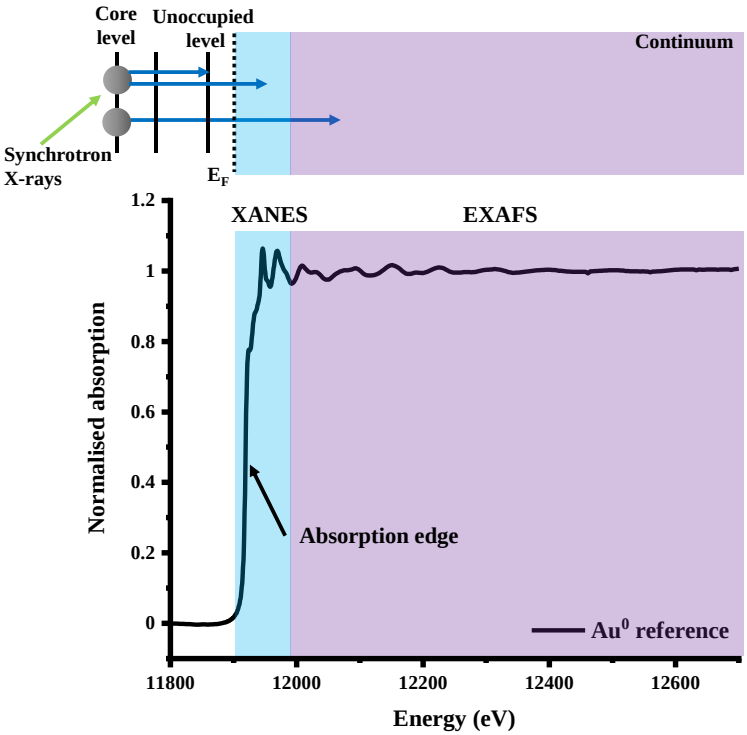

Figure 2-10. *Graphical representation of the origin of electron transitions caused by interaction of the sample core level with synchrotron X-ray radiation and how it relates to an acquired Au^0 reference XAFS spectra.*

2.8.1.1 X-ray Absorption Near-Edge Structure

The XANES region of the absorption spectra, is found within ~ 50 eV of the absorption edge, giving detail of any change to the samples' oxidation state *via* shifts to the absorption edge position, i.e. greater shielding of the nucleus causes higher binding energy of photoelectron and thus higher oxidation states. The signal acquired in XANES is much larger than that of the post absorption edge, and so can be performed at trace concentrations.[64] The transition from the core-level toward unoccupied electronic states is probed and named representative of the absorption edge: K ($s \rightarrow p$), L_I ($2s \rightarrow p$), L_{II} ($2P_{1/2}$) and L_{III} ($2P_{3/2}$) both produced by the transition from $p \rightarrow d$. Further to this, the local geometry around the absorbing atom can be determined through variations in pre-edge peaks caused by electronic transitions to empty higher energy states obeying dipole selection rules (*Equation 2-11*). Pre-edge peaks are common for the K-edge of first row transition metals as well as metals with an open 3*d* orbital, and arise from bound state transitions.[65]

$$\Delta l = \pm 1$$

$$\Delta j = \pm 1$$

$$\Delta s = 0$$

Equation 2-11. *Dipole selection rules that must be adhered to for electronic transitions to take place in the XANES region of XAFS spectra.*

Determination of the average oxidation state is possible using linear combination fittings (LCF) of the XANES spectra, which is fitted to reference compounds of the elemental edge measured. Through this, ratios of the oxidation states can be easily assessed using the previously mentioned Demeter software packages.[66] This method of calculation cannot, however, describe fully the structure, nor the adjacent atoms to the absorbing atom. Complete analysis of XAFS spectra therefore requires the application of a further technique to characterise the higher energy oscillations within the EXAFS region.

2.8.1.2 Extended X-ray Absorption Fine Structure

Analysis of the oscillatory EXAFS region is based upon variations in absorption as a function of the wave vector, k, (*Equation 2-9*), and are denoted by $\chi(k)$.[70] This change in absorption is the deviation between the observed absorption jump above E_0 from the expected jump if there were no EXAFS features (*Equation 2-12*).[63]

$$\chi(k) = \frac{\mu(k) - \mu_0(k)}{\mu_0(k)}$$

Equation 2-12. *Mathematical expression of the changes in absorption as a function of $\chi(k)$, and is measured as the change in absorption between the observed absorption jump above E_0 from the expected jump if no EXAFS features were observed. Where, μ_0 is the absorption of a free atom, resultant of elastic and inelastic X-ray scattering, $\mu_0(k)$ is the background edge jump, the difference between the two backgrounds and $\mu(k)$ is the difference between the pre-edge background and the observed absorption.*

Therefore, to measure $\chi(k)$, E_0 must first be identified from the acquired spectrum and extrapolating through the data and identifying the absorption edge, as if no EXAFS region were present.[30,63] Contributions to the EXAFS from scattering and backscattering from different nearest neighbours can be described as a function $\chi(k)$ (*Equation 2-13*).[64,71]

$$\chi(k) = \sum_j \frac{N_j f_j(k) e^{-2k^2\sigma_j^2}}{k\, R_j^2} \sin\left[2kR_j + \delta_j(k)\right]$$

Equation 2-13. *EXAFS equation, used in the quantification of the EXAFS region as a function of χ(k), where j is the coordination shell. The formula is a summation of the different scattering events of the photoelectron from the absorbing atom within a narrow distance. N is the number of neighbouring atoms to the absorbing atom (coordination number), f(k) and δ(k) are scattering properties of the atoms neighbouring the excited atom, R is the distance to the neighbouring atom, and σ^2 is the disorder in the distance between neighbour atoms.*

The amplitude of the EXAFS declines as $1/R^2$, and represents the decrease in photoelectron amplitude per unit area as it moves further from the absorbing atom.[65] This dampening therefore limits the EXAFS information to the closest neighbours of the absorbing atom. Another source of dampening is the disorder in the distance between atoms, σ^2. The "Debye-Waller" factor, σ, describes dampening due to more than one absorber-scatter distance, as each distance contributes to the EXAFS oscillations with marginally altered frequencies, destructive interference of the signal can dampen the EXAFS amplitude.[30,64,65,67] Typically these result from distortions that are either (1) *Static*, where disorder arises from intrinsic variation within the structure, or (2) *Dynamic*, where disorder arises from thermal vibrations.

2.8.2 X-ray Absorption Fine Structure Data Acquisition

Data acquired during experiments on various beamtimes (DLS: B18, I20-Scanning and ESRF: BM28) were obtained in one of two modes.

2.8.2.1 Transmission Mode

XAFS acquisition set-up involves the movement of the X-ray beam through a crystal monochromator, and through three ion chambers: I_0, I_t and I_{ref} (*Figure 2-11*). Transmission mode experiments are based upon measuring the variance in X-ray intensity throughout the three ion chambers, the sample and/or sample cell windows, and are performed when the sample element has a satisfactory concentration. Each ion chamber is filled with an inert gas mixture and charged metal plates with a constant potential between them (*Figure 2-12*).[63] As the X-ray beam passes through the chamber, the gas becomes ionised and attracted toward the opposing charge region; electrons within the chamber similarly move toward an area of positive charge. A detectable current is produced corresponding to the X-ray photons

entering the chamber (*Equation 2-14*).

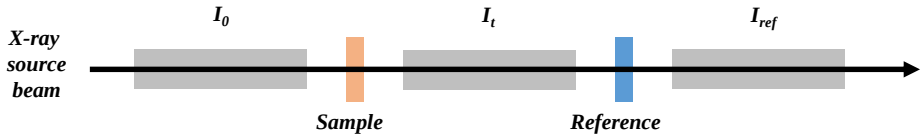

***Figure 2-11**. Schematic representation of the X-ray source path through ion chambers and the sample in acquisition of XAFS in transmission mode.*

$$Ar + h\nu \rightarrow Ar^{+} + e^{-}$$

***Equation 2-14.** Ionisation of gaseous Ar inside of the ionisation chambers during exposure to the X-ray source beam, generating a detectable current.*

Using the collected values from each ion chamber, X-ray absorption by the sample can be calculated:

$$A = \ln \frac{I_0}{I_t}$$

***Equation 2-15.** X-ray absorption (A) calculated by changes in energy from the initial (I_0) and post sample chambers (I_t).*

Acquisition of data from the reference chamber, I_{ref}, allows for the energy of the X-ray beam to be calibrated against an internal reference foil.

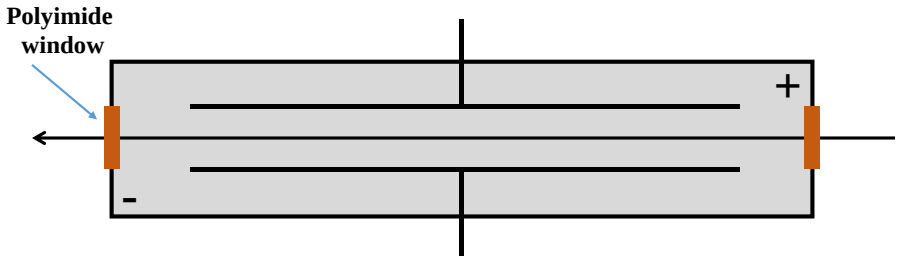

***Figure 2-12.** Simplistic schematic of the inside of an ion chamber used for data acquisition in XAFS transmission measurements; image adapted from J. Evans, in X-ray Absorption Spectroscopy for the Chemical and Material Sciences, ed. J. Evans, Wiley, 1st edn., 2018, pp. 117-162.*[67]

Transmission experiments are conducted when the target element of the sample materials and sample cell are adequate; if the element concentration is too low, the signal/noise ratio of the data will be insufficient. If the concentration of the target element is too high, complete

absorption of the X-ray beam will occur and data cannot be acquired. The ideal mass of the sample should provide an absorption edge in the range of: $0.1 < \mu x < 1.5$ (*Equation 2-16*).

$$\text{mass} = \frac{(\mu x)\,(a)}{\left(\frac{\mu}{\rho}\right)}$$

Equation 2-16. *Sample mass calculation for adequate XAFS transmission, where a is the area (usually pellets are prepared for samples, meaning the surface area is needed in this calculation) and ρ is the sample density.*

2.8.2.2 Fluorescence Mode

In cases where samples do not have high enough concentrations for adequate absorption through transmission, fluorescence experiments are performed. Similar to that mentioned previously for XRF; data acquisition is dependent on the excitation of a photoelectron, leaving an electron hole in the ground state. Subsequent to this, filling of the electron hole by an electron from a higher valence results in a photoemission, equal in energy to the difference between the core and higher vacancy shell, yielding an element specific fluorescence radiation.

Acquisition of XAFS data in fluorescence mode requires the position of a solid state elemental detector at a 90° horizontally to the sample, with the sample placed at a 45° angle to the incidence beam (*Figure 2-13*). Large fluctuations in the abundance of scattered X-rays are concerning when collecting data, therefore, the detector is placed at an optimal distance from the sample and longer acquisition times are required to enable sufficient X-ray collection with reduced signal/noise ratios. X-ray absorption in fluorescence mode (*Equation 2-17*) and the signal/noise ratio of the data are given below (*Equation 2-18*).

$$\mu(E) = \frac{I_f}{I_0}$$

Equation 2-17. *Calculation of X-ray absorption in fluorescence mode, where I_f is the absorption through the fluorescence detector and I_0 is the absorption energy through the initial ion chamber prior to interaction with the sample.*

$$\frac{S}{N} = \left[\frac{I_f t}{1 + \frac{I_b}{I_f}}\right]^{\frac{1}{2}}$$

Equation 2-18. *Signal/noise ratio calculation for fluorescence mode XAFS measurements, where I_f is the absorption through the fluorescence detector, I_b is the background signal and t is the acquisition time.*[67]

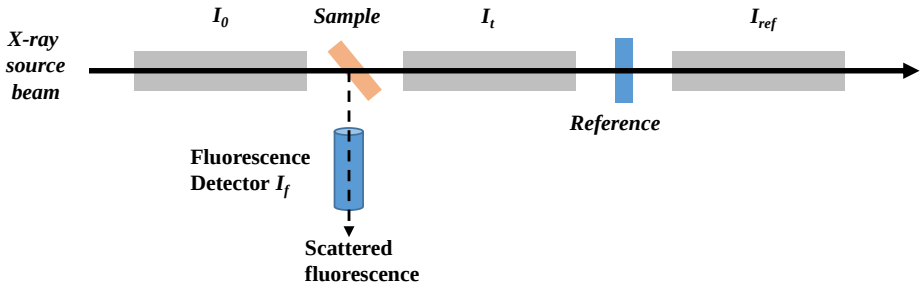

Figure 2-13. *Schematic representation of the X-ray path through ion chambers and specimen during XAFS acquisition in fluorescence mode.*

2.8.3 Data Reduction

Data reduction of acquired XAFS spectra is necessary for the presentation of both XANES and EXAFS collected in both transmission and fluorescence modes, fortunately, both modes are reduced following similar procedures. Data processing in this work was performed using the Demeter suite, primarily using the Athena and Artemis programs.[72] Raw XAFS datasets were exported to the Athena software program, where the process of data reduction was performed:[30,64,65,73]

(1) Measured intensities are converted to absorption $\mu(E)$ and plotted as a function of energy (eV).

(2) The data were checked for monochromator glitches or irregularities (and removed if necessary); if multiple datasets had been acquired for the same sample they were then merged into one spectrum.

(3) Next a smooth pre-edge function is subtracted from $\mu(E)$, removing any absorption from overlapping edges or instrumental backgrounds that may be present.

(4) A similar function is subtracted from the post-edge region, this smoothed background is drawn through the oscillatory region. Subtraction of pre- and post-edge functions normalises the intensity of the data to an edge jump of 1 (*Figure 2-14*a-b).

(5) The E_0 of the data is set to a value of 0 eV relative to the energy scale, and is achieved by plotting the 1st derivative of the absorption energy. The maximum of the 1st derivative is thus E_0, and corresponds to the max rising slope of the absorption energy.

(6) The data is converted from $\chi(E)$ to $\chi(k)$ and *k*-weighting of the XAFS is performed, where the weighting is k^1, k^2 *or* k^3 and have amplitudes that are more evenly displayed along the x-axis (*Figure 2-14*c).

(7) The obtained $\chi(k)$ data is then Fourier transformed to yield a plot in R space, significant of the radial distribution of the most probable nearest neighbours to the absorbing atom (*Figure 2-14*d).

(8) Before fitting of the EXAFS data can be performed, the amplitude reduction factor (S_0^2) is determined by fitting the oscillatory EXAFS region of a measured reference foil with an appropriate database crystallographic information file (*.cif*) in the Artemis software package.

(9) The measured samples are then fitted using appropriate *.cif* files corresponding to the composition of the sample and the scattering pathways the photoelectron can take, e.g. for PdO, one pathway would be Pd-O and another would be Pd-Pd scattering paths. Fitting of the data affords the coordination number and the Debye-Waller factor, as well as an additional R_{factor} parameter is which indicates the quality of the fit.

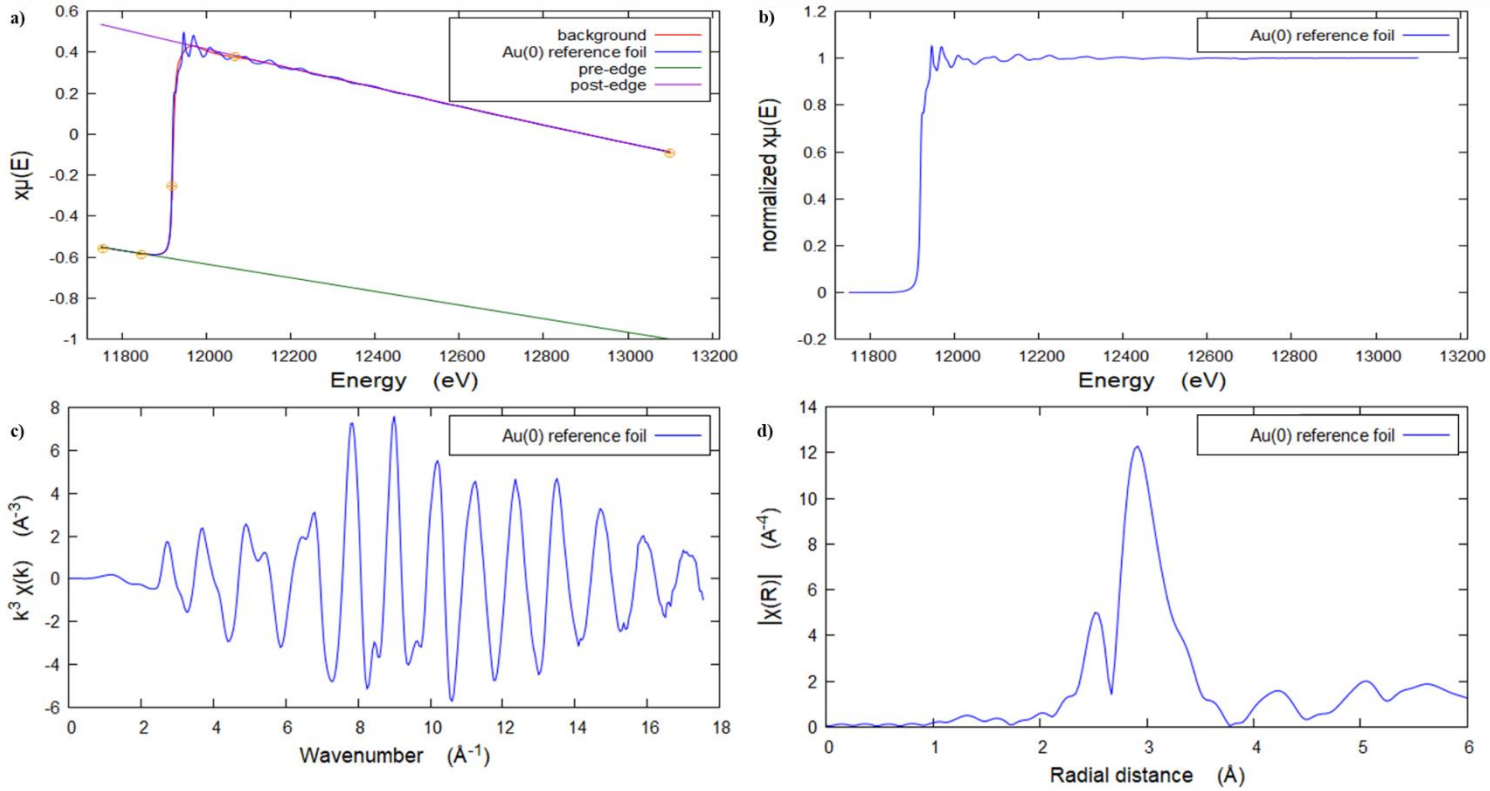

Figure 2-14. *XAFS data acquired at the Au L_3-edge for a Au^0 reference foil; a) plotted raw data of the absorption (xμ), background, pre- and post-edge lines, b) normalised absorption after background subtraction, c) removal of background (χ), giving oscillatory data in k-space and d) Fourier transform of χ, giving the EXAFS region as a function of the radial distance.*

2.9 Synchrotron-Based X-ray Source

The advent of synchrotron light sources in the 1970s transformed the ability to perform XAFS experiments whilst also revolutionising the time-scales for data acquisition.[63] With this, a greater demand was seen for research using synchrotron white light, and for the production of "second and third generation" light sources, which can be found across the globe. Fortunately, the manner in which an X-ray source beam is generated within a synchrotron does not vary between different synchrotrons. For example, to manufacture the source beam at DLS, U.K. the follow steps are taken:

(1) Low energy electrons are emitted by the heating of a high voltage cathode under vacuum, these are then accelerated by earthed anodes.

(2) A linear accelerator (LINAC) accelerates the electrons further to an energy of 100 MeV.

(3) These energised electrons are injected into the booster ring and undergo further acceleration using a voltage source.

(4) When the electrons have reached a final energy of 3 GeV (this differs depending on the light source) they enter the storage ring, comprised of 24 straight sections, and remain under vacuum to limit interactions between air molecules and the electrons (*Figure 2-15*).

Inside of the storage ring, magnets control the trajectory of the electrons and ensure a small beam size is maintained and are named to identify the source of the beamline's radiation, e.g. B/BM for bending magnets or I/ID for insertion devices.

Bending magnets (dipoles) are commonly used to direct the electron path between straight sections of the storage ring, quadrupoles aid in focussing the beam and sextupoles reduce the chromaticity (energy dispersions of the electrons). As the electrons travel around the storage ring, they interact with bending magnets positions at various corners, emitting synchrotron radiation that encompasses a broad and continuous spectrum at relatively low intensities tangentially to the plane of the electron beam.[74,75]

Insertion devices are comprised from arrays of small magnets and are found along straight regions of the storage ring and are present in two forms: (1) multipole wigglers, which deviate the electron path along a sinusoidal path using magnets of alternating polarity, yielding a broad range of X-rays at harder energies (> 8 KeV) with greater flux, (2) undulators, whereby the principle of beam modification is similar to wigglers, but the

distance between the magnetic poles is decreased, forming a narrower source beam with greater brilliance.

Flux: photons s^{-1} $mrad^{-1}$

Brightness: flux $mrad^{-1}$

Brilliance: brightness mm^{-2}

XAFS data presented in this thesis were acquired on bending magnet and insertion device based beamlines. The Pd NP catalysts were measured using two bending magnet beamlines, B18 at DLS and BM28 (UK CRG XMaS) at the European Synchrotron Research Facility (ESRF). B18 was used due to the emitted synchrotron light being broad enough in energy to measure at the Pd *K* edge (24,3503 eV) and the QEXAFS functionality allowing for the instantaneous collection of large numbers of spectra during the forward and reverse movements of the beamline monochromator, where full XAFS spectra acquisition can be achieved at resolutions of < 60 seconds $spectrum^{-1}$.[76,77] BM28 was used to study XANES at much softer energy edges; Cl K (2822 eV) and S K-edges (2472 eV). Acquisition of Au L_3-edge (11919 KeV) XAFS for supported Au NPs is possible on BM beamlines, however the low flux offered is detrimental for liquid solutions of low metal concentration. For the colloidal Au study presented in Chapters 5 and 6, XAFS measurements were performed on the insertion device fed I20-Scanning beamline at DLS due to the higher flux and greater brilliance offered.[78–80]

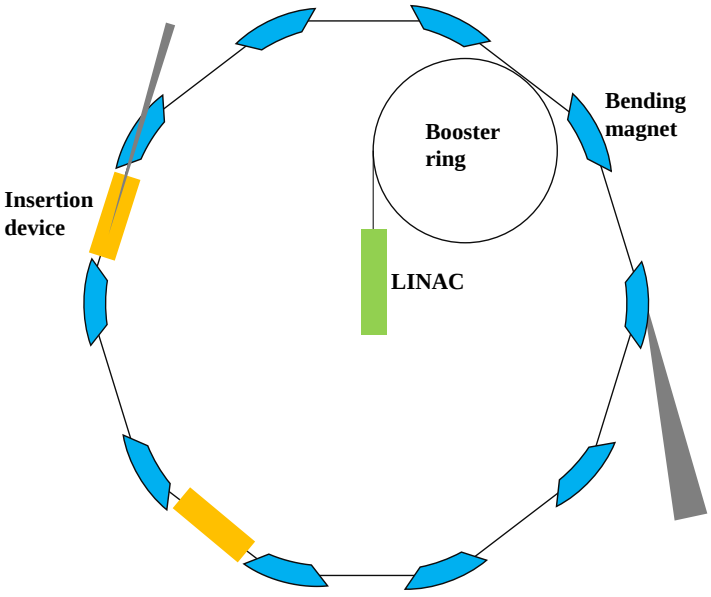

Figure 2-15. *Schematic of a synchrotron radiation source showing the LINAC, inner booster ring, outer storage ring, and the magnetic devices used to generate synchrotron X-ray radiation (bending magnets and insertion devices); image adapted from Mitchell et al., Structure, 1999, **7**, R111-R121.*[81]

2.10 Laboratory Based X-ray Fluorescence

X-ray fluorescence is a widely accessible technique used to elucidate chemical compositions of materials, usually in a solid or liquid state, and can be performed using laboratory and synchrotron-based X-ray sources. Three principle steps occur in the emission of XRF. Firstly, the interaction of an X-ray source beam with the sample leads to the ejection of photoelectrons from an inner shell, leaving a "hole" in the electronic structure of the atom. In addressing this, electrons within the sample rearrange and an electron from a higher energy shell drops to fill the hole. This relaxation causes the emission of an X-ray photon whose energy is equal to the difference in energies between the initial and end state, this is fluorescence. Detection of this emission allows quantification of the element and the specific electronic transition that occurs.

XRF analysis was employed to measure the polyimide tubing used in the design of the microfluidic cell for *in situ* measurement of Au NPs. Samples were prepared by cutting the tubing into 5 distinct sections, each 2 cm in length, and then slicing these small pieces of tubing in half lengthways. They were then placed into holders with Mylar polyester thin film windows (Chemplex Industries Inc.), with trace impurities of Ca, P, Fe, Zn, Cu, Zr, Ti and Al present. The sample holders were then loaded into a PANalytical Epsilon3-XL X-ray fluorescence spectrometer, and elemental analysis of Au deposition was performed. The measurements were acquired at the ISIS Materials Characterisation laboratory at the ISIS Neutron and Muon Source, Didcot, U.K.

2.11 Chromatography

Chromatography is a widely used technique across different scientific disciplines to separate product components, and distinguishes between components within the sample due to the varied rates at which they move through a set medium, i.e. interactions of a mobile and a stationary phase. The components are carried through a chromatography column in the mobile phase, and are eluted at various rates (retention times) dictated by the difference of polarity between the two phases. In this work gas chromatography (GC) is used, whereby the mobile phase consists of reactant gases. Data acquired using gas chromatography can be used to qualitatively (comparison of retention time with known standards) and quantitatively (peak area) characterise separation products.

Samples for GC analysis must be in a gaseous state or vaporised whilst not undergoing decomposition before analysis. The sample is injected at the injection port, or through an autosampler, under a constant carrier gas flow and are separated by their affinity of the sample to the stationary phase (*Figure 2-16*), and passes through the column, which is then subject to a temperature ramp inside of an oven. Once the sample has separated and eluted from the column, the various components of the original sample pass through a product appropriate detector.

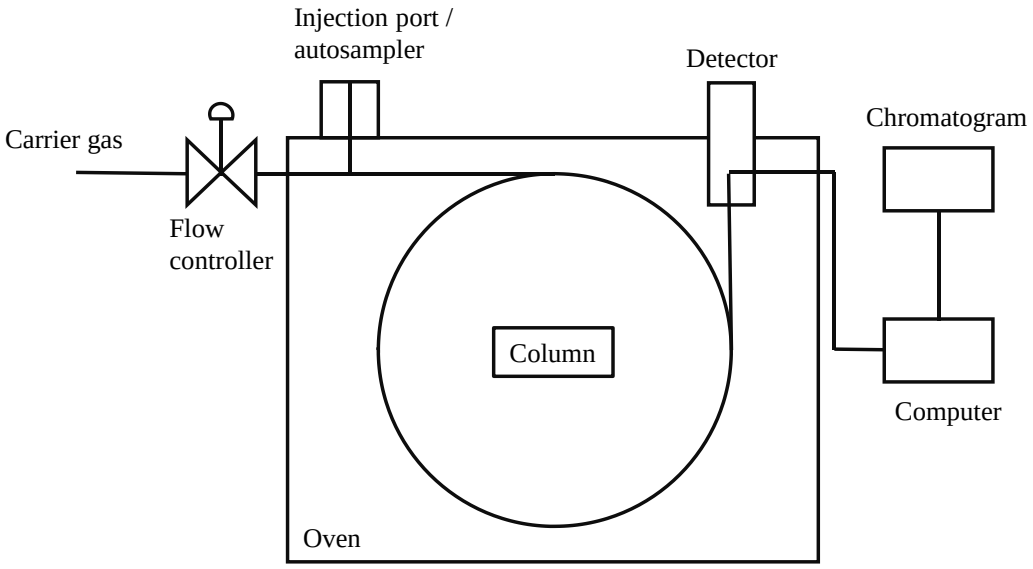

Figure 2-16. *Simplistic schematic of the gas chromatography set-up used in the separation and identification of furfural hydrogenation products.*

2.11.1 Flame Ionisation Detector

Flame ionisation detectors are used in conjunction with the GC instrument allowing for analysis of hydrocarbon reaction products, however, this detector is not sensitive toward small molecules such as CO_x gases. The mode of action for an FID is the burning of the sample in an H_2 flame, ionising the sample, the formed ions are then attracted toward collectors inside of the detector, and the number of ions impacting on the detector are measured, producing a corresponding signal.

2.11.2 Thermal Conductivity Detector

Thermal conductivity detectors are commonly used within GC instruments and as the main detector in many TPR processes. Due to the non-destructive nature of the detector, it can be placed in series with other detectors such as FIDs. The detector works by comparing the

thermal conductivities of two gas flows: (1) a pure carrier gas flow and (2) a mixed carrier gas and sample flow. Within the TCD is an electrically heated filament, held at a constant temperature greater than that of the detector. Once at temperature, alternating streams of the carrier and mixed sample gas are passed over the filament, decreasing the rate of heat removal, raising the temperature of the wire and altering the resistance. The detector then measures the change in resistance resulting from the differing temperatures. Unlike the flame ionised detectors, all compounds have thermal conductivity different from He, a commonly used carrier gas and so, both organic and inorganic compounds can be measured by a TCD.

2.12 Hydrogenation of Furfural

2.12.1 Catalyst Testing

All catalytic testing of Pd catalysts was performed at the Università degli Studi di Milano under the supervision of Dr. A. Villa and with the help of Dr. S. Alijani. Furfural hydrogenation was performed at 50 °C using a stainless steel reactor (30 mL capacity), and placed into a heating jacket equipped stirrer plate, furnished with a heater, mechanical stirrer, gas supply system and digital thermometer (*Figure 2-17*).

A solution of furfural, 10 mL, 0.3 M in IPA, was placed into the reactor along with the desired quantity of catalyst, furfural/metal = 500 mol/mol, and a stirrer bar. The reaction vessel was purged with 3 bar N_2 before being depressurised and again pressurised with H_2 to 5 bar and sealed. The mixture was left to reach 50 °C before being mechanically stirred at 1000 rpm. At the end of the reaction, the autoclave was cooled to room temperature and pressure was relieved. The process of pressurising the vessel was repeated after reaction samples were withdrawn.

Figure 2-17. *Reactor set-up used at the Università degli Studi di Milano, Milan, Italy used in the Laboratories of Dr. A. Villa; a) stainless steel reactor vessel used for furfural hydrogenation over various catalysts. At the top of the reactor (marked by arrows) is the inlet and outlet for both N_2 and H_2 gases used during catalyst pre-treatment and hydrogenation, respectively, b) reactor vessel nestled inside of the walled stirrer plate, where coned design affords for well distributed heat throughout the reactor vessel.*

2.12.2 Product Analysis

Reaction samples were removed periodically (0.2 mL, at 0, 15, 30, 60, 120, 300 minutes) and prepared for GC analysis by firstly separating the catalyst from the analyte using an ALC 4236-A centrifuge. The reaction mixture (200 µL) was then mixed with an external standard (200 µL dodecanol) and 600 µL of the reaction solvent (IPA). Reaction samples were then analysed using an Agilent 6890 GC equipped with a Zebron, ZB-5 60 m × 0.32 mm × 1µm (thickness) column and an FID. The response factors, R_F, for the reaction products were determined by injection of a known concentrations of the pure compound standard (i.e. furfuryl alcohol) along with a constant volume of the external standard (0.1 M dodecanol) in the calibration standards. Calibration of the standards was

calculated measuring the ratio of the analyte's peak area with the peak area of the external standard, plotting as a function of analyte concentration to external standard concentration (*Figure 2-18*) (*Equation 2-19*). This can be used further to identify the concentration of both substrates (furfural) and products within the analyte.

$$R_F = \frac{(A_i)(M_{\mathrm{ISTD}})}{(M_i)(A_{\mathrm{ISTD}})}$$

Equation 2-19. *Relation of response factor (R_F) to the peak area (A) and molarities (M) of the compound (i) and the internal standard (ISTD).*

The temperature program employed by the GC for the analysis of furfural hydrogenation involved: heating to 100 °C where the temperature was held for 2 minutes. After this the temperature was increased to 170 °C (15 °C min^{-1}), and held for 2 minutes. Finally the temperature was raised to 300 °C and held for 9 minutes. Controllable parameters used within the GC are given below (*Table 2-4*).

Table 2-4. *GC parameters employed at the Università degli Studi di Milano by Dr. Alberto Villa for quantitative analysis of furfural hydrogenation products.*

Time	24 minutes
Hydrogen flow	35 mL min^{-1}
Air flow	350 mL min^{-1}
Makeup flow	12 mL min^{-1}
Carrier gas	He
Make up gas	Nitrogen
Detector temperature	300 °C
Injector temperature	300 °C
Split ratio	1:20

Analyte peak areas were manually integrated and used to calculate the concentration of a compound or standard (*Equation 2-20*) (*Figure 2-18*), substrate (furfural) conversion (*Equation 2-21*), product selectivities (*Equation 2-22*), and the catalyst activity (turnover frequency, TOF) (*Equation 2-23*).

$$C_i = C_{\text{ISTD}} \times R_F \times \left(\frac{A_i}{A_{\text{ISTD}}}\right)$$

Equation 2-20. *Calculation of analyte concentration (C_i) using the concentration of an internal standard (C_{ISTD}), response factor (R_F), area of the analyte peak (A_i) and the area of the internal standard peak (A_{ISTD}). GC Calibration plots are presented in Figure 2-18.*

$$\left(\frac{(\text{mol}_{\text{furfural}(T_0)} - \text{mol}_{\text{furfural }(T_n)})}{\text{mol}_{\text{furfural}(T_0)}}\right) \times 100$$

Equation 2-21. *Calculation of furfural conversion. T_0 is the initial time point, and T_n indicates a specific time point post the start of the reaction, i.e. 15, 60, 120, 180 or 300 minutes.*

$$\left(\frac{\text{mol}_{\text{product}}}{\text{mol}_{\text{furfural (in)}} - \text{mol}_{\text{furfural (out)}}}\right) \times 100$$

Equation 2-22. *Calculation of product selectivity dependent on the moles of the product compared to the sum of the moles of furfural before and after product formation.*

$$\left(\frac{\text{mol}_{\text{furfural converted}}}{\text{mol}_{\text{Pd}}}\right) \times \text{hr}^{-1}$$

Equation 2-23. *Turnover frequency (TOF) calculation used to describe the activity of the Pd catalysts per mol catalyst per hr during the hydrogenation of furfural.*

Further analysis was required to successfully identify ether and acetal by-products formed during catalytic testing. These products were identified using GC coupled with mass spectroscopy (GC-MS) (*Figure 2-19*). Aliquots of the reaction mixture were analysed using a Thermo Scientific ISQ QD, equipped with an Agilent VF-5 ms column, 60 m × 0.32 mm × 1 µm (inner diameter thickness). Unknown peaks were then identified through comparison of MS profiles with available data within the software database.

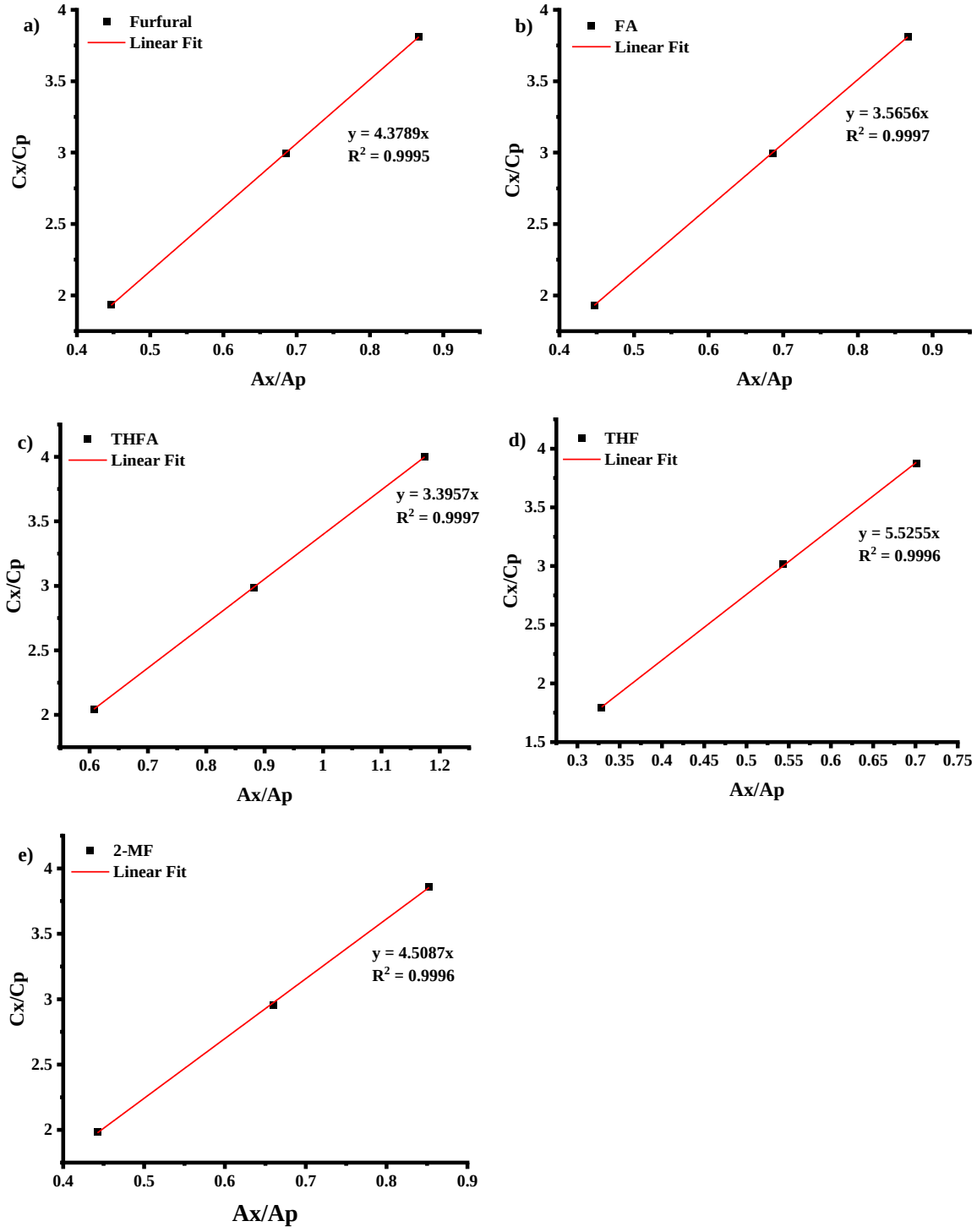

Figure 2-18. *Gas chromatogram calibration for the reaction substrate (furfural) and the other reaction products identified using GC analysis. The internal solvent for calibration was IPA and the external was dodecanol.*

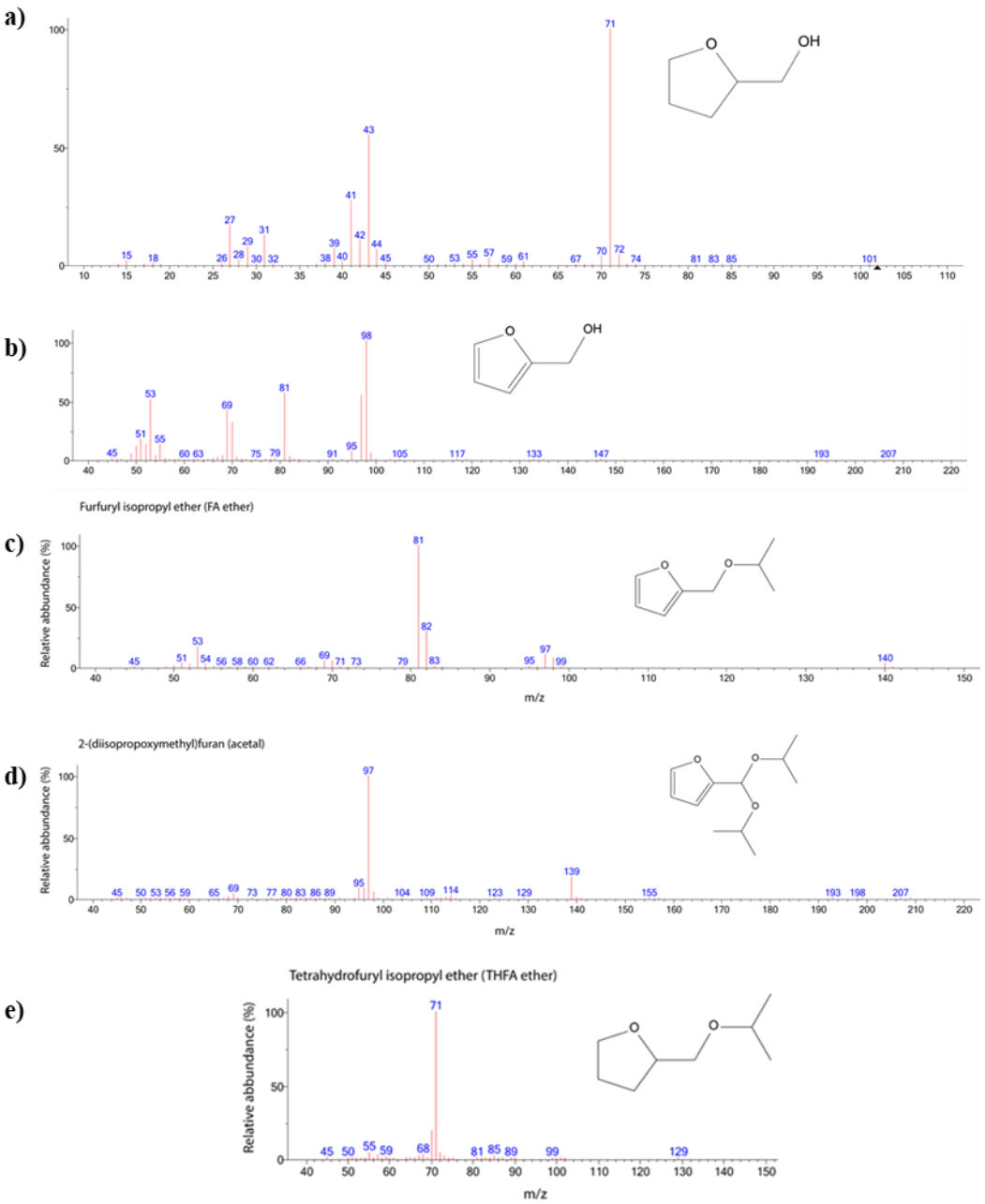

Figure 2-19. *GC-MS data acquired for all products formed through the hydrogenation of furfural over the prepared Pd/TiO_2 catalysts. GC-MS measurements were performed using a Thermo Scientific ISQ QD, equipped with an Agilent VF-5 ms column, 60 m × 0.32 mm × 1 µm (inner diameter thickness). Spectra shown are for: a) tetrahydrofurfuryl alcohol, b) furfuryl alcohol, c) isopropyl furfuryl ether, d) 2-(diisopropoxymethyl) furan and e) isopropyl tetrahydrofurfuryl ether.*

2.13 References

1 A. Villa, D. Wang, G. M. Veith, F. Vindigni and L. Prati, *Catal. Sci. Technol.*, 2013, **3**, 3036–3041.

2 S. Campisi, D. Ferri, A. Villa, W. Wang, D. Wang, O. Kro and L. Prati, *J. Phys. Chem. C*, 2016, **120**, 14027–14033.

3 L. Prati and A. Villa, *Acc. Chem. Res.*, 2014, **47**, 855–863.

4 L. Prati and A. Villa, *Catalysts*, 2012, **2**, 24–37.

5 S. M. Rogers, C. R. A. Catlow, C. E. Chan-Thaw, D. Gianolio, E. K. Gibson, A. L. Gould, N. Jian, A. J. Logsdail, R. E. Palmer, L. Prati, N. Dimitratos, A. Villa and P. P. Wells, *ACS Catal.*, 2015, **5**, 4377–4384.

6 N. Dimitratos, A. Villa, L. Prati, C. Hammond, C. E. Chan-Thaw, J. Cookson and P. T. Bishop, *Appl. Catal. A Gen.*, 2016, **514**, 267–275.

7 C. E. Chan-Thaw, A. Villa and L. Prati, in *Gold Catalysis: Preparation, Characterization, and Applications*, eds. L. Prati and A. Villa, Pan Stanford, 1st edn., 2015, pp. 59–63.

8 S. Campisi, M. Schiavoni, C. E. Chan-thaw and A. Villa, *Catalysts*, 2016, **6**, 1–21.

9 P. K. Khanna, P. V. More, J. P. Jawalkar and B. G. Bharate, *Mater. Lett.*, 2009, **63**, 1384–1386.

10 O. Lidor-Shalev and D. Zitoun, *RSC Adv.*, 2014, **4**, 63603–63610.

11 S. M. Rogers, C. R. A. Catlow, C. E. Chan-Thaw, A. Chutia, N. Jian, R. E. Palmer, M. Perdjon, A. Thetford, N. Dimitratos, A. Villa and P. P. Wells, *ACS Catal.*, 2017, **7**, 2266–2274.

12 T. Teranishi and M. Miyake, *Chem. Mater.*, 1998, **4756**, 594–600.

13 J. Turkevich, P. C. Stevenson and J. Hillier, *Discuss. Faraday Soc.*, 1951, **11**, 55–75.

14 A. Mehri, H. Kochkar, S. Daniele, V. Mendez, A. Ghorbel and G. Berhault, *J. Colloid Interface Sci.*, 2012, **369**, 309–316.

15 L. Espinosa-Alonso, K. P. de Jong and B. M. Weckhuysen, *Phys. Chem. Chem. Phys.*, 2010, **12**, 97–107.

16 E. Tomaszewska, K. Soliwoda, K. Kadziola, B. Tkacz-Szczesna, G. Celichowski, M. Cichomski, W. Szmaja and J. Grobelny, *J. Nanomater.*, 2013, 1–10.

17 D. D. Evanoff Jr. and G. Chumanov, *ChemPhysChem*, 2005, **6**, 1221–1231.

18 G. C. Papavassiliou, *Prog. Solid State Chem.*, 1979, **12**, 185–271.

19 T. Ghodselahi, M. A. Vesaghi, A. Shafiekhani, A. Baghizadeh and M. Lameii, *Appl.*

Surf. Sci., 2008, **255**, 2730–2734.

20 L. Xu, J. Peng, C. Srinivasakannan, L. Zhang, D. Zhang, C. Liu, S. Wang and A. Q. Shen, *RSC Adv.*, 2014, **4**, 25155.

21 U. Kreibig and L. Genzel, *Surf. Sci.*, 1985, **156**, 678–700.

22 NanoHybrids, Plasmonics & Surface Plasmon Resonance, https://nanohybrids.net/pages/plasmonics, (accessed 10 May 2021).

23 E. Mackinnon, *Am. J. Phys.*, 1976, **44**, 1047–1055.

24 A. World, Basic principle of transmission of electron microscope, http://www.hk-phy.org/atomic_world/tem/tem02_e.html, (accessed 6 June 2021).

25 C. A. Schneider, W. S. Rasband and K. W. Eliceiri, *Nat. Methods*, 2012, **9**, 671–675.

26 Z. Li, *Scanning transmission electron microscopy studies of mono- and bimetallic nanoclusters*, Elsevier Ltd, 1st edn., 2012, vol. 3.

27 D. Titus, E. J. J. Samuel and S. M. Roopan, in *Green Synthesis, Characterization and Applications of Nanoparticles*, eds. A. K. Shukla and S. Iravani, Elsevier Inc., 1st edn., 2019, pp. 303–319.

28 F. Hofer, F. P. Schmidt, W. Grogger and G. Kothleitner, *IOP Conf. Ser. Mater. Sci. Eng.*, 2016, **109**, 1–9.

29 R. F. Egerton, *Electron Energy Loss Spectroscopy in the Electron Microscope*, New York: Plenum., 2nd edn., 1996.

30 B. Ravel, in *X-ray Absorption and X-ray Emission Spectroscopy. Theory and Applications*, eds. J. A. van Bokhoven and C. Lamerbiti, Wiley, 2016, p. 283.

31 R. Brydson, *Aberration-Corrected Analytical Transmission Electron Microscopy*, 2011.

32 T. Lear, R. Marshall, J. A. Lopez-sanchez, S. D. Jackson, T. M. Klapötke, G. Rupprechter, H. Freund and D. Lennon, *J. Chem. Phys.*, 2005, **123**, 1–13.

33 J. C. Lavalley, *Catal. Today*, 1996, **27**, 377–401.

34 G. Busca, *Catal. Today*, 1998, **41**, 191–206.

35 F. Giraud, C. Geantet, N. Guilhaume, S. Loridant, S. Gros, L. Porcheron, M. Kanniche and D. Bianchi, *Catal. Today*, 2020, **373**, 69–79.

36 V. V. Kumar, G. Naresh, M. Sudhakar, J. Tardio, S. K. Bhargava and A. Venugopal, *Appl. Catal. A Gen.*, 2015, **505**, 217–223.

37 L. K. Noda, R. M. De Almeida, N. S. Gonçalves, L. F. D. Probst and O. Sala, *Catal. Today*, 2003, **85**, 69–74.

38 I. Lezcano-Gonzalez, U. Deka, B. Arstad, A. Van Yperen-De Deyne, K. Hemelsoet,

M. Waroquier, V. Van Speybroeck, B. M. Weckhuysen and A. M. Beale, *Phys. Chem. Chem. Phys.*, 2014, **16**, 1639–1650.

39 M. Bensitel, O. Saur and J. C. Lavalley, *Mater. Chem. Phys.*, 1991, **28**, 309–320.

40 C. D. Zeinalipour-Yazdi, D. J. Willock, L. Thomas, K. Wilson and A. F. Lee, *Surf. Sci.*, 2016, **646**, 210–220.

41 A. A. Ismail, F. R. van de Voort and J. Sedman, in *Instrumental Methods in Food Analysis*, eds. J. R. . Pare and J. M. . Belanger, 1997, p. 100.

42 A. M. McCullagh, R. Warringham, C. G. A. Morisse, L. F. Gilpin, C. Brennan, C. J. Mitchell and D. Lennon, *Top. Catal.*, , DOI:10.1007/s11244-021-01435-y.

43 M. Manzoli, *Catalysts*, 2019, **9**, 1–34.

44 P. K. Gallagher, *MRS Bull.*, 1988, **13**, 23–27.

45 A. Mekki-Berrada and A. Auroux, in *Characterization of Solid Materials and Heterogenous Catalysts*, eds. M. Che and J. C. Védrine, Wiley-VCH Verlag GmbH & Co., 1st edn., 2012, pp. 777–782.

46 K. Leistner, K. Xie, A. Kumar, K. Kamasamudram and L. Olsson, *Catal. Letters*, 2017, **147**, 1882–1890.

47 S. Chettibi, Y. Benguedouar and N. Keghouche, *Phys. Procedia*, 2009, **2**, 707–712.

48 O. Bayraktar and E. L. Kugler, *Appl. Catal. A Gen.*, 2004, **260**, 125–132.

49 T. Hengsawad, T. Jindarat, D. E. Resasco and S. Jongpatiwut, *Appl. Catal. A Gen.*, 2018, **566**, 74–86.

50 E. Nowicka, S. Althahban, T. D. Leah, G. Shaw, D. Morgan, C. J. Kiely, A. Roldan and G. J. Hutchings, *Sci. Technol. Adv. Mater.*, 2019, **20**, 367–378.

51 D. A. M. Monti and A. Baiker, *J. cat*, 1983, **823**, 323–335.

52 H. Knözinger, in *Handbook of Heterogeneous Catalysis*, eds. G. Ertl, H. Knözinger and J. Weitkamp, Wiley-VCH, Weinheim, 1st edn., 1997, pp. 676–688.

53 P. Malet and A. Caballero, *J. Chem. Soc. Faraday Trans. 1*, 1988, **84**, 2369–2375.

54 S. J. Gentry, N. W. Hurst and A. Jones, *J. Chem. Soc. Faraday Trans. 1 Phys. Chem. Condens. Phases*, 1979, **75**, 1688–1699.

55 L. J. Gillespie and F. P. Hall, *J. Am. Chem. Soc.*, 1926, **48**, 1207–1219.

56 P. D. Cobden, B. E. Nieuwenhuys, V. V. Gorodetskii and V. N. Parmon, *Platin. Met. Rev*, 1998, **42**, 141–144.

57 L. M. Gómez-Sainero, X. L. Seoane, J. L. G. Fierro and A. Arcoya, *J. Catal.*, 2002, **209**, 279–288.

58 M. Bonarowska, B. Burda, W. Juszczyk, J. Pielaszek, Z. Kowalczyk and Z. Karpiński, *Appl. Catal. B Environ.*, 2001, **35**, 13–20.

59 G. Neri, M. G. Musolino, C. Milone, D. Pietropaolo and S. Galvagno, *Appl. Catal. A Gen.*, 2001, **208**, 307–316.

60 C. Amorim and M. A. Keane, *J. Colloid Interface Sci.*, 2008, **322**, 196–208.

61 K. Honda, *Sci. Rep Tohoku Imp Univ*, 1915, **4**, 97–103.

62 Y. Saito and J. Morikawa, *J. Therm. Anal. Calorim.*, 2013, **113**, 1157–1168.

63 J. Evans, in *X-ray Absorption Spectroscopy for the Chemical and Materials Science*, 2018, pp. 9–32.

64 M. Newville, *Rev. Mineral. Geochemistry*, 2014, **78**, 33–74.

65 J. E. Penner-Hahn, in *Comprehensive Coordination Chemistry II*, 2003, vol. 2, pp. 159–186.

66 M. Newville, *J. Synchrotron Radiat.*, 2001, **8**, 96–100.

67 J. Evans, in *X-ray Absorption Spectroscopy for the Chemical and Materials Science*, ed. J. Evans, Wiley, 1st edn., 2018, pp. 9–32.

68 D. C. Koningsberger, B. L. Mojet, G. E. Van Dorssen and D. E. Ramaker, *Top. Catal.*, 2000, **10**, 143–155.

69 M. A. Newton, R. Nicholls, J. B. Brazier, B. N. Nguyen, C. J. Mulligan, K. Hellgardt, E. M. Barreiro, H. Emerich, K. K. Mii, I. Snigireva, P. B. J. Thompson, K. Kuok, M. Hii, I. Snigireva and P. B. J. Thompson, *Catal. Struct. React.*, 2017, **3**, 149–156.

70 J. J. Rehr, *Rev. Mod. Phys.*, 2000, **72**, 621–654.

71 J. Evans, *X-Ray Absorption Spectroscopy for the Chemical and Materials Sciences*, Wiley, 2018.

72 B. Ravel and M. Newville, *J. Synchrotron Radiat.*, 2005, **12**, 537–541.

73 J. Evans, in *X-ray Absorption Spectroscopy for the Chemical and Materials Science*, ed. J. Evans, Wiley, 1st edn., 2018, pp. 117–162.

74 G. Margaritondo, in *X-ray Absorption and X-ray Emission Spectroscopy. Theory and Applications*, eds. J. A. van Bokhoven and C. Lamberti, Wiley, 2016, pp. 25–29.

75 J. Evans, in *X-ray Absorption Spectroscopy for the Chemical and Materials Science*, ed. J. Evans, Wiley, 1st edn., 2018, pp. 33–60.

76 R. Frahm, *Nucl. Inst. Methods Phys. Res. A*, 1988, **270**, 578–581.

77 A. J. Dent, G. Cibin, S. Ramos, A. D. Smith, S. M. Scott, L. Varandas, M. R. Pearson, N. A. Krumpa, C. P. Jones and P. E. Robbins, *J. Phys. Conf. Ser.*, 2009, **190**, 1–4.

78 S. Hayama, G. Duller, J. P. Sutter, M. Amboage, R. Boada, A. Freeman, L. Keenan,

B. Nutter, L. Cahill, P. Leicester, B. Kemp, N. Rubies and S. Diaz-moreno, *J. Synchrotron Radiat.*, 2018, **25**, 1556–1564.

79 S. Diaz-Moreno, M. Amboage, M. Basham, R. Boada, N. E. Bricknell, G. Cibin, T. M. Cobb, J. Filik, A. Freeman, K. Geraki, D. Gianolio, S. Hayama, K. Ignatyev, L. Keenan, I. Mikulska, J. Frederick, W. Mosselmans, J. J. Mudd and S. A. Parry, *J. Synchrotron Rad*, 2018, 1–12.

80 G. F. Tierney, D. Decarolis, N. Abdullah, S. M. Rogers, S. Hayama, B. de Gutierrez, A. Villa, C. R. A. Catlow, P. Collier, N. Dimitratos and P. P. Wells, *Nanoscale Adv.*, 2019, **1**, 2546–2552.

81 E. Mitchell, P. Kuhn and E. Garman, *Structure*, 1999, **7**, R111–R121.

Chapter 3 Investigating the Influence of Short Chain Alcohols on Colloidal Pd Synthesis

3.1 Introduction

The preparation of metal NP catalysts with well-defined and tuneable metal particle sizes is desirable, owing to their unique physical properties and wealth of potential applications.[1–3] To that end, colloidal synthesis has been recognised as a leading preparation route for favourable control of NP properties, e.g. size, shape and surface morphologies. The literature primarily focuses on how the reducing agents,[4–7] or stabilising agents,[8–12] can be easily modified to optimise these properties. One underexplored parameter is the solvent system employed in colloid preparation. Not only does the choice of solvent impact upon the solvation of the precursor salt,[13] it has been shown to also influence NP growth and colloid assembly *via* interactions between the NP surface and solvent molecules, or through solvent and stabiliser molecule interactions.[14–16]

Variations made to the composition of the reaction medium have focussed on using abundant, biodegradable and inexpensive solvents, such as alcohols, to produce environmentally friendly processes.[3,17] An example of this type of study was performed by Nasikin *et al*. to prepare silica particles using C_1-C_3 chain alcohols.[18] In their work, the morphology of the silica was shown to be dependent on the solubility of the precursor in the solvent, whereby the solubility of silica was greater in MeOH and EtOH than PrOH, leading to rapid nucleation and particle growth in the former.[18] Not only does the solubility influence NP size, the use of the solvent system as the stabilising and/or reducing agent(s) has also been reported, particularly in the preparation of metallic NPs.[19] The alcohol-based reduction of polyvinylpyrrolidone (PVP) capped Ag, Pd, Au and Cu salts to their respective NPs was described by Ayyappan *et al*. *via* a 12 hour reflux at 86 °C using ethanol as the reducing alcohol.[20] In this study, EtOH successfully reduced the Ag and Pd precursors, however, addition of an external reducing agent (Mg metal powder) was necessary to form the Au and Cu NPs. Control of NP size was also observed and deemed a consequence of the metal salt (Mx) to PVP ratio employed (1:5 or 1:10), with smaller NP sizes formed using a 1:10 Mx:PVP ratio. Teranishi and Miyake reported the formation of PVP-capped Pd NPs (< 3 nm average NP size) using short chain alcohols (C_1-C_3) as reducing agents under a shorter reflux

procedure (3 hours, flowing air).[19] Here, NP size was found to be dependent on the concentration of the reducing agent employed, with an optimal alcohol concentration found at 40 vol. %. Interestingly, the average NP size decreased with increasing alkyl chain length (MeOH > EtOH > PrOH).This was rationalised by the oxidising nature of the alcohol, which controlled the rate of $[PdCl_4]^{2-}$ reduction.[19] However, control of NP growth in this study was attributed to the quantity of the stabiliser added during synthesis, with the smallest Pd NPs observed using a molar ratio of PVP/Pd = 40.

The synthesis of stabiliser-free NPs has been reported in both water and alcoholic solutions in the preparation of Au NPs.[21–23] Abis *et al*. reported the preparation of 1 wt. % Au/TiO_2 in water only solvent systems with (PVA capped = 2.7 ± 0.6 nm, PVP capped = 3.5 ± 1.6 nm) and without (stabiliser free = 5.4 ± 1.6 nm) the inclusion of a stabilising agent during colloidal synthesis. From their work, the necessity of a stabiliser was apparent in controlling Au NP at [Au] ranging from 1 to 7 wt. %.[21,22] Kurawaki *et al*. studied Au NP formation in binary solutions of $XOH:H_2O$ (XOH = MeOH, EtOH, or PrOH). The smallest Au NPs with the narrowest size distributions (Au NP size = 24 ± 7 nm) formed in solvent systems comprised of 35 vol. % PrOH. The control over size was attributed to the longer carbon chain length and increased hydrophobicity of PrOH, which enhanced NP dispersion and suppressed agglomeration.[23] In addition, Liu *et al*. observed a similar trend of during the synthesis of stabiliser free Te NPs, wherein the polarity and dielectric constant of the solvent molecule was suggested to dictate the extent and time frame of NP growth.[14,24]

The influence of solvent polarity on NP size as a function of aliphatic chain length in the presence of a stabiliser has been investigated by Kimber *et al.* in the synthesis of citrate capped ZnO NPs. They showed that polar and non-polar solvents (C_1-C_6) restructured themselves within the synthesis solvent in ordered layers away from the NP surface.[16] Characterisation of these colloidal solutions using X-ray pair distribution function, found the more polar short chain alcohols reorganised themselves to form hydrogen bonds with neighbouring alcohol molecules. This rearrangement of the alcohols results in alternating layers of the alkyl chain and the hydroxyl groups. The aliphatic chain length, and its packing ability, was therefore found to substantially impact solvent restructuring and thus NP size.[16]

Interestingly, the polarity of the synthesis solvent not only influences NP size, but also the shape of the NP.[25] Hussain *et al*. reported that PVP-capped Au NPs (0.15 mM) prepared in $EtOH:H_2O$ mixtures of varying solvent polarity, and reduced using L-ascorbic acid

(1.5 mM), displayed lesser control of NP size as the solvent polarity decreased (20 vol. % EtOH:H_2O solution Au NP size = 9.7 ± 1.0 nm, 80 vol. % EtOH:H_2O solution Au NP size = 53.1 ± 15.2 nm). Control over Au NP shape, however, was consistent up to 50 vol. % EtOH, producing spherical Au NPs; the use of high [$EtOH_{(aq)}$] (> 50 vol. %) led to the formation of irregularly shaped Au NPs. Poor control of NP size and shape was hypothesised by Hussain *et al.* to be a result of the increased [$EtOH_{(aq)}$] causing asymmetric interactions between the solvent components (H_2O and EtOH), the stabiliser and the NP surface, which cause an increase in the surface energy of the Au NPs.[25] In order to minimise the increase in surface energy, aggregation of the NPs in solution occurs readily thus producing larger, more irregularly shaped NPs.[26]

Interactions of the capping agents, solvent systems and the catalyst surface have also been shown to impact Pd NP size and surface site availability. Rogers *et al*. investigated the sol-immobilisation of PVA-capped Pd NPs in equal vol. % ethanol:H_2O mixtures for the upgrading of furfural;[27] however, in this study the Pd precursor salt was reduced within 30 minutes by employing the use of a strong reducing agent ($NaBH_4$, 5:1 molar ratio $NaBH_4$:Pd).[27] Solvent polarity was not observed to influence NP size within this study in contrast to those previously mentioned; instead, NPs prepared in solvents with lower polarity (50:50 vol. %:vol. % EtOH:H_2O) produced Pd NPs with tighter control over size (Pd NP size = 2.1 ± 0.6 nm) than the H_2O only solvent (Pd NP size = 2.5 ± 0.8 nm), which was confirmed *via* EXAFS analysis. Not only did the presence of EtOH decrease the average Pd NP size, it also impacted the NP surface site availability, displaying greater probe molecule accessibility to corner and edge sites than the water prepared analogue. The improved control of NP size and surface site availability was described as a result of precursor salt addition, PVA solubility in the synthesis medium, and interactions between the solvent, the metal salt, and the formed colloid.[27] Interactions between the stabilising agent and the solvent system, and their subsequent influence on Pd NP size and activity, has also been reported by Chowdhury *et al*..[28] In the preparation of PVA-capped Pd NPs in varied EtOH:H_2O mixtures, NP size was observed to increase with gradual addition of EtOH to the synthesis solvent. This was rationalised to be a direct result of increased NP mobility in less viscous mediums (i.e. higher [$EtOH_{(aq)}$]). Moreover, complete encapsulation of the Pd NPs in solution by the stabilising agent increased with increasing [$EtOH_{(aq)}$], and was preserved in the final catalyst following drying (*Figure 3-1*).[28] This closer association of PVA to the Pd NP was explained as a reduction in interactions between H_2O and PVA as EtOH favours inter-solvent

interactions (EtOH with H_2O). A preference for inter-solvent interactions would thus leave a much greater quantity of OH functionalities in PVA to bind more strongly to the Pd surface, restricting access to active sites.[28] The addition of a stabilising agent solution to "stabiliser-free" Au/TiO_2 catalysts was reported by Abis *et al*. Wherein the activity of the catalysts in glycerol oxidation to glyceric and tatronic acids was studied.[21] Here, they demonstrated that the layering and blocking of glycerol binding sites on the Au NP surface can be achieved by adding polymer solutions (PVA or PVP) to the reaction catalyst. In doing so, the size of the surface NPs was shown to have little influence on activity, agreeing with the previously stated work by Rogers *et al.*[27] In this instance, full substrate conversion was achieved with and without capping by a stabilising agent. However, on addition of the stabilising agent solutions, optimised selectivity to glyceric acid with decreased glycerol conversions was observed, signifying influence of polymers on the oxidation pathway.[21]

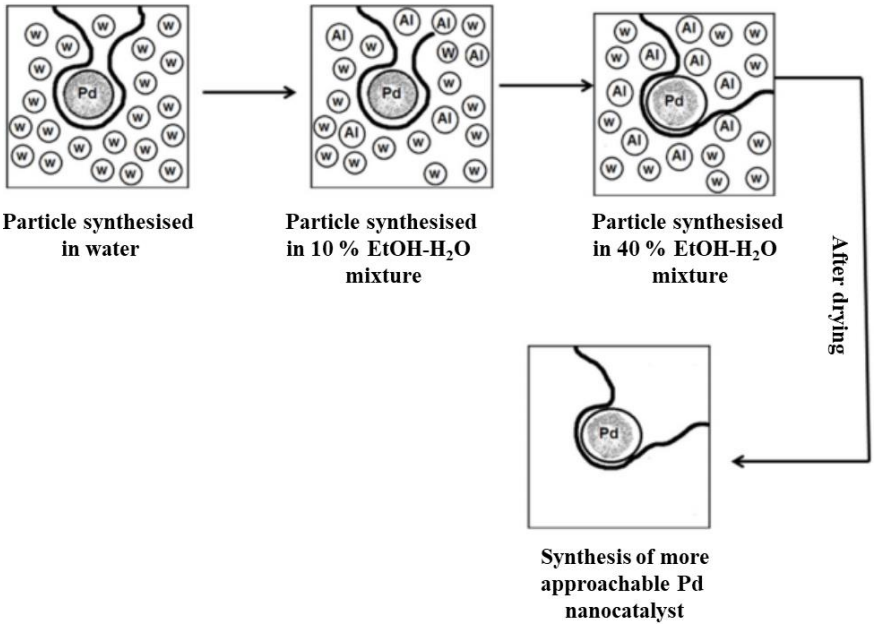

Figure 3-1. *Visualisation of changes to PVA encapsulation for a Pd nanoparticle synthesised in increasing [$EtOH_{(aq)}$] in the synthesis medium; image adapted from Chowdhury et al., Adv. Nat. Sci.: Nanosci. Nanotechnol, 2017,* ***8****, 1-10.*[28]

Further investigation into how the solvent system (50:50 XOH:H_2O) influences the $NaBH_4$ aided synthesis of PVA capped Pd NPs is presented in this chapter. The impact of the linear alkyl chain length (C_1-C_3), and associated branched alcohols (C_3-C_4), on the textural properties of the Pd NPs (size and surface site availability) are elucidated using MP-AES, TEM, XAFS and CO probe IR. Once the most optimal alcohol was established, incremental vol. % XOH from 0 to 100 vol. % were explored.

3.2 Experimental

3.2.1 Catalyst Preparation

TiO_2 supported Pd NPs were prepared following a standard sol-immobilisation synthesis method where the temperature of chemical reduction was kept constant at 1 °C. Pd colloids were prepared using K_2PdCl_4 ([Pd] = 128 μM) solvated into solution using deionised water (18.2 MΩ cm). For the catalysts presented in the first section, equal volume mixtures of alcohols and water (XOH = MeOH, PrOH, IsOH, *t*BuOH, all > 99 % trace impurity, Merck, *Table 3-1*) were used, and, following this, incremental volume ratios of MeOH to H_2O (0, 25, 50, 75 and 100 vol. % MeOH,

Table 3-2) were explored. All catalysts were capped with PVA prior to reduction (PVA/Pd (wt/wt) = 0.65, 0.01 g mL). Solutions of $NaBH_4$ (0.1 M; $NaBH_4$/Pd (mol/mol) = 5) were prepared fresh and added dropwise to each solution over the course of 1 minute, changing the colour of the solution from pale yellow to dark brown as the colloids formed. Reduction of the precursor salt was monitored over the course of 90 minutes to ensure full reduction. Once achieved, the sols were mixed with TiO_2 (P25), acidified to pH 1-2 using H_2SO_4, and vigorously stirred for 1 hour. The quantity of support material was calculated to yield final catalysts with metal loadings of 1 wt. % Pd. The catalyst slurries were filtered, washed thoroughly using deionised water, and dried overnight in air at room temperature.

Table 3-1. *Catalyst notation denoting the composition of the synthesis solvent employed during sol-immobilisation synthesis of 1 wt. % Pd/TiO_2 catalysts. The addition of PVA and an acidification step during synthesis are represented as P and A respectively.*

Catalyst Notation	Alcohol in Synthesis Solvent	Alcohol Abbreviation	XOH:H_2O (vol. %:vol. %)
PdWPA	-	-	100:0
Pd50MePA	Methanol	Me	50:50
Pd50EtPA	Ethanol	Et	50:50
Pd50PrPA	Propanol	Pr	50:50
Pd50IsPA	*Iso*propanol	Is	50:50
Pd50*t*BuPA	*tert*-Butanol	*t*Bu	50:50

Table 3-2. *Catalyst notation for 1 wt. % Pd/TiO_2 catalysts synthesised in solvent systems with increasing volume % methanol. The addition of PVA and an acidification step during synthesis are represented as P and A respectively.*

Catalyst Notation	MeOH:H_2O (vol. %:vol. %)
PdWPA	0:100
Pd25MePA	25:75
Pd50MePA	50:50
Pd75MePA	75:25
PdMePA	100:0

3.2.2 *Ex Situ* Characterisation

3.2.2.1 UV-Vis Spectroscopy

Reduction of the precursor Pd salt was analysed *via* UV-Vis spectroscopy. 4 mL of the catalyst solution was analysed at a time, with samples measured every 15 minutes for 90 minutes. Full reduction of the Pd species was observed when a broad absorbance band appeared in the spectrum (between 200-800 nm). Samples were characterised using a

Shimadzu UV-1800 spectrophotometer in a quartz cuvette, with the synthesis solvent as a reference (i.e. an equal volume of propanol and water were mixed thoroughly and used as the reference solution for the propanol solvated precursor salt).

3.2.2.2 Microwave Plasma–Atomic Emission Spectroscopy

Pd metal wt. % loadings were calculated using MP-AES, and were prepared by adding fresh Pd/TiO_2 catalysts (0.1 g) to a solution of aqua regia (3 × 8 mL, 3:1, $HCl:HNO_3$, Merck, trace metal purities). These solutions were then sealed in PTFE tubes and placed into an Anton-Paar Microwave 3000 centrifuge with one tube containing an aqua regia blank. Samples were heated to 200 °C and held for 40 minutes before cooling to room temperature. They were then diluted to 10 vol. % metal using deionised water (18.2 MΩ cm). Support particulates were removed from solution by filtering through a syringe filter-tip (Cole-Parmer, PTFE, 22 µm, 50 mm diameter) prior to analysis. Pd metal standards were first prepared and measured to calibrate the emission spectrometer. All standards, blanks and samples were vaporised and passed through a microwave induced plasma, exciting electrons in the sample. On their return to the ground state the element specific emission was detected using an Agilent Technologies 4100 MP-AES at four wavelengths of light corresponding to the atomic transitions of Pd (324.270, 340.458, 360.955 and 363.470 nm).

3.2.2.3 Transmission Electron Microscopy

Catalysts imaged using TEM were first sonicated in EtOH, then a small aliquot of the supernatant was pipetted onto a 300 mesh Cu TEM grid. TEM images were acquired by the author using a JEOL JEM 2100 EM, operating at 200 kV, at the Research Complex at Harwell, Didcot, U.K.

3.2.2.4 X-ray Absorption Fine Structure Spectroscopy

XAFS studies were performed to examine the Pd oxidation state (XANES), and to elucidate any NP size trends as a function of the 1st shell coordination sphere and the neighbouring environments surrounding the absorbing atom (EXAFS). Pd K-edge XAFS studies were carried out on the B18 beamline at DLS, Didcot, U.K. Measurements were performed in fluorescence mode using the QEXAFS setup with a fast-scanning Si(311) double-crystal monochromator, and multi-element Ge and ion chamber detectors (for sample and reference foils, respectively). Spectra were acquired at a time resolution of 1 min spectrum^{-1} (k_{max} = 18), with 3 scans acquired per sample. The composition of the oxidation state for

each sample was analysed using LCF of the XANES data, where the energy range fitted was -40 to +60 eV around the absorption edge, E_0. The weightings of the Pd^0 and PdO standards were constrained to be between 0 and 1 and to total a max value of 1. EXAFS data were fitted using the Artemis software package;[29] here, the amplitude reduction factor (S_0^2) was determined by fitting the Pd reference foil with a *.cif* file for Pd^0 (FCC structure, coordination number of Pd = 12, ICSD collection code = 52251). From the fit shown in *Figure 3-2*, S_0^2 was determined to be 0.75 and the fitting range was $1 < R < 3.4$ and $3 < k < 11.5$.

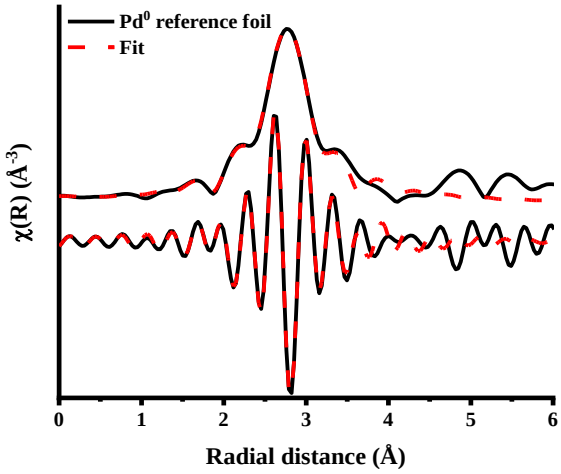

Figure 3-2. *Fitting of the Pd^0 reference foil EXAFS in order to determine the amplitude reduction factor to be applied to all palladium NP EXAFS data; fitting range: $1 < R < 3.4$, and $3 < k < 11.5$.*[29]

3.2.2.5 Fourier Transform Infrared

FTIR transmission spectra were acquired using a Nicolet iS10 spectrometer at a spectral resolution of 4 cm^{-1} and an accumulation of 64 scans. For each catalyst, ~ 25 mg of the catalyst was pressed to form a 13 mm diameter pellet and placed inside of the transmission cell. The chamber was purged with He (30 mL min^{-1}) for 30 minutes, and a background spectrum was recorded. Next, 10 % CO/He (10 mL min^{-1}) was pulsed into the chamber for 30 seconds between scans. CO was dosed over the pellet until complete saturation of the pellet surface was achieved, normally 3-4 pulses. At this point the gas was switched to He (30 mL min^{-1}) for 30 minutes, removing all gaseous and physisorbed CO from the chamber and pellet surface, respectively. Data processing and background subtractions were performed using the OMNIC software package.

3.3 Results and Discussion

3.3.1 Influence of Short Chain Alcohols on Colloidal Pd NP Synthesis

3.3.1.1 Ultraviolet-Visible Spectroscopy

Solutions of K_2PdCl_4 ([Pd] = 128 µM) were prepared in C_1-C_4 XOH:H_2O solvent systems and characterised *via* UV-Vis spectroscopy. Analysis of the precursor salt and reduced colloidal Pd solutions enabled monitoring of the reduction process before support immobilisation. The UV-Vis absorbance bands observed for PdWPA (*Figure 3-3* and *Figure 3-4*) correspond to those reported in the literature for the aqueous $[PdCl_4]^{2-}$ anion: 212, 237, and 310 nm (**I**-**III**) are assigned as ligand-to-metal charge transfer (LMCT) transitions and the peak at 410 nm (**IV**) corresponds to the *Laporte* forbidden *d-d* transitions, hence the very low intensity and broad nature of the peak .[30–33]

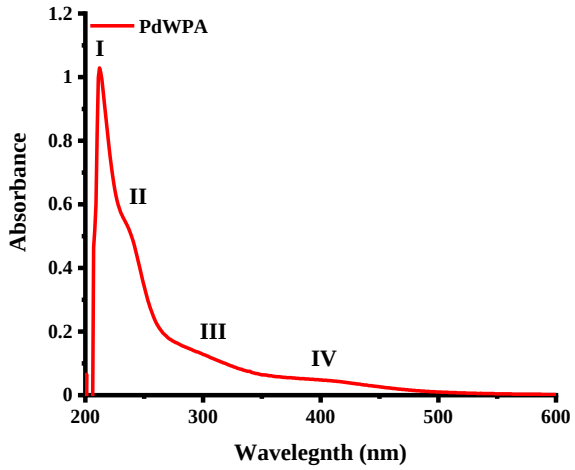

Figure 3-3. *UV-Vis spectrum of the PVA-capped Pd precursor salt solution K_2PdCl_4 ([Pd] = 128 µM) prepared in water (PdWPA). Positions of the LMCT bands are denoted by I, II and III, and d-d transitions are marked with IV.*

Similar features are observed in the UV-Vis spectra for the alcohol prepared Pd precursor solutions; however, the LMCT peaks are blue shifted by < 10 nm (*Figure 3-4*a-c). After the addition of $NaBH_4$, the reduction of the precursor salt was monitored every 15 minutes until a broad absorbance band was observed across the measured spectrum, signifying the complete reduction of Pd^{2+} to Pd^0 (*Figure 3-4*d).[27,34]

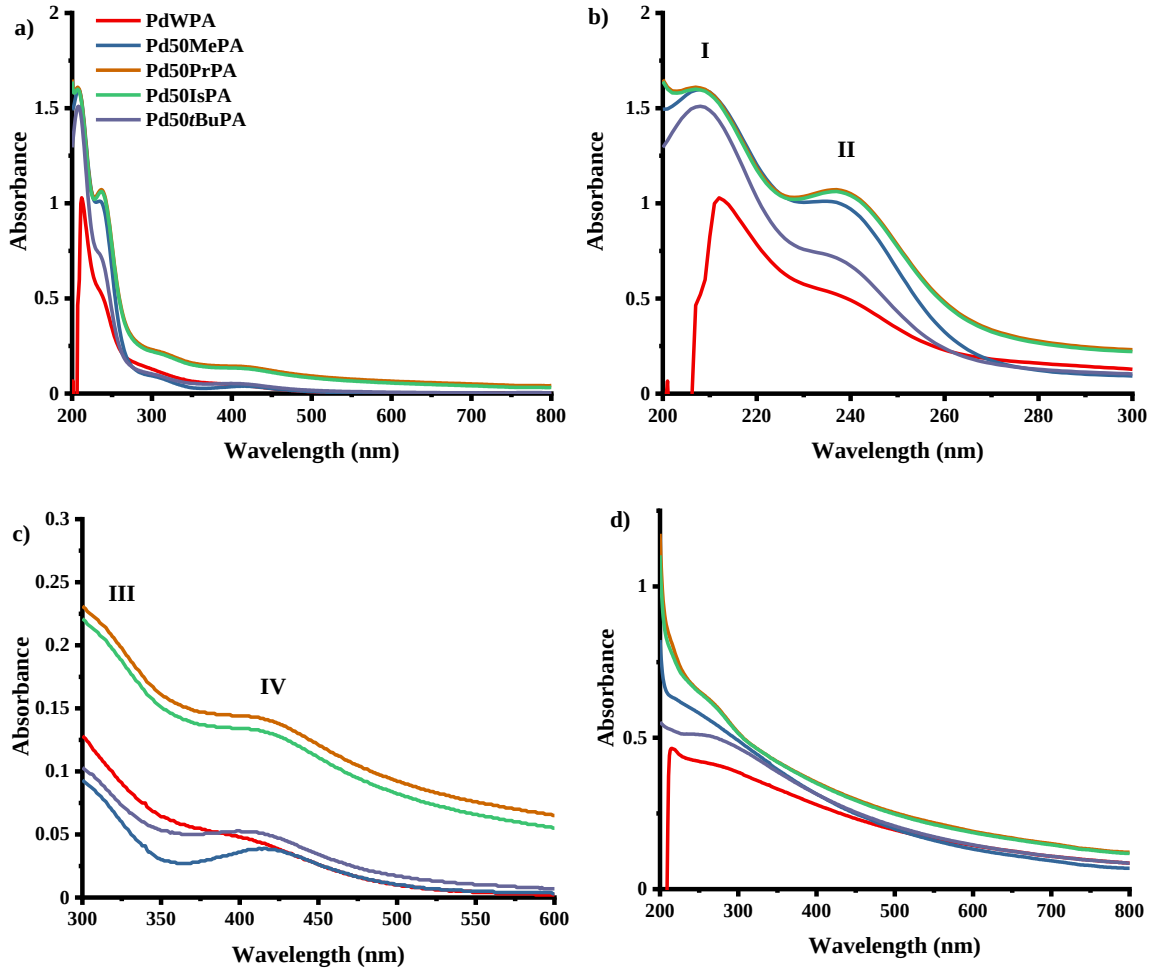

Figure 3-4. *UV-Vis spectra detailing a) Pd precursor salt solutions, b) the ligand-to-metal charge transfer bands, c) d-d band transitions and d) Pd colloids formed after reduction of the precursor salt solutions. Pd NPs were prepared in different XOH:H_2O solvent systems with equal alcohol concentrations (50 vol. %), except PdWPA which was prepared in 100 vol. % H_2O.*

3.3.1.2 Microwave Plasma – Atomic Emission Spectroscopy

The Pd wt. % loading for all catalysts was determined *via* MP-AES. Though the highest Pd loadings observed are for the literature Pd50EtPA catalyst,[27] both pure water and methanol:water mixed solvent systems produced metal loadings of > 80 % of the theoretical 1 wt. % Pd (*Table 3-3*). By increasing the linear chain length from C_2 to C_3, less than half of the theoretical Pd was successfully anchored onto TiO_2, i.e. 1 wt. % Pd50PrPA = 0.45 wt. % Pd. The branched chain alcohols, IsOH and *t*BuOH, also displayed incomplete loading of the Pd NPs. Interestingly, 1 wt. % Pd50IsPA achieved a higher Pd loading (0.57 wt. %) than its linear chain isomer (1 wt. % Pd50PrPA = 0.45 wt. % Pd). Immobilisation of the colloidal

NPs onto TiO_2 requires an acidic pH to induce charge interactions between PVA-capped NPs and the charged support surface as stated in the literature for water-based catalysts.[1,35,36] The comparable metal loadings observed for the pure water, methanol and ethanol based solvent systems may result from the stronger acidity of these solvents in solution aiding the catalyst slurry pH below the pI of TiO_2 (pI of TiO_2 is at pH = 6.1).[37] This rationale, however, does not explain the drop in loading observed from Pd50EtPA to Pd50PrPA as their synthesis solvents have similar pK_a values.[38] Another plausible explanation for this could be due to the attractive forces between the colloidal NPs and the support surface being affected by the pH of the alcohol. As the longer chain alcohols are more basic than the more polar, shorter chain alcohols, the attractive forces between the Pd50PrPA, Pd50IsPA, or Pd50*t*BuPA NPs in solution and the TiO_2 support surface are dampened compared to the catalysts that display higher Pd loadings.

Table 3-3. *Pd wt. % loadings calculated via MP-AES determined by the average sample weight (mg) and the average Pd concentration per sample (ppm). The Pd wavelength studied was 340.458 nm. Values for Pd50EtPA are taken from Rogers et al., ACS Catal., 2017, **7**, 2266-2274.*[27]

Catalyst	**pKa Value in H_2O**[38]	**Sample Mass (g)**	**Ave. [Pd] (ppm)**	**Ave. [Pd] (wt. %)**
PdWPA	14.0	0.099	8.27	0.83
Pd50MePA	15.5	0.100	8.08	0.81
Pd50EtPA[27]	15.5	-	-	0.88
Pd50PrPA	16.1	0.104	4.71	0.45
Pd50IsPA	17.2	0.099	5.70	0.57
Pd50*t*BuPA	19.2	0.099	5.60	0.56

3.3.1.3 Transmission Electron Microscopy

Average Pd nanoparticle sizes were assessed *via* TEM. It is evident that the inclusion of the linear, shorter chain alcohols, bar PrOH, leads to supported Pd NPs with size distributions narrower than those measured for PdWPA. The trend in the controlled particle sizes observed for MeOH (1.1 ± 0.6 nm) and EtOH (2.1 ± 0.6 nm) (*Figure 3-5* and *Figure 3-6*) is still apparent with the associated errors (*Table 3-4*).[27] Colloidal synthesis in IsOH and *t*BuOH solutions produced supported Pd NPs with better control of size than PdWPA; however, this can be attributed to the much lower Pd loadings observed for these catalysts (0.56 and 0.57 wt. %, respectively). The lower [Pd] on the TiO_2 support means that mobilisation and coalescence of the NPs on the surface is less likely to occur. Though 200 – 300 particles were counted per image, it should be noted that whilst TEM gives an indication of NP size, it is still a user subjective technique.[39,40]

Table 3-4. *Average Pd NP sizes for the prepared Pd/TiO_2 catalysts and Pd50EtPA. NP size was calculated for the fresh catalysts using a population size of 200-300 Pd NPs per sample. Values for Pd50EtPA are taken from Rogers et al., ACS Catal., 2017, **7**, 2266-2274.*[27]

Catalyst	Ave. TEM Pd NP size (nm)
PdWPA	2.6 ± 1.4
Pd50MePA	1.1 ± 0.6
Pd50EtPA[27]	2.1 ± 0.6
Pd50PrPA	2.8 ± 1.6
Pd50IsPA	1.9 ± 0.9
Pd50*t*BuPA	2.0 ± 0.9

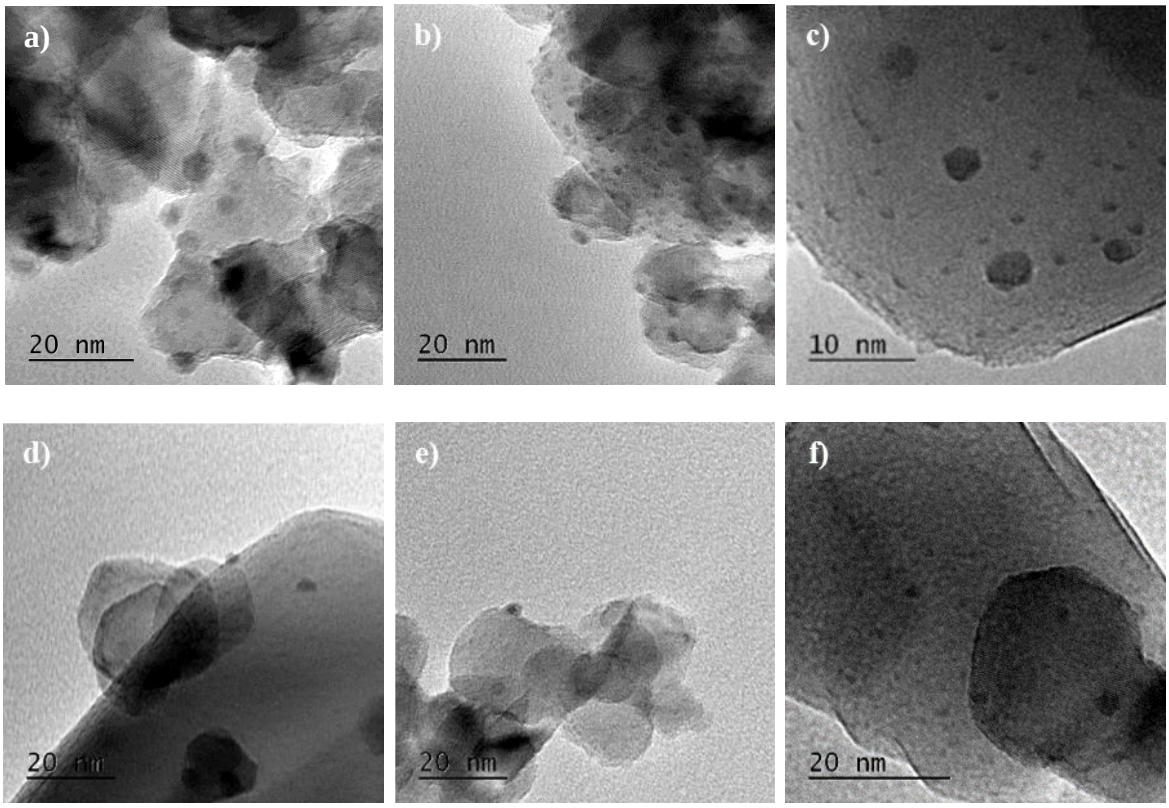

Figure 3-5. *Indicative TEM images of the prepared 1 wt. % Pd/TiO_2 catalysts; a) PdWPA, b) Pd50MePA, c) Pd50EtPA taken from Rogers et al., ACS Catal., 2017, **7**, 2266-2274,[27] d) Pd50PrPA, e) Pd50IsPA, f) Pd50tBuPA.*

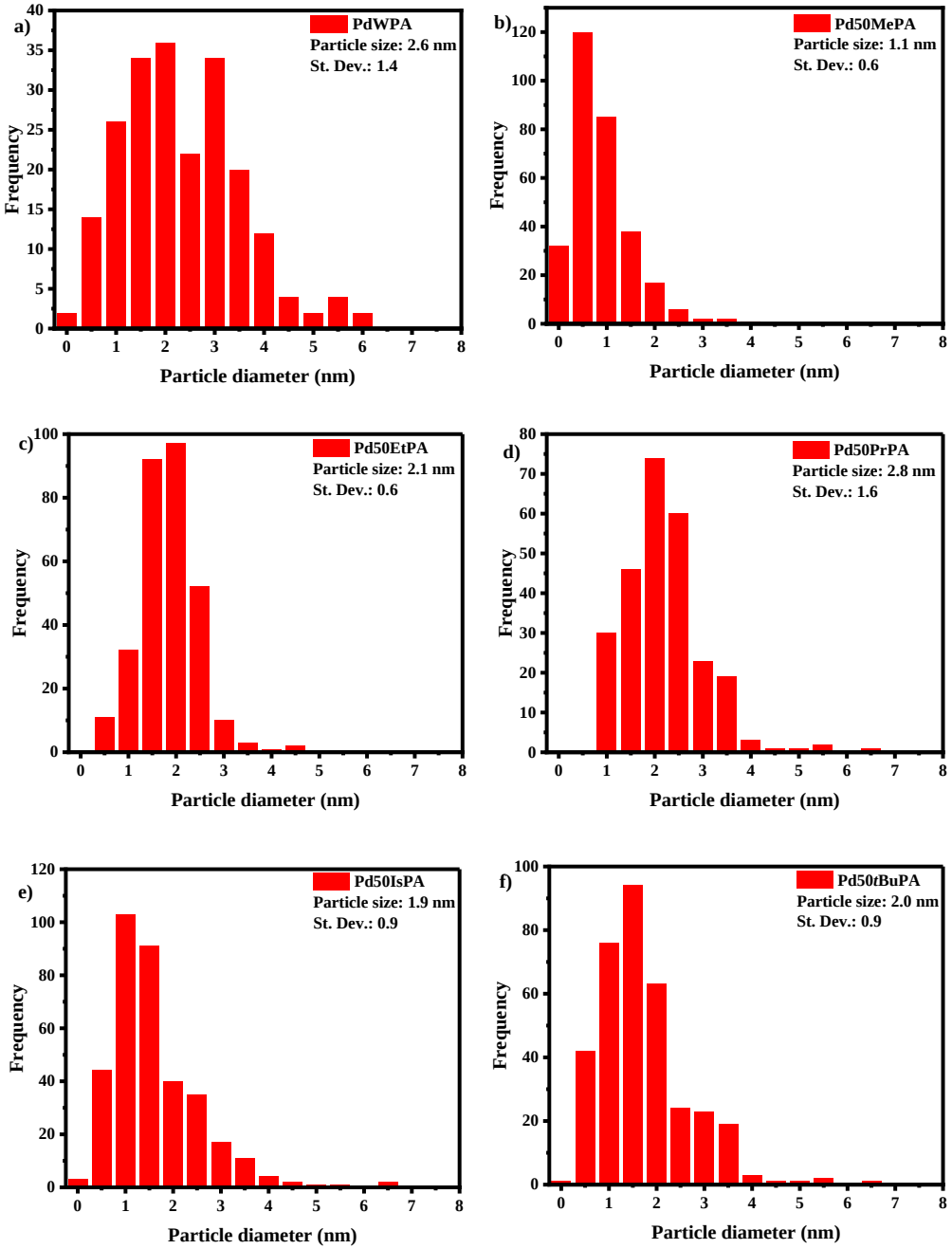

Figure 3-6. *Size distribution histograms of the prepared 1 wt. % Pd/TiO_2 catalysts; a) PdWPA, b) Pd50MePA, c) Pd50EtPA taken from Rogers et al., ACS Catal., 2017, **7**, 2266-2274,[27] d) Pd50PrPA, e) Pd50IsPA, f) Pd50tBuPA. Histograms were compiled from image analysis of 200-300 Pd NPs per sample.*

3.3.1.4 Pd K-edge X-ray Absorption Fine Structure

Pd K-edge XAFS data were recorded for the XOH modified Pd catalysts as well as select Pd reference complexes: Pd^0 foil, PdO and $PdCl_2$. XAFS is a bulk characterisation technique, therefore, acquired data is representative of an average of the whole sample. Speciation at the NP surface can thus influence the data acquired for NPs of small sizes, where the surface:core ratio of species increases with decreasing NP diameter.

3.3.1.4.1 X-ray Absorption Near-Edge Structure

Pd K-edge XANES allowed the average Pd oxidation state to be determined *via* shifts in energy or changes to the intensity of features within the XANES region. Though sample geometry can be extrapolated from pre-edge features for many metal species,[41,42] the reduced Pd NPs have a full *d* valance thus excitement of electrons is not feasible before the edge jump (i.e. the Pd K-edge energy, 24350 eV). Pd-Cl bonding is not the cause of the Pd^{2+} oxidation state observed as a broad feature is not seen between 24360-24380 eV (*Figure 3-7*a-c).[43] Instead, the greater intensity of the edge jump describes an increased proportion of the allowed electronic transitions occurring from the Pd *1s*→4*d* orbital. Here, the increased absorption of the white line peak resembles slight Pd-O (Pd^{2+}) character. Using linear combination fitting (LCF) of the XANES region, the Pd oxidation state can thus be determined, the error associated with this fitting is given as the R_{factor}, where the confidence of the fit is represented by the smallest value above zero. The trend in the absorption edge intensity observed with increasing linear chain length is quantified as a percentage: Pd50MePA = 50 %, Pd50EtPA = 36 %, Pd50PrPA = 21 % (*Table 3-5*). Preparation of Pd NPs in branched chain alcohols display comparable Pd^{2+} character to PdWPA: PdWPA = 30 %, Pd50IsPA = 34 %, Pd50*t*BuPA = 34 %. The Pd^{2+} oxidation state can indicate the formation of either crystalline PdO or a passivated oxide layer that forms on exposure to air.[44] Despite the colloidal oxidation state being determined as Pd^0 *via* UV-Vis, oxidation of the Pd may have occurred during the drying stage of synthesis.

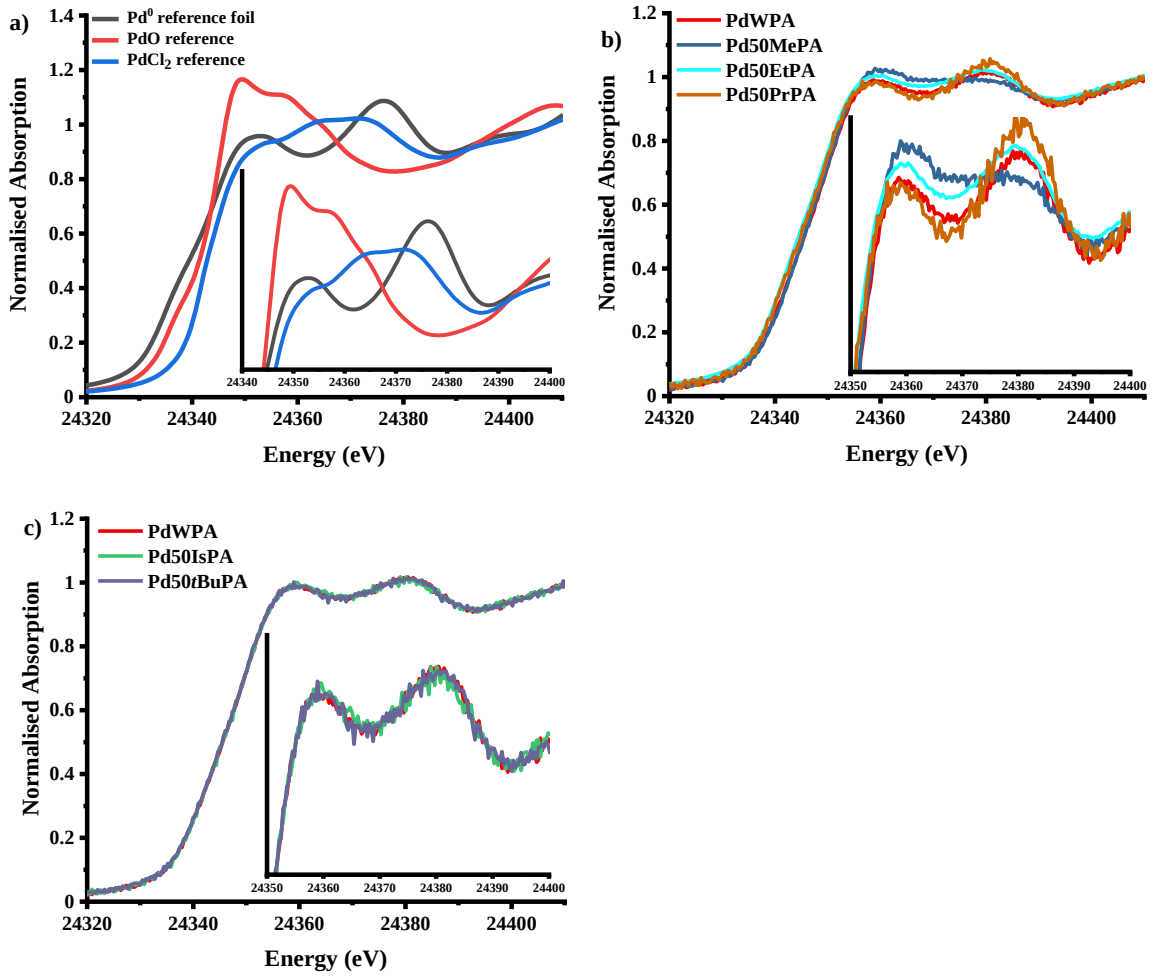

Figure 3-7. *XANES spectra acquired for the 1 wt. % Pd/TiO_2 catalysts prepared using various short chain alcohols in the synthesis solvent. Spectra were measured at the Pd K-edge; XANES data are presented as the normalised absorption. Pd50EtPA spectrum is taken from Rogers et al., ACS Catal., 2017, **7**, 2266-2274.*[27]

Table 3-5. *XANES linear combination fit reference standards for the 1 wt. % Pd/TiO_2 synthesised using varied short chain alcohols. The accuracy of the fit is described by an R_{factor} value, where the confidence of the fit is represented by the smallest value above zero.*

Catalyst	Reference standard (%)			R_{factor}
	Pd^{2+}	Pd^0	Pd^{2+}/Pd^0	
PdWPA	30	70	0.43	0.002
Pd50MePA	50	50	1.0	0.003
Pd50EtPA[27]	36	64	0.56	0.002
Pd50PrPA	21	79	0.27	0.093
Pd50IsPA	34	66	0.52	0.004
Pd50*t*BuPA	34	66	0.52	0.002

3.3.1.4.2 Extended X-ray Absorption Fine-Structure

The local structure of neighbouring atoms with respect to the absorbing Pd atom was investigated using EXAFS (*Figure 3-8*). Whilst it is hard to determine the nature of the scattering path at ~ 1.7 Å in the Fourier transformed EXAFS figures (*Figure 3-8*a, c, e), oscillations in the unprocessed $\chi(k)$ EXAFS data (*Figure 3-8*b, d, f) resembles the reference PdO at lower *k*-range and the Pd^0 foil at higher *k*-range. The scattering pathway at ~ 1.7 Å can therefore be associated with Pd-O bonding, which complements the Pd^{2+} oxidation state observed in the XANES LCF. Contrastingly, complete reduction of the Pd species was confirmed *via* UV-Vis, therefore, a neighbouring atom to the Pd absorber should be Pd and not O. Two principle scattering paths are present in the PdO reference FT EXAFS, corresponding to crystalline PdO (~ 3.2 Å) and a layering of oxide on the Pd surface (~ 1.7 Å). The former scattering path corresponds to Pd-O bonding in a large crystalline lattice and is known to form above 200 °C.[45] The smaller Pd-O scattering path denotes the

formation of very small Pd NPs, with increased surface area to volume ratios. With larger ratios, the passivation of the Pd surface in air occurs with greater ease, forming oxide monolayers covering the NP.[27,44,46] The Pd NP size determined *via* TEM analysis agrees with the EXAFS and suggests that small Pd NPs have been formed with the aforementioned oxide layering.

Pd nanoparticle size trends can be inferred by assessing the magnitude of scattering at ~ 2.7 Å, which is the 1st shell Pd-Pd scattering distance in metallic Pd^0 (FCC). A decrease in magnitude suggests fewer Pd atoms in the immediate surroundings to the absorber; hence, smaller Pd NPs. Quantification of the EXAFS data is possible through computational fittings, enabling the localised coordination number of the absorbing atom to be determined (*Figure 3-9* and *Table 3-6*).[47] The increase in NP size with chain length observed *via* TEM is consistent with the trend of the fitted EXAFS data, where changes in the coordination numbers (CN_{Pd-Pd} and CN_{Pd-O}) is indicative of variations to NP size. As the linear chain length doubles from MeOH to EtOH, an increase in the local Pd environment is observed though these are within error of one another (Pd50MePA: $CN_{Pd-Pd} = 4.9 \pm 0.4$, Pd50EtPA: $CN_{Pd-Pd} = 5.7 \pm 0.4$).[27] The largest growth in the number of nearest Pd neighbours occurs from Pd50EtPA to Pd50PrPA, with the EXAFS detailing the formation of larger, more bulk-like Pd NPs (Pd50PrPA: $CN_{Pd-Pd} = 9.1 \pm 0.3$). The low magnitude of bonding for the passivated oxide layer (scattering path of ~ 1.7 Å) also agrees with larger Pd NP formation (Pd50PrPA: $CN_{Pd-O} = 0.9 \pm 0.2$). Synthesis using an aqueous branched alcohol mixture produces Pd NPs with no observable differences in the Pd-Pd and Pd-O scattering paths discussed above. When compared to the standard PdWPA, the fitted CNs (Pd-Pd and Pd-O) for both Pd50IsPA and Pd50*t*BuPA are within error of it (PdWPA: $CN_{Pd-Pd} = 7.2 \pm 0.5$, $CN_{Pd-O} = 1.6 \pm 0.3$, Pd50IsPA: $CN_{Pd-Pd} = 6.9 \pm 0.4$, $CN_{Pd-O} = 1.6 \pm 0.3$, Pd50*t*BuPA: $CN_{Pd-Pd} = 7.1 \pm 0.4$, $CN_{Pd-O} = 1.5 \pm 0.3$), suggesting that the addition of branched alcohols only detrimentally impacts the achieved metal loading. Furthermore, whilst TEM gave an indication that controlled NP sizes (≤ 2 nm) were achieved for Pd50IsPA and Pd50*t*BuPA, the per atom averages acquired *via* EXAFS suggest that the NP sizes would be similar to that observed for PdWPA (2.6 ± 1.4 nm). Nonetheless, XAFS and TEM are valuable techniques when employed in tandem, enabling the size and shape of the NPs to be evaluated, respectively. It is thus apparent that the greatest control over Pd NP size was achieved using a synthesis solvent composed of equal vol. % MeOH:H_2O.

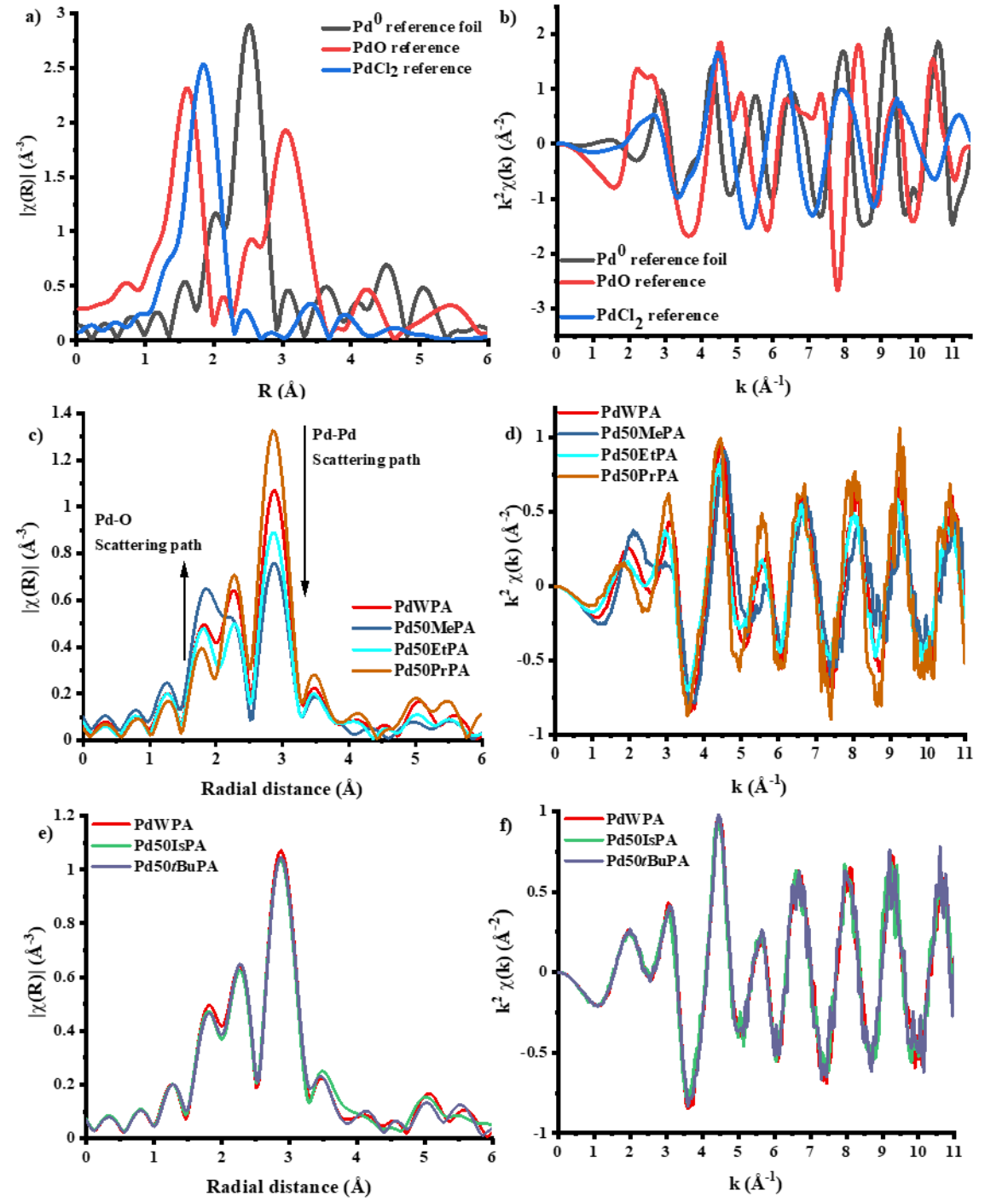

Figure 3-8. *Pd K-edge XAFS data collected ex situ. The data displays the experimental FT χ(k) (a, c & e) and χ(k) data (b, d & f) for the varied alcohol chain length prepared 1 wt. % Pd/TiO₂ catalysts. Pd references data are displayed in figures a) & b), samples prepared using linear chain short chain alcohols in the synthesis solvent are displayed in figures c) & d), samples prepared using branched chain alcohols in the synthesis solvent are displayed in figures e) & f). Pd50EtPA data is taken from Rogers et al., ACS Catal., 2017, **7**, 2266-2274.*[27]

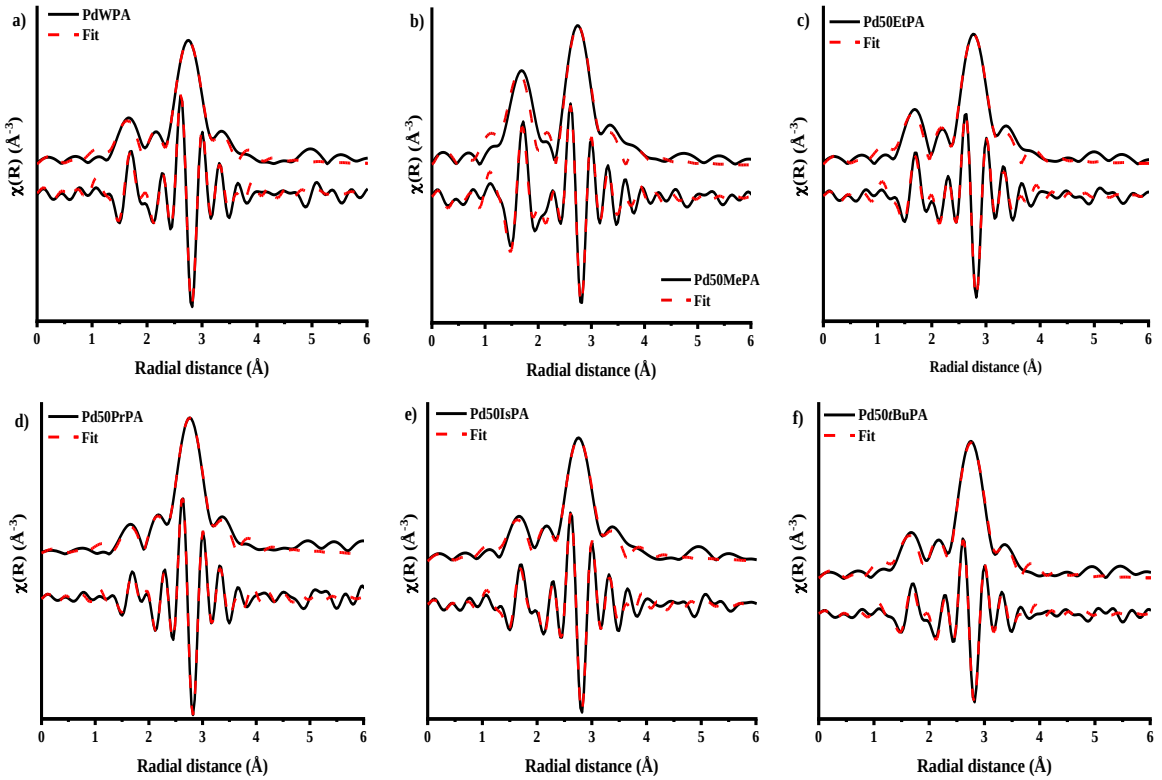

Figure 3-9. *Fitted experimental FT χ(k) data, both the magnitude and real components for Pd/TiO_2 catalysts prepared using various short chain alcohols in equal volume mixtures with water as the synthesis solvent: a) H_2O only solvent system, b) MeOH:H_2O system, c) EtOH:H_2O taken from Rogers et al., ACS Catal., 2017, **7**, 2266-2274,[27] d) PrOH:H_2O system, e) IsOH:H_2O system and f) tBuOH:H_2O system.*

Table 3-6. *1st shell EXAFS fitting parameters derived from the k^2 weighted Fourier transform of the Pd K-edge EXAFS data for the XOH solvent system catalysts. Amplitude reduction factor, S_0^2 = 0.75, was determined from fitting an acquired Pd metal reference foil. EXAFS fittings range: 3 < k < 11.5, 1 < R < 3.4, number of independent points = 11.2. The accuracy of the fit is described by an R_{factor} value, where the confidence of the fit is represented by the smallest value above zero.*

Catalyst	Abs-Sc	CN	R (Å)	$2\sigma^2$ (Å^{-2})	E_0 (eV)	R_{factor}
PdWPA	Pd-Pd	7.2 ± 0.5	2.74 ± 0.08	0.008	0.2 ± 0.9	0.017
	Pd-O	1.6 ± 0.3	1.99 ± 0.07	0.005		
Pd50MePA	Pd-Pd	4.9 ± 0.4	2.73 ± 0.06	0.008	3.2 ± 0.6	0.030
	Pd-O	2.5 ± 0.2	1.98 ± 0.03	0.005		
Pd50EtPA[27]	Pd-Pd	5.7 ± 0.4	2.74 ± 0.01	0.008	1.8 ± 0.8	0.016
	Pd-O	1.5 ± 0.2	1.98 ± 0.06	0.005		
Pd50PrPA	Pd-Pd	9.1 ± 0.3	2.74 ± 0.04	0.008	2.4 ± 0.5	0.005
	Pd-O	0.9 ± 0.2	1.98 ± 0.09	0.005		
Pd50IsPA	Pd-Pd	6.9 ± 0.4	2.74 ± 0.01	0.008	0.5 ± 0.8	0.015
	Pd-O	1.6 ± 0.3	1.98 ± 0.07	0.005		
Pd50*t*BuPA	Pd-Pd	7.1 ± 0.4	2.74 ± 0.01	0.008	0.3 ± 0.8	0.018
	Pd-O	1.5 ± 0.3	1.98 ± 0.09	0.005		

3.3.1.5 Infrared Spectroscopy

Implications of catalyst activity cannot be gained solely through comparison of NP sizes; instead, the nature and accessibility of NP surface sites have been shown to play an important role in catalysis.[8,10,48,49] Characterisation of free surface sites on the Pd NPs has been performed through transmission IR measurements, in which characteristic CO stretching vibrations are used to determine the type and abundance of NP sites. Variations to the NP surface, that arise as a result of the synthesis procedure applied, are identified through comparisons of this work and the literature.[50–59] Probing of the catalyst surface with CO yields two different types of binding (*Figure 3-10*a): (1) bridged (2000-1800 cm^{-1}) and (2) linear (2150-2000 cm^{-1}). Bridged CO adsorption modes are observed at wavenumbers < 2000 cm^{-1} and correspond to: 3-fold bridging CO (μ_3, 1875 cm^{-1}, i), 2-fold bridging CO on Pd(100) facets (μ_2(100), 1945 cm^{-1}, ii), and 2-fold bridging CO on Pd(111) planes (1980 cm^{-1}, iii). Linear adsorption of CO to NP surfaces can take place *via*: edge sites (~ 2063 cm^{-1}, iv), corner sites of Pd^0 (~ 2090 cm^{-1}, v), Pd^+ species (2120 cm^{-1}, vi), and Pd^{2+} species (2140 cm^{-1}, not labelled).[8,56,60]

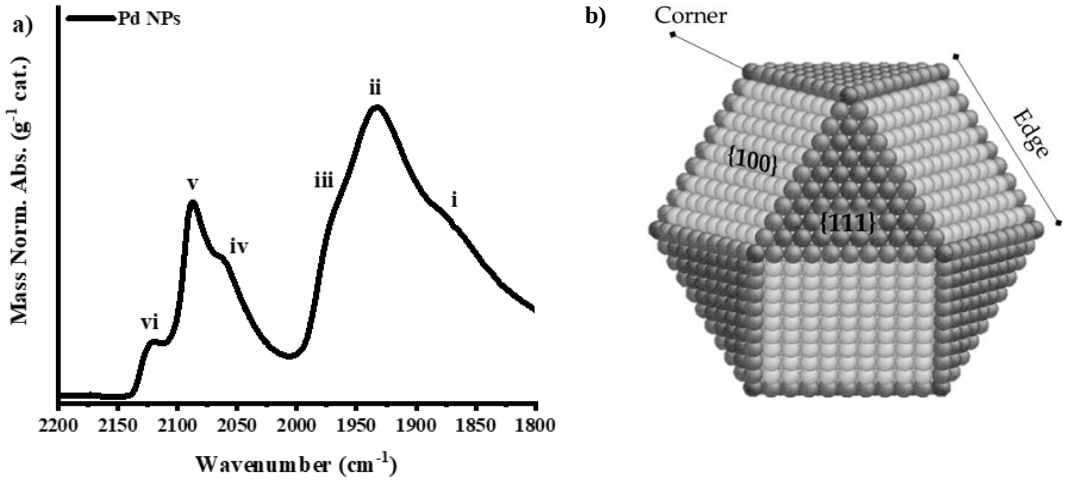

Figure 3-10. *a) FTIR spectrum detailing the different CO adsorption modes visible over TiO_2 supported Pd NPs. Bands i-iii detail CO adsorption to Pd^0 atoms via bridging CO bonds (i is μ_3, and both ii and iii are μ_2 binding modes). Linear CO adsorption vibrations are found at higher wavenumber and are labelled as iv-vi (iv is linear to Pd^0, v is linear adsorption to a corner site on Pd^0 and vi is linear adsorption to Pd^+), b) is a representation of the typical active sites available on a cuboctahedral metal nanoparticle; image taken from Campisi et al., Catalysts, 2016, **6**, 8.*[8]

Introduction of MeOH and EtOH into the synthesis solvent decreases the abundance of the bridging CO adsorption sites, particularly μ_2(100) (*Figure 3-11*a-c). However, it is hard to determine if this is a result of interactions between the solvent and PVA suppressing access to the surface sites,[27] or if the formation of smaller NPs reduces the abundance of NP planes where CO bridging is more likely to occur.[60] Interestingly, Pd50EtPA shows a marked increase in the μ_2-CO binding at ~ 1975 cm^{-1}, whereas this band is observed as a slight shoulder for the other alcohol prepared catalysts (*Figure 3-11*d-f). Both Pd50PrPA and Pd50*t*BuPA display a reduction in the adsorption of CO on edge sites (~ 2063 cm^{-1}), whilst Pd50IsPA displayed the largest abundance of CO adsorption on all aforementioned surface sites. It would thus be expected that Pd50IsPA would be the least selective for a particular product, whereas PdWPA would be more selective for products formed at bridge sites, and Pd50EtPA would be more selective for products formed at linear sites.[8,10,61]

The preparation of Pd NPs with high metal loadings and controlled NP sizes (< 3 nm) has been discussed, utilising solvent systems of equal vol. % XOH:H_2O. From the data presented, sol-immobilisation benefits from synthesis solvents composed of H_2O:XOH mixtures (where X = Me or Et). The remaining linear and branched alcohol systems require higher degrees of optimisation to bring their metal loadings to levels comparable with PdWPA, which is outside of the scope of this chapter.

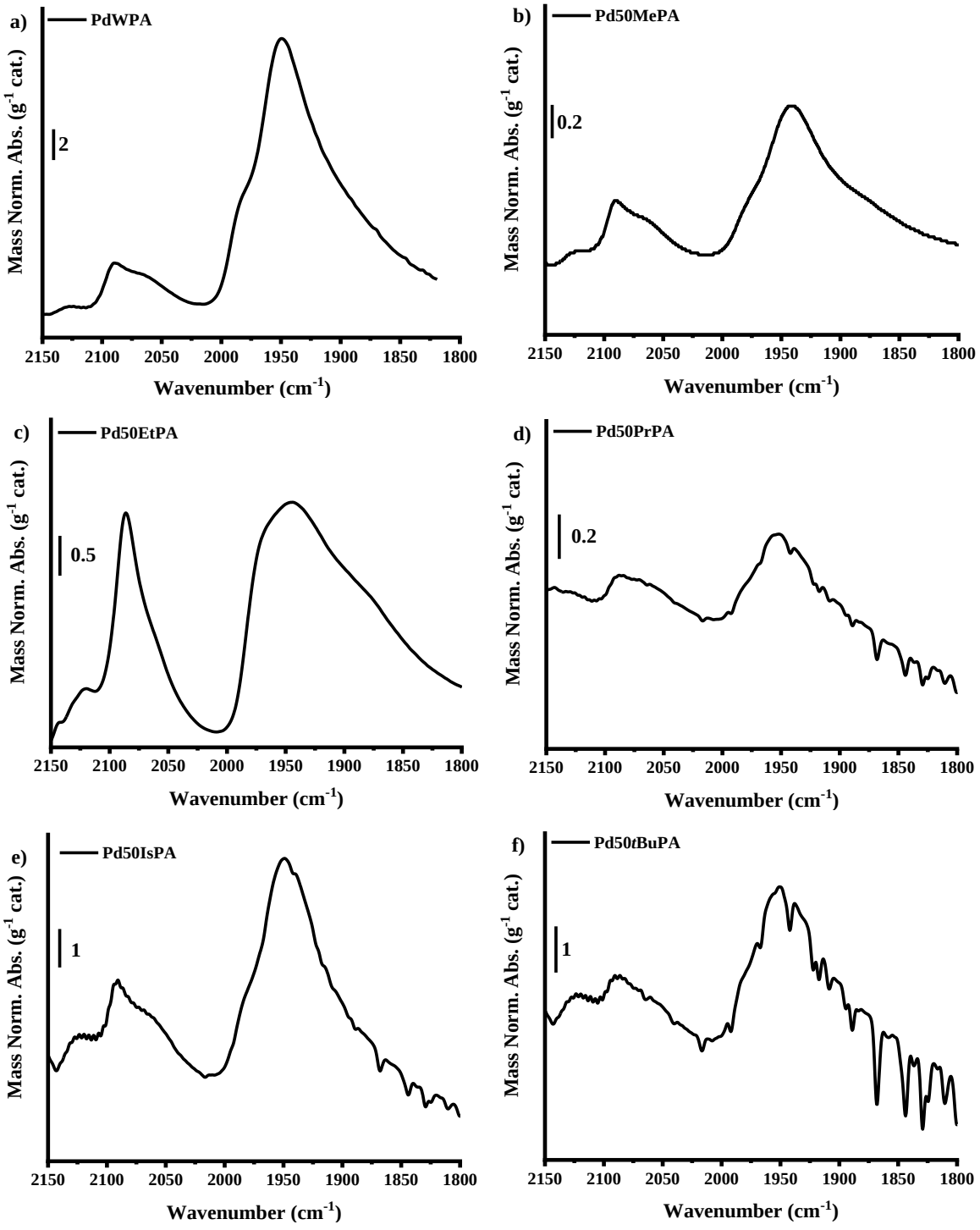

Figure 3-11. *FTIR spectra acquired for CO-adsorption studies on Pd/TiO_2 catalysts prepared at 1 °C under varied solvent environments, where the ratio of XOH:H_2O is 50:50 unless otherwise stated: a) PdWPA, water only solvent system, b) Pd50MePA, c) Pd50EtPA taken from Rogers et al., ACS Catal., 2017, **7**, 2266-2274,[27] d) Pd50PrPA, e) Pd50IsPA, and f) Pd50tBuPA.*

3.3.2 Increasing [Methanol] in Colloidal Pd Nanoparticle Synthesis

The influence of the synthesis solvent on the final catalyst is further explored in this section by varying the [alcohol] which produced the smallest NP size with the highest metal loading. Therefore, synthesis solvents comprised of 25 vol. % increments of MeOH (0-100 vol. %) were used in the preparation of 1 wt. % Pd/TiO_2, named PdWPA, Pd25MePA, Pd50MePA, Pd75MePA, and PdMePA, where M = MeOH and the number states the $[MeOH_{(aq)}]$.

3.3.2.1 Ultraviolet-Visible Spectroscopy

The solutions of K_2PdCl_4 were prepared in varied ratios of $MeOH_{(x)}$:$H_2O_{(100-x)}$ and examined using UV-Vis spectroscopy. As described previously, the bands observed in the pre-reduced solutions (*Figure 3-12*a) are LMCT (~ 212, ~ 237, ~ 310 nm) and *d-d* transition (~ 400 nm) bands consistent with polymer capped $[PdCl_4]^{2-}$.[12,27,30–34] Increases to the intensity of the absorption is noticeable with increasing MeOH concentration in the synthesis solvent (*Figure 3-12*a-c). Complete reduction of the Pd precursor salt solution was observed for all samples after 30 minutes, displaying a broad absorption band across the spectrum (*Figure 3-12*d).

3.3.2.2 Microwave Plasma–Atomic Emission Spectroscopy

Elemental analysis of the prepared Pd catalysts shows that optimal loading is achieved without the addition of methanol to the synthesis solvent (*Table 3-7*). An equal vol. % solution of MeOH:H_2O produced the MeOH based catalyst with the highest loading. However, as the solvent system becomes more alcoholic, the achieved Pd loading decreases to below 40 wt. % of the ideal loading (Pd75MePA: 0.24 wt. % and PdMePA: 0.37 wt. % Pd). Decreased Pd loading at higher MeOH concentrations could be attributed to: (1) insufficient solvation of both the precursor salt, K_2PdCl_4, and the stabilising agent, PVA,[19] or (2) interactions between MeOH and the support surface altering the surface pH, and subsequent pI charge, potentially dampening the charge attractions between TiO_2 and the Pd NPs.

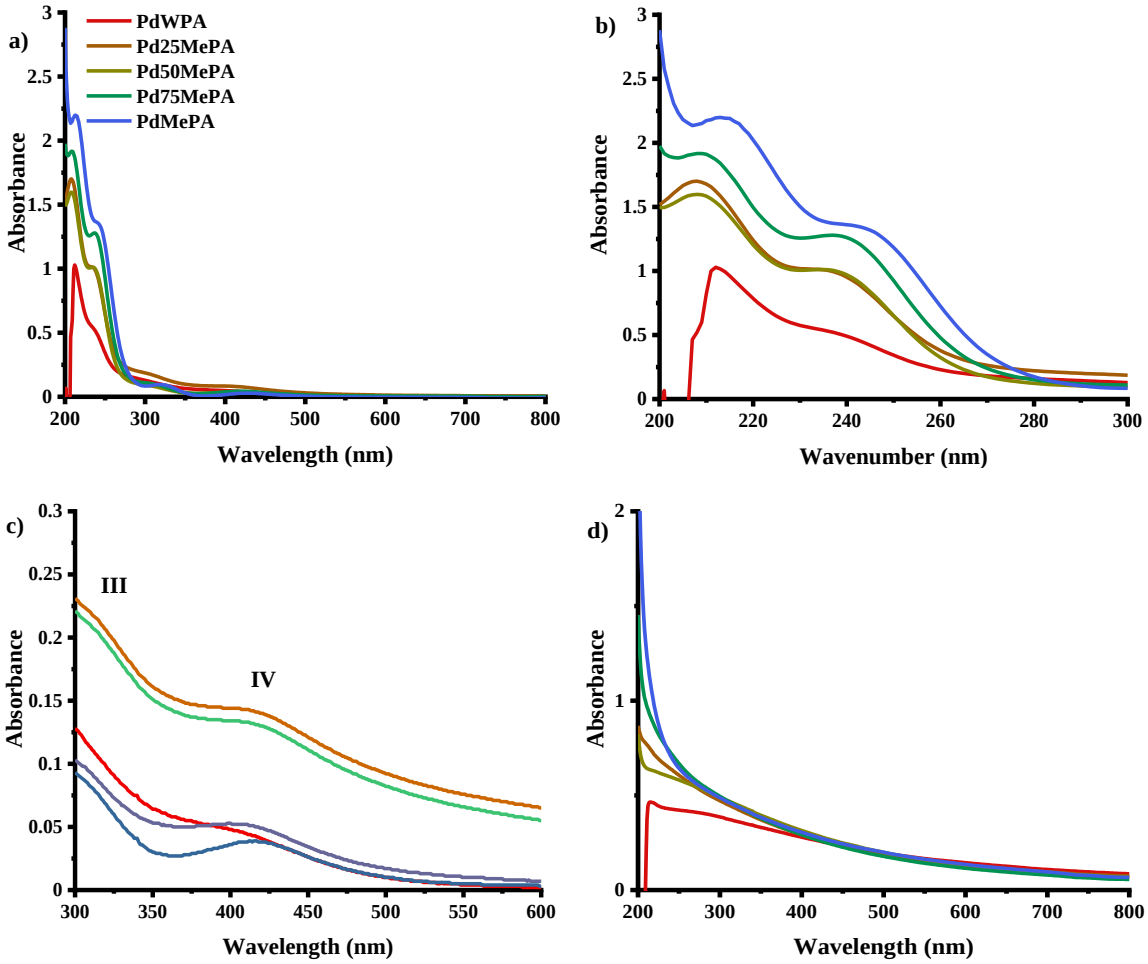

Figure 3-12. *UV-Vis spectra detailing a) Pd precursor salt solutions, b) the ligand-to-metal charge transfer bands, c) d-d band transitions and d) Pd colloids formed after reduction of the precursor salt solutions. Pd NPs were prepared in increasing* $[MeOH_{(aq)}]$ *in the synthesis solvent.*

Table 3-7. *MP-AES Pd wt. % loading values for Pd/TiO_2 catalysts prepared to 1 wt. % in varying methanol and/or H_2O solvent systems.*

Catalyst	Sample Mass (g)	Ave. [Pd] (ppm)	Ave. [Pd] (wt. %)
PdWPA	0.099	8.27	0.83
Pd25MePA	0.0989	7.27	0.74
Pd50MePA	0.100	8.08	0.81
Pd75MePA	0.102	2.47	0.24
PdMe	0.0952	3.48	0.37

3.3.2.3 Transmission Electron Microscopy

Pd NPs with average diameters < 3 nm were confirmed for all catalysts in this series *via* TEM imaging (*Figure 3-13* & *Figure 3-14*). The smallest average size was observed for the 50 vol. % MeOH catalyst. Interestingly, the average Pd NP size decreases from 0 vol. % MeOH to 50 vol. % (2.6 ± 1.4 nm to 1.1 ± 0.6 nm, respectively), and increases again toward 100 vol. % MeOH (1.8 ± 0.9 nm). It is believed that, similar to the average NP sizes observed for Pd50IsPA and Pd50*t*BuPA, the higher MeOH concentration systems display smaller NP sizes than PdWPA due to the low loading of the metal species.

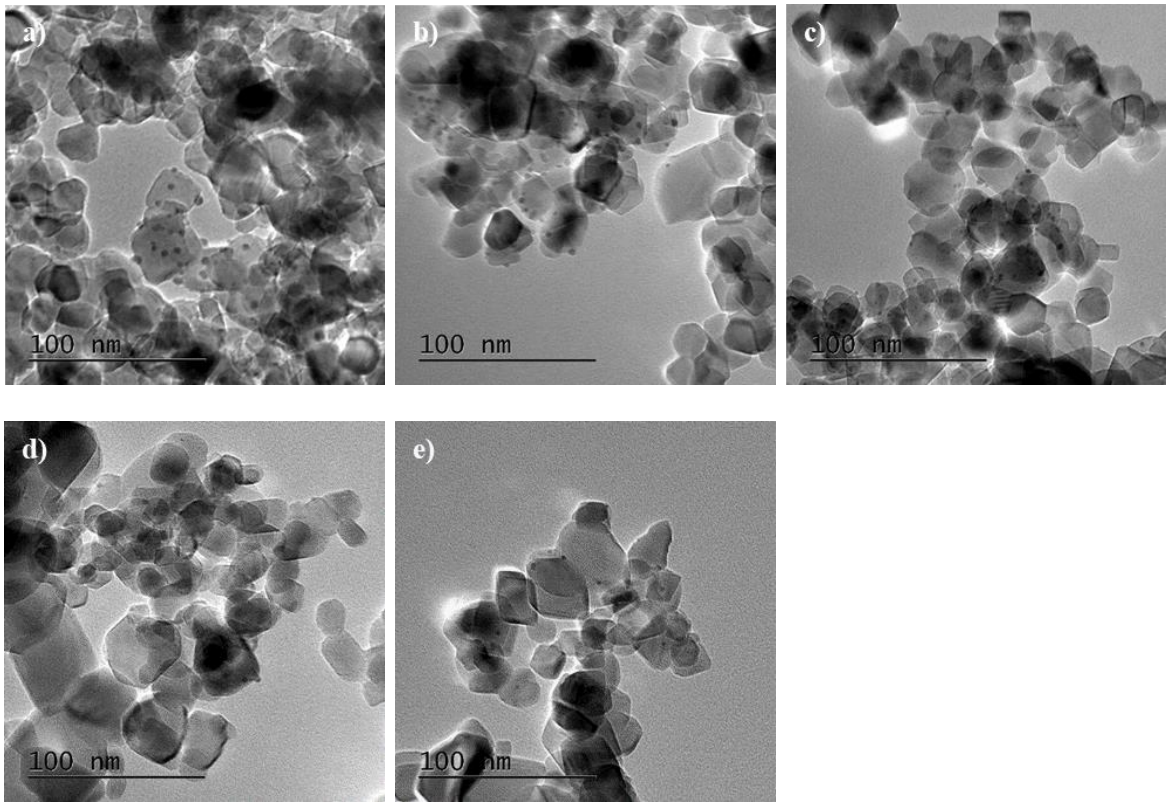

Figure 3-13. *TEM images of the 1 wt % Pd/TiO_2 catalysts prepared in increasing vol. % MeOH in the synthesis solvent: a) PdWPA, b) Pd25MePA, c) Pd50MePA, d) Pd75MePA, and e) PdMePA.*

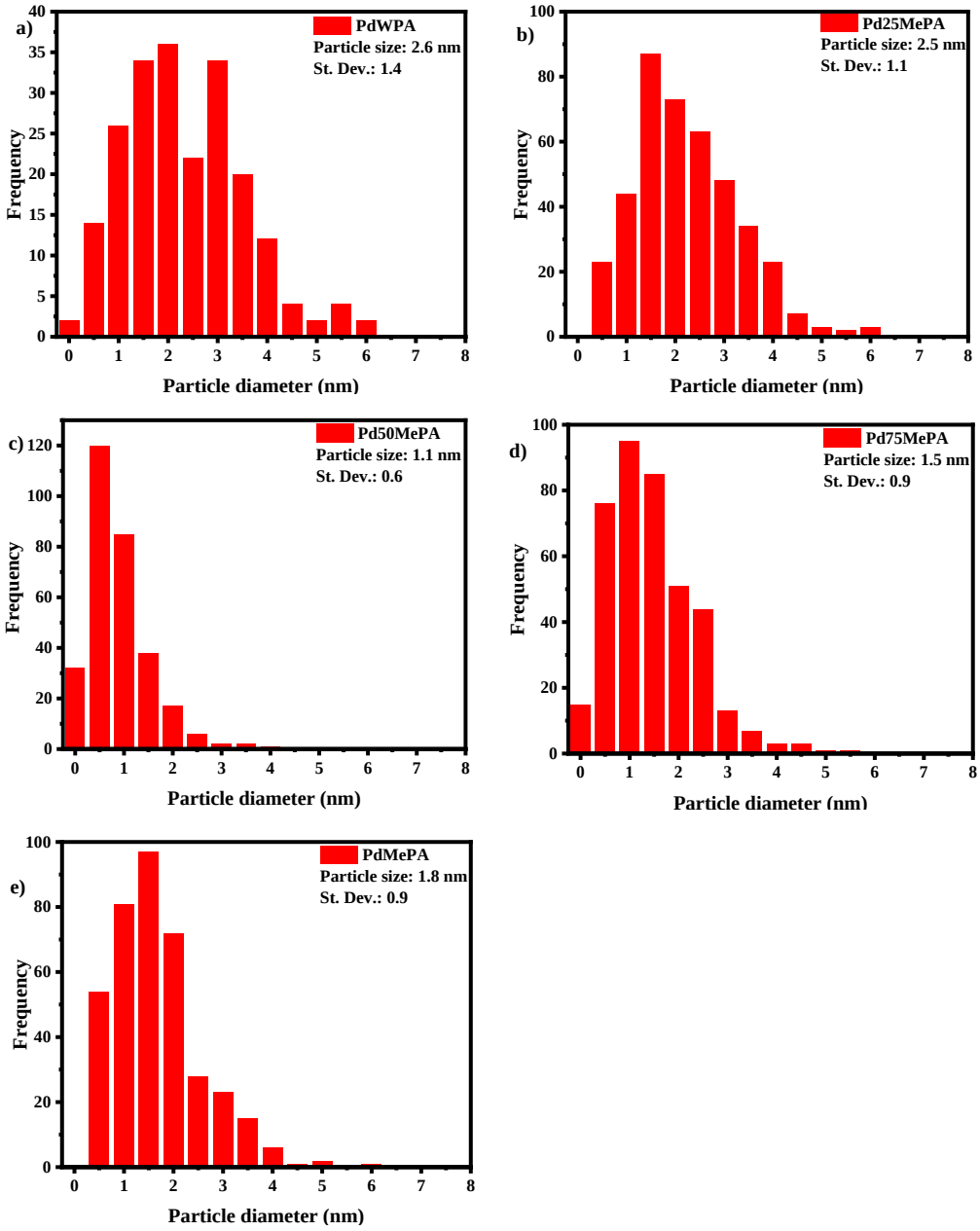

Figure 3-14. *Standard deviation histogram for the 1 wt % Pd/TiO₂ catalysts prepared in increasing volume % of methanol in the synthesis solvent, a) PdWPA, b) Pd25MePA, c) Pd50MePA, d) Pd75MePA, and e) PdMePA. Data was calculated from NP population sizes of 200-300 Pd NPs per sample.*

3.3.2.4 X-ray Absorption Fine Structure

3.3.2.4.1 X-ray Absorption Near-Edge Structure

Characterisation of the average Pd oxidation state was performed *via* XANES analysis (*Figure 3-15*). Initial assessment of the white line peak suggests that addition of 25 vol. % MeOH increases the Pd^{2+} oxidation state of the supported NPs. Comparison to the Pd^{0} and PdO reference XANES shows a shift in the position of the absorption edge with increasing oxidation state (*Figure 3-15*a).[62] However, there is no noticeable shift in the absorption edge from 0 to 100 vol. %, only a slight difference in the intensity of the white line peak, indicating that the oxidation states for the methanol prepared Pd catalysts are similar (*Figure 3-15*b). The XANES LCFs elucidates that the inclusion of MeOH into the synthesis solvent in 25 vol. % increments is beneficial in increasing the Pd^{2+} character of the formed NPs. Furthermore, the highest Pd^{2+} % measured was for Pd50MePA, and decreased towards a MeOH-only solvent system: Pd50MePA = 50 %, Pd75MePA = 50 % and PdMePA = 48 % (*Table 3-8*).

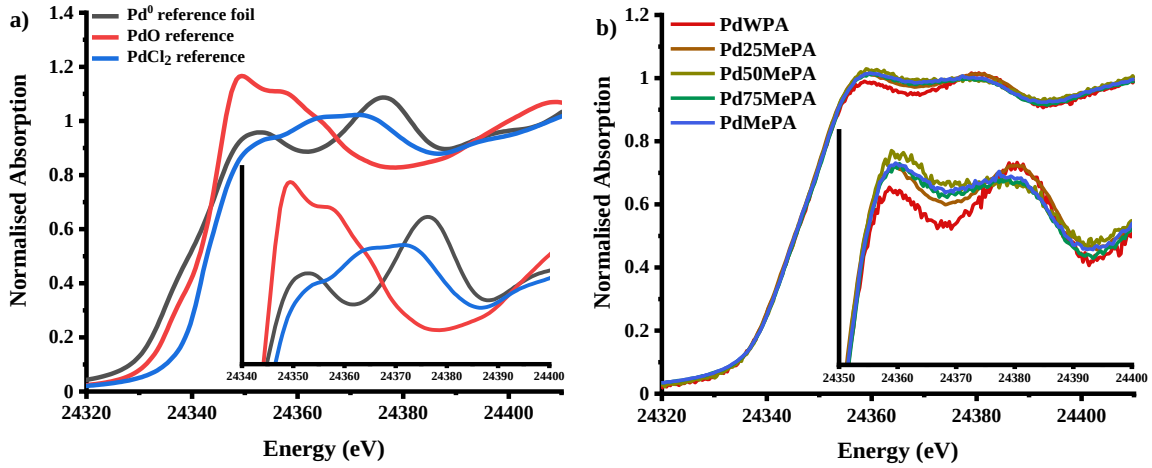

Figure 3-15. *Pd K-edge XANES spectra for a) Pd^{0}, PdO and $PdCl_2$ references and b) Pd/TiO_2 catalysts prepared in increasing incremental vol. % of MeOH in the synthesis solvent.*

Table 3-8*. XANES linear combination fit reference standards for the 1 wt. % Pd/TiO₂ synthesised in varying [MeOH(aq)] solvent systems. The accuracy of the fit is described by an R_{factor} value, where the confidence of the fit is represented by the smallest value above zero.*

Catalyst	[MeOH] used in Synthesis (vol. %)	Reference standards (%)			R_{factor}
		Pd^{2+}	Pd^0	Pd^{2+}/Pd^0	
PdWPA	0	30	70	0.43	0.002
Pd25MePA	25	40	60	0.67	0.0103
Pd50MePA	50	50	50	1.0	0.015
Pd75MePA	75	50	50	1.0	0.011
PdMePA	100	48	52	0.92	0.012

3.3.2.4.2 Extended X-ray Absorption Fine Structure

Analysis of the higher energy oscillatory EXAFS region details the formation of small Pd NPs and not crystalline PdO due to the absence of a scattering path at ~ 3.2 Å for all samples (*Figure 3-16*). As discussed for the previous group of catalysts, the Pd-O scattering path located at ~ 1.7 Å indicates the formation of small Pd NPs.[44] However, synthesis solvents composed of ≥ 50 vol. % MeOH show comparable magnitudes of Pd-O scattering, therefore, assessment of the 1st shell Pd-Pd scattering magnitude (~ 2.7 Å) offers a more accurate representation of the NP size trend for Pd50MePA, Pd75MePA and PdMePA. Fitting of the first shell Pd-Pd and Pd-O paths agree with the trends established from the TEM data (*Figure 3-16*, *Table 3-9*). Increasing the [$MeOH_{(aq)}$] from 0 to 25 vol. % shows a slight decrease in the magnitude of the Pd-Pd scattering path, as well as a small increase in the magnitude of Pd-O scattering (PdWPA: $CN_{Pd\text{-}Pd} = 7.2 \pm 0.5$, $CN_{Pd\text{-}O} = 1.6 \pm 0.3$, Pd25MePA: $CN_{Pd\text{-}Pd} = 6.6 \pm 0.3$, $CN_{Pd\text{-}O} = 1.8 \pm 0.2$). The fitted CNs for both the Pd-Pd and Pd-O pathways resulted in similar average environments surrounding the absorbing Pd, further agreeing with the calculated TEM NP sizes. Preparation of Pd NPs in equal vol. %

MeOH:H_2O produced the smallest apparent Pd NP size, also evident from the smaller magnitude of Pd-Pd scattering ($CN_{Pd\text{-}Pd}$ = 4.9 ± 0.4). Again, as Pd NPs become smaller, the abundance of Pd-O scattering at ~ 1.7 Å becomes larger, which is observed from Pd25MePA to Pd50MePA (Pd50MePA: $CN_{Pd\text{-}O}$ = 2.5 ± 0.2). Synthesis solvents comprised of greater [$MeOH_{(aq)}$], i.e. 75 and 100 vol. % MeOH, lead to the formation of NPs with fitted $CN_{Pd\text{-}O}$ that are not only within error of one another but also within error of Pd50MePA, agreeing with the literature that a lesser control of (Pd) NP size is afforded from syntheses in highly concentrated, or less polar, alcohol solutions.[23,25]

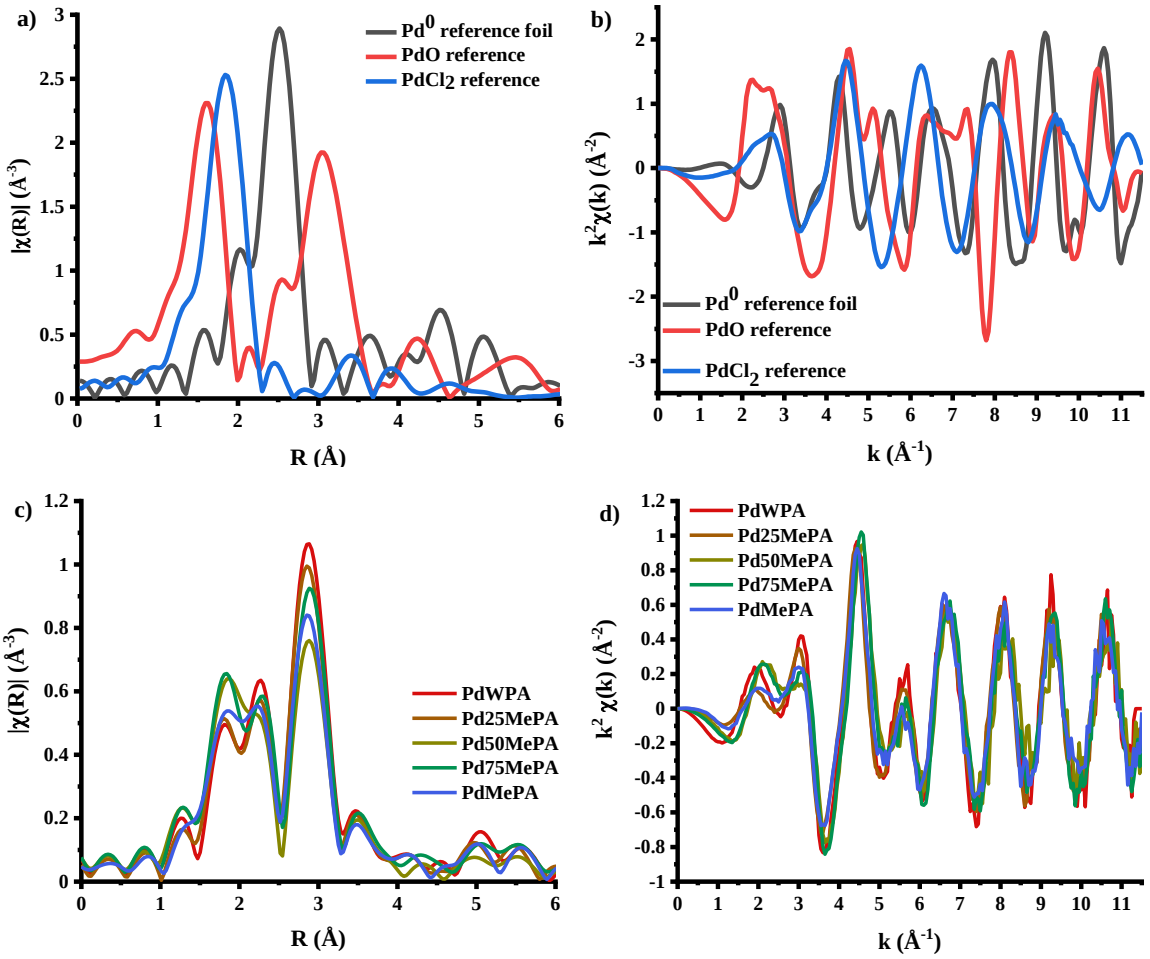

Figure 3-16. *Pd K-edge EXAFS data displaying the experimental FT χ(k) (a & c) and χ(k) data (b & d) for the prepared 1 wt. % Pd/TiO_2 catalyst;. where Pd references are displayed in figures a) & b), and the influence of increasing the vol. % MeOH in the synthesis solvent is displayed in figures c) & d).*

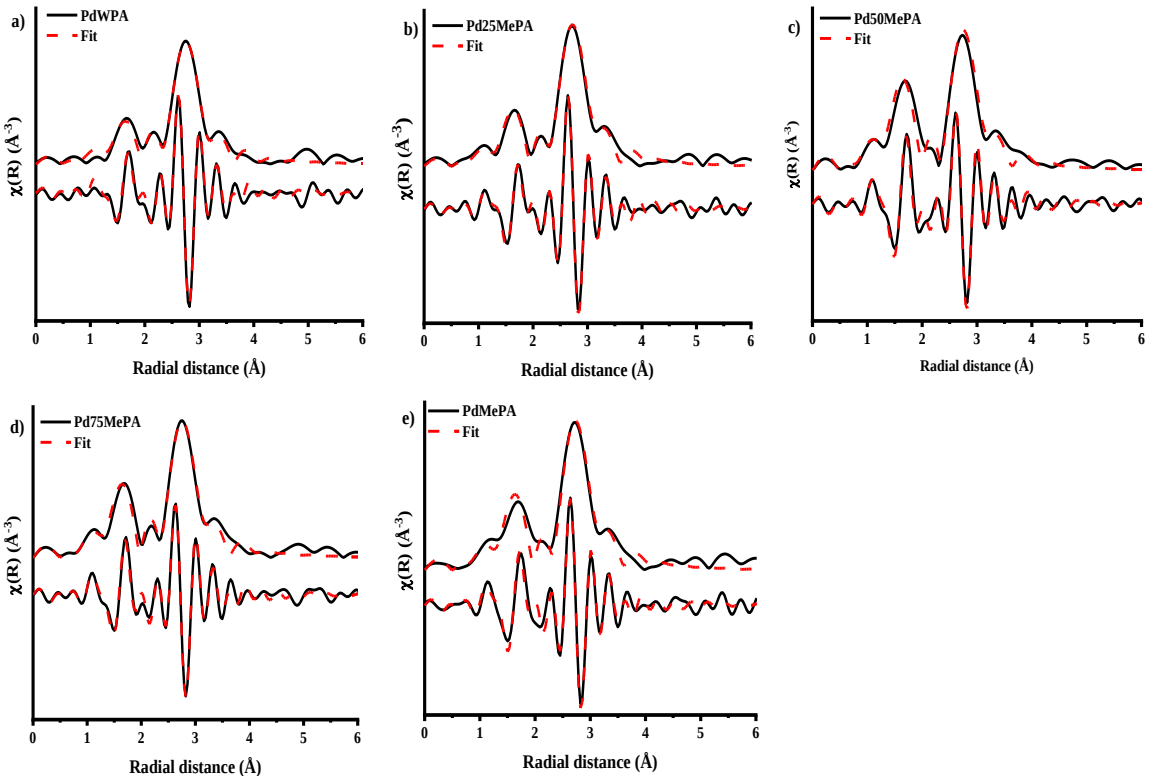

Figure 3-17. *Fitted experimental FT χ(k) data, both the magnitude and real components, for prepared Pd/TiO₂ catalysts using increasing vol. % MeOH in the synthesis solvent: a) PdWPA, b) Pd25MePA, c) Pd50MePA, d) Pd75MePA and e) PdMePA.*

TEM analysis of Pd50MePA, Pd75MePA and PdMePA suggests that the average Pd NP size increases linearly with rising [$MeOH_{(aq)}$]; however, the fitted EXAFS data suggests that the average NP sizes for Pd75MePA and PdMePA are closer than the TEM data implies. Though it should be noted that as the 1st shell $CN_{Pd\text{-}Pd}$ increases towards 12, the number of atoms present in the NP sharply increases, leading to a broad range of particle sizes and shapes possible.[63]

Table 3-9. *1st shell EXAFS fitting parameters derived from the k^2 weighted FT for the Pd K-edge EXAFS data for the MeOH based solvent system catalysts. Amplitude reduction factor, $S_0^2 = 0.75$, was determined from fitting an acquired Pd metal reference foil. EXAFS fittings range: $3 < k < 11.5$, $1 < R < 3.4$, number of independent points = 11.2. The accuracy of the fit is described by an R_{factor} value, where the confidence of the fit is represented by the smallest value above zero.*

Catalyst	Abs-Sc	CN	R (Å)	$2\sigma^2$ (Å^{-2})	E_0 (eV)	R_{factor}
PdWPA	Pd-Pd	7.2 ± 0.5	2.74 ± 0.08	0.008	0.2 ± 0.9	0.017
	Pd-O	1.6 ± 0.3	1.99 ± 0.07	0.005		
Pd25MePA	Pd-Pd	6.6 ± 0.3	2.74 ± 0.01	0.008	0.0 ± 1.0	0.008
	Pd-O	1.8 ± 0.2	1.98 ± 0.06	0.005		
Pd50MePA	Pd-Pd	4.9 ± 0.4	2.73 ± 0.06	0.008	3.2 ± 0.6	0.031
	Pd-O	2.5 ± 0.2	1.98 ± 0.03	0.005		
Pd75MePA	Pd-Pd	5.9 ± 0.3	2.74 ± 0.05	0.008	2.8 ± 0.6	0.016
	Pd-O	2.4 ± 0.2	1.98 ± 0.02	0.005		
PdMePA	Pd-Pd	5.6 ± 0.5	2.74 ± 0.01	0.008	0.0 ± 1.0	0.030
	Pd-O	2.1 ± 0.3	1.98 ± 0.06	0.005		

3.3.2.5 Infrared Spectroscopy

Pd/TiO_2 prepared in the absence of MeOH showed a favourability towards bridging CO adsorption, particularly μ_2-CO on the Pd(100) facets (~ 1983 cm^{-1}, *Figure 3-18*).[8] Linear CO adsorption on corner and edge sites (2090 cm^{-1} and 2063 cm^{-1}, respectively) also occurs, but to a lesser extent with increasing $[MeOH_{(aq)}]$. Concurrently, a reduction in the abundance of bridged adsorption sites is identifiable at higher $[MeOH_{(aq)}]$: μ_2 bridge-bonding on Pd NPs

at Pd FCC (100) facets and Pd(111) planes ~ 1980 and 1940 cm^{-1}, respectively.[64] The decrease in CO adsorption observed on inclusion of MeOH in the synthesis solvent suggests that Pd surface sites are more accessible for the water prepared catalyst.

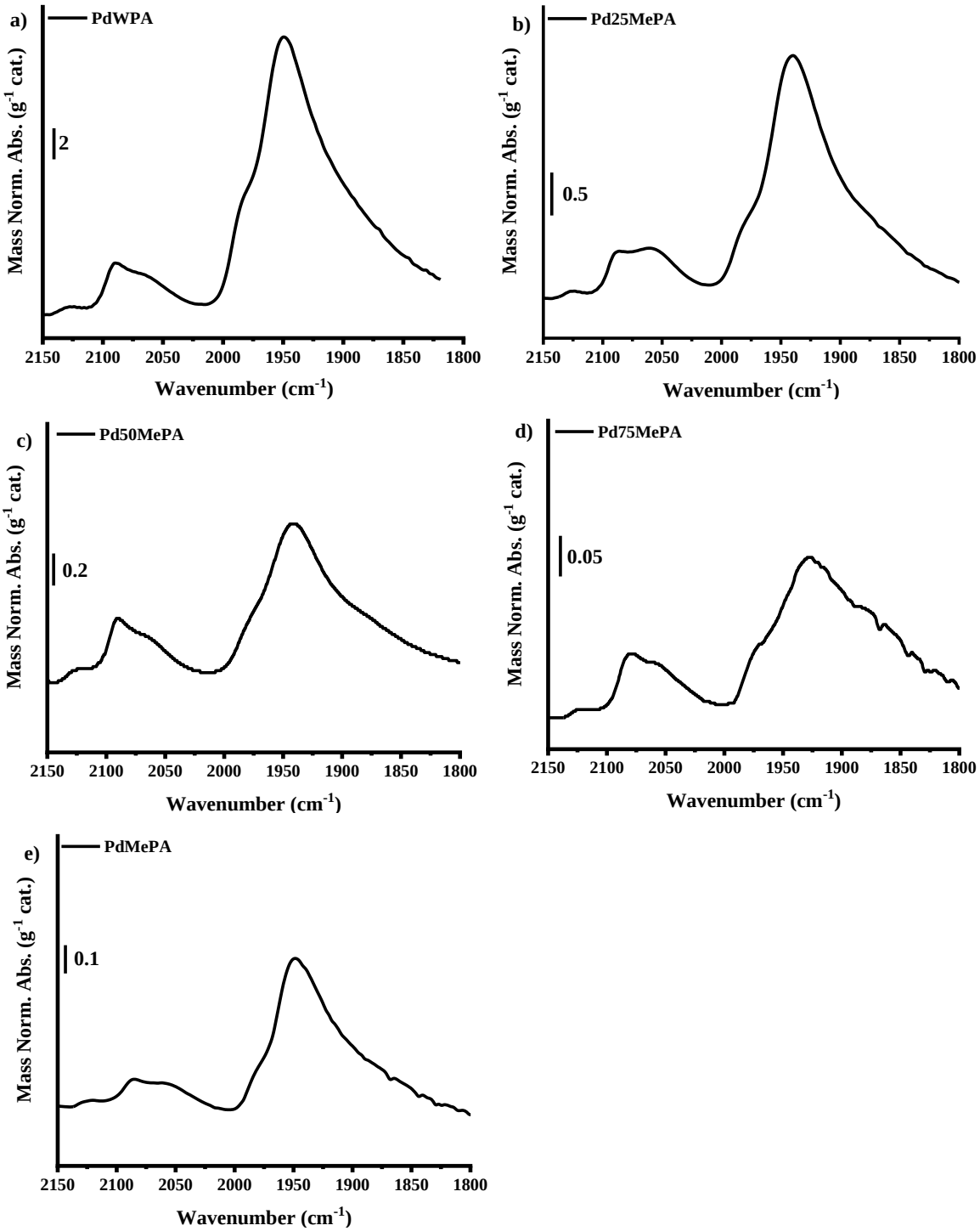

Figure 3-18. *CO probe molecule FTIR spectra of Pd/TiO_2 catalysts prepared using increasing vol. % MeOH in the synthesis solvent: a) PdWPA, b) Pd25MePA, c) Pd50MePA, d) Pd75MePA and e) PdMePA.*

With decreasing NP size, an increase in the linear binding modes at corner and edge sites would be expected; however, this is not the case for the Pd50MePA.[60] Instead, the low abundance of CO adsorption appears consequential of PVA interactions with MeOH resulting in excessive polymer clustering around the Pd NPs.[8]

3.4 Conclusions

The purpose of this chapter was to determine how the inclusion of short chain alcohols (C_1-C_4), with differing sterics (linear or branched chain alcohols), in the sol-immobolisation synthesis solvent influenced the metal loading and NP size of the TiO_2 supported Pd NP catalysts. This fundamental study expanded on the work reported by Rogers *et al.* who prepared 1 wt. % Pd/TiO_2 catalysts in 50 vol. % EtOH:H_2O synthesis solvents.[27]

It was found that MeOH or EtOH incorporation into the synthesis solvent did not significantly impact the desired metal loading and produced Pd NPs comparable to those prepared in H_2O (Pd50MePA: 0.81 wt. % Pd, Pd50EtPA: 0.88 wt. % Pd, PdWPA: 0.83 wt. % Pd). Conversely, sol-immobilisation synthesis involving longer chain alcohols (PrOH), with increased sterics (IsOH, *t*BuOH), produced catalysts with Pd loadings < 50 % of the ideal. The influence of the alcohols was best observed through control of nanoparticle size, increasing as a function of the solvent system's linear alcohol chain length (MeOH < EtOH < PrOH), which is contrary to the literature.[23,25] The use of secondary (IsOH) and tertiary (*t*BuOH) alcohols in the synthesis solvent formed supported Pd NPs ≤ 2 nm; however, the small size and narrow distributions of the particles were attributed to the lower metal loading of these systems limiting instances of coalescence on the support surface. Moreover, the accessibility of Pd surface sites was shown to be altered by the presence of alcohol in the solvent system, which is expected to influence the prepared Pd/TiO_2 catalytic selectivity.[8,10,61]

The methanol based solvent system proved to be the most promising to produce uniformly small Pd NPs with high metal loading. The optimisation necessary for the C_2-C_4 alcohol systems to afford metal loadings or NP sizes at comparable levels to Pd50MePA was not within the scope of this work. Nevertheless, further investigation into the preparation of Pd NPs was performed exploring the effect of incremental [$MeOH_{(aq)}$] in the synthesis solvent. Here, 1 wt. % Pd/TiO_2 catalysts were prepared in synthesis solvents of 0, 25, 50, 75 and 100 vol. % [$MeOH_{(aq)}$]. Pd loading on the support surface was the main property impacted by the

use of varying MeOH concentrations, where the highest loading was achieved using an equal vol. % MeOH:H_2O solvent (Pd50MePA: 0.81 wt. % Pd). The smallest NP size was also found for this catalyst as determined by TEM and EXAFS analysis. The achieved Pd loading decreased to below 0.4 wt. % Pd as the [$MeOH_{(aq)}$] increased > 50 vol. % (Pd75MePA: 0.24 wt. % Pd, PdMePA: 0.37 wt. % Pd). It is the author's hypothesis that this results from either interactions between the Pd surface and PVA stabilising agent prevent anchoring of Pd NPs,[28] or insufficient solvation of PVA and the precursor salt in increasing [$MeOH_{(aq)}$] in the solvent system.[19]

The work presented in this chapter details the influence the solvent system has on the textural properties of sol-immobilisation prepared 1 wt. % Pd/TiO_2 catalysts. It also provides a platform for the work of the succeeding chapter, wherein further optimisation of the MeOH based sol-immobilisation procedure is investigated in the preparation of Pd/TiO_2 catalysts for furfural hydrogenation.

3.5 References

1 C. E. Chan-Thaw, A. Villa and L. Prati, in *Gold Catalysis: Preparation, Characterization, and Applications*, eds. L. Prati and A. Villa, Pan Stanford, 1st edn., 2015, pp. 59–63.

2 L. Prati and A. Villa, *Acc. Chem. Res.*, 2014, **47**, 855–863.

3 K. Pitchumani and M. Kumarraja, in *Reducing Agents in Colloidal NP Synthesis*, ed. S. Mourdikoudis, Royal Society of Chemistry, London, 1st edn., 2021, pp. 28–50.

4 P. K. Khanna, P. V. More, J. P. Jawalkar and B. G. Bharate, *Mater. Lett.*, 2009, **63**, 1384–1386.

5 J. Turkevich, P. C. Stevenson, B. J. Turkevich and P. C. Stevenson, *J. Phys. Chem.*, 1953, **57**, 670–673.

6 I. J. Godfrey, A. J. Dent, I. P. Parkin, S. Maenosono and G. Sankar, *ACS Omega*, 2020, **5**, 13664–13671.

7 J. Ohyama, K. Teramura, Y. Higuchi, T. Shishido, Y. Hitomi, K. Kato, H. Tanida, T. Uruga and T. Tanaka, *ChemPhysChem*, 2011, **12**, 127–131.

8 S. Campisi, M. Schiavoni, C. E. Chan-Thaw and A. Villa, *Catalysts*, 2016, **6**, 1–21.

9 O. Rac, P. Suchorska-Woźniak, M. Fiedot and H. Teterycz, *Beilstein J. Nanotechnol.*, 2014, **5**, 2192–2201.

10 S. H. Pang, C. A. Schoenbaum, D. K. Schwartz and J. W. Medlin, *Nat. Commun.*, 2013, **4**, 1–6.

11 N. Dimitratos, A. Villa, L. Prati, C. Hammond, C. E. Chan-Thaw, J. Cookson and P. T. Bishop, *Appl. Catal. A Gen.*, 2016, **514**, 267–275.

12 W. Hoogsteen and L. G. J. Fokkink, *J. Colloid Interface Sci.*, 1995, **175**, 12–26.

13 M. Niederberger and N. Pinna, in *Metal Oxide Nanoparticles in Organic Solvents*, Springer, London, 1st edn., 2009, pp. 53–95.

14 J. Liu, C. Liang, X. Zhu, Y. Lin, H. Zhang and S. Wu, *Sci. Rep.*, 2016, **6**, 1–10.

15 M.-S. Kim, H.-S. Song, H. J. Park and S.-J. Hwang, *Chem. Pharm. Bull.*, 2012, **60**, 543–547.

16 M. Zobel, R. B. Neder and S. A. J. J. Kimber, *Science*, 2015, **347**, 292–294.

17 C. Capello, U. Fischer and K. Hungerbühler, *Green Chem.*, 2007, **9**, 927–934.

18 A. Ismail, D. Asrianti, A. A. Dwiatmoko, B. H. Susanto and M. Nasikin, *Int. J. Eng. Res. Technol.*, 2019, **12**, 2341–2345.

19 T. Teranishi and M. Miyake, *Chem. Mater.*, 1998, **4756**, 594–600.

20 S. Ayyappan, R. Srinivasa Gopalan, G. N. Subbanna and C. N. R. Rao, *J. Mater. Res.*, 1997, **12**, 398–401.

21 L. Abis, N. Dimitritatos, M. Sankar, S. J. Freakley and G. J. Hutchings, *Top. Catal.*, 2020, **63**, 394–402.

22 L. Abis, N. Dimitratos, M. Sankar, S. J. Freakley and G. J. Hutchings, *Catal. Letters*, 2020, **150**, 49–55.

23 A. Mihata, R. Usman and J. Kurawaki, *J. Surf. Sci. Nanotechnol.*, 2015, **13**, 427–430.

24 S. Leekumjorn, S. Gullapalli and M. S. Wong, *J. Phys. Chem. B*, 2012, **116**, 13063–16070.

25 M. H. Hussain, N. B. A. Fitrah, A. N. Mustapa, K.-F. Low, N. H. Othman and F. Adam, *Nanoscale Res. Lett.*, 2020, **15**, 140–150.

26 J. Gregory and S. Barany, *Adv. Colloid Interface Sci.*, 2011, **169**, 1–12.

27 S. M. Rogers, C. R. A. Catlow, C. E. Chan-Thaw, A. Chutia, N. Jian, R. E. Palmer, M. Perdjon, A. Thetford, N. Dimitratos, A. Villa and P. P. Wells, *ACS Catal.*, 2017, **7**, 2266–2274.

28 S. R. Chowdhury, P. S. Roy and S. K. Bhattacharya, *Adv. Nat. Sci. Nanosci. Nanotechnol.*, 2017, **8**, 1–10.

29 B. Ravel and M. Newville, *J. Synchrotron Radiat.*, 2005, **12**, 537–541.

30 A. Gniewek, A. M. Trzeciak, J. J. Ziółkowski, L. Kępiński, J. Wrzyszcz and W. Tylus, *J. Catal.*, 2005, **229**, 332–343.

31 H. Hei, H. He, R. Wang, X. Liu and G. Zhang, *Soft Nanosci. Lett.*, 2012, **2**, 34–40.

32 K. H. Leong, H. Y. Chu, S. Ibrahim and P. Saravanan, *Beilstein J. Nanotechnol.*, 2015, **6**, 428–437.

33 L. I. Elding and L. F. Olsson, *J. Phys. Chem.*, 1978, **82**, 69–74.

34 N. Dimitratos, J. A. Lopez-Sanchez, D. Morgan, A. F. Carley, R. Tiruvalam, C. J. Kiely, D. Bethell and G. J. Hutchings, *Phys. Chem. Chem. Phys.*, 2009, **11**, 5142–5153.

35 A. Villa, D. Wang, G. M. Veith, F. Vindigni and L. Prati, *Catal. Sci. Technol.*, 2013, **3**, 3036–3041.

36 F. Porta, L. Prati, M. Rossi, S. Coluccia and G. Martra, *Catal. Today*, 2000, **61**, 165–172.

37 I. Sameut Bouhaik, P. Leroy, P. Ollivier, M. Azaroual and L. Mercury, *J. Colloid Interface Sci.*, 2013, **406**, 75–85.

38 Phenols, alcohols and carboxylic acids - pKa values,

https://www.engineeringtoolbox.com/paraffinic-benzoic-hydroxy-dioic-acids-structure-pka-carboxylic-dissociation-constant-alcohol-phenol-d_1948.html, (accessed 13 July 2021).

39 N. S. Marinkovic, K. Sasaki and R. R. Adzic, *Zast. Mater.*, 2016, **57**, 101–109.

40 A. Frenkel, *Z. Krist.*, 2007, **222**, 605–611.

41 J. Evans, in *X-ray Absorption Spectroscopy for the Chemical and Materials Science*, ed. J. Evans, Wiley, 1st edn., 2018, pp. 117–162.

42 R. L. Barton, D. J. Gardenghi, W. C. Stolte and R. K. Szilagyi, *J. Phys. Chem. A*, 2015, **119**, 5579–5586.

43 J. B. Brazier, M. A. Newton, E. M. Barreiro, S. Parry, L. A. Adrio, C. J. Mulligan, K. Hellgardt, K. K. Hii, P. B. J. Thompson, R. Nichols, B. N. Nguyen, K. K. Mii, P. B. J. Thompson, R. Nichols and B. N. Nguyen, *Catal. Struct. React.*, 2017, **3**, 54–62.

44 P. P. Wells, E. M. Crabb, C. R. King, R. Wiltshire, B. Billsborrow, D. Thompsett and A. E. Russell, *Phys. Chem. Chem. Phys.*, 2009, **11**, 5773–5781.

45 S. C. Su, J. N. Carstens and A. T. Bell, *J. Catal.*, 1998, **176**, 125–135.

46 S. M. Rogers, N. Dimitratos, W. Jones, M. Bowker, A. G. Kanaras, P. P. Wells, C. R. A. Catlow and S. F. Parker, *Phys. Chem. Chem. Phys.*, 2016, **18**, 17265–17271.

47 M. Newville, *J. Synchrotron Radiat.*, 2001, **8**, 96–100.

48 Z. S. Pillai and P. V. Kamat, *J. Phys. Chem. B*, 2004, **108**, 945–951.

49 J. Piella, N. G. Bastús and V. Puntes, *Chem. Mater.*, 2016, **28**, 1066–1075.

50 T. Lear, R. Marshall, J. A. Lopez-sanchez, S. D. Jackson, T. M. Klapötke, G. Rupprechter, H. Freund and D. Lennon, *J. Chem. Phys.*, 2005, **123**, 1–13.

51 C. D. Zeinalipour-Yazdi, D. J. Willock, L. Thomas, K. Wilson and A. F. Lee, *Surf. Sci.*, 2016, **646**, 210–220.

52 V. Vorotnikov, G. Mpourmpakis and D. G. Vlachos, *ACS Catal.*, 2012, **2**, 2496–2504.

53 K. Föttinger, W. Emhofer, D. Lennon and G. Rupprechter, *Top. Catal.*, 2017, **60**, 1722–1734.

54 M. Bowker, P. Stone, R. Bennett and N. Perkins, *Surf. Sci.*, 2002, **497**, 155–165.

55 E. V Benvenutti, L. Franken and C. C. Moro, *Langmuir*, 1999, **15**, 8140–8146.

56 A. Bourane, O. Dulaurent and D. Bianchi, *J. Catal.*, 2000, **196**, 115–125.

57 S. Bertarione, D. Scarano, A. Zecchina, V. Johánek, J. Hoffmann, S. Schauermann, M. M. Frank, J. Libuda, G. Rupprechter and H.-J. Freund, *J. Phys. Chem. B*, 2004, **108**, 3603–3613.

58 H. Zhu, Z. Qin, W. Shan, W. Shen and J. Wang, *J. Catal.*, 2004, **225**, 267–277.

59 K. I. Hadjiivanov and G. N. Vayssilov, *Adv. Catal.*, 2002, **47**, 307–511.

60 K. Kinoshita, *J. Electrochem. Soc.*, 1990, **137**, 845–848.

61 K. Chen, H. Wu, Q. Hua, S. Chang and W. Huang, *Phys. Chem. Chem. Phys.*, 2013, **15**, 2273–2277.

62 J. A. McCaulley, *Phys. Rev. B*, 1993, **47**, 4873–4879.

63 A. Jentys, *Phys. Chem. Chem. Phys.*, 1999, **1**, 4059–4063.

64 S. Campisi, D. Ferri, A. Villa, W. Wang, D. Wang, O. Kro and L. Prati, *J. Phys. Chem. C*, 2016, **120**, 14027–14033.

Chapter 4 Optimising Pd Nanoparticle Catalysts for Furfural Hydrogenation

The influence of the sol-immobilisation synthesis solvent on catalyst activity is presented in this chapter. Laboratory and synchrotron techniques have been employed to elucidate how changes to the synthesis solvent can influence textural NP properties and the resultant catalytic selectivity of the final catalyst, with a manuscript submitted to *ChemCatChem* titled 'Controlling the production of acid catalysed products of furfural hydrogenation by Pd/TiO_2': G. F. Tierney, S. Alijani, M. Panchal, D. Decarolis, M. Briceno de Gutierrez, K. M. H. Mohammed, J. Callison, E. K. Gibson, P. B. J. Thompson, P. Collier, N. Dimitratos, E. C. Corbos, F. Pelletier, A. Villa and P. P. Wells, *ChemCatChem*, 2021, DOI 10.1002/cctc.202101035R1.

Authors listed on this paper all contributed to the manuscript in the following capacities: S. Alijani performed catalytic testing in Milan; M. Panchal performed TPD/TPR measurements; K. M. H. Mohammed performed synthesis of beamtime samples; J. Callison performed MP-AES for the author; D. Decarolis and P. B. J. Thompson assisted on beamtime measurements as support and as beamline staff, respectively; M. Briceno de Gutierrez performed HRTEM, and STEM-HAADF analysis; E. K. Gibson gave advice on TPD/TPR measurements; P. Collier was included due to their industrial involvement with Johnson Matthey; E. C. Corbos and F. Pelletier were industrial supervisors for this project; N. Dimitratos and A. Villa were academic collaborators for this project; P. P. Wells was the academic supervisor of this project.

4.1 Introduction

Rising global demand for energy and reduced dependence on fossil fuels has led to the utilisation of lignocellulose materials, an undesirable by-product of agricultural processes.[1] The conversion of biomass has proven to be an incredibly important step toward the production of value-added chemicals, and energy, as well as offering a cheaper, more sustainable source of fuel than those acquired from crude oil.[2] Food derived fuels, or 1st generation biofuels, relied heavily on the use of edible organic materials, e.g. wheat. However, the high costs and ethics associated with using edible plant matter makes the use of 1st generation biofuels not ideal. Instead, sourcing biomass from non-edible, or lignocellulosic, origins, e.g. oat husks or agricultural wastes, has provided a cost effective

and more ethical route to 2nd generation biofuels. Non-edible lignocellulose biomass is primarily composed of cellulose, hemicellulose and lignin, and represents the most abundant form of biomass.[3] Conversion of lignocellulose into liquid fuels can be achieved *via* three processes:[2]

(1) Gasification, where liquid or solid carbonaceous materials are reacted with air, oxygen or a mixture, to yield syngas or produce gas containing CO, H_2, CH_4, CO_2 and N_2 in varied concentrations dependent on the reactant gas.[4]

(2) Pyrolysis, predominantly used in the synthesis of bio-oils by the heating of biomass in the absence of oxygen or steam to gaseous, liquid and solid products, which can be controlled using various residence times, heating rates and temperature conditions.[5]

(3) Hydrolysis, where the conversion of cellulose to sugar polymers is performed using enzymes or acid catalysts.[2]

The acid catalysation of hemicellulose has been used to prepare valuable sugars from its reaction products. Importantly, one major product of hemicellulose transformation is the C_5 sugar xylose, which can be further hydrolysed and dehydrated to yield furfural.[6] Furfural is a focal platform compound in the preparation of non-petroleum derived chemicals,[7,8] such as resins and fuel additives.[9-11] The preparation of furfural from oat husks was first noted by the Quaker Oats Company in the 1920s[12] and, since then, the global production of furfural has reached 461,380 tons annually (as of 2020).[13] The versatility of furfural as a feedstock affords the preparation of a multitude of valuable chemicals *via* hydrogenolysis, decarbonylation or hydrogenation (*Scheme 4-1*).[14]

Whilst the products acquired from the hydrogenolysis and decarbonylation of furfural, methyl furan and furan, respectively, are utilised in the production of a wide range of chemicals and solvents, it is the selective hydrogenation of furfural that is of interest in this work. Primary hydrogenation of furfural yields furfuryl alcohol (FA), a sought after chemical with wide applications in the production of resins and synthetic fibres.[15,16] The subsequent hydrogenation of FA produces tetrahydrofurfuryl alcohol (THFA), used in the preparation of green industrial solvents and pharmaceuticals.[17,18] The selective nature of the hydrogenation reaction arises from furfural being an α,β-unsaturated aldehyde; however, in terms of thermodynamics and kinetics, C=C hydrogenation is more easily performed than C=O hydrogenation,[19] and so, THFA production is favoured.

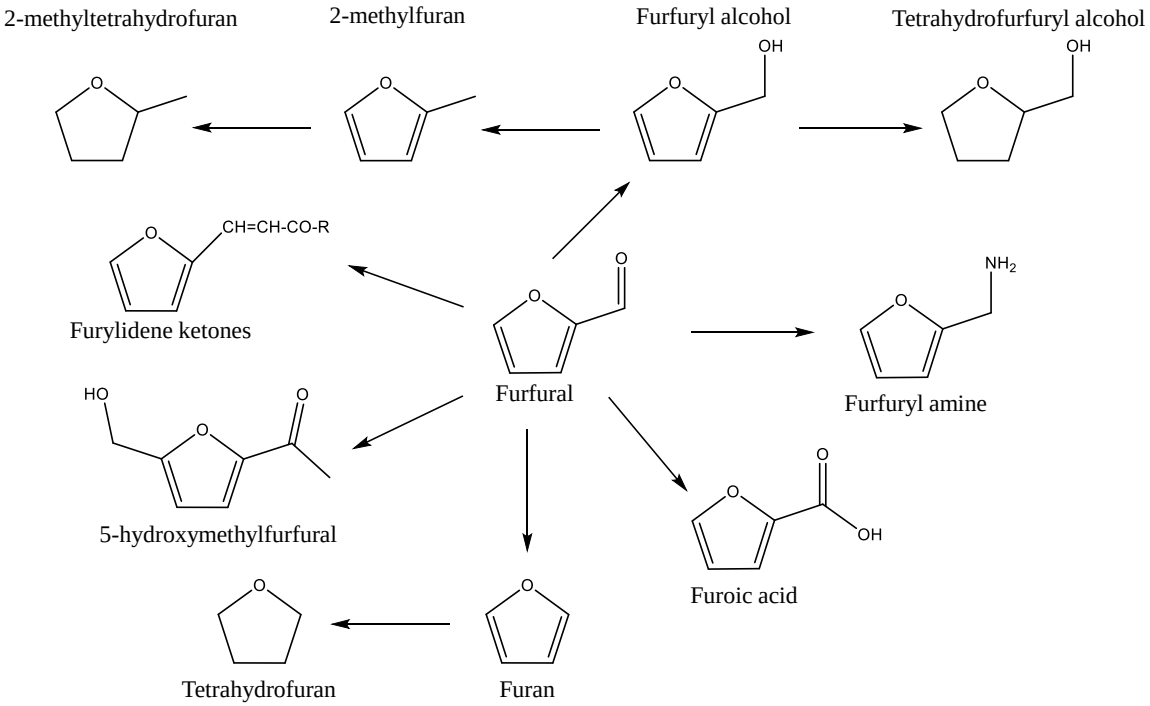

Scheme 4-1. *Representation of the versatility of furfural to transform into value-added chemicals; schematic taken from Corma et al., Chem. Rev., 2007,* ***107****, 2411-2502.*[14]

Heterogeneous catalysts containing Cu, Pd, Pt and Ni have been utilised for decades for the hydrogenation of furfural in gaseous and liquid phases.[10,16,18,20–22] Commercially, Cu and CuCr catalysts have been employed for the hydrogenation of furfural, favouring FA formation.[14] This is resultant of the preferential adsorption of furfural *via* the oxygen lone pair on the aldehyde functionality. Furthermore, association of the furan ring parallel to the Cu surface is not experienced due to net repulsion between the Cu 3*d* band and the furan ring.[23] Adsorption of furfural *via* the furan ring is, however, allowed over Pd, Ni and Pt, with the η^2(C-O) binding mode favoured.[16] The high FA selectivities observed using CuCr based catalysts are coupled with the issue of Cr toxicity, with many attempts made to prepare Cu based catalysts that are as active but less detrimental to human health and the environment.[14,24] Metal oxide supported Pt catalysts have also been used, but favour the hydrogenolysis and decarbonylation of furfural over hydrogenation;[25] however, selectivity towards the hydrogenation products can be improved either by doping the catalyst or incorporating a monolayer support.[26] Pd based catalysts have shown promise in hydrogenation processes due to their ability to dissociate H_2 under ambient conditions, which has allowed for hydrogenation reactions to be performed over Pd catalysts at low reaction temperatures and H_2 pressures.[8,27–29] Moreover, product selectivity has been attributed to the

binding mode of furfural on the Pd surface, e.g. η^1(CO), η^1(O), η^2(C-O) and η^2(C-C), which have shown preference with NP size.[30,31] The presence of stabilising agents associated to the NP surface has also been shown to impact product selectivity by blocking access to reagent binding sites.[9,32,33] Campisi *et al*. reported improved selectivity for benzyl alcohol oxidation over PVA-capped Pd NPs due to suppression of the decarbonylation reaction pathway. Using CO probe DRIFTS measurements, PVA was observed to preferentially bind and block the Pd(111) facets, which are known to promote the unwanted side reaction.[33] Moreover, Medlin *et al*. studied the selectivity of furfural hydrogenation over Pd NPs modified by self-assembled monolayers (SAMs) of alkanethiolate.[9] In their study, the selective binding of the thiolate SAMs to the Pd surface and their sterics were found to increase the selectivity to hydrogenation products over those formed *via* decarbonylation or ring opening. This was proposed to be resultant of the SAMs limiting access to three-fold terrace sites on the Pd surface, limiting the quantity of furfural binding in the η^2(C-O) and η^2(C-C) modes parallel to the surface, instead favouring η^1(CO) adsorption (*Figure 4-1*).[9]

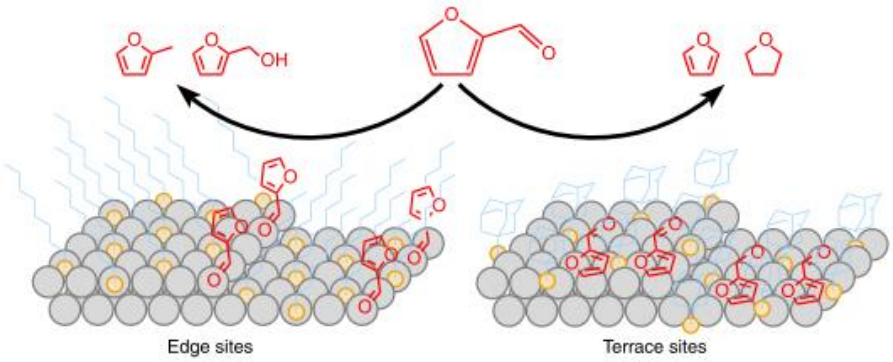

Figure 4-1. *Site isolation and selective blocking effects for the selective hydrogenation of furfural over self-assembled monolayer modified Pd NPs; image taken from Medlin et al., Nat. Commun., 2013,* ***4****, 1–6.*[9]

Sol-immobilisation synthesis of PVA-capped Pd NPs in EtOH:H_2O mixtures was reported by Rogers *et al*. and the activity of the prepared catalysts was determined by their selectivity for furfural hydrogenation.[27] Interactions between the solvent system and the stabilising agent were found to benefit a greater abundance of corner and edge sites on the NPs, which meant that furfural adsorption perpendicular to the surface was favoured; this resulted in a higher selectivity to FA over THFA.[27,34] It is clear that sol-immobilisation is beneficial for the formation of NP catalysts with both controlled size and tailored surface sites. Nevertheless, there is still an ongoing challenge: how can NP catalysts with preferential

properties (size, morphology and surface site availability) be prepared with the specificity afforded by sol-immobilisation without the large number of process steps?

In this chapter, systematic changes to the solvent of synthesis are used to prepare Pd/TiO_2 catalysts. As determined in Chapter 3, a 50:50 (vol. %:vol. %) $MeOH:H_2O$ solvent afforded the greatest control of NP size. At higher [MeOH], however, substantially lower Pd loadings were observed. Further streamlining of the synthesis procedure is also investigated, with the properties and activities of the sol-immobilisation prepared Pd NP catalysts analysed as a function of the reduced number of process steps during synthesis. Here, the importance of the stabiliser and the acidification procedure is assessed for all solvent systems ($[MeOH_{(aq)}]$ = 0, 50 and 100 vol. %). The prepared Pd catalysts in this chapter are characterised using MP-AES, TEM, STEM HAADF coupled with EDX or EELS, XAFS, CO probe IR, NH_3-DRIFTS, TPD/TPR and TGA to determine how the solvent system influences metal loading, NP properties and the spillover of H_2 to the support surface.

4.2 Experimental

4.2.1 Catalyst Preparation

Supported Pd NPs were prepared following a standard sol-immobilisation method where the temperature of chemical reduction was kept at 1 °C. Pd colloids were prepared using $Na_2[PdCl_4]$ solvated into solutions using deionised H_2O (18.2 MΩ cm, denoted by W), mixed H_2O:MeOH systems (50:50 (vol. %:vol.%), denoted by 50Me) or MeOH (denoted by Me) to the desired Pd metal concentration (128 μM). For catalysts synthesised with the inclusion of a stabilising agent (PVA, denoted by P), an aqueous solution (PVA:Pd (wt/wt) = 0.65, 0.01 g mL) was prepared. Solutions of $NaBH_4$ (0.1 M; $NaBH_4$:Pd (mol/mol) = 5) were prepared fresh and added dropwise to each solution, over the course of 1 minute with stirring, to form dark brown-black sols. The solutions were kept at a constant temperature (1 °C) during the reduction process and monitored every 15 minutes until complete reduction of the precursor salt had occurred. The prepared colloids were anchored onto TiO_2 (P25, Degussa) under vigorous stirring conditions, with the quantity of support material calculated to yield a final metal loading of 1 wt. % Pd. Where required, the catalyst slurry was acidified to pH 1-2 using sulfuric acid (denoted by A). All catalyst slurries were left to stir for 1 hr to accomplish full immobilisation of the colloid to the metal oxide support. The catalyst slurries were filtered, washed thoroughly using deionised H_2O, and dried

overnight at room temperature. A description of the catalyst preparations used in this chapter is available in *Table 4-1*.

***Table 4-1**. Synthesis variations applied to the standard sol immobilisation procedure studied in this chapter. Pd/TiO_2 catalysts were prepared at 1 °C using either 0, 50 or 100 vol. % MeOH in the synthesis solvent. PVA was used as a capping agent for the catalysts labelled with P, and the acidification step performed during the standard synthesis was only performed for PdWPA.*

Catalyst	Preparation Protocol			
	Reduction Temp. (°C)	**[MeOH] (vol. %)**	**PVA**	**Acidification**
PdWPA	1	0	✓	✓
PdWP	1	0	✓	×
Pd50MeP	1	50	✓	×
PdMeP	1	100	✓	×
PdW	1	0	×	×
Pd50Me	1	50	×	×
PdMe	1	100	×	×

4.2.2 Ultraviolet-Visible Spectroscopy

Reduction of the precursor Pd salt was monitored *via* ultraviolet-visible spectroscopy. 4 mL of the precursor or colloidal solution was analysed at a time, with samples measured at 15 minute intervals until reduction of the Pd species had been observed. Full reduction was observed when a broad absorbance band appeared in the spectra (between 200-800 nm). Samples were characterised using a Shimadzu UV-1800 spectrophotometer in a quartz cuvette, using the synthesis solvent as a reference (i.e. MeOH was used for catalysts prepared using solely MeOH as the mother solvent).

4.2.3 Microwave Plasma-Atomic Emission Spectroscopy

Pd metal wt. % loadings were analysed using microwave plasma-atomic emission spectroscopy. Fresh Pd/TiO_2 catalyst (3 × 0.1 g) was added to a solution of aqua regia (3:1 HCl:HNO_3, 3 × 8 mL, trace metal purities). These solutions were then sealed in PTFE tubes

and placed into an Anton-Paar Microwave 3000 centrifuge, with one tube containing an aqua regia blank. Samples were heated to 200 °C and held for 40 minutes before cooling to room temperature; on returning to room temperature, the solutions were diluted to 10 vol. % metal solutions using deionised H_2O (18.2 MΩ cm). Support particulates were removed from solution before analysis by filtering through a syringe filter-tip (Cole-Parmer, PTFE, 22 µm pore size, 50 mm diameter). Initially, Pd metal standards were prepared and measured to calibrate the emission spectrometer. All standards, blanks and samples were vaporised and passed through a microwave induced plasma, exciting electrons in the sample. On their return to the ground state, the element specific emission was detected using an Agilent Technologies 4100 MP-AES at four wavelengths of light corresponding to Pd atomic transitions (324.270, 340.458, 360.955 and 363.470 nm).

4.2.4 Electron Microscopy

Catalysts characterised using TEM, HAADF/BF STEM and HRTEM were prepared *via* sonication of the sample in EtOH. An aliquot of the supernatant was pipetted onto either a 300 mesh Cu TEM grid (TEM) or onto a 300 mesh holey carbon mesh Cu TEM grid (STEM and HRTEM). TEM images were acquired by the author using a JEOL JEM 2100 EM, operating at 120 kV, at the Research Complex at Harwell, Didcot, U.K. Both STEM images and EELS measurements were acquired by Dr. Briceno de Gutierrez and Dr. Dung, respectively, using the probe-corrected JEOL ARM200CF Scanning TEM, operating at 200 kV, on Johnson Matthey's electron microscope at the I14 (ePSIC) beamline, DLS, Didcot, U.K.

4.2.5 X-ray Absorption Fine Structure

X-ray absorption fine structure measurements were performed to examine the Pd oxidation state (XANES) and the average Pd atom cluster size from the 1st shell coordination number (EXAFS) of the fresh and used Pd/TiO_2 catalysts. Pd K-edge XAFS studies were carried out on the B18 beamline at DLS, Didcot, U.K. Measurements were performed in fluorescence mode using the QEXAFS setup with a fast-scanning Si(311) double-crystal monochromator, multi-element Ge and ion chamber detectors (for sample and reference foils, respectively). Spectra were acquired at a time resolution of 1 min spectrum^{-1} (k_{max} = 18), with 3 scans acquired per sample. Fitting of the Pd K-edge EXAFS data were performed using the 1st shell scattering paths of a Pd^0 foil (ICSD collection code = 52251) and a PdO reference (ICSD collection code = 24692).

Cl K- and S K-edge XAFS measurements were performed to evaluate the presence, local geometry and oxidation state of the target element both in the catalyst structure and on its surface. Cl and S K-edge measurements were carried out on the BM28 beamline[35] (UK CRG-XMaS) at the ESRF, Grenoble, France. On BM28, datasets were measured by running a variable point density macro (*XESCAN.MAC – Extended Escan: Variable point density*); in particular, energy scans were performed for multiple consecutive energy regions, with equal or different steps (variable point density). Prior to measurement, the samples were placed within a sample chamber and put under vacuum (~ 10^{-6} mbar) to minimise air absorption at these 'tender' energies (< 8 KeV). The fluorescent signal was detected using a silicon drift diode detector and processed using a Mercury XIA digital signal processor. All spectra acquired at the Cl and S K-edges were in fluorescence mode.[36]

All XAFS data were processed using the Demeter software package.[37,38] The Cl K-edge XANES data were normalised using a Na_2PdCl_4 reference standard, where the energy of the rising edge was calibrated according to literature values of similar $[PdCl_4]^{2-}$ data.[39,40] S K-edge XANES data were aligned to a pre-run sulfur containing compound, $CuSO_4$, using the Athena software package. As H_2SO_4 was used during the immobilisation of PdWPA, it is appropriate to compare the measured data to another sulfate species. The absorption edge of $CuSO_4$ was aligned to 2482.0 eV, the literature value for the SO_4^{2-} sulfur compound.[41,42] The shift in the energy obtained from alignment of $CuSO_4$ was then applied to the Pd/TiO_2 samples

4.2.6 Infrared CO Chemisorption Studies

FTIR transmission spectra were acquired using a Nicolet iS10 spectrometer at a spectral resolution of 4 cm^1 and an accumulation of 64 scans. For each catalyst, ~ 30 mg of the catalyst was pressed to form a 13 mm diameter pellet. After placing the pellet inside of the transmission cell, the chamber was purged with He (30 mL min^{-1}) for 30 minutes, and a background spectrum was recorded. Next, 10 % CO/He (10 mL min^{-1}) was pulsed into the chamber for 30 seconds between scans. CO was dosed over the pellet until complete saturation of the pellet surface was achieved, normally 3-4 pulses. At this point, the gas was switched to He (30 mL min^{-1}) for 30 minutes, removing all gaseous and physisorbed CO from the chamber and pellet surface, respectively. Data processing and background subtractions were performed using the OMNIC software package.

4.2.7 Hydrogenation of Furfural

Furfural hydrogenation was performed at 50 °C using a stainless steel reactor (30 mL capacity), equipped with a heater, mechanical stirrer, gas supply system and thermometer. All testing was carried out by the author and Dr. S. Alijani at the Universitá degli Studi di Milano, under the supervision of Dr. A. Villa. A fresh solution of furfural (10 mL, 0.3 M in IPA) was placed into the reactor along with the desired quantity of catalyst (furfural:metal (mol/mol) = 500). The reaction vessel was purged with N_2 (3 × 3 bar) before being depressurised and repressurised using H_2 (5 bar) and sealed. The mixture was heated to 50 °C before being mechanically stirred (1000 rpm), ensuring kinetic regime conditions. At the end of the reaction, the autoclave was cooled to room temperature (25 °C), and the pressure was relieved. The process of pressurising the vessel was repeated after reaction samples were withdrawn at 0 min, 15 min, 1 hr, 3 hrs and 5 hrs of reaction time. Reaction samples were removed periodically (0.2 mL) and mixed with the internal solvent (IPA, 0.1 mL) and external standard (dodecanol, 0.2 mL) before being analysed in an Agilent 6890 gas chromatograph equipped with a Zebron ZB-5 60 m × 0.32 mm × 1 µm column. Authentic products (FA, THFA, etc.) were analysed to determine separation times. Quantitative analyses were performed using the external standard method, whereby the GC peak area of each product was compared against a known standard (dodecanol). Unidentified ether products were identified using gas chromatograph-mass spectroscopy (GC-MS); for this, aliquots of the reaction mixture were analysed using a Thermo Scientific ISQ QD, equipped with an Agilent VF-5ms column, 60 m × 0.32 mm × 1 µm.

4.2.8 Thermal Characterisation Techniques

4.2.8.1 Temperature Programmed Desorption

Ammonia-TPD measurements were used to elucidate the strength of acidic surface sites on the relevant catalysts and were examined through diffuse reflectance infrared Fourier transform spectroscopy and by measuring the mass fragments produced during temperature programmed desorption using mass spectroscopy. DRIFTS datasets were acquired using a Harrick DRIFTS cell integrated with an Agilent Carey 680 Fourier-transform infrared spectrometer. Data was recorded taking 64 scans at 4 cm^{-1} resolution using the liquid nitrogen cooled MCT detector. The composition of the effluent gas was measured using a Hiden QGA mass spectrometer. Two experimental procedures were used: (1) pre-reduction of the sample surface performed in 4 % H_2:He (40 mL min^{-1}) for 30 minutes at 150 °C, and

(2) pre-treatment in He (40 mL min^{-1}) at 150 °C for 30 minutes. The cell was then cooled to 25 °C in He (40 mL min^{-1}). The temperature was increased to 100 °C; once at temperature, NH_3 (5 % NH_3/He, 40 mL min^{-1}) was introduced to the cell until the surface was adequately saturated. Once saturated, the gaseous mixture was switched to He (40 mL min^{-1}) and the temperature was increased to 450 °C (10 °C min^{-1}). Background DRIFTS spectra were recorded in flowing He (40 mL min^{-1}) at 100 °C and were subtracted from the sample spectrum for each measurement.

4.2.8.2 Temperature Programmed Reduction

Hydrogen-TPR experiments were performed using an Anton Paar ChemBet Pulsar. Sample surfaces were purged at room temperature with Ar (25 mL min^{-1}) for 45 minutes. Analysis was performed in 4 % H_2/Ar (25 mL min^{-1}), during linear heating of the sample from room temperature to 500 °C (8 °C min^{-1}). The quantity of hydrogen consumed and produced during the TPR measurement was determined using a thermal conductivity detector. Prior to TPR measurements, the TCD was calibrated at room temperature by pulsing pure H_2 (5 mL min^{-1}) into the ChemBet chamber under pure Ar (30 mL min^{-1}) until the gas volume reached 125 mL.

4.2.8.3 Thermogravimetric Analysis

Thermal analysis of PVA, TiO_2 (P25), PdWPA, PdMeP and PdMe were performed using a thermogravimetric analyser, data were acquired on a TGA 5500 (TA Instruments). Pt TGA pans were used for all measurements and subjected to a cleaning process prior to sample characterisation: any trace sample was removed, the pan was washed with acetone, heated to 1000 °C (20 °C min^{-1}) in N_2 (20 mL min^{-1}) and held for 5 minutes before cooling to room temperature. 10-20 mg of sample was placed into the clean TGA pan for all samples except TiO_2, where 6 mg was used due to the low density of the material. Thermal properties were investigated and characterised with increasing temperature, 25 to 700 °C (5 °C min^{-1}), and performed in flowing N_2 (20 mL min^{-1}).

4.3 Results and Discussion

The data presented herein further builds on the results presented in the previous chapter; briefly, the greatest control of Pd NP size was observed by preparing colloidal Pd in a solvent system composed of equal vol. % MeOH:H_2O. However, increases to the alcohol concentration in the synthesis solvent (75-100 vol. %) yielded a sharp decrease in the Pd wt. % loading achieved, < 0.4 wt. % Pd. The optimisation of the sol-immobilisation synthesis procedure investigated in this work focuses on the synthesis of 1 wt. % Pd/TiO_2 catalysts in three reaction mixtures: (1) water (denoted by W), (2) an equivalent vol. % MeOH:H_2O (denoted by 50Me), and (3) methanol (denoted by Me). The control of NP size with and without the addition of a capping agent is also measured in this study for all solvent systems, with samples prepared using PVA denoted with P. To improve the loading achieved by the high [MeOH] Pd catalysts, the influence of the acidification procedure in the alcoholic systems is also studied, with only the standard PVA capped water based Pd catalyst immobilised at an acidic pH value.

4.3.1 Characterisation of Prepared 1 wt. % Pd/TiO_2 Catalysts

4.3.1.1 Ultraviolet-Visible Spectroscopy

Solutions of Na_2[PdCl4] ([Pd] = 128 μM) were prepared in $(MeOH)_x$:$(H_2O)_{1-x}$ solvent mixtures (x = 0, 0.5 or 1) and initially characterised *via* UV-Vis (*Figure 4-2*). Changes to the precursor salt complex are noted through shifts in the $[PdCl_4]^{2-}$ absorbance bands: 210, 238, 329 nm (LMCT) and 410 nm (*d-d* transition). These bands are observed for catalysts PdWPA, PdWP and PdW and are consistent with values reported in the literature for water solvated $[PdCl_4]^{2-}$.[43–45] Catalysts prepared with increasing volumes of MeOH (Pd50MeP, PdMeP, Pd50Me and PdMe) display shifts in the positions and intensities of the LMCT and *d-d* transitions (*Figure 4-2*a-c). Variations in these peak positions and intensities could be resultant of changes to the solution pH with increasing [MeOH] as hypothesised for the catalysts prepared in the previous chapter.[46] Another explanation for this could be the active ligand exchange of Cl^- with OH^- functionalities within the solvent.[47] Once full reduction of the precursor salt is achieved, the appearance of a broad absorbance band across the spectra is evidenced for all solutions (*Figure 4-2*d).[27,48] The colloidal solutions described were

immobilised onto TiO_2 (P25) without acidification of the support, except for PdWPA, where the solution was acidified to pH 1-2 upon immobilisation.

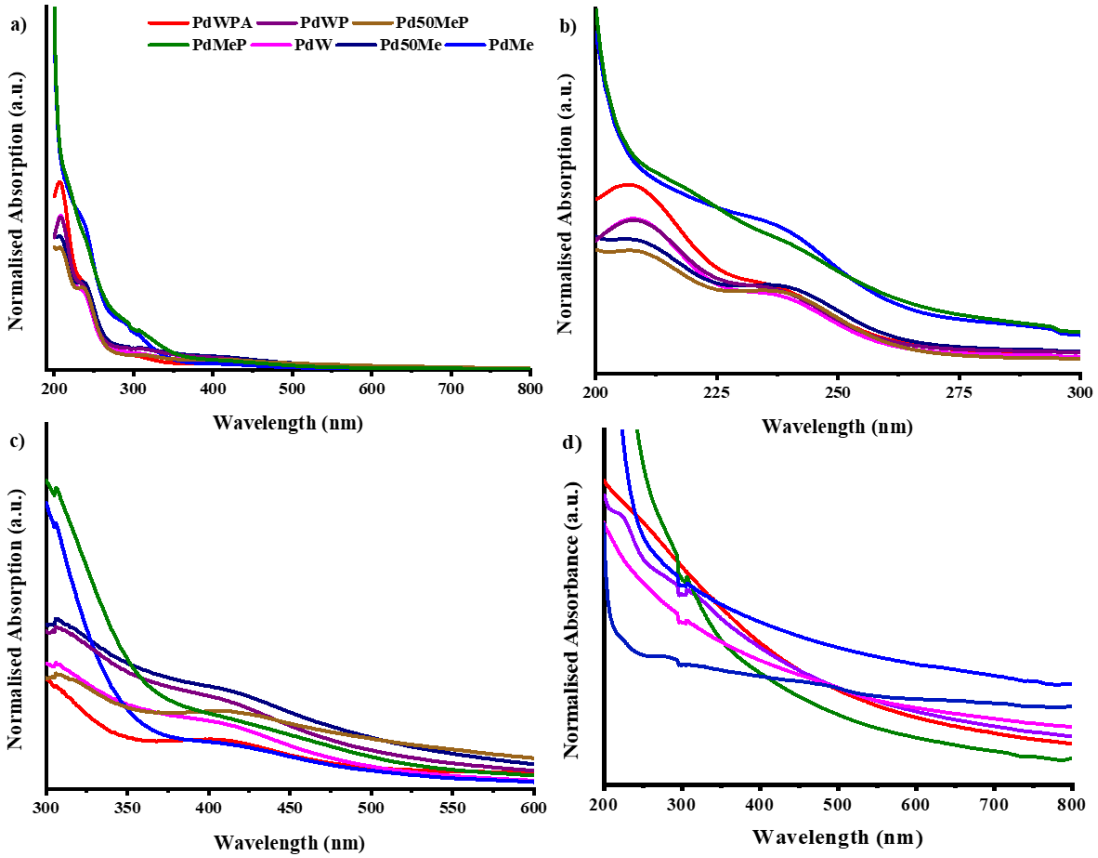

Figure 4-2. *UV-Vis spectra of a) the precursor salt solutions prior to reduction; where Pd NPs were prepared in solutions of H_2O, 50 vol. % MeOH:H_2O, and 100 vol. % MeOH, with and without PVA (P) added as a stabilising agent. PdWPA was the only catalyst synthesised with an acidification step; b) the ligand-metal charge transfer band region, c) the d-d transition band, and d) the broad absorption band formed across the Pd spectra once reduced.*

4.3.1.2 Microwave Plasma-Atomic Emission Spectroscopy

The Pd wt. % loading of each catalyst was determined using MP-AES (*acidic protons.*

Table 4-2). Preparation of Pd/TiO_2 following the standard route, including acidification and a water solvent system (PdWPA), led to the immobilisation of 0.83 wt. % Pd, as is commonly found.[27] Removal of this acidification process impacts on the loading of catalysts prepared in a water only solvent; the Pd loading of PdWP and PdW, are 0.25 and 0.3 wt. % Pd, respectively. This decrease in loading is anticipated as acidification is required to enable colloidal adhesion to the TiO_2 surface.[49] Interestingly, when the acidification step is removed

and MeOH is present in solvent, similar (PdMeP = 0.86 wt. % Pd) and higher (PdMe = 0.96 wt. % Pd) levels of immobilisation were observed. At present, the higher Pd wt. % loadings in MeOH are proposed to be caused by the amphoteric nature of the alcohol aiding in the immobilisation in the absence of acidic protons.

Table 4-2. *MP-AES results for the 1 wt. % Pd/TiO_2 catalysts prepared using a standard and an altered sol-immobilisation process. The Pd wavelength was measured at 340.5 nm.*

Catalyst	Sample Mass (g)	MP-AES Ave. [Pd] per sample (ppm)			Ave. [Pd] (ppm)	Ave. [Pd] (wt. %)
PdWPA	0.1004	8.49	8.46	8.18	8.37	0.83
PdWP	0.0863	2.57	2.53	2.54	2.56	0.30
Pd50MeP	0.0851	7.83	7.73	7.67	7.75	0.91
PdMeP	0.0995	9.59	9.59	9.53	9.56	0.86
PdW	0.0865	2.20	2.18	2.19	2.20	0.25
Pd50Me	0.0887	8.15	8.15	8.08	8.12	0.91
PdMe	0.1057	9.12	9.04	9.07	9.10	0.96

4.3.1.3 Transmission Electron Microscopy

All powdered catalysts were characterised using TEM, with their average NP sizes and particle size distributions/dispersions evaluated using ImageJ software (*Figure 4-3* and *Figure 4-4*, respectively).[50] An initial comparison of catalysts PdWPA and PdWP shows that employing an acidified immobilisation step increases the average NP size (PdWP = 1.7 ± 0.7 nm, PdWPA = 2.6 ± 1.4 nm). The greater NP size and dispersion observed for PdWPA can be ascribed to the interaction of the stabilising agent, PVA, with the acid, H_2SO_4, during the immobilisation phase. As the acid is added into the catalyst slurry, it strips away the PVA from the NP surface, which can lead to aggregation of the NPs on the TiO_2 surface.[51] MeOH synthesised catalysts (PdMeP and Pd50MeP) achieved good immobilisation without the need for acidification and, importantly, formed Pd NPs with smaller average sizes compared to PdWPA (Pd50MeP = 1.7 ± 0.7 nm, PdMeP = 1.8 ± 0.8 nm). As expected, the absence of a stabilising agent increases the instances of particle agglomeration for Pd50Me and PdMe.[9,32,52,53] However, whilst the

average NP size remains fairly small (< 5 nm) for all uncapped Pd catalysts, the associated error for each sample increases in proportion to the [$MeOH_{(aq)}$]: PdW = 3.1 ± 1.5 nm, Pd50Me = 3.6 ± 1.6 nm, and PdMe 3.3 ± 2.3 nm.

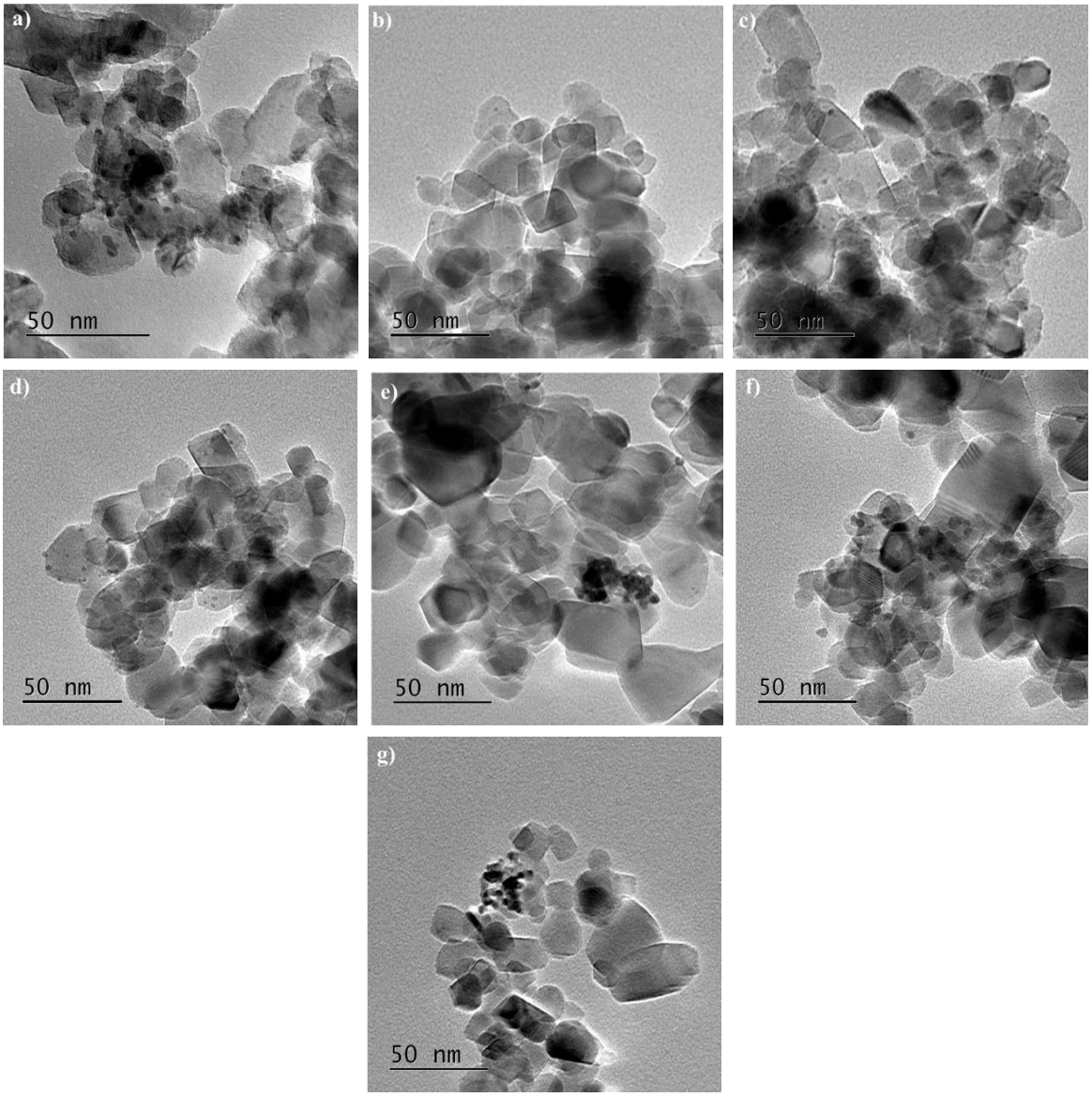

Figure 4-3. *TEM images acquired for the 1 wt % Pd/TiO_2 catalysts prepared with the inclusion of PVA as a stabilising agent: a) PdWPA, b) PdWP, c) Pd50MeP, d) PdMeP, e) PdW, f) Pd50Me, and g) PdMe.*

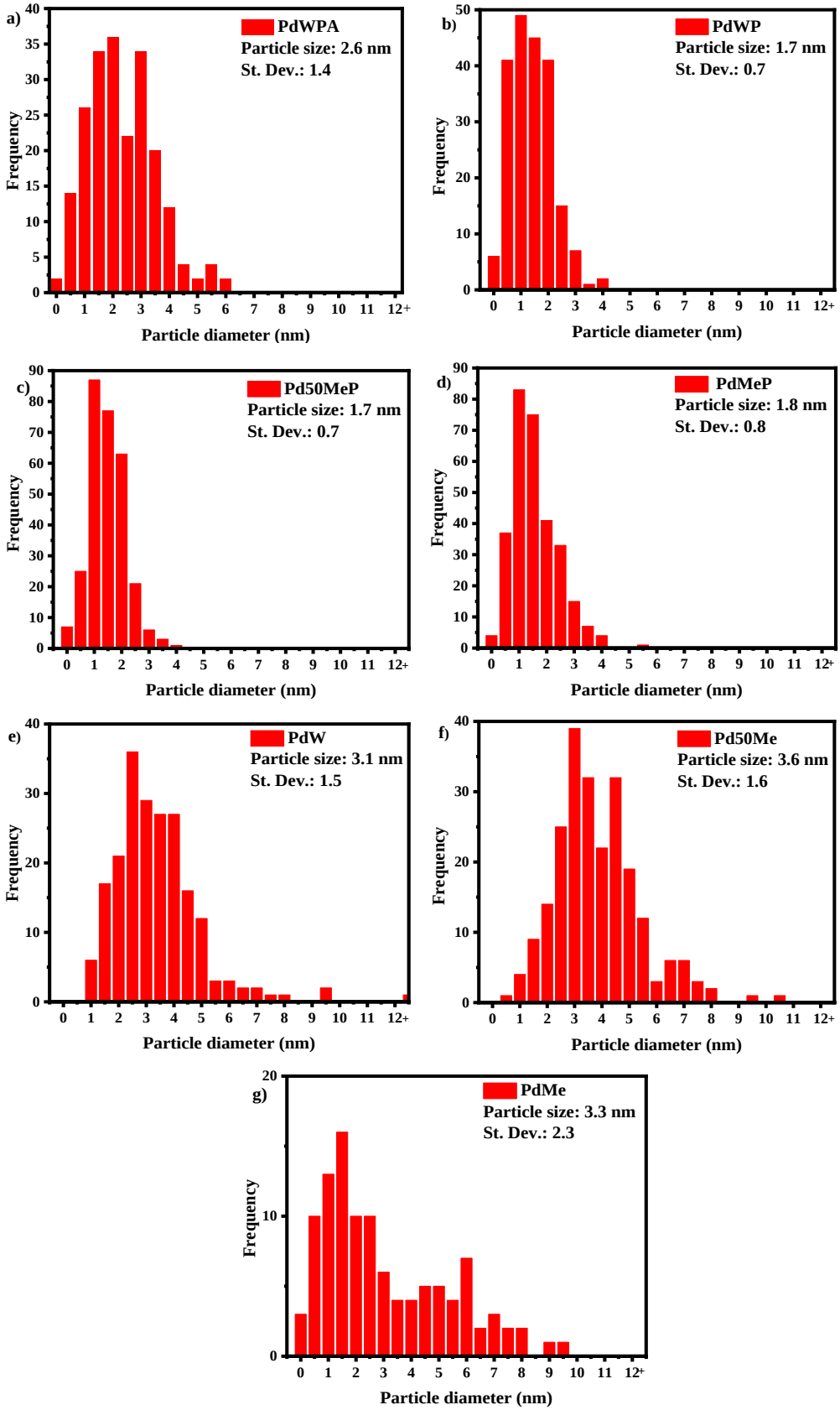

Figure 4-4. *Standard deviation histograms corresponding to the prepared 1 wt. % Pd/TiO_2 catalysts: a) PdWPA, b) PdWP, c) Pd50MeP, d) PdMeP, e) PdW, f) Pd50Me, and g) PdMe. Nanoparticle sizes and distributions were calculated using a sample population of 200-300 Pd NPs.*

4.3.1.4 Scanning Transmission Electron Microscopy-Energy Dispersive X-ray Analysis

STEM images were acquired using a high angle annular dark field detector coupled with EDX analysis, affording greater insight into the morphology, size and dispersion of the supported Pd NPs prepared in the capped MeOH:H_2O series. The formation of small and well dispersed Pd NPs is most evident for the water only system, PdWP (*Figure 4-5*a); conversely, by preparing the PVA capped colloid in 100 vol. % MeOH (PdMeP, *Figure 4-5*b), larger Pd clusters were observed on the support surface. Standard TEM measurements did not distinguish between this size disparity due to the far lower Pd loading achieved in PdWP (PdWP = 0.3 wt. % Pd, and PdMeP = 0.86 wt. % Pd). Agglomeration is also prevalent for the uncapped catalysts (PdW and PdMe, *Figure 4-5*c and d), with the higher metal loading achieved for PdMe increasing the probability of Pd NP coalescence taking place. It is therefore evident that the addition of a stabilising agent is necessary to suppress unfavourable growth of NPs, even in alcoholic systems.

4.3.1.5 X-ray Absorption Fine Structure

XAFS measurements are used within this chapter to characterise the oxidation state and structural environment of the supported Pd nanoparticles (Pd K-edge XANES and EXAFS, respectively).[54] The use of 'softer' edge energies to probe the environment (Cl and S K-edge XANES) of any residual Cl or S remaining on the catalysts following synthesis is also described.[55]

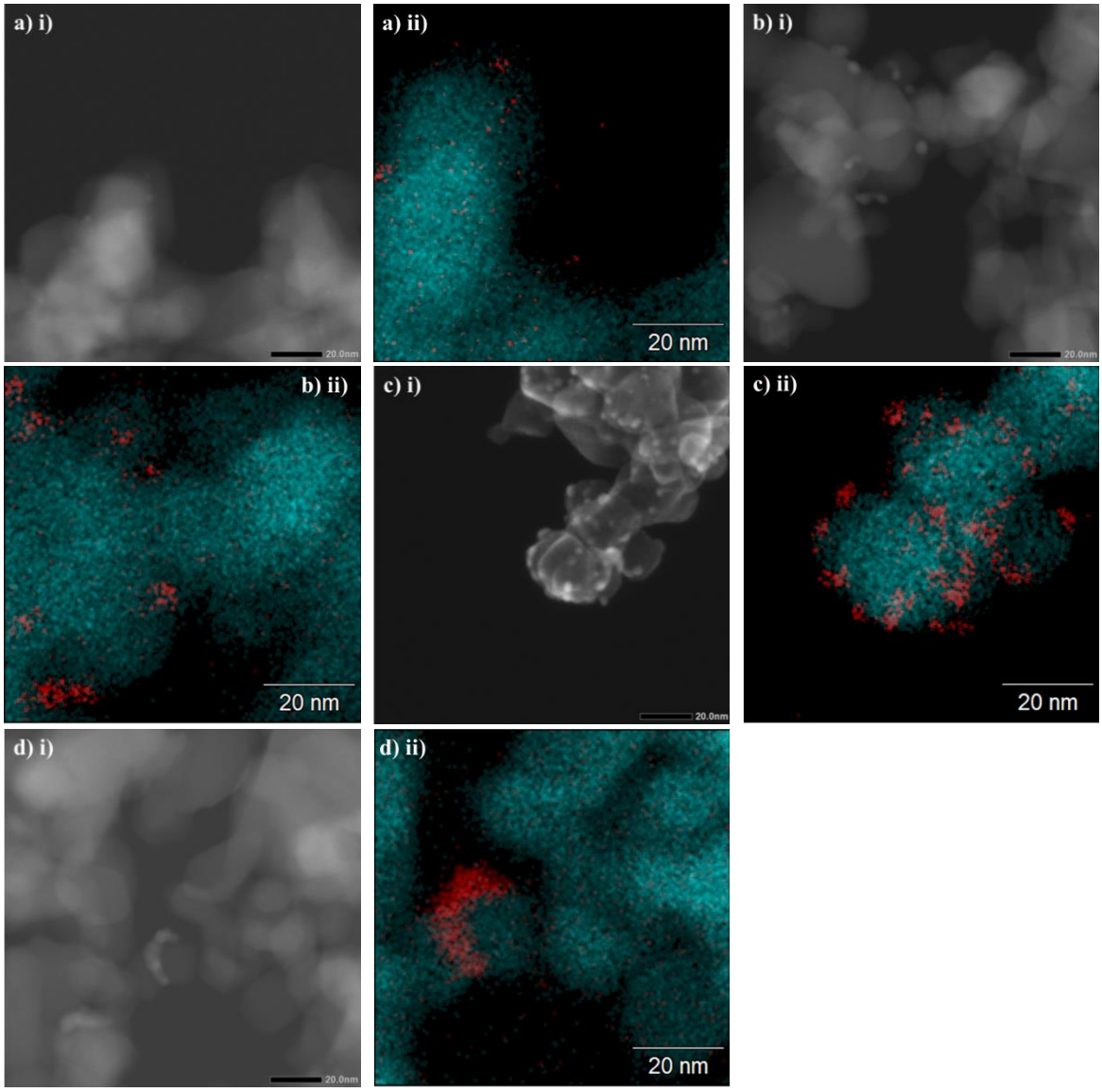

Figure 4-5. *Images of the 1 wt. % Pd/TiO_2 catalysts prepared in the capped MeOH:H_2O series acquired via i) STEM HAADF, and ii) EDX analysis of a small area of i); depicting a) PdWP, b) PdW, c) PdMeP and d) PdMe.*

4.3.1.5.1 Pd K-edge X-ray Absorption Near-Edge Structure

The per atom average provided by XAFS allowed the zero-valent (Pd^0) and oxidised (Pd^{2+}) components of the catalysts to be calculated through LCF of the XANES region (*Figure 4-6*). The LCF data confirms that when PVA is present in the solvent system, the Pd bulk contains higher average Pd^{2+} character: PdWPA = 27.9 %, Pd50MeP = 31.7%, PdMeP = 41.2 % (*Table 4-3*). In addition, by not performing the acidification step during PdWP synthesis an increase in the average amount of Pd^{2+} state is observed: PdWP = 31.9 %, PdWPA = 27.9 %. As discussed in Chapter 3, this Pd^{2+} character observed for all samples is indicative of the formation of passivated oxide layers occurring readily over NPs with decreasing sizes.[56] However, the average TEM NP size measured for PdMeP

does not correlate with the Pd^{2+} % fitted, therefore, further assessment of the EXAFS data is necessary to evaluate the disparity in NP sizes for the prepared catalysts.

Table 4-3. *Synthesis conditions applied for the prepared 1 wt. % Pd/TiO_2 catalysts; Pd bulk oxidation state composition determined by XANES LCF, and average TEM Pd NP size calculated from a sample population of 200-300 Pd NPs. The accuracy of the fit is described by an R_{factor} value, where the confidence of the fit is represented by the smallest value above zero.*

Sample Notation	**Reference Standard (%)**				**Ave. TEM Pd NP Size (nm)**
	Pd^{2+}	Pd^0	Pd^{2+}/Pd^0	R_{factor}	
PdWPA	28	72	0.39	0.012	2.6 ± 1.4
PdWP	32	68	0.47	0.017	1.7 ± 0.7
Pd50MeP	31	69	0.45	0.014	1.7 ± 0.7
PdMeP	41	59	0.69	0.026	1.8 ± 0.8
PdW	32	68	0.47	0.017	3.1 ± 1.5
Pd50Me	13	87	0.15	0.006	3.6 ± 1.6
PdMe	15	85	0.18	0.005	3.3 ± 2.3

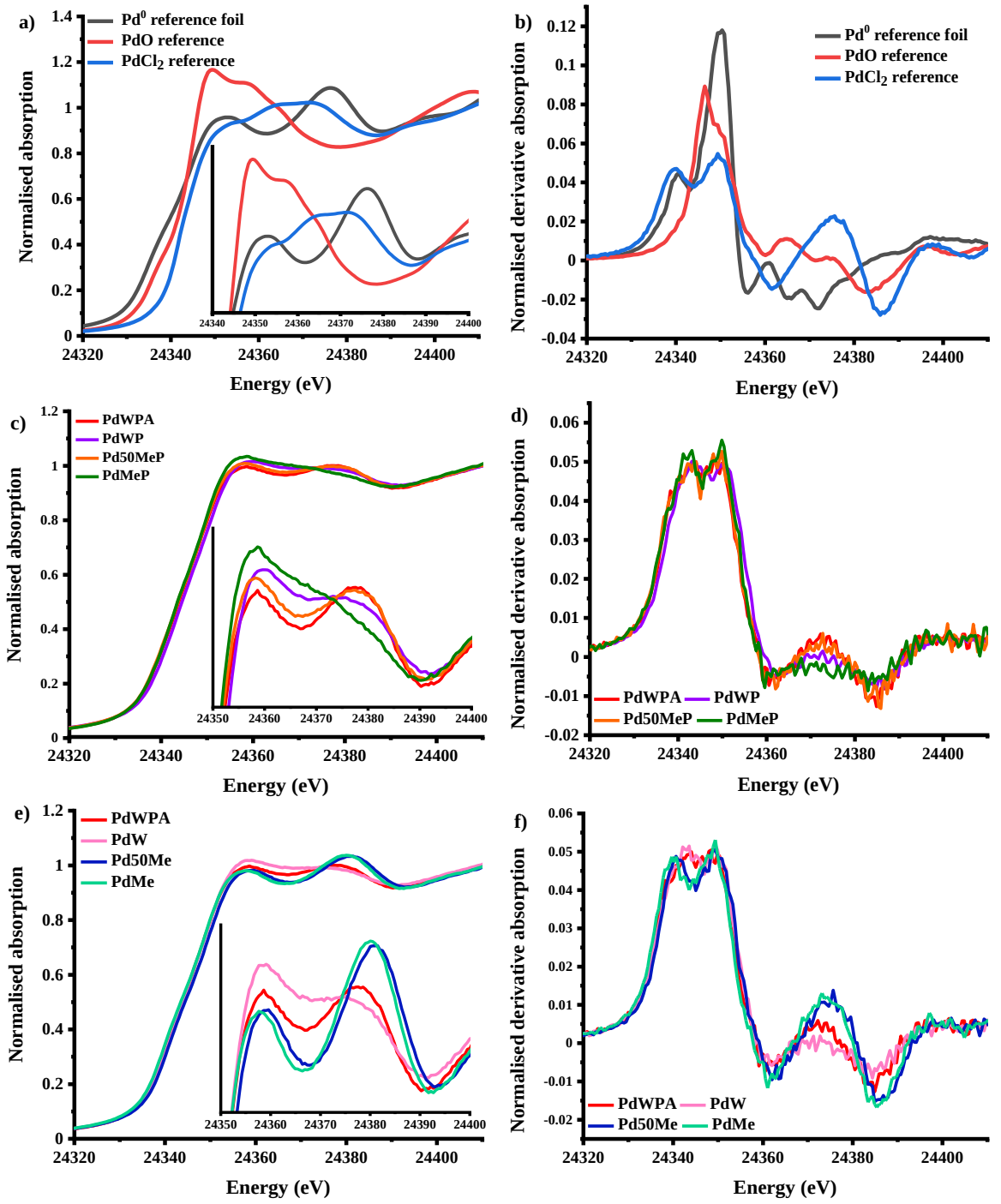

Figure 4-6. *XANES spectra acquired for all prepared 1 wt. % Pd/TiO_2 catalysts measured on the B18 beamline at DLS, Didcot, U.K. Spectra were measured at the Pd K-edge; XANES data are presented in normalised energy (a, c & e), and as the normalised 1st derivative energy (b, d & f). Pd reference data are shown in images a) & b), catalysts prepared using PVA are presented in figures c) & d), and catalysts prepared without PVA are shown in figures e) & f). PdWPA is shown for comparison.*

4.3.1.5.2 Pd K-edge Extended X-ray Absorption Fine Structure

EXAFS was used to evaluate the prepared Pd catalysts' local structure and Pd NP size (*Figure 4-7*a-f). The formation of small Pd NPs is confirmed for these catalysts through two distinct features: (1) a decrease in the magnitude of the 1st shell Pd-Pd scattering path (~ 2.8 Å), and (2) an increase in the scattering path at 1.7 Å, which is indicative of a passivated oxide layer forming on exposure of the Pd NPs to air.[56] The formation of large crystalline PdO phases is discounted by the absence of a Pd-O scattering path at ~ 3 Å (*Figure 4-7*a, c and e).[57] Evaluation of the EXAFS data, coupled with the XANES component, confirms that there are very small Pd NPs present on the catalyst surface which is consistent with the TEM analysis.

Prior to fitting of the data, the amplitude reduction factor (S_0^2) was found by fitting the Pd foil measured during the beamtime with a Pd^0 standard *.cif* file acquired from the ICSD database: $S_0^2 = 0.75$. Noise in the data, due to fluorescence acquisition, limited the extent to which the *k* range could be fitted; for these samples, the *k* range was $3 < k < 10.5$, and the *R* range was $1 < R < 3.4$ (*Figure 4-8*a-g). When PdWPA and PdWP are compared, removal of the acidification step displays a decrease in the magnitude of the 1st shell Pd-Pd scattering path and an increase in the magnitude of the 1st shell Pd-O scattering path. This agrees with the data previously shown for the XANES and TEM of these samples.

Fitting of the Fourier transformed χ-data enables the average localised CN of the absorbing atom to be quantified.[58] Introducing methanol to the synthesis solvent proved to have limited effect on the localised coordination of the supported Pd, as seen for Pd50MeP, ($CN_{Pd\text{-}Pd} = 5.0 \pm 0.3$, $CN_{Pd\text{-}O} = 2.2 \pm 0.2$) were calculated within error of the values for PdWP ($CN_{Pd\text{-}Pd}$: 4.8 ± 0.3, $CN_{Pd\text{-}O}$: 2.1 ± 0.2). This agrees with the values found through XANES LCF and average TEM NP size (*Table 4-4*). When MeOH was used as the synthesis solvent for PdMeP, the fitted FT EXAFS data shows the smallest Pd NPs are formed ($CN_{Pd\text{-}Pd} = 4.6 \pm 0.4$, $CN_{Pd\text{-}O} = 2.7 \pm 0.2$). The importance of employing a stabilising agent in colloidal synthesis is evident in the EXAFS data for the uncapped samples (PdW, Pd50Me and PdMe), which all show greater $CN_{Pd\text{-}Pd}$ than their stabilised counterparts as a consequence of Pd agglomerating within the colloid and upon the support surface; this is in agreement with the average NP size increases observed through TEM measurements.[59,60]

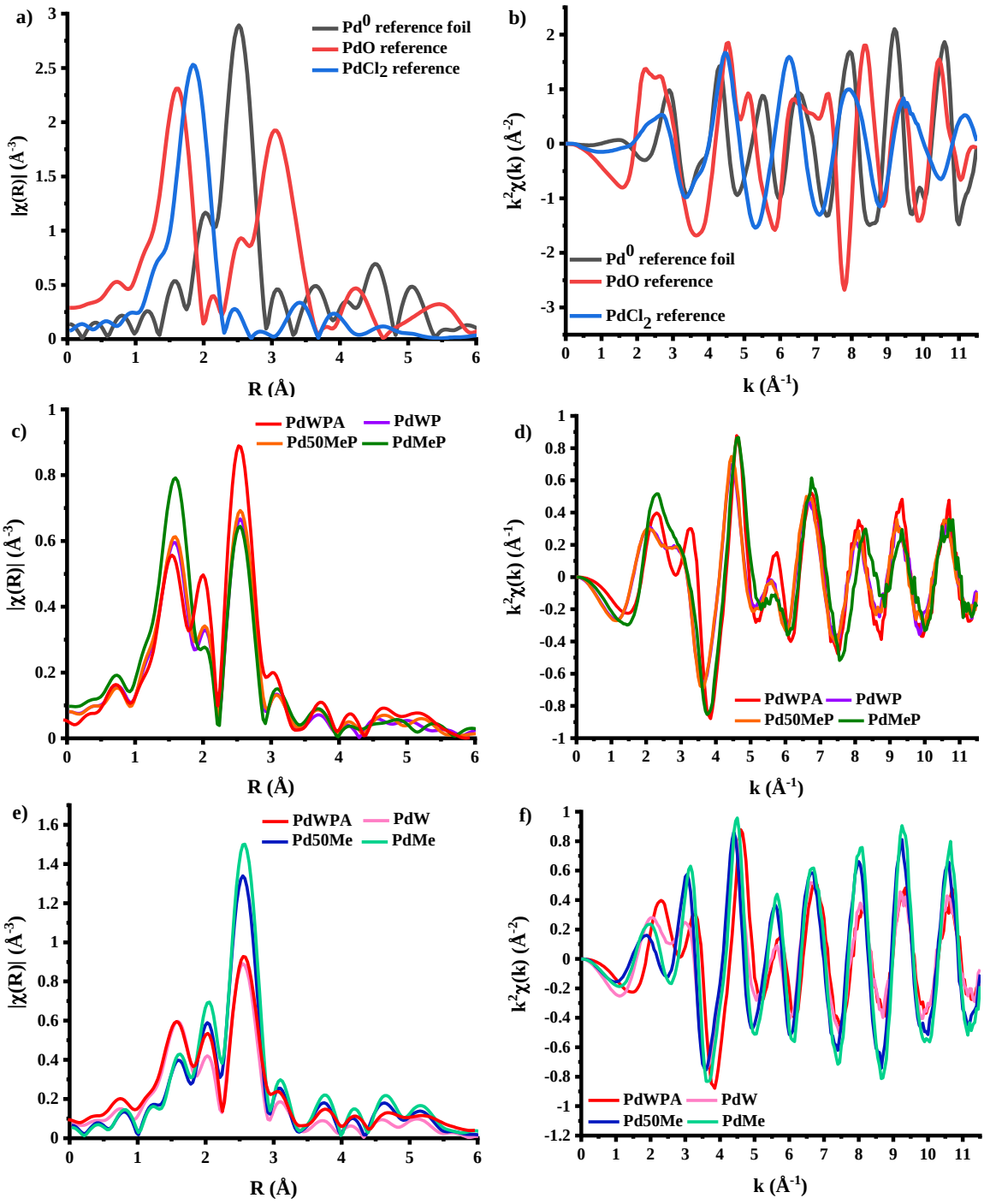

Figure 4-7. *Pd K-edge XAFS data collected ex situ, measured on the B18 beamline at DLS, Didcot, U.K. The data displays the experimental FT χ(k) (a, c & e) and χ(k) data (b, d & f) for the prepared 1 wt. % Pd/TiO₂ catalysts. Pd reference data are displayed in figures a) & b); samples prepared using PVA as a stabilising agent are shown in c) & d) and samples prepared without PVA are presented in e) & f) PdWPA is shown in figures e) & f) for comparison.*

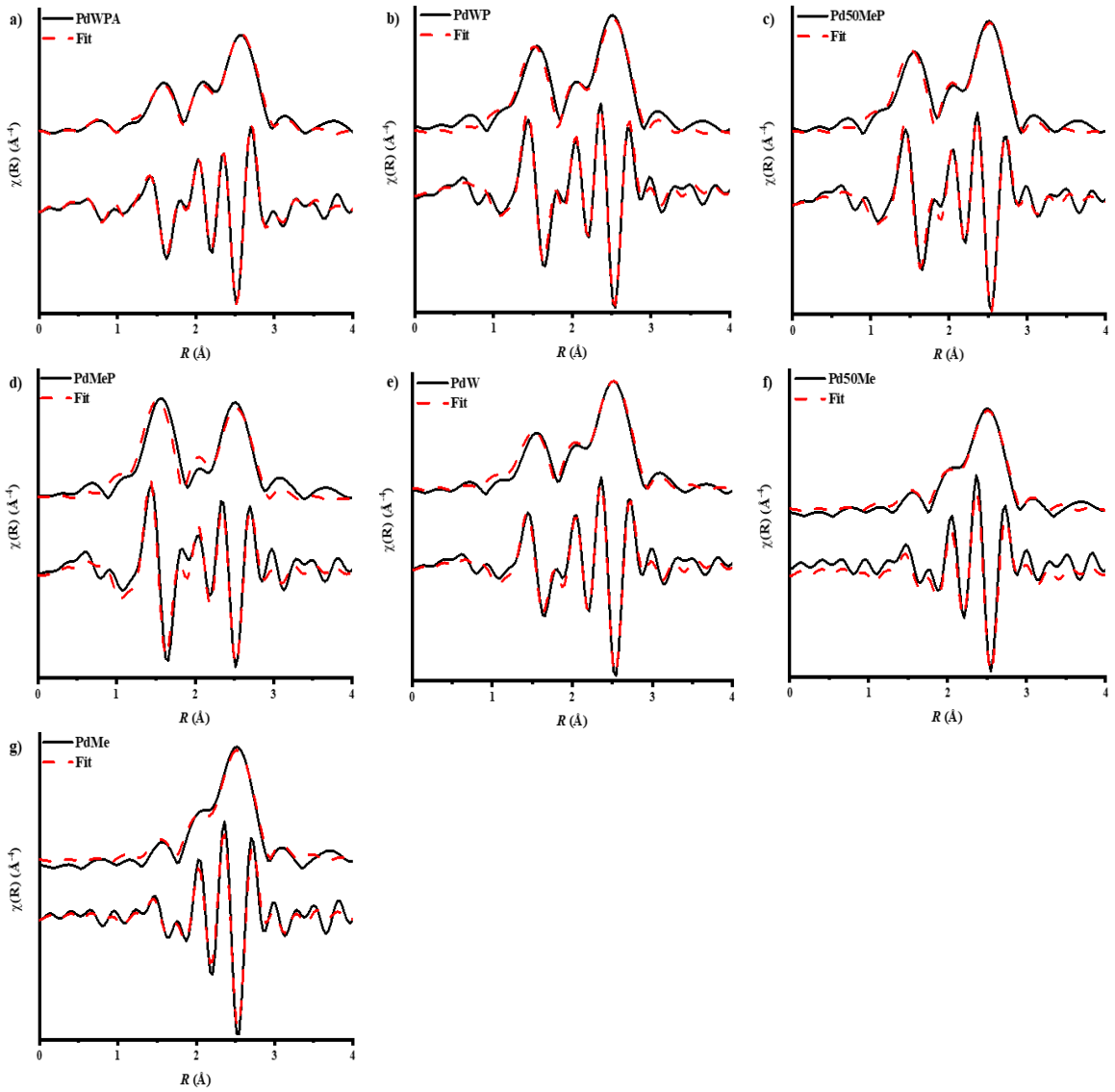

Figure 4-8. *Fitted experimental FT χ(k) data (both the magnitude and real components) for the Pd/TiO₂ catalysts prepared with and without PVA (P) and acidification (A) in varied synthesis solvent compositions: a) PdWPA, b) PdWP, c) Pd50MeP, d) PdMeP, e) PdW, f) Pd50Me, and g) PdMe.*

Table 4-4. *1st shell EXAFS fitting parameters derived from the k^2 weighted Fourier transform for the Pd K-edge EXAFS data for all fresh catalysts. Amplitude reduction factor, $(S_0^2) = 0.75$, was determined from fitting an acquired Pd^0 reference foil. EXAFS fittings range: $3 < k < 10.5$, $1 < R < 3.4$, number of independent points = 11.2. The accuracy of the fit is described by an R_{factor} value, where the confidence of the fit is represented by the smallest value above zero.*

Catalyst	Abs-Sc	CN	R (Å)	$2\sigma^2$ (Å^{-2})	E_0 (eV)	R_{factor}
PdWPA	Pd-Pd	6.7 ± 0.3	2.76 ± 0.01	0.010 ± 0.001	0.0 ± 0.3	0.012
	Pd-O	1.8 ± 0.2	1.97 ± 0.04	0.006 ± 0.003		
PdWP	Pd-Pd	4.8 ± 0.3	2.745 ± 0.005	0.010 ± 0.001	0.4 ± 0.4	0.018
	Pd-O	2.1 ± 0.2	1.97 ± 0.04	0.005 ± 0.003		
Pd50MeP	Pd-Pd	5.0 ± 0.3	2.747 ± 0.004	0.010 ± 0.001	0.4 ± 0.4	0.017
	Pd-O	2.2 ± 0.2	1.97 ± 0.04	0.006 ± 0.003		
PdMeP	Pd-Pd	4.6 ± 0.4	2.73 ± 0.02	0.011 ± 0.002	1.7 ± 0.7	0.031
	Pd-O	2.7 ± 0.2	1.98 ± 0.04	0.004 ± 0.002		
PdW	Pd-Pd	6.2 ± 0.3	2.76 ± 0.01	0.010 ± 0.001	0.2 ± 0.5	0.018
	Pd-O	1.8 ± 0.2	1.97 ± 0.05	0.005 ± 0.003		
Pd50Me	Pd-Pd	8.9 ± 0.1	2.74 ± 0.01	0.0091 ± 0.0002	2.0 ± 0.1	0.036
	Pd-O	0.7 ± 0.7	1.97 ± 0.04	0.005 ± 0.002		
PdMe	Pd-Pd	8.7 ± 0.2	2.74 ± 0.01	0.0078 ± 0.0006	0.3 ± 0.3	0.006
	Pd-O	0.9 ± 0.2	1.96 ± 0.06	0.008 ± 0.004		

4.3.1.6 Cl and S K-edge X-ray Absorption Fine Structure

4.3.1.6.1 Cl K-edge X-ray Absorption Near-Edge Structure

Analysis of the Cl K-edge XANES region (*Figure 4-9*) provides invaluable information about the composition of the absorbing atom's orbitals and the covalent nature of any associated bond(s). As with the data presented for harder X-ray edge energies, comparison of the acquired data with its precursor salt (Na_2PdCl_4) is paramount to reliably interpret the results. Changes to the pre-edge and rising-edge positions elucidate how the Cl speciation on the catalyst surface alters as a function of the sol-immobilisation procedure employed. It is known that the following factors affect the position of the XANES pre-edge energy: (i) the metal coordination geometry, (ii) *n*d orbital energy, (iii) ligand field splitting of the *n*d orbitals, and (iv) the charge of the Cl absorber.[39] As seen in *Figure 4-9*a, the most intense pre-edge peak is observed for the precursor salt Na_2PdCl_4. This is expected as $[PdCl_4]^{2-}$ is square planar in geometry with regards to the Pd^{2+} centre – it possesses two degenerate electron holes in the Pd 4*d* orbital.

The peak at 2821.7 eV represents the excitation of the dipole-allowed Cl 1*s*→3*p* transition into the doubly unoccupied LUMO (b_{1g} of the complex), and is described as having predominantly Cl 3*p* and Pd $4d_{x^2-y^2}$ character.[39,40,61] A second pre-edge peak is observed as a slight shoulder at 2823.5 eV which is ascribed to shake-up satellite transitions, where the excess energy within the system excites a valence electron following the formation of a core hole by the incident X-ray source beam.[40,62,63] The rising edge position of $[PdCl_4]^{2-}$ (~ 2825.0 eV) corresponds to the transition of an electron from the core Cl 1*s* towards the 4*p* orbital *via* four terminal Cl ligands to the Pd^{2+} centre.[64,65] However, Cl 4*p* orbitals are only involved in a limited capacity. Any slight changes to the rising energy position therefore indicates a change in the energy of the Cl 1*s* orbital, correlating to the Z_{eff} (Cl), which has been associated with bridged bonding Cl species.[40,39]

All prepared Pd/TiO_2 catalysts display slight shoulders on the absorption edge at similar energies to the pre-edge feature in the $[PdCl_4]^{2-}$ complex. The presence of this feature suggests either: (1) a small quantity of the unreduced precursor remains in the sample, or (2) Cl is present as Cl^- ions on the catalyst surface. The former has been discounted due to UV-Vis measurements acquired during colloid formation (*Figure 4-2*). The latter theory has been previously reported by Thompson *et al.*, wherein Cl K-edge XANES were acquired for $RhCl_3$ as a function of [Cl].[36] In their study, they found that dilution of the precursor complex using water resulted in ligand exchange of the Cl with H_2O, leading to the production of

solvated Cl^- ions. However, in the presence of Cl^-, mixing of the Cl and Rh orbitals does not occur. Instead, a post-edge feature appears in the XANES at ~ 2825.0 eV, representative of the solvated Cl^- ions.

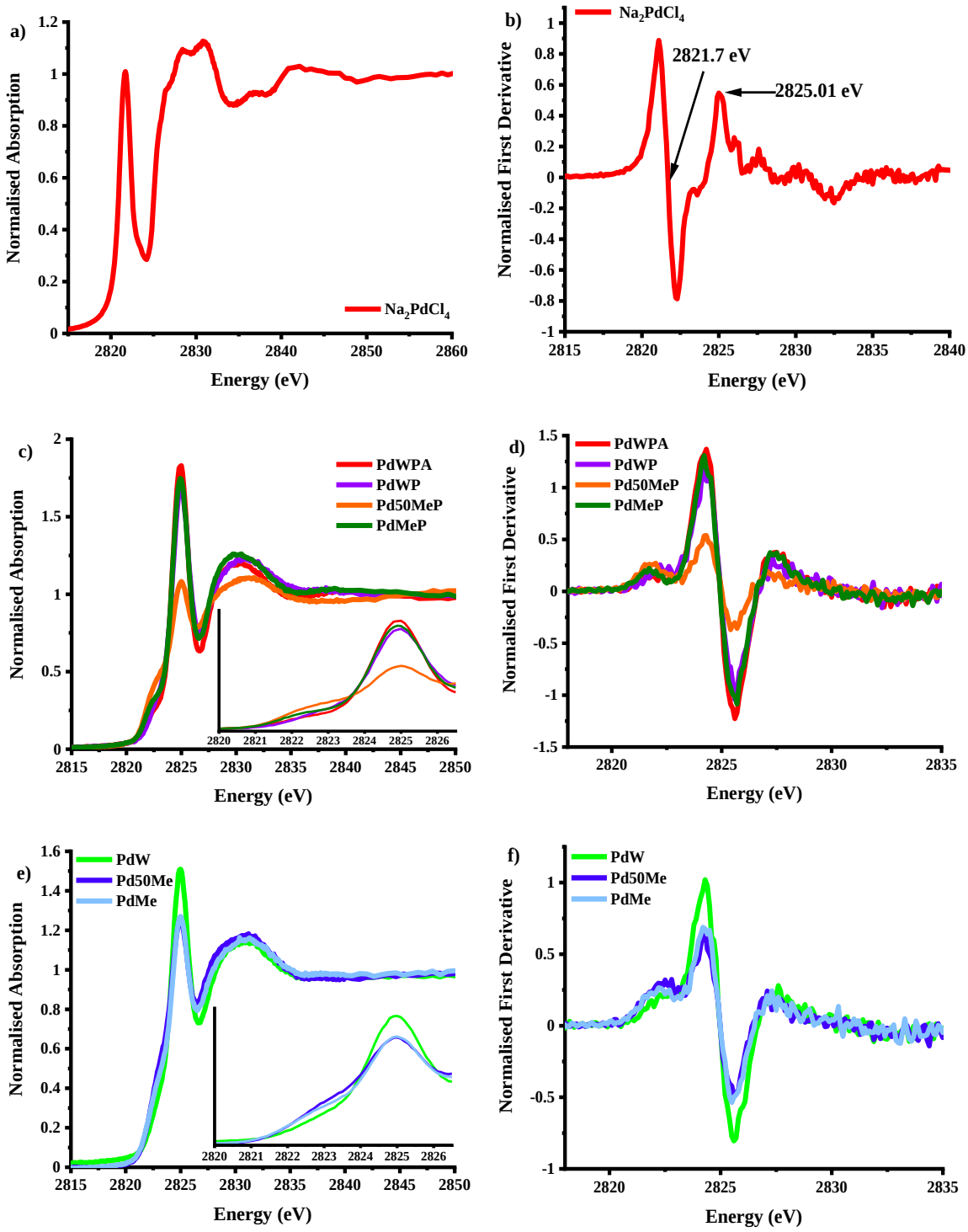

Figure 4-9. *Normalised Cl K-edge (a, c, & e) and 1st derivative XANES (b, d, & f) data for the Na_2PdCl_4 precursor salt (a & b) and the sol-immobilisation prepared Pd/TiO_2 catalysts (c-f). Cl K-edge measurements were performed on the BM28 beamline at the ESRF, Grenoble, France.*

For the investigated $RhCl_3$ samples, this feature increased as the reaction progressed, reflecting the growing predominance of solvated Cl^- on the catalyst surface.[36] Therefore, even after catalyst washing, remnants of the precursor salt can be detected on the catalyst surface that could detrimentally act as a source for Cl poisoning.[2,66]

4.3.1.6.2 S K-edge X-ray Absorption Near-Edge Structure

The necessity of acidification during the immobilisation of Pd NPs prepared in water only solvent systems has already been discussed; however, the consequence of introducing sulfur species onto the catalyst surface must be considered as it is a known poison for many reactions and processes involving Pd based catalysts.[67–69] In an effort to reduce the residual S content present on the catalyst, the catalysts were washed with copious amounts of H_2O during filtration. S K-edge XANES is utilised to assess the extent and speciation of S residing on the catalysts, probing the S $1s \rightarrow 3p$ transition, which is reported to be very sensitive to the oxidation state of the absorbing S.[41,61] Due to the low signal of the non-acidified samples compared to the acidified PdWPA, normalisation of the XANES could not be achieved. The data are instead presented as the intensity of the absorption as a function of energy ($\mu(E)$) (*Figure 4-10*).

Interestingly, even without its addition, sulfur was observed on all catalysts; however, the intensity of the S fluorescence signal was significantly higher for PdWPA. The oxidation state and the geometry of the XANES spectrum for PdWPA shows a distinct white line peak at 2482.0 eV, which is identified as S^{6+} (e.g. SO_4^{2-}).[41,42] A low intensity peak is observed for all samples at ~ 2472.0 eV and could be representative of either S^0, sulfide formation or Pd-S interactions. Unfortunately, there is limited S K-edge XANES literature available for these systems and the negligible energy shifts of this feature makes accurate assignment difficult.[41,70–73] That being said, from this data, it is demonstrated that a MeOH optimised synthetic protocol is able to significantly reduce the residual S present on supported Pd NP catalysts.

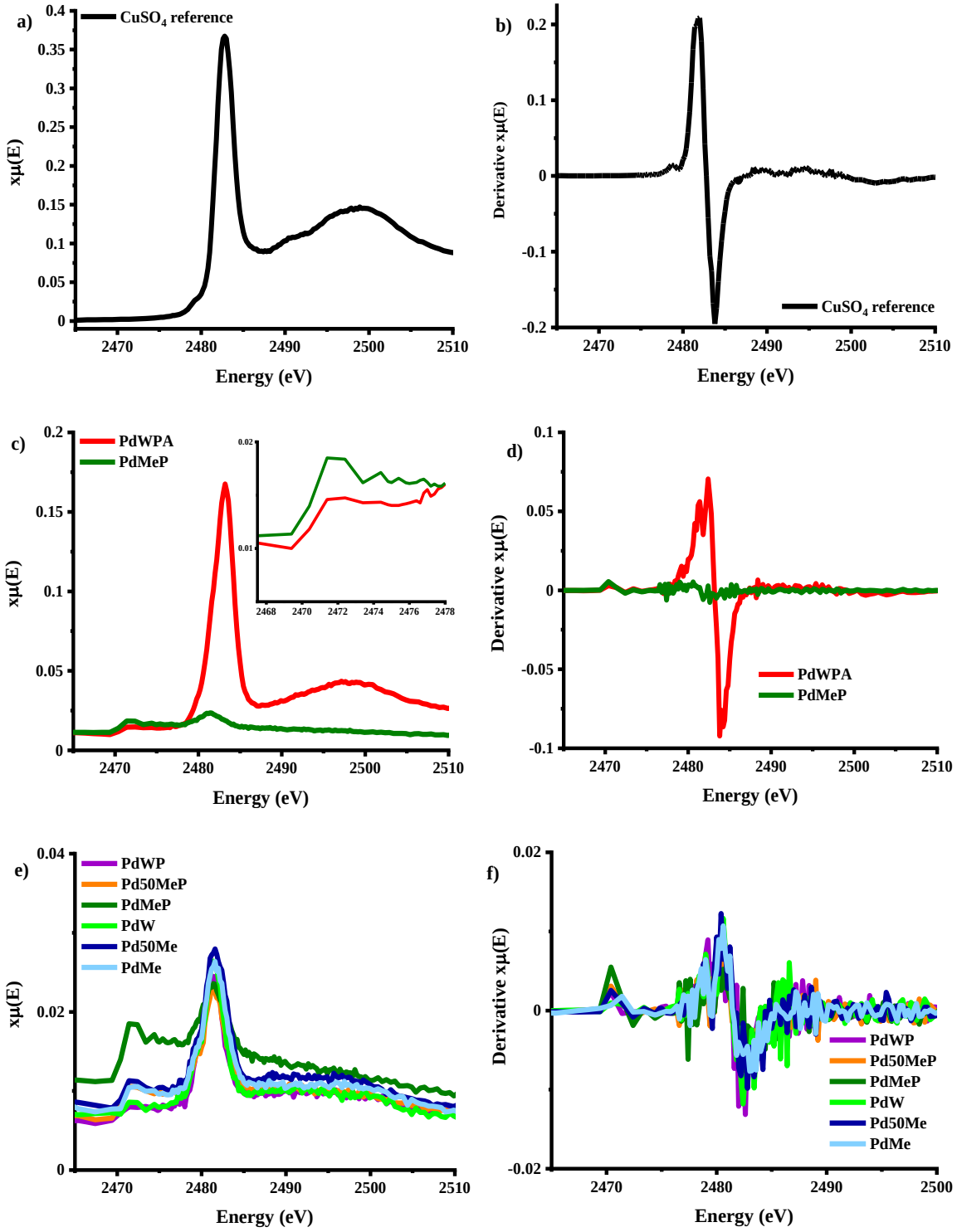

Figure 4-10. *S K-edge XANES data presented as the absorption profile μ(E) and as the 1st derivative μ(E) for the $CuSO_4$ reference (a & b) and the sol-immobilisation prepared Pd/TiO_2 catalysts (c & d) compare the acidified PdWPA and non-acidified PdMeP, and e) & f) show the remaining non-acidified catalysts prepared in this work. S K-edge measurements were performed on the BM28 beamline at the ESRF, Grenoble, France.*

4.3.1.7 Infrared CO Chemisorption Studies

CO adsorption on the supported Pd NPs was performed to characterise the Pd surface sites. Variations to the NP surface, that arise as a consequence of parameters used during synthesis, are identified through comparisons of this work to the literature.[27,34,74–76] The adsorption band present at ~ 2086 cm^{-1} is assigned to CO linearly adsorbed on corner sites of Pd NPs.[77] Pd nanoparticle edge sites are characterised through the linear CO band at 2063 cm^{-1}. IR bands at ~ 1975 and 1945 cm^{-1} indicate bridge-bonding of CO to the Pd NP surface (*Figure 4-11*).

Blue-shifting of the observed peak maximum for PdWPA, is attributed to dipole-dipole coupling of adsorbed CO as the surface coverage increases (*Figure 4-11*a).[78–80] The remaining adsorption bands visible at 2140, 2120 and 1875 cm^{-1} describe the adsorption of CO on Pd^{2+}, Pd^{+} and 3-fold surface sites, respectively.[81,82] As seen in Chapter 3, the nature of the synthesis solvent and its interactions with PVA influence the relative amounts of available Pd surface sites.[27] Here, however, the use of MeOH without PVA primarily leads to a much lower CO coverage per gram of catalyst as a consequence of dense agglomeration, as observed *via* TEM (*Figure 4-11*b). On the inclusion of PVA, the stabilising effect caused by the polymer increases the total number of surface adsorption sites.[27,32,53]

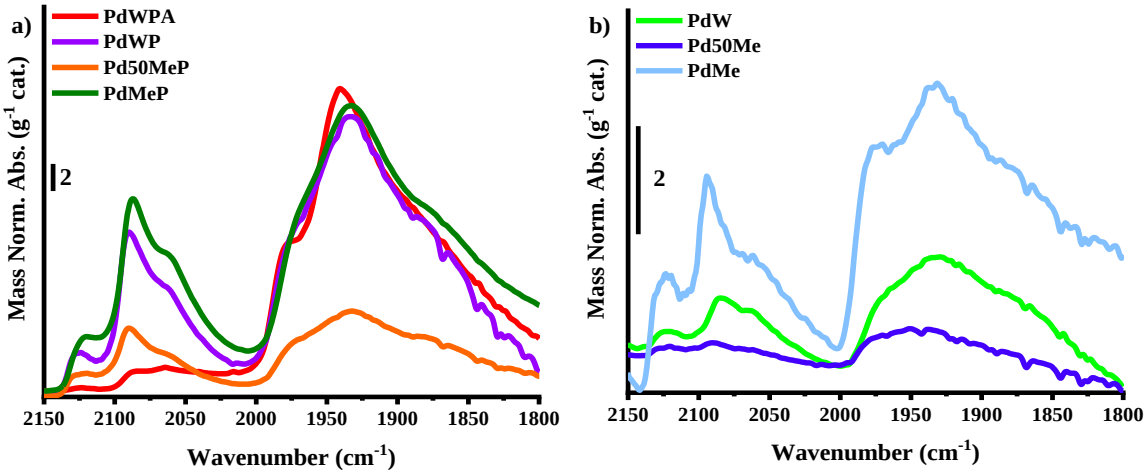

Figure 4-11. *FTIR spectra of CO-adsorption studies performed on Pd/TiO_2 catalysts prepared at 1°C under varied solvent environments; where a) displays the PVA-capped catalysts, and b) displays the catalysts prepared without PVA. The samples were prepared in solutions of H_2O, 50 vol. % MeOH:H_2O, and 100 vol. % MeOH. PdWPA was the only sample to have the acidification step performed during synthesis.*

4.3.2 Hydrogenation of Furfural

All catalysts were evaluated for the hydrogenation of furfural at 50 °C (*Scheme 4-2*, *Figure 4-12*, *Table 8-1*, and *Table 8-2*). Unidentified products were interrogated using GC-MS (*Figure 2-19*). The reaction conditions were optimised to ensure operation under kinetic regime.[27] The XANES, EXAFS and TEM data all confirm that PdMeP contains the smallest NPs; thus, if activity is dependent on size, it would be expected to be the most active. However, the initial catalytic activity confirms that PdWPA has a significant increase in initial TOF (PdWPA = 288 mol (mol Pd^{-1}) hr^{-1} *vs.* PdMeP = 195 mol (mol Pd^{-1}) hr^{-1}) (*Figure 4-12*a-b and *Table 4-5*). Considering that PdMeP is known to contain smaller particles, why is there such a pronounced change in performance? On closer inspection, although the absolute conversion suggests a stark change in performance, analysis of the product distribution goes some way to mitigating this. The initial yield (% conversion) of products derived from hydrogenation processes (i.e. furfuryl alcohol (FA), tetrahydrofurfuryl alcohol (THFA), tetrahydrofurfuryl methyl ether (THF-ME), isopropyl furfuryl ether (FIE) and isopropyl tetrahydrofurfuryl ether (THFIE)) for PdWPA and PdMeP are 11 % and 8 %, respectively. There is still an observable difference between these two values, but it is not as significant as the TOF implies. The other products produced from PdWPA are acetals that arise from the direct reaction of furfural with IPA, and are known to form selectively over TiO_2 surfaces.[6,83,84] It should be noted that the formation of THFA and FA has not been shown to occur on interaction of furfural with IPA under the reaction conditions chosen without the presence of a catalyst. Although the ratio of THFA:FA changes with respect to the catalyst preparation route, the consumption of FA in the generation of the acid catalysed product must be considered. It is clear that NP size, whilst important, does not always play the most significant role in increasing catalytic activity. Instead, the availability of free surface sites on both the supported Pd nanoparticle and the metal oxide support is paramount in determining catalytic activity and selectivity.[9,27] Furfural hydrogenation performed over the bare TiO_2 support displays 99 % selectivity to the acetal product (2-(diisopropoxymethyl) furan); at isoconversion, PdWPA is 19 % selective for acetal formation (

Table 4-6).

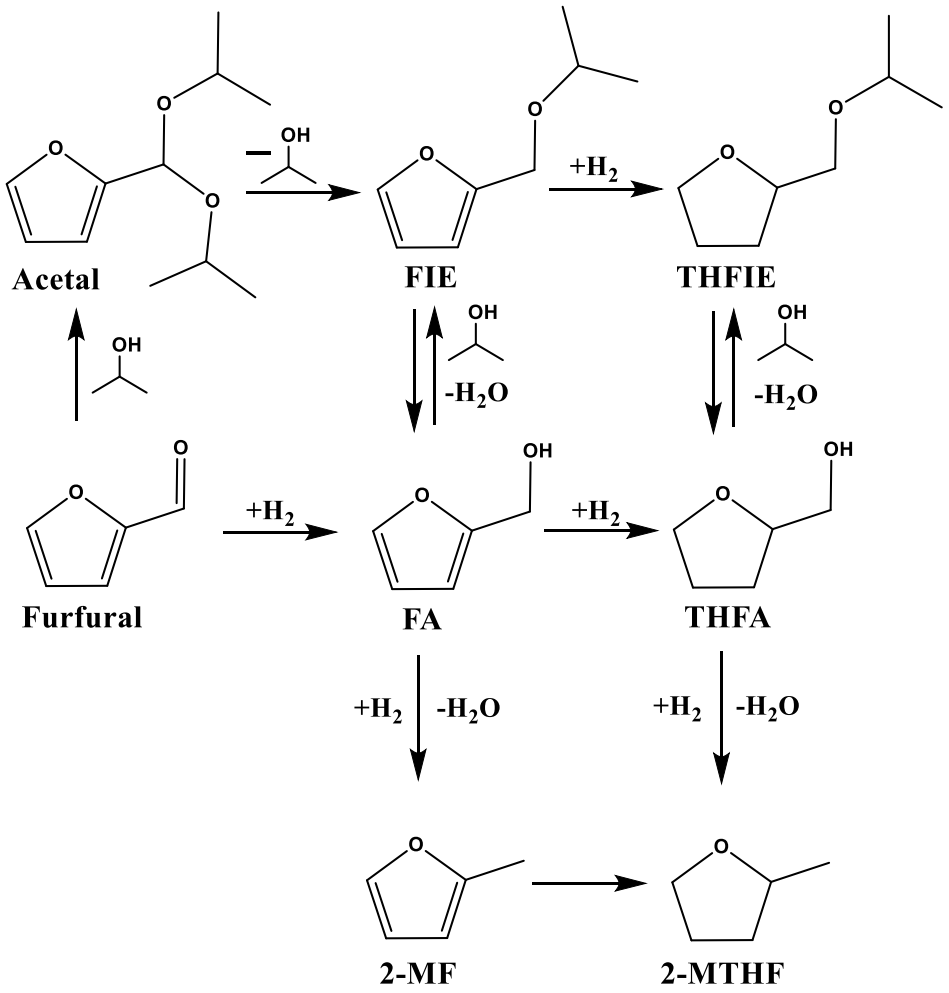

Scheme 4-2. *Possible reaction pathways during furfural hydrogenation over prepared Pd/TiO_2 catalysts. Reaction products shown are: furfuryl alcohol (FA), tetrahydrofurfuryl alcohol (THFA), furfuryl isopropyl ether (FIE), tetrahydrofurfuryl isopropyl ether (THFIE), 2-methylfuran (2-MF), 2-tetrahydrofuran (2-MTHF) and (2-(diisopropoxymethyl) furan) (acetal).*

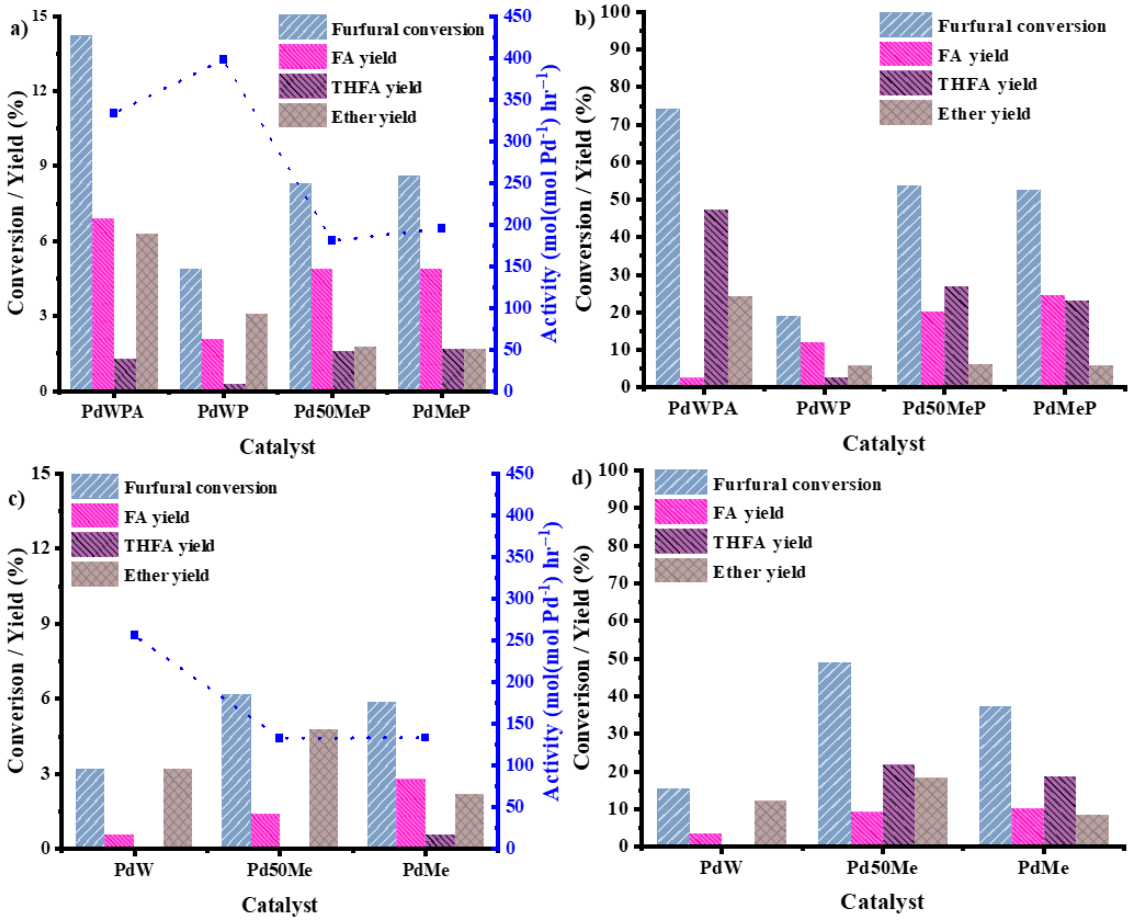

Figure 4-12. *Catalytic performance plots for the hydrogenation of furfural using Pd/TiO_2 catalysts synthesised in varying solvent environments. Conversion and selectivity were calculated after 15 minutes (a & c), and 5 hrs (b & d). Reaction conditions: furfural 0.3 M, furfural:metal ratio 500 mol:mol, 5 bar H_2, solvent: IPA. Catalytic activity (■) calculated after 15 minutes of reaction time are presented in a & c.*

After 5 hrs of reaction time, the picture is very similar; PdWPA results in higher overall conversion, however, the yield of the desired FA and THFA hydrogenation products are very comparable for PdWPA (50 %), Pd50MeP (47 %), and PdMeP (48 %) (*Figure 4-12*c-d). Although PdWPA demonstrates greater absolute conversion, the greater selectivity towards various ether and over hydrogenation products reduces the overall atomic efficiency of the catalyst. The PdWPA catalyst also shows a minor yield of FA, which can be ascribed to FA being consumed in the subsequent production of ethers. The catalysts prepared without PVA have lower absolute conversion of furfural after 5 hrs and a higher yield of the acid catalysed products. This is because the conversion to acetals requires accessibility to the Brønsted acid sites on the TiO_2 surface.[85,86] Campisi *et al*. published an article on Pd/NiO catalysts and were able to demonstrate a dual-site hydrogenation mechanism, where spillover of hydrogen onto the NiO support played a significant part in the acetal mechanism.[87]

The rationale of hydrogen spillover aiding the generation of Brønsted acid sites on TiO_2, and their role in the production of ethers, is not without precedent. It is well documented that TiO_2 (both anatase and rutile phases) contains Brønsted acid hydroxyl groups.[88–91] It has also been established that the availability of these acid sites can be enhanced through hydrogen spillover.[92] Furthermore, the role of dual-site catalytic mechanisms of Pd/TiO_2 facilitated by hydrogen spillover from Pd to TiO_2 has previously been discussed.[93] Surfaces of TiO_2 also contain catalytically active Lewis acid sites;[94] however, recent studies have shown that without the presence of Brønsted acid functionalities, furfural cannot be readily converted to furnanic ethers.[95] Recently, it has been proposed that Pd-X interactions allow for heterolytic H-H cleavage which gives rise to Brønsted acidity.[96] Cl K-edge XANES presented earlier in this work suggest that all catalysts prepared have similar quantities of surface Cl (*Figure 4-9*). Therefore, if interactions between the residual Cl and Pd had produced Brønsted acid sites, PdWPA and PdMeP would both have similar selectivity to the acetal, however, this is not the case.

Table 4-5. *Catalytic activity of catalysts used during the hydrogenation of furfural at 50 °C. Catalytic activity was calculated after 15 minutes of reaction time. MP-AES calculated Pd wt. % loadings are also shown for each sample.*

Catalyst	**Activity (mol(mol Pd^{-1}) hr^{-1})**	**[Pd] (wt. %)**
PdWPA	288.4	0.83
PdWP	397.5	0.25
Pd50MeP	287.5	0.91
PdMeP	194.9	0.86
PdW	256.0	0.30
Pd50Me	133.0	0.91
PdMe	133.3	0.96

Table 4-6. *Conversion and selectivity of prepared Pd/TiO_2 catalysts and fresh TiO_2 for the hydrogenation of furfural. Selectivities were calculated at 25 % conversion unless otherwise stated. Conditions: 50 °C, 5 bar H_2. Furfural 0.3 M; furfural:metal ratio (500 mol:mol), solvent IPA.*

Sample	Furfural Conversion (%)	Selectivity (%)								Mass Balance (%)
		FA	THFA	Acetal	THF-ME	THFIE	FIE	2-MF	2-MTHF	
PdWPA	74	45	13	19	1	17	5	0	0	99
Pd50MeP	54	54	30	10	0	7	0	0	0	100
PdMeP	53	60	25	0	0	4	10	0	0	100
Pd50Me	49	35	29	22	1	13	1	0	0	100
PdMe	37	48	15	28	0	10	0	0	0	100
PdWP[§]	19	56	12	29	0	2	0	0	0	100
PdW[§]	15	20	0	0	0	0	79	0	0	99
TiO_2[†] (P25)	25	2	0	98	0	0	0	0	0	100

[§] Selectivity calculated at 12.5 % conversion of furfural. [†] TiO_2 data are presented after 5 hrs of reaction time. Furfural conversion and mass balance are given after 5 hrs of reaction time.

4.3.3 High Resolution Transmission Electron Microscopy

The next step in understanding why PdMeP has lower activity than PdWPA, was to acquire images of the catalyst surface to identify any potential compounds covering the NP and/or the support surfaces. High resolution TEM was used to image the PdMeP catalyst *(Figure 4-13*a-c). Thick amorphous layering of an organic species surrounding the support surface and the NPs is clearly visible, particularly in *Figure 4-13*c, where the layer surrounds an unsupported Pd NP and the TiO_2 support adjacent to the NP.[32,97,98] The absence of PVA during the MeOH based synthesis is shown in *Figure 4-13d,* where the amorphous layer

present for *Figure* ***4-13***a-c is not present. The source of this amorphous organic layer at present is believed to be clumping of PVA due to its poor solubility in MeOH at room temperature, causing it to aggregate on the catalyst and support surfaces.

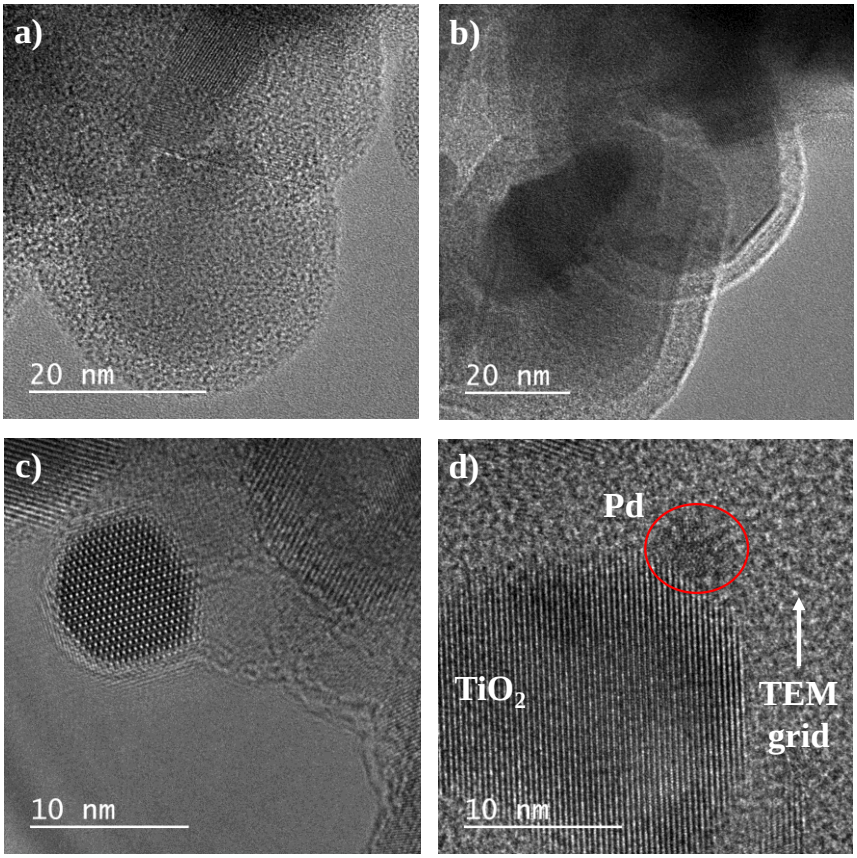

Figure 4-13. *HRTEM images of (a-c) fresh PdMeP and (d) PdMe. Layering of the organic PVA can be seen surrounding both the TiO_2 support (a & b) as well as the Pd NPs (c).*

4.3.4 Ammonia-Temperature Programmed Desorption

The influence of the colloidal solvent on the accessibility of TiO_2 Brønsted acid sites was investigated using a combination of diffuse reflectance infrared Fourier transform spectroscopy and mass spectrometry, monitoring both the adsorption and desorption of NH_3 as a function of increasing temperature (100-450 °C). In order to determine the sites generated following reduction during furfural hydrogenation, the PdWPA and PdMeP catalysts were subjected to a TPD treatment without first cleaning the catalyst surface at high temperature. In addition, the two samples were measured with and without a H_2 pretreatment. It should be noted that the NH_3-TPD data showed the decomposition of PVA on all catalysts beginning at ~ 250 °C, therefore data above this temperature was not included in the plotted DRIFTS spectra. For the fresh TiO_2 support, one would expect NH_3

adsorption bands at ~ 1460 and 1689 cm^{-1} (NH_4^+ coordinated to Brønsted acid sites and marked by *, *Figure 4-14*).[99–102]

As a consequence of the carbonyl bands of PVA, which appear in the region of interest (1700-1300 cm^{-1}), the bands of NH_3 adsorption on Brønsted acid could not be distinguished.[99,101] Pyridine adsorption would also result in bands in this area of the spectrum and so this was not pursued further.[103,104] Inspection of the NH_3 TPD MS data is also a hard task, with the low signal/noise preventing the weak and medium NH_3 desorption sites from being elucidated, ~ 150 °C and ~ 400 °C, respectively (*Figure 4-15*a-e). Interestingly, the mass spec signal of PdWPA and PdMeP prepared with a pre-treatment of flowing $H_{2(g)}$ displayed quite different uptake and release of H_2 before stabilisation of the gas feed was achieved (*Figure 4-16*).

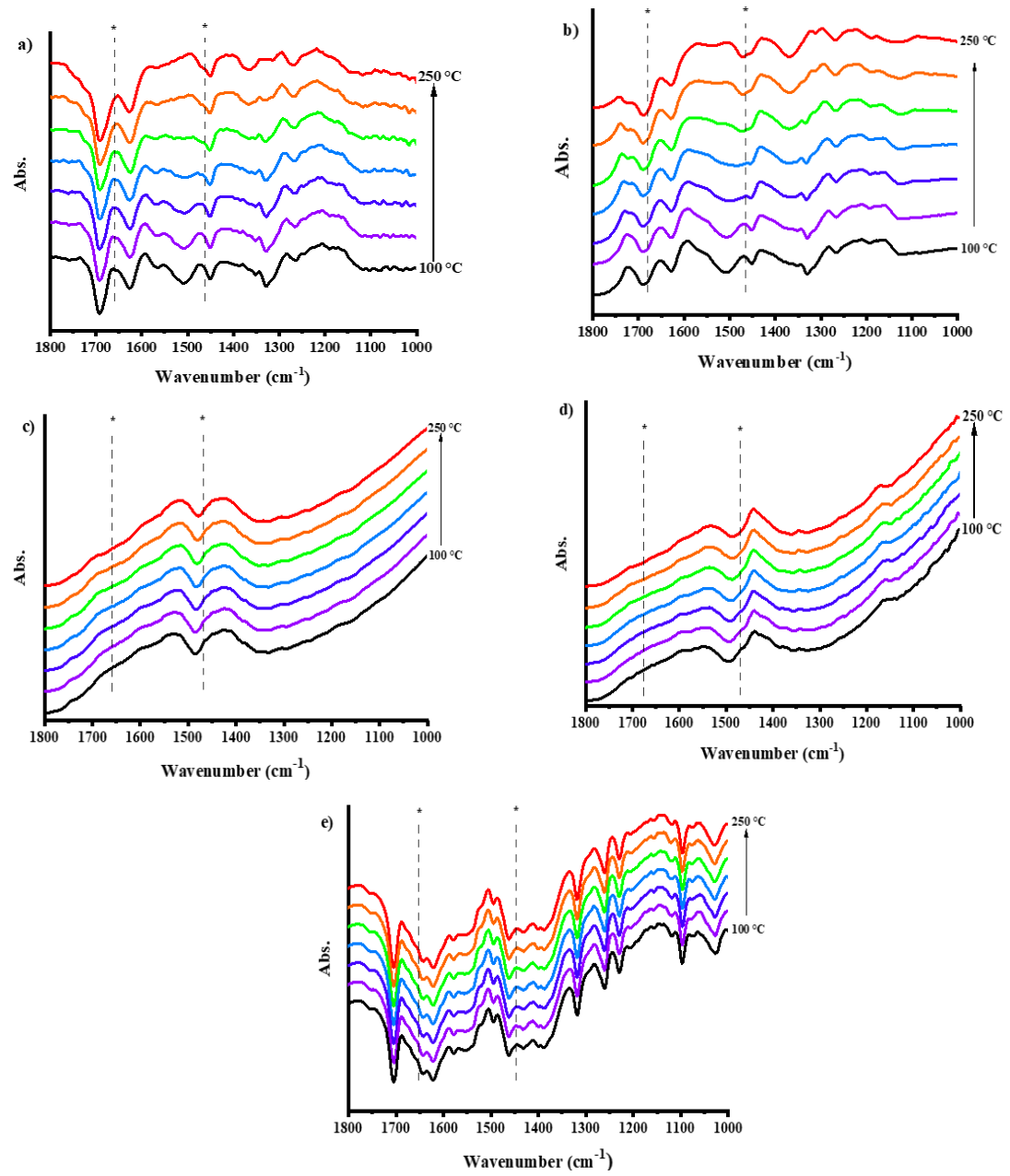

Figure 4-14. *DRIFTS NH_3 adsorption data for prepared 1 wt. % Pd/TiO_2 catalysts and TiO_2 (P25): where a) PdWPA, c) PdMeP and e) TiO_2 (P25) were subject to a thermal pre-treatment at 150 °C for 1 hr in flowing He, and b) H_2-PdWPA and d) H_2-PdMeP were subjected to the same heat treatment under flowing H_2. NH_4^+ Brønsted acid sites are signified by *.*

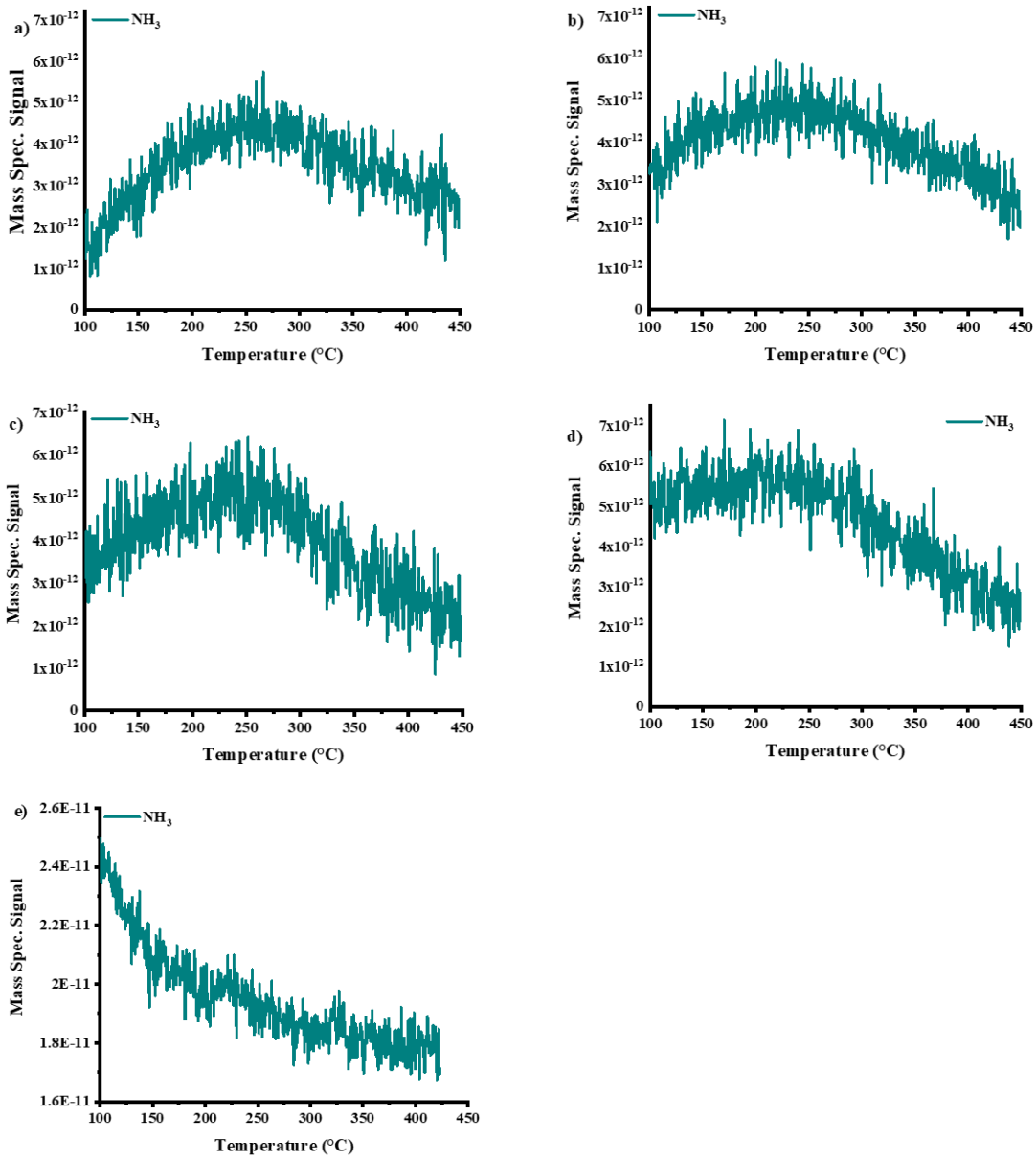

Figure 4-15. *Mass spectrometry signals for NH_3 adsorption and desorption over prepared 1 wt. % Pd/TiO_2 catalysts: where a) PdWPA, c) PdMeP and e) TiO_2 (P25) were subject to a thermal pre-treatment at 150 °C for 1 hr in flowing He, and b) H_2-PdWPA and d) H_2-PdMeP were subjected to the same heat treatment under flowing H_2.*

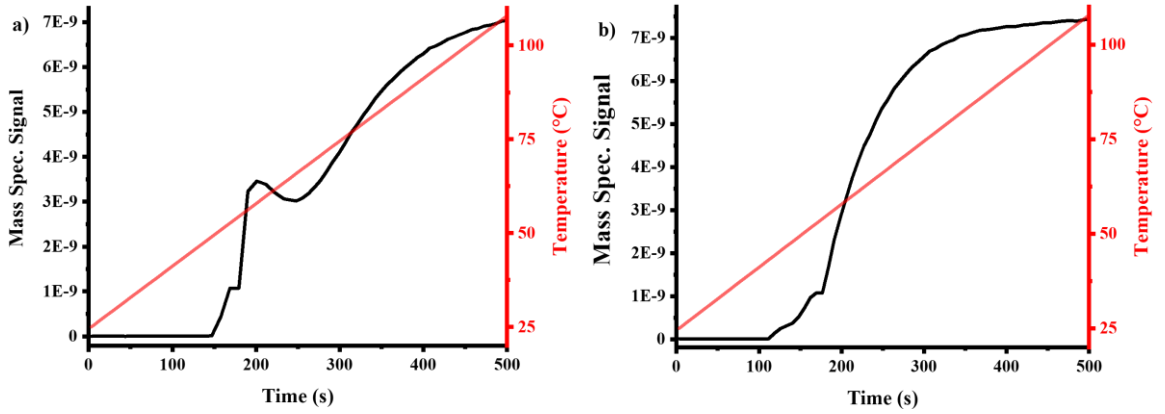

Figure 4-16. *Mass spectrometry H_2 signal obtained during reduction of the Pd catalysts prior to NH_3 TPD measurements: a) PdWPA and b) PdMeP.*

4.3.5 Hydrogen-Temperature Programmed Reduction

To understand the influence the colloidal solvent has on the accessibility of TiO_2 Brønsted acid sites, hydrogen-temperature programmed reduction was utilised to measure the uptake of H_2 for the PdWPA and PdMeP catalysts (*Figure 4-17*). H_2-TPR data for both catalysts exhibit three features below 350 °C: (I) a negative peak between 50-75 °C, which is assigned to the decomposition of Pd hydride,[105–109] (II) an additional negative peak between 100-150 °C that is indicative of dehydration,[110] and (III) a positive feature between 200-350 °C that is reported to be the reduction of Ti^{4+} to Ti^{3+} in the vicinity of Pd, i.e., hydrogen spillover from Pd to the support.[111–113] Typically, in the absence of hydrogen spillover, reduction of Ti^{4+} to Ti^{3+} is found to occur at temperatures > 600 °C.[111] Comparing the TPR traces for PdWPA and PdMeP, it is clear that the amount of hydrogen adsorbed through H_2 spillover is far greater for PdWPA (1.64 µL g^{-1} Pd) than for PdMeP (0.10 µL g^{-1} Pd). This observation is consistent with the hypothesis of a dual-site mechanism forming the acid catalysed products, which are produced most significantly for the PdWPA system.

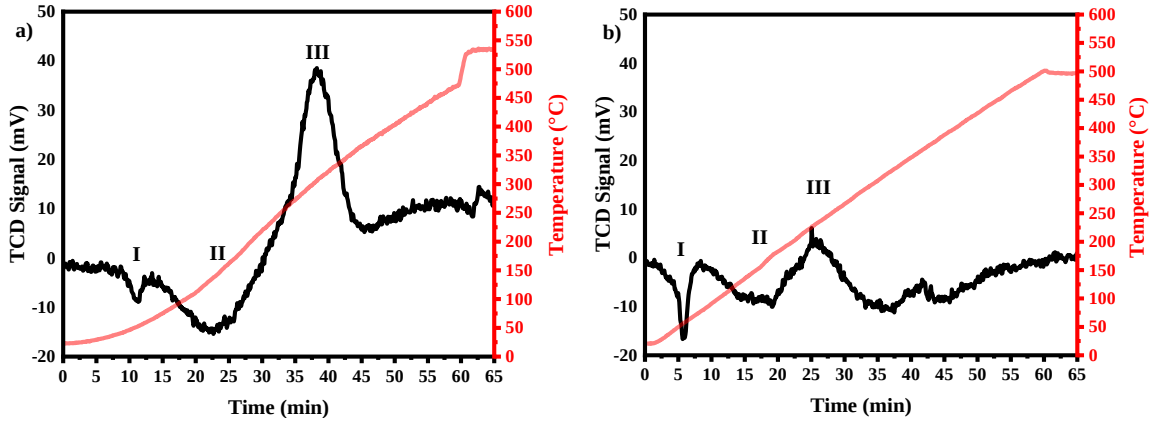

Figure 4-17. *TPR profiles generated for a) PdWPA and b) PdMeP, H_2 consumption and production events are indicated on the images by I, II or III: where I shows the decomposition of the Pd hydride phase, II is dehydration of the sample and III illustrates spillover of hydrogen onto the TiO_2 support.*

4.3.6 Thermogravimetric Analysis

Thermogravimetric analysis was used to measure the extent of decomposition and carbonisation of any bound organics to the fresh Pd/TiO_2 catalyst surfaces (*Figure 4-18*a-c). For reference, both the blank support TiO_2 and PVA (M_w = 9000-10,000 g mol^{-1} 80 % hydrolysed) were also assessed (*Figure 4-18*d-e). Removal of water from the catalyst and reference compounds occurred within similar ranges, 100-340 °C, and corresponds to the origin of the trapped water, i.e. in the polymer. Loss of absorbed water is responsible for the decrease in weight between 100-120 °C observed for TiO_2 (*Figure 4-18*d) **I**) and between 50-200 °C in PVA (*Figure 4-18*e) **III**).[114–116]

Furthermore, TiO_2 displays a secondary weight loss between 120-250 °C which is attributed to the dehydroxylation of adsorbed water and –OH functionalities (*Figure 4-18*d) **II**).[115,117] PVA displays a large weight loss between 200-340 °C that is resultant of water bound to the polymer matrix being removed (*Figure 4-18*e) **IV**).[118] PdWPA, PdMeP and PdMe all showed comparable weight loss over this range, suggesting that the catalysts have similar quantities of trapped water. Weight loss is observed for both PdWPA and PdMeP between 340-450 °C, and corresponds to two individual decomposition processes: (1) decomposition of the side chain occurring at ~ 350 °C, and (2) decomposition of the main chain occurring above 420 °C (*Figure 4-18*e).[116] Comparing the region of PVA decomposition for both PdWPA and PdMeP suggests a greater presence of PVA on the MeOH prepared catalyst surface (PdWPA = 0.005 %/°C and PdMeP = 0.011 %/°C). Greater loading of PVA on the MeOH catalyst after synthesis is in agreement with the data found *via* HRTEM and,

importantly, its clustering surrounding both Pd NPs and the support surface suppress H_2 spillover during hydrogenation. This prevents acid catalysation over the Brønsted acid sites of TiO_2.[92]

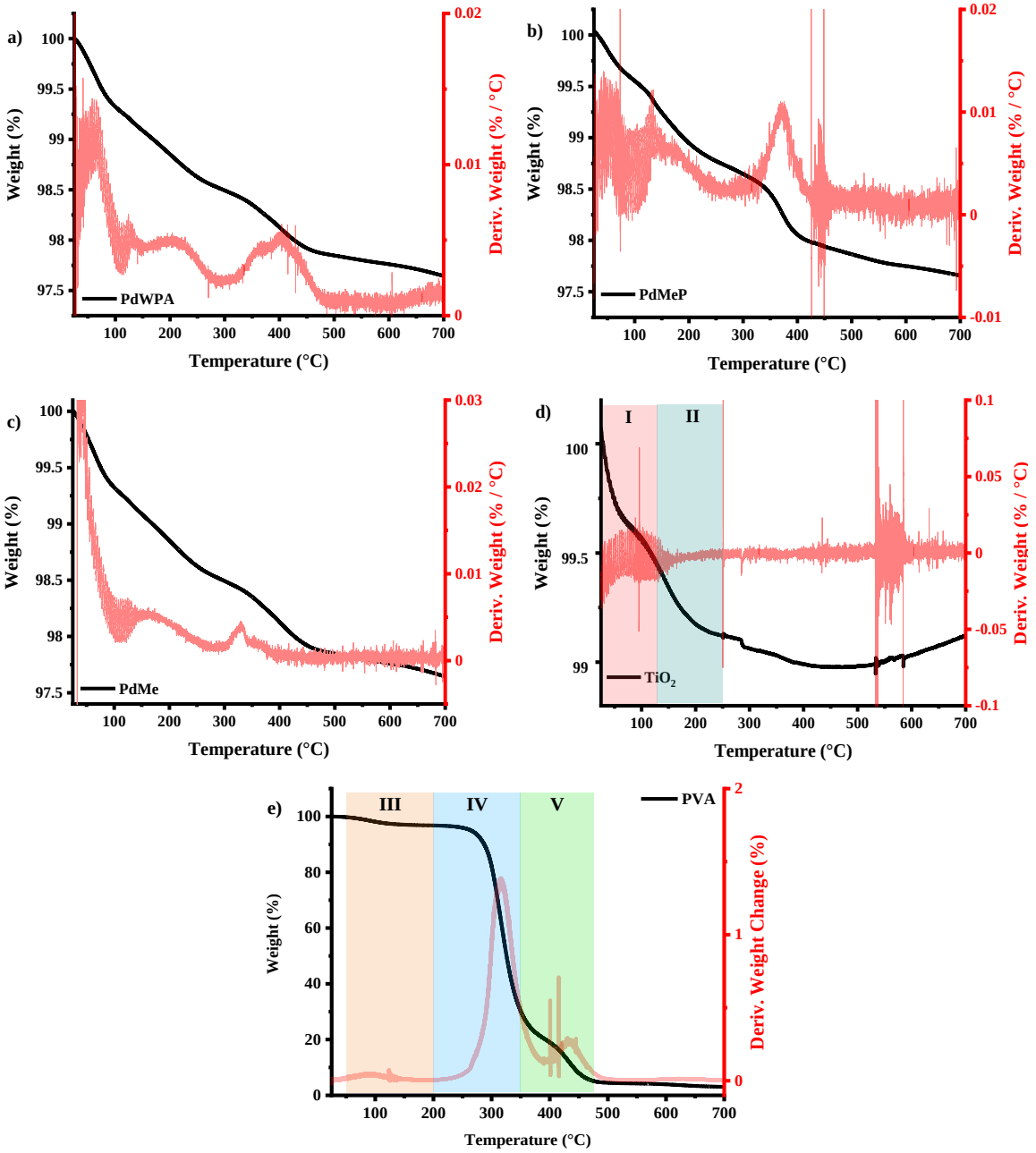

Figure 4-18. *Thermogravimetric analysis of the prepared 1 wt. % Pd/TiO_2 catalysts: a) PdWPA, b) PdMeP and c) PdMe, as well as the reference materials, d) TiO_2 (P25) and e) PVA. Measurements were performed from 25-700 °C in flowing air: I is the loss of absorbed water in TiO_2, II is the dehydroxylation of adsorbed H_2O & -OH functionalities, III is the loss of absorbed water from PVA, and IV is the removal of water bound to the polymer complex.*

4.3.7 Reusability testing

It is important to evaluate the stability of the synthesised catalysts to establish its lifecycle; therefore, catalyst-recycling reactions were performed using PdWPA, PdMeP and PdMe over six successive hydrogenation cycles (*Figure 4-19*, *Table 8-3*, *Table 8-4* and *Table 8-5*). The catalysts prepared without PVA, i.e. PdMe, quickly deactivated with almost negligible performance by the sixth successive cycle.

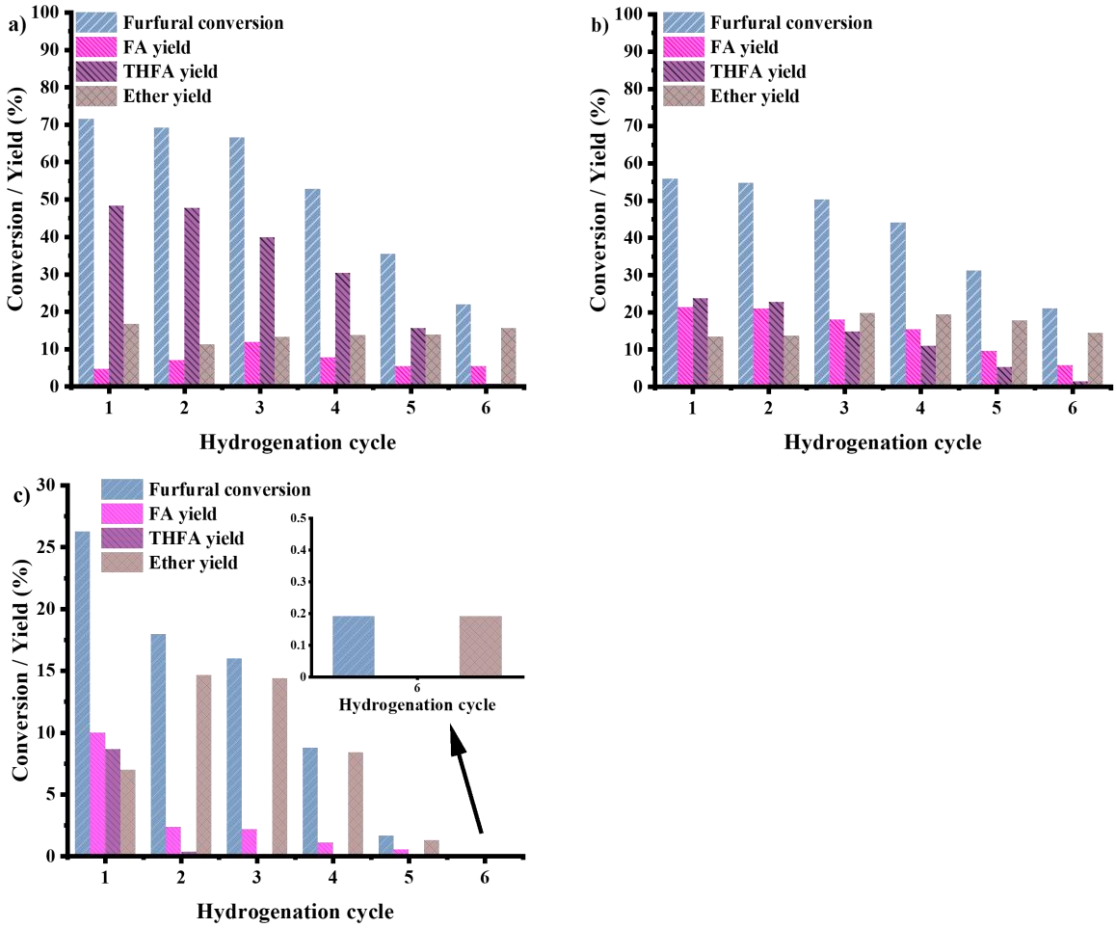

Figure 4-19. *Catalytic performance plots for the hydrogenation of furfural over prepared Pd/TiO_2 catalysts. All catalysts were tested in six successive hydrogenation cycles, where they were recovered from the previous test, dried and reused. Substrate conversion and product selectivities were calculated after 3 hrs for each catalyst: a) PdWPA, b) PdMeP and c) PdMe. Reaction conditions: 50 °C, furfural 0.3 M; furfural:metal ratio 500 mol:mol, 5 bar H_2, solvent: IPA.*

Both PdWPA and PdMeP are shown to lose activity to varying extents over the six cycles. From this there are two key observations: (1) they both exhibit comparable activity and selectivity profiles after 6 successive cycles, and (2) the production of THFA drops to a negligible amount during the recyclability tests (PdWPA = 1 % yield, and PdMeP = 2 %

yield). What causes this change in performance over successive cycles? The consistent selectivity profile for both PdMeP and PdWPA, where both produce a majority of acid catalysed product. This is concurrent with the progressive removal of PVA (PdWPA = 1 % acetal yield, and PdMeP = 1 % acetal yield). The disappearance of THFA in the product distribution can be attributed to the Pd NPs becoming carbidised which is, in part, responsible for a loss in overall catalytic activity.[27]

4.3.8 Characterisation of Recycled Catalysts

To assess the structural changes of these used catalysts in more detail, they were studied using STEM-HAADF analysis (*Figure 4-20*) and XAFS spectroscopy (*Figure 4-23* and *Figure 4-24*).

4.3.8.1 Scanning Transmission Electron Microscopy and Electron Energy Loss Spectroscopy

Particle agglomeration is visible for the recycled catalysts (*Figure 4-20*a-c). The average Pd NP size remained broadly constant for PdWPA, changing from 2.6 ± 1.4 to 2.8 ± 1.0 nm, similar to the NP growth reported by Rogers *et al*.[27] An increase in the average particle size from 1.8 ± 0.8 to 2.3 ± 0.9 nm is observed for PdMeP (*Figure 4-21*). The extent of particle growth was harder to calculate for PdMe as there were only a limited number of large particles (e.g. > 20 nm) detected.

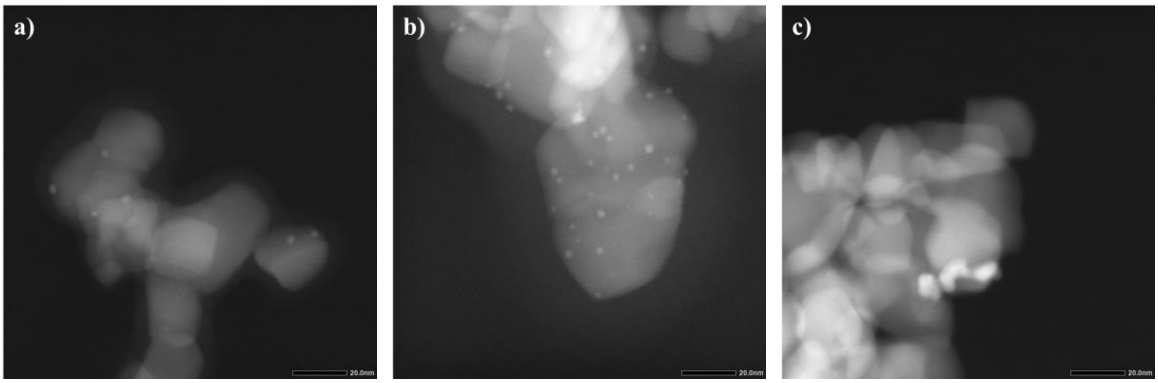

Figure 4-20. *STEM-HAADF images of used 1 wt. % Pd/TiO_2 catalysts after one cycle of furfural hydrogenation: a) PdWPA, b) PdMeP and c) PdMe.*

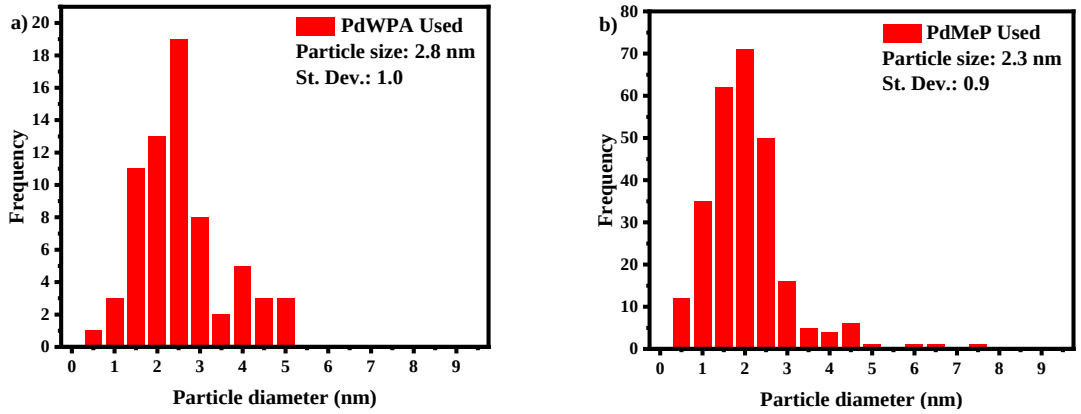

Figure 4-21. *Histograms of Pd nanoparticle sizes calculated from TEM images of a) PdWPA after furfural hydrogenation, sample population was 68 Pd NPs, and b) PdMeP after furfural hydrogenation, sample population was 265 Pd NPs.*

Electron energy loss spectroscopy was used to determine the dispersion of Pd, C and Ti for PdMeP before and after furfural hydrogenation (*Figure 4-22*a-b). The fresh PdMeP catalyst displays a thick layering of carbon surrounding and covering the TiO_2 support surface, which resembles the amorphous PVA layering present in the HRTEM images (*Figure 4-13*). After one cycle of furfural hydrogenation, the quantity of carbon on the catalyst surface is drastically reduced, suggesting PVA is removed during the reaction over PdMeP. This would explain the gradual increase in ether formation after successive hydrogenations observed, i.e. as PVA is removed, H_2 spillover occurs to a greater extent, forming Brønsted acid sites on the support material. The carbon signal acquired on the used PdMeP catalyst, however, does not indicate if carbidisation of Pd has occurred.

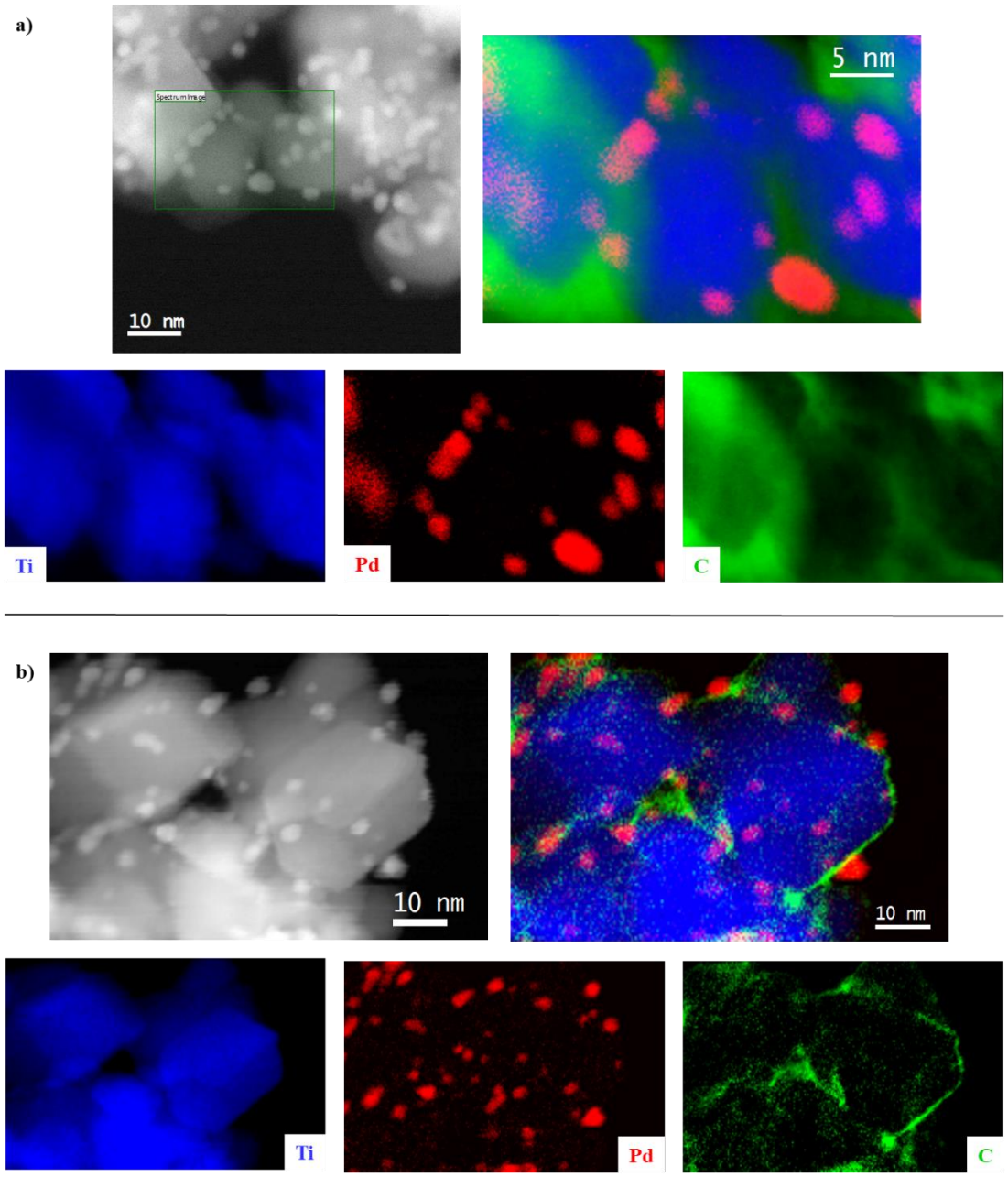

Figure 4-22. *HRTEM images and EELS data acquired for PdMeP a) before and b) after hydrogenation of furfural, with a false colour image of the catalyst and the composite elements measured: Ti = blue, Pd = red and C = green.*

4.3.8.2 X-ray Absorption Fine Structure

XAFS was used to assess the average extent of NP growth and also to elucidate whether either catalyst had formed Pd carbide.[119]

4.3.8.2.1 Pd K-edge X-ray Absorption Near-Edge Structure

XANES acquired for the spent catalysts show a reduction in the appearance of an oxidised Pd state through a decrease to the intensity of the main edge transition (*Figure 4-23*).

Broadening of the white line peak and a shift in the second peak maximum to lower energy is indicative structural change to the Pd lattice. This shift in the post-edge towards lower energy is consistent with lattice expansion and the formation of Pd carbide.[27,119,120]

4.3.8.2.2 Pd K-edge Extended X-ray Absorption Fine-Structure

The corresponding Fourier transforms of the χ-data further confirms the formation of an interstitial carbide phase (*Figure 4-24*). An increase in the Pd NP size post hydrogenation is described by both the FT EXAFS data and its fitting (*Figure 4-25*). Removal of the passivated oxide layer during hydrogenation is confirmed here as the scattering path at ~ 1.7 Å seen in the fresh catalysts is no longer present. Instead, growth in the magnitude of the 1st shell Pd-Pd path is observed for all recycled catalysts (*Table 4-7*). Not only is there an increase in the abundance of Pd-Pd scattering, there is also a shift to the position of this scattering path towards larger radial distance (*R*) is consistent with the formation of Pd carbide.[121] The hydride phase is not stable without an overpressure of hydrogen and the carbide hinders the adsorption of oxygen. The formation of Pd carbide is known to be detrimental to the activity of Pd catalysts in hydrogenation reactions.[69] Considering the extent of THFA production decreases through successive cycles, it is proposed that the reduced efficacy of parallel furfural binding on Pd carbide surfaces is responsible for this change in selectivity.

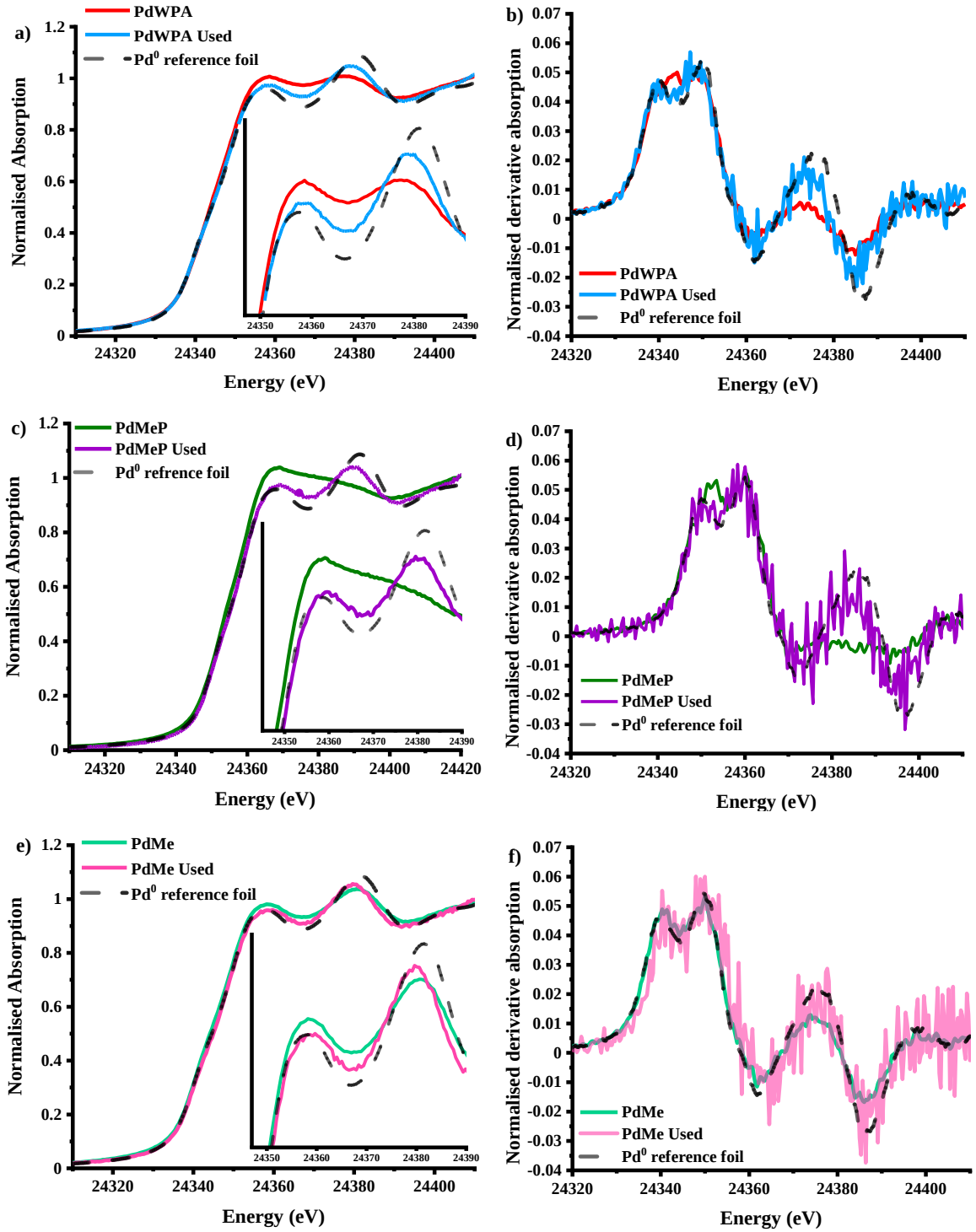

Figure 4-23. *Pd K-edge XANES spectra for the fresh and used Pd/TiO_2 catalysts measured on the B18 beamline at DLS, Didcot, U.K.; used data were acquired after six successive hydrogenation cycles. The normalised absorption energy is shown for each recycled catalyst (a, c & e) and the normalised 1st derivative XANES (b, d & f).*

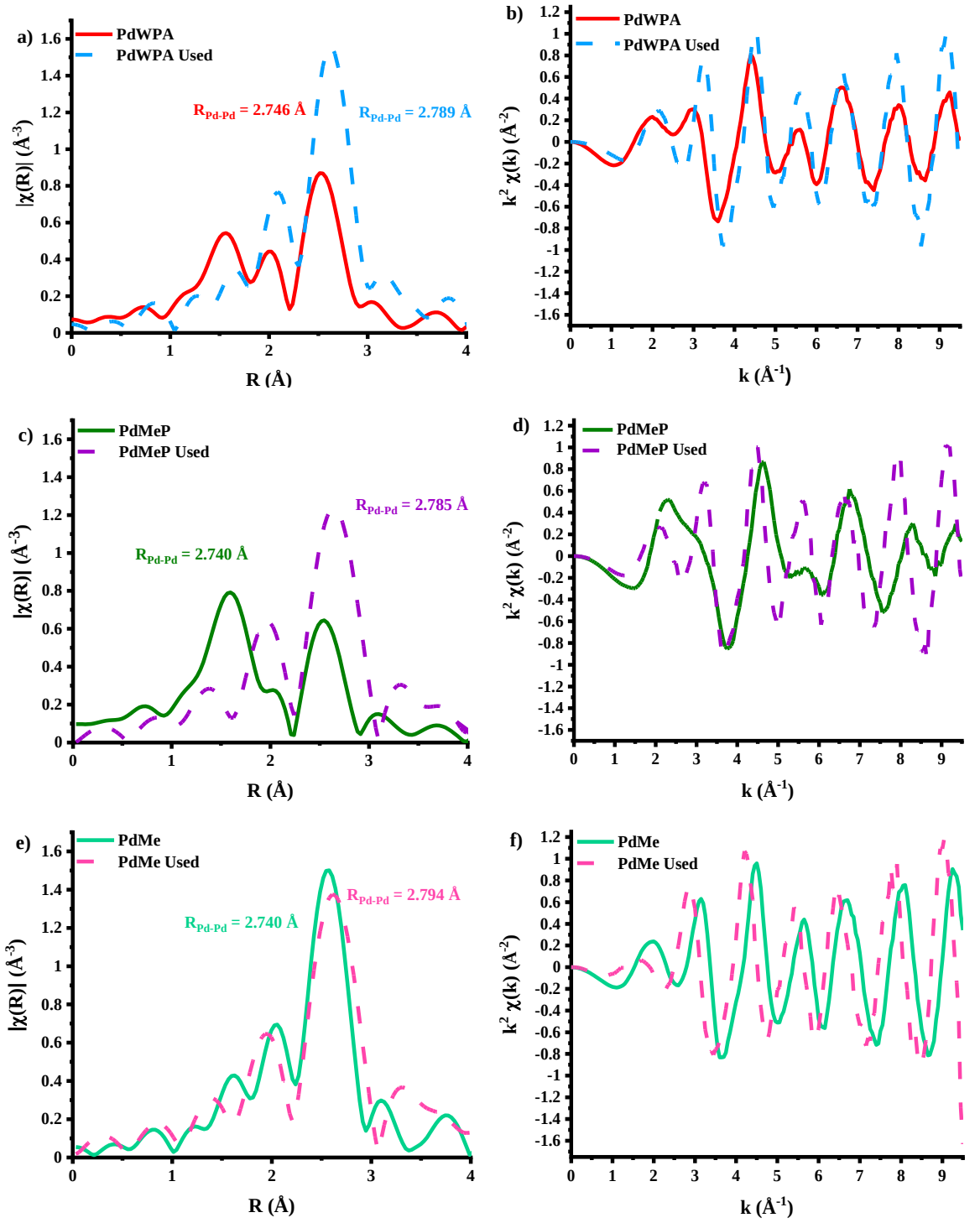

Figure 4-24. *Pd K-edge XAFS spectra for the fresh and used catalysts, used data acquired after six successive hydrogenation cycles. FT EXAFS data are presented for each recycled sample (a, c & e) and the corresponding χ(k) data for each catalyst (b, d & f). Expansion of the Pd lattice is observed for all FT EXAFS datasets. Pd K-edge data were measured on the B18 beamline at DLS, Didcot, U.K.*

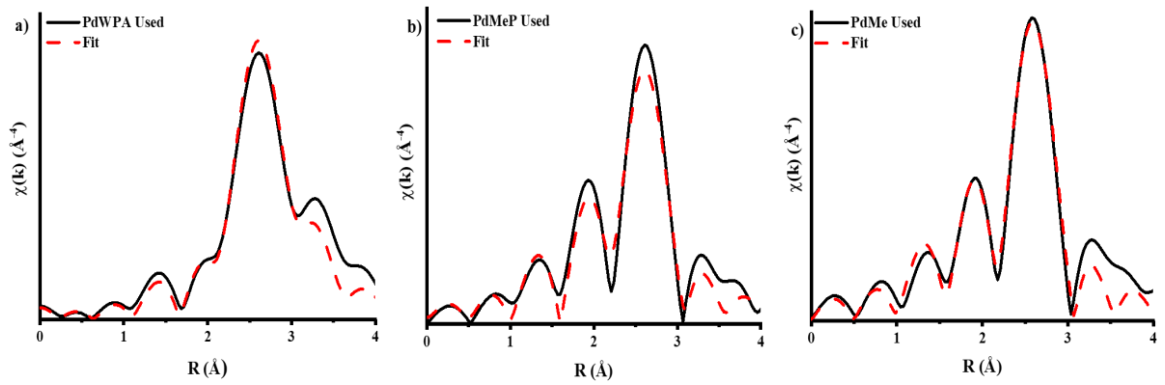

Figure 4-25. *Fitted experimental Fourier transform (FT) χ(k) data, for Pd/TiO₂ catalysts after one cycle of furfural hydrogenation; a) PdWPA, b) PdMeP and c) PdMe.*

Table 4-7. *1st shell EXAFS fitting parameters derived from the k^2 weighted FT of the Pd K-edge data for the Pd/TiO₂ catalysts after six successive hydrogenation cycles. Amplitude reduction factor, (S_0^2) = 0.75, was found by fitting an acquired Pd^0 reference foil. EXAFS fittings range: 3 < k < 9.5, 1 < R < 3.4, number of independent points = 10.5. The accuracy of the fit is described by an R_{factor} value, where the confidence of the fit is represented by the smallest value above zero.*

Catalyst	Abs-Sc	CN	R (Å)	$2\sigma^2$ (Å^{-2})	E_0 (eV)	R_{factor}
PdWPA	Pd-Pd	11.2 ± 0.4	2.79 ± 0.04	0.0092 ± 0.0008	4.0 ± 0.3	0.015
	Pd-O	-	-	-		
PdMeP	Pd-Pd	10.9 ± 0.5	2.79 ± 0.04	0.0091 ± 0.0009	3.2 ± 0.4	0.020
	Pd-O	-	-	-		
PdMe	Pd-Pd	11.6 ± 0.5	2.80 ± 0.05	0.0085 ± 0.0009	1.7 ± 0.4	0.018
	Pd-O	-	-	-		

Table 4-8. *Textural properties and related catalytic activity for the 1 wt. % Pd/TiO_2 catalysts prepared in this chapter. Catalysts are named based on the synthesis procedure applied: synthesis solvent composition – W = water, 50Me = 50:50 vol:vol MeOH:H_2O and Me = methanol; PVA added as a stabiliser = P; acidification performed during immobilisation = A.*

Catalyst	MP-AES [Pd] (wt. %)	TEM NP Size (nm)	XANES LCF Oxidation State (%)	EXAFS Fitted CN		Pd NP $CO_{(ads)}$ Surface Sites	Conversion of Furfural (%)[a]	Activity (mol(mol Pd^{-1})hr^{-1})[b]	Selectivity to FA (%)[c]	Selectivity to THFA (%)[c]	Selectivity to Acetal (%)[c]	Selectivity to other products (%)
			Pd^{2+}/Pd^0	Pd-Pd	Pd-O	Linear/Bridged						
PdWPA	0.83	2.6 ± 1.4	0.39	6.7± 0.3	1.8 ± 0.2	0.10	74	288.4	45	13	19	23
PdWP[d]	0.30	1.7 ± 0.7	0.47	4.8 ± 0.3	2.1 ± 0.2	0.55	19	397.5	56	12	29	3
Pd50MeP	0.91	1.7 ± 0.7	0.45	5.0 ± 0.3	2.2 ± 0.2	0.74	54	287.5	54	30	10	6
PdMeP	0.86	1.8 ± 0.8	0.69	4.6 ± 0.4	2.7 ± 0.2	0.67	53	194.9	60	25	0	15
PdW[d]	0.25	3.1 ± 1.5	0.47	6.2 ± 0.3	1.8 ± 0.2	0.79	15	256.0	20	1	0	79
Pd50Me	0.91	3.6 ± 1.6	0.15	8.9 ± 0.1	0.7 ± 0.7	0.92	49	133.0	35	29	22	14
PdMe	0.96	3.3 ± 2.3	0.18	8.7 ± 0.2	0.9 ± 0.2	0.62	37	133.3	48	15	28	9

a: Conversion given after 5 hrs of reaction; b: activity determined after 15 minutes of reaction time; c: selectivity presented at isoconversion at 25 % furfural conversion; d: isoconversion calculated at 12.5 % furfural conversion.

4.4 Conclusions

In this chapter, an updated sol-immobilisation procedure for the preparation of supported Pd NPs using colloidal methods is reported. The adapted colloidal method utilises MeOH within the solvent mixture during colloidal formation, yielding Pd/TiO_2 catalysts with an increased Pd loading compared to the conventional water based preparation (PdWPA) presented in this work. Furthermore, it was shown that particles with an average size of ~ 3 nm could be prepared in the absence of a capping agent. However, smaller Pd NPs (< 2 nm) were only found to form when using PVA as a stabiliser.

Elsewhere, the use of MeOH in the solvent mixture had a major impact on catalyst selectivity for the hydrogenation of furfural, completely suppressing the production of acid catalysed by-products during the course of the reaction. PdWPA displayed 23 % selectivity to the acetal product at the initial time point, decreasing to 1 % at the end of the reaction (it should be noted that this end value is within the experimental error of the GC, ± 3 %). Hydrogenation over PdMeP, however, showed no selectivity to the acetal at any measured time point during the reaction, *Figure 8-1*. The formation of acetals and ethers is rationalised by the spillover of hydrogen, which occurs to a much greater extent for PdWPA compared to PdMeP, as determined *via* H_2-TPR measurements. The increased amount of hydrogen spillover leads to the formation of Brønsted acid sites on the TiO_2 surface, which then promote the acid-catalysed side reactions.[85,86] For Pd nanoparticles prepared using MeOH as a solvent, a thick layering of PVA at the metal-support interface was observed *via* electron microscopy. This additional layering of PVA is proposed to hinder the spillover of hydrogen onto the support, thus suppressing Brønsted acid formation on the TiO_2 surface (*Figure 4-26*).

This work provides valuable insights into the impact of reducing process steps in catalyst preparation, as well as highlighting new routes to optimise catalytic selectivity. Both of which are important objectives as the chemical industry moves toward more sustainable processes.

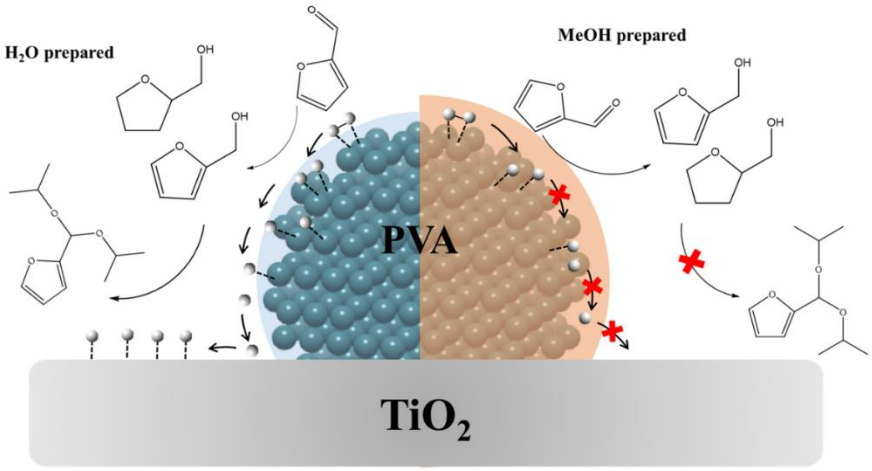

Figure 4-26. *Graphical representation displaying the suppression of H_2 spillover from Pd to the TiO_2 support resultant from increased PVA clustering in MeOH solvent prepared NPs. Limiting of H_2 spillover resulted in the reduction in by-product formation, particularly 2-diisopropoxymethyl furan.*

4.5 References

1 J. P. Lange, E. van der Heide, J. van Buijtenen and R. Price, *ChemSusChem*, 2012, **5**, 150–166.

2 G. W. Huber, S. Iborra and A. Corma, *Chem. Rev.*, 2006, **106**, 4044–4098.

3 Y. Jing, Y. Guo, Q. Xia, X. Liu and Y. Wang, *Chem*, 2019, **5**, 2520–2546.

4 A. V. Bridgwater, *Appl. Catal. A, Gen.*, 1994, **116**, 5–47.

5 A. V. Bridgwater and G. V. C. Peacocke, *Renew. Sustain. energy Rev.*, 2000, **4**, 1–73.

6 R. Kosydar, D. Duraczyńska, J. Gurgul, J. Kryściak-Czerwenka and A. Drelinkiewicz, *React. Kinet. Mech. Catal.*, 2019, **126**, 417–437.

7 F. W. Lichtenthaler and S. Peters, *Comptes Rendus Chim.*, 2004, **7**, 65–90.

8 R. Albilali, M. Douthwaite, Q. He and S. H. Taylor, *Catal. Sci. Technol.*, 2018, **8**, 252–267.

9 S. H. Pang, C. A. Schoenbaum, D. K. Schwartz and J. W. Medlin, *Nat. Commun.*, 2013, **4**, 1–6.

10 Y. Nakagawa, H. Nakazawa, H. Watanabe and K. Tomishige, *ChemCatChem*, 2012, **4**, 1791–1797.

11 O. Aldosari, H. Alshammari, M. Alhumaimess and I. Wawata, *Turkish J. Chem.*, 2019, **43**, 24–38.

12 H. J. Brownlee and C. S. Miner, *Ind. Eng. Chem.*, 1948, **40**, 201–204.

13 Grand View Research, Furfural Market Size, Share & Trends Analysis Report By Process, By Raw Material (Corncob, Sugarcane Bagasse), By Application (Furfuryl Alcohol, Solvent), By End-use (Pharmaceutical, Refineries), And Segment Forecasts, 2020 - 2027, https://www.grandviewresearch.com/industry-analysis/furfural-market, (accessed 20 June 2021).

14 A. Corma, S. Iborra and A. Velty, *Chem. Rev.*, 2007, **107**, 2411–2502.

15 Á. O'Driscoll, J. J. Leahy and T. Curtin, *Catal. Today*, 2017, **279**, 194–201.

16 R. Mariscal, P. Maireles-Torres, M. Ojeda, I. Sádaba and M. López Granados, *Energy Environ. Sci.*, 2016, **9**, 1144–1189.

17 C. Li, G. Xu, X. Liu, Y. Zhang and Y. Fu, *Ind. Eng. Chem. Res.*, 2017, **56**, 8843–8849.

18 Y. Wang, D. Zhao, D. Rodríguez-Padrón and C. Len, *Catalysts*, 2019, **9**, 1–33.

19 G. G. Millán and H. Sixta, *Catalysts*, 2020, **10**, 1–23.

20 M. Lesiak, M. Binczarski, S. Karski, W. Maniukiewicz and J. Rogowski, *J. Mol.*

Catal. A Chem., 2014, **395**, 337–348.

21 S. Chen, R. Wojcieszak, F. Dumeignil, E. Marceau and S. Royer, *Chem. Rev.*, 2018, **118**, 11023–11117.

22 Y. Nakagawa, M. Tamura and K. Tomishige, *ACS Catal.*, 2013, **3**, 2655–2668.

23 S. Sitthisa, T. Sooknoi, Y. Ma, P. B. Balbuena and D. E. Resasco, *J. Catal.*, 2011, **277**, 1–13.

24 G. Seo and H. Chon, *J. Catal.*, 1981, **67**, 424–429.

25 W. E. Kaufmann and R. Adams, *J. Am. Chem. Soc.*, 1923, **45**, 3029.

26 J. Kijeński, P. Winiarek, T. Paryjczak, A. Lewicki and A. Mikołajska, *Appl. Catal. A Gen.*, 2002, **233**, 171–182.

27 S. M. Rogers, C. R. A. Catlow, C. E. Chan-Thaw, A. Chutia, N. Jian, R. E. Palmer, M. Perdjon, A. Thetford, N. Dimitratos, A. Villa and P. P. Wells, *ACS Catal.*, 2017, **7**, 2266–2274.

28 R. Huang, Q. Cui, Q. Yuan, H. Wu, Y. Guan and P. Wu, *ACS Sustain. Chem. Eng.*, 2018, **6**, 6957–6964.

29 C. Wang, A. Wang, Z. Yu, Y. Wang, Z. Sun, V. M. Kogan and Y. Y. Liu, *Catal. Commun.*, 2021, **148**, 106178.

30 K. Kinoshita, *J. Electrochem. Soc.*, 1990, **137**, 845–848.

31 Z. L. Wu, J. Wang, S. Wang, Y. X. Zhang, G. Y. Bai, L. Ricardez-Sandoval, G. C. Wang and B. Zhao, *Green Chem.*, 2020, **22**, 1432–1442.

32 S. Campisi, M. Schiavoni, C. E. Chan-Thaw and A. Villa, *Catalysts*, 2016, **6**, 1–21.

33 S. Campisi, D. Ferri, A. Villa, W. Wang, D. Wang, O. Kro and L. Prati, *J. Phys. Chem. C*, 2016, **120**, 14027–14033.

34 V. Vorotnikov, G. Mpourmpakis and D. G. Vlachos, *ACS Catal.*, 2012, **2**, 2496–2504.

35 P. Thompson, O. Bikondoa, L. Bouchenoire, S. Brown, M. Cooper, T. Hase, C. Lucas and D. Wermeille, in *AIP Conference*, 2019, vol. 2054.

36 P. B. J. J. Thompson, B. N. Nguyen, R. Nicholls, R. A. Bourne, J. B. Brazier, K. R. J. J. Lovelock, S. D. Brown, D. Wermeille, O. Bikondoa, C. A. Lucas, T. P. A. A. Hase and M. A. Newton, *J. Synchrotron Radiat.*, 2015, **22**, 1426–1439.

37 B. Ravel, in *X-ray Absorption and X-ray Emission Spectroscopy. Theory and Applications*, eds. J. A. van Bokhoven and C. Lamerbiti, Wiley, 2016, p. 283.

38 B. Ravel and M. Newville, *J. Synchrotron Radiat.*, 2005, **12**, 537–541.

39 R. L. Barton, D. J. Gardenghi, W. C. Stolte and R. K. Szilagyi, *J. Phys. Chem. A*, 2015, **119**, 5579–5586.

40 R. B. Boysen and R. K. Szilagyi, *Inorganica Chim. Acta*, 2008, **361**, 1047–1058.

41 P. Frank, B. Hedman, R. M. K. Carlson, T. A. Tyson, A. L. Roe and K. O. Hodgson, *Biochemistry*, 1987, **26**, 4975–4979.

42 S. Pongpiachan, K. Thumanu, C. Kositanont, K. Schwarzer, J. Prietzel, P. Hirunyatrakul and I. Kittikoon, *J. Anal. Methods Chem.*, 2012, **2012**, 1–12.

43 A. Gniewek, A. M. Trzeciak, J. J. Ziółkowski, L. Kępiński, J. Wrzyszcz and W. Tylus, *J. Catal.*, 2005, **229**, 332–343.

44 H. Hei, H. He, R. Wang, X. Liu and G. Zhang, *Soft Nanosci. Lett.*, 2012, **2**, 34–40.

45 K. H. Leong, H. Y. Chu, S. Ibrahim and P. Saravanan, *Beilstein J. Nanotechnol.*, 2015, **6**, 428–437.

46 L. Xu, X. C. Wu and J. J. Zhu, *Nanotechnology*, 2008, **19**, 1–6.

47 L. Espinosa-Alonso, K. P. de Jong and B. M. Weckhuysen, *Phys. Chem. Chem. Phys.*, 2010, **12**, 97–107.

48 N. Dimitratos, J. A. Lopez-Sanchez, D. Morgan, A. F. Carley, R. Tiruvalam, C. J. Kiely, D. Bethell and G. J. Hutchings, *Phys. Chem. Chem. Phys.*, 2009, **11**, 5142–5153.

49 F. Porta, L. Prati, M. Rossi, S. Coluccia and G. Martra, *Catal. Today*, 2000, **61**, 165–172.

50 C. A. Schneider, W. S. Rasband and K. W. Eliceiri, *Nat. Methods*, 2012, **9**, 671–675.

51 Y. Zhao, L. Jia, J. A. Medrano, J. R. H. Ross and L. Le, *ACS Catal.*, 2013, **3**, 2341–2352.

52 O. Rac, P. Suchorska-Woźniak, M. Fiedot and H. Teterycz, *Beilstein J. Nanotechnol.*, 2014, **5**, 2192–2201.

53 N. Dimitratos, A. Villa, L. Prati, C. Hammond, C. E. Chan-Thaw, J. Cookson and P. T. Bishop, *Appl. Catal. A Gen.*, 2016, **514**, 267–275.

54 O. A. Usoltsev, A. L. Bugaev, A. A. Guda, S. A. Guda and A. V. Soldatov, *Top. Catal.*, 2020, **63**, 58–65.

55 L. C. Witjens, J. H. Bitter, A. J. van Dillen, K. P. de Jong and F. M. F. de Groot, *Phys. Chem. Chem. Phys.*, 2004, **6**, 3903–3906.

56 P. P. Wells, E. M. Crabb, C. R. King, R. Wiltshire, B. Billsborrow, D. Thompsett and A. E. Russell, *Phys. Chem. Chem. Phys.*, 2009, **11**, 5773–5781.

57 M. A. Newton, *Catal. Sci. Technol.*, 2016, **6**, 8525–8531.

58 M. Newville, *J. Synchrotron Radiat.*, 2001, **8**, 96–100.

59 C. E. Chan-Thaw, A. Villa and L. Prati, in *Gold Catalysis: Preparation,*

Characterization, and Applications, eds. L. Prati and A. Villa, Pan Stanford, 1st edn., 2015, pp. 59–63.

60 M. Signoretto, F. Menegazzo, A. Di Michele and E. Fioriniello, *Catalysts*, , DOI:10.3390/catal6060087.

61 G. Malta, S. A. Kondrat, S. J. Freakley, D. J. Morgan, E. K. Gibson, P. P. Wells, M. Aramini, D. Gianolio, P. B. J. Thompson, P. Johnston and G. J. Hutchings, *Chem. Sci.*, 2020, **11**, 7040–7052.

62 M. Calandra, J. P. Rueff, C. Gougoussis, D. Céolin, M. Gorgoi, S. Benedetti, P. Torelli, A. Shukla, D. Chandesris and C. Brouder, *Phys. Rev. B - Condens. Matter Mater. Phys.*, 2012, **86**, 165102.

63 H. Ågren and V. Carravetta, *Int. J. Quantum Chem.*, 1992, **42**, 685–718.

64 T. Glaser, B. Hedman, K. O. Hodgson and E. I. Solomon, *Acc. Chem. Res.*, 2000, **33**, 859–868.

65 S. E. Shadle, B. Hedman, K. O. Hodgson, E. I. Solomon, B. Hedman and K. O. Hodgson, *J. Am. Chem. Soc.*, 1995, **117**, 2259–2272.

66 C. E. Mitchell, U. Terranova, I. Alshibane, D. J. Morgan, T. E. Davies, Q. He, J. S. J. Hargreaves, M. Sankar and N. H. De Leeuw, *New J. Chem.*, 2019, **43**, 13985–13997.

67 L. J. Hoyos, M. Primet, H. Praliaud, I. U. Claude, B. Lyon and A. A. Einstein, *J. Chem. Soc. Faraday. Trans.*, 1992, **88**, 3367–3373.

68 N. S. Fígoli and P. C. L'Argentiere, *J. Mol. Catal. A Chem.*, 1997, **122**, 141–146.

69 P. Albers, J. Pietsch and S. F. Parker, *J. Mol. Catal. A Chem.*, 2001, **173**, 275–286.

70 H. Lichtenberg, A. Prange, U. Steiner, E.-C. Oerke and J. Hormes, *J. Phys. Conf. Ser.*, 2009, **190**, 0–4.

71 F. Jalilehvand, *Chem. Soc. Rev.*, 2006, **35**, 1256–1268.

72 G. Almkvist, K. Boye and I. Persson, *J. Synchrotron Radiat.*, 2010, **17**, 683–688.

73 S. C. Cook, J. D. Padmos and P. Zhang, *J. Chem. Phys.*, 2008, **128**, 154705.

74 C. D. Zeinalipour-Yazdi, D. J. Willock, L. Thomas, K. Wilson and A. F. Lee, *Surf. Sci.*, 2016, **646**, 210–220.

75 K. Föttinger, W. Emhofer, D. Lennon and G. Rupprechter, *Top. Catal.*, 2017, **60**, 1722–1734.

76 M. Bowker, P. Stone, R. Bennett and N. Perkins, *Surf. Sci.*, 2002, **497**, 155–165.

77 T. Lear, R. Marshall, J. A. Lopez-sanchez, S. D. Jackson, T. M. Klapötke, G. Rupprechter, H. Freund and D. Lennon, *J. Chem. Phys.*, 2005, **123**, 1–13.

78 E. V Benvenutti, L. Franken and C. C. Moro, *Langmuir*, 1999, **15**, 8140–8146.

79 A. Bourane, O. Dulaurent and D. Bianchi, *J. Catal.*, 2000, **196**, 115–125.

80 S. Bertarione, D. Scarano, A. Zecchina, V. Johánek, J. Hoffmann, S. Schauermann, M. M. Frank, J. Libuda, G. Rupprechter and H.-J. Freund, *J. Phys. Chem. B*, 2004, **108**, 3603–3613.

81 H. Zhu, Z. Qin, W. Shan, W. Shen and J. Wang, *J. Catal.*, 2004, **225**, 267–277.

82 K. I. Hadjiivanov and G. N. Vayssilov, *Adv. Catal.*, 2002, **47**, 307–511.

83 H. Rojas, J. J. Martínez and P. Reyes, *Dyna*, 2010, **163**, 151–159.

84 S. Yilmaz, S. Ucar, L. Artok and H. Gulec, *Appl. Catal. A Gen.*, 2005, **287**, 261–266.

85 P. Lanzafame, G. Papanikolaou, S. Perathoner, G. Centi, M. Migliori, E. Catizzone, A. Aloise and G. Giordano, *Catal. Sci. Technol.*, 2018, **8**, 1304–1313.

86 M. E. Manríquez, T. López, R. Gómez and J. Navarrete, *J. Mol. Catal. A Chem.*, 2004, **220**, 229–237.

87 S. Campisi, C. E. Chan-Thaw, L. E. Chinchilla, A. Chutia, G. A. Botton, K. M. H. Mohammed, N. Dimitratos, P. P. Wells and A. Villa, *ACS Catal.*, 2020, **10**, 5483–5492.

88 Y. Harima, T. Fujita, Y. Kano, I. Imae, K. Komaguchi, Y. Ooyama and J. Ohshita, *J. Phys. Chem. C*, 2013, **117**, 16364–16370.

89 Y.-K. Peng, H.-L. Chou and S. C. E. Tsang, *Chem. Sci.*, 2018, **9**, 2493–2500.

90 R. Prins, *Chem. Rev.*, 2012, **112**, 2714–2738.

91 T. Huizinga and R. Prins, *J. Phys. Chem.*, 1981, **85**, 2156–2158.

92 C. Lv, X. Lan, F. Li, L. Wang, L. Xiao, C. Wang, J. Shi and S. Yu, *Catal. Sci. Technol.*, 2020, **10**, 690–699.

93 V. V. Gorodetskii and A. V. Matveev, *Hydrogen spillover in H2 oxidation on Pd-Ti3+/TiO2*, Elsevier Science B.V., 1st edn., 2001, vol. 138.

94 N. Shibayama, H. Ozawa, M. Abe, Y. Ooyama and H. Arakawa, *Chem. Commun.*, 2014, **50**, 6398–6401.

95 D. Padovan, A. Al-Nayili and C. Hammond, *Green Chem.*, 2017, **19**, 2846–2854.

96 D. Wu, W. Y. Hernández, S. Zhang, E. I. Vovk, X. Zhou, Y. Yang, A. Y. Khodakov and V. V. Ordomsky, *ACS Catal.*, 2019, **9**, 2940–2948.

97 W. Hoogsteen and L. G. J. Fokkink, *J. Colloid Interface Sci.*, 1995, **175**, 12–26.

98 S. R. Chowdhury, P. S. Roy and S. K. Bhattacharya, *Adv. Nat. Sci. Nanosci. Nanotechnol.*, 2017, **8**, 1–10.

99 I. Lezcano-Gonzalez, U. Deka, B. Arstad, A. Van Yperen-De Deyne, K. Hemelsoet, M. Waroquier, V. Van Speybroeck, B. M. Weckhuysen and A. M. Beale, *Phys.*

Chem. Chem. Phys., 2014, **16**, 1639–1650.

100 S. Vorakitkanvasin, W. Phongsawat, K. Suriye, P. Praserthdam and J. Panpranot, *RSC Adv.*, 2017, **7**, 38659–38665.

101 N. Y. Topsøe, *Science*, 1994, **265**, 1217–1219.

102 F. Liu and H. He, *J. Phys. Chem. C*, 2010, **114**, 16929–16936.

103 L. K. Noda, R. M. de Almeida, N. S. Gonçalves, L. F. D. Probst and O. Sala, *Catal. Today*, 2003, **85**, 69–74.

104 M. I. Zaki, M. A. Hasan, F. A. Al-Sagheer and L. Pasupulety, *Colloids Surfaces A Physicochem. Eng. Asp.*, 2001, **190**, 261–274.

105 L. M. Gómez-Sainero, X. L. Seoane, J. L. G. Fierro and A. Arcoya, *J. Catal.*, 2002, **209**, 279–288.

106 M. Bonarowska, B. Burda, W. Juszczyk, J. Pielaszek, Z. Kowalczyk and Z. Karpiński, *Appl. Catal. B Environ.*, 2001, **35**, 13–20.

107 G. Neri, M. G. Musolino, C. Milone, D. Pietropaolo and S. Galvagno, *Appl. Catal. A Gen.*, 2001, **208**, 307–316.

108 C. Amorim and M. A. Keane, *J. Colloid Interface Sci.*, 2008, **322**, 196–208.

109 N. K. Nag, *J. Phys. Chem. B*, 2001, **105**, 5945–5949.

110 U. S. Ozkan, M. W. Kumthekar and G. Karakas, *Catal. Today*, 1998, **40**, 3–14.

111 T. Hengsawad, T. Jindarat, D. E. Resasco and S. Jongpatiwut, *Appl. Catal. A Gen.*, 2018, **566**, 74–86.

112 E. Nowicka, S. Althahban, T. D. Leah, G. Shaw, D. Morgan, C. J. Kiely, A. Roldan and G. J. Hutchings, *Sci. Technol. Adv. Mater.*, 2019, **20**, 367–378.

113 W. J. Shen, M. Okumura, Y. Matsumura and M. Haruta, *Appl. Catal. A Gen.*, 2001, **213**, 225–232.

114 X. Hong, L. Zou, J. Zhao, C. Li and L. Cong, *IOP Conf. Ser. Mater. Sci. Eng.*, 2018, **439**, 1–5.

115 N. C. T. Martins, J. Ângelo, A. V. Girão, T. Trindade, L. Andrade and A. Mendes, *Appl. Catal. B Environ.*, 2016, **193**, 67–74.

116 H. Awada and C. Daneault, *Appl. Sci.*, 2015, **5**, 840–850.

117 R. Mueller, H. K. Kammler, K. Wegner and S. E. Pratsinis, *Langmuir*, 2003, **19**, 160–165.

118 M. M. Gomaa, C. Hugenschmidt, M. Dickmann, E. E. Abdel-Hady, H. F. M. Mohamed and M. O. Abdel-Hamed, *Phys. Chem. Chem. Phys.*, 2018, **20**, 28287–28299.

119 M. W. Tew, M. Nachtegaal, M. Janousch, J. A. Van Bokhoven, T. Huthwelker and

J. A. van Bokhoven, *Phys. Chem. Chem. Phys.*, 2012, **14**, 5761–5768.

120 W. Jones, P. P. Wells, E. K. Gibson and A. Chutia, *ChemCatChem*, 2019, **11**, 1–7.

121 Y.-F. Han, D. Kumar, C. Sivadinarayana, A. Clearfield and D. W. Goodman, *Catal. Letters*, 2004, **94**, 131–134.

Chapter 5 Systematic Process Changes in Dilute Colloidal Au Synthesis Investigated *via* X-ray Absorption Fine Structure Spectroscopy

This chapter presents work investigating the influence of the synthesis temperature and [precursor metal] on colloidal and supported Au NP size. Laboratory and synchrotron techniques have been used to elucidate the synthesis protocols effect on NP growth with a manuscript published in *Nanoscale Advances* titled 'Extracting Structural Information of Au Colloids at Ultra-Dilute Concentrations: Identification of Growth during Nanoparticle Immobilization': George F. Tierney, Donato Decarolis, Norli Abdullah, Scott M. Rogers, Shusaku Hayama, Martha Briceno de Gutierrez, Alberto Villa, C. Richard A. Catlow, Paul Collier, Nikolaos Dimitratos and Peter P. Wells, *Nanoscale Advances,* 2019, **1**, 2546-2552.

Authors listed on this paper all contributed to the manuscript in the following capacities: D. Decarolis had input in writing of the manuscript; N. Abdullah, S. M. Rogers and S. Hayama supported beamtime measurements as support (N.A. and S. M. R) and as beamline staff (S. H.), respectively; M. Briceno de Gutierrez performed STEM-HAADF analysis; P. Collier was included due to their industrial involvement with Johnson Matthey; C. R. A. Catlow was included as the academic supervisor of S. M. Rogers; N. Dimitratos and A. Villa were academic collaborators for this project; P. P. Wells was the academic supervisor of this project.

5.1 Introduction

Systematic variations to the sol-immobilisation synthesis procedure and the resultant influence on NP growth has been established in Chapter 3. However, these studies have been, in the main, concerned with investigating the relationship of the procedure and the final supported catalysts.[1–7] This has left a gap in the knowledge concerning the changes undergone by the colloidal NPs as a result of the applied synthesis. It is therefore unknown whether changes to the synthesis parameters is asserted on the colloidal NPs or if they are implemented during immobilisation.

To better control NP size, greater understanding of the fundamental nucleation and growth steps in NP formation is necessary. Au NPs are one of the most extensively studied nano-

particulate systems due to their wide range of potential applications, ranging from medicine to catalysis.[8–11]

The structural properties of colloidal Au NP solutions have been measured by employing high brilliance X-rays produced by synchrotrons, *via* XAFS spectroscopic techniques and small angle X-ray scattering (SAXS). Much work in this area has followed the formation of Au NPs using time-resolved studies to elucidate the changes to Au as it transitions from the precursor species to defined entities.[12–17] Using XAFS, these studies have assessed the formation of Au NPs within precursor Au solutions ranging from [Au] = 100 mM to 7 mM,[12,16–22] with data acquisition times spanning minutes to 10^2 ms. They have continually increased their sophistication, moving from simple sample environments, such as a large volume cell, towards precision engineered microfluidic reactors[19,20] and acoustic levitation systems.[12]

Other than XAFS, SAXS has proved successful in studying colloidal Au NP systems.[12,15] It allows for very fast measurements, in the order of milliseconds, and is able to provide information regarding the particle size and shape during the reaction procedure.[15,23] Unfortunately, SAXS resolution is limited to NP sizes ≥ 1 nm,[24] below which meaningful data cannot be extracted. Moreover, a minimum concentration of ≥ 200 µM is needed to achieve the required electronic contrast.[14] As a consequence, the [Au precursors] employed in these XAFS and SAXS studies do not always reflect the optimal conditions published in recent literature for the preparation of Au NPs, e.g. 5-100 µM.[4,25–32] At such low concentrations, the application of these forms of characterisation becomes challenging. Furthermore, these studies do not explore the changes to the NP properties once they have been supported. It is well known that there is a special interplay between metal NPs and their supports; once immobilised, the NPs are influenced by the strong metal-support interactions,[33] evidenced by their wettability.[34–37] To understand how best to optimise the catalytic performance of supported NPs, it is important to separate the contributions of synthesis conditions during the colloidal step and immobilisation on the resultant colloidal NP structures.

In this chapter, the influence of the synthesis procedure on NP growth in colloidal solutions and on support surfaces was investigated. Systematic variations were made to the synthesis temperature (1, 25, 50 and 75 °C) and to the [Au] in the precursor solution (50, 100 and

1000 µM) and were characterised using UV-Vis of colloids, TEM, STEM HAADF and XAFS.

5.2 Experimental

5.2.1 Sample Preparation

Synthesis of colloidal and supported Au NPs was performed using a conventional sol-immobilisation method; the [Au metal salt precursor] and temperature during reduction were altered. The colloidal solutions were prepared from $HAuCl_4.3H_2O$ ([Au] = 50 µM, 100 µM and 1000 µM) and diluted with H_2O (18.2 MΩ cm). PVA was incorporated as a stabilising agent (PVA:Au (wt/wt) = 0.65, 0.01 g mL^{-1}). Subsequently, solutions of $NaBH_4$ (0.1 M, $NaBH_4$:Au (mol/mol) = 5) were added drop-wise over the course of a minute, under continuous stirring, and left to reduce for 30 minutes. TiO_2 (0.99 g P25, Degussa) was then added to give a final Au loading of 1 wt. %. The Au/TiO_2 slurry was acidified to pH 1-2 using H_2SO_4 under vigorous stirring for 1 hr, ensuring full immobilisation of the Au NPs on TiO_2. The mixture was filtered, washed with H_2O (18.2 MΩ cm), and dried overnight at room temperature. The systematic variations made to the synthesis procedure presented in this chapter are listed in *Table 5-1*.

Table 5-1. *Concentration and reduction temperature conditions used in the preparation of colloidal and TiO_2 supported Au nanoparticles.*

[Au] (µM)	Reduction temperature (°C)
100	1
100	25
100	50
100	75
50	1
1000	1

5.2.2 Characterisation Methods

5.2.2.1 Ultraviolet-Visible Spectroscopy

The reduction of the Au precursor salt solution was monitored using UV-Vis spectroscopy over 30 minutes. The reduction of the Au species from Au^{3+} to Au^{0} was observed with the formation of a surface plasmon resonance (SPR) band (*Figure 5-1*). 4 mL of the reaction mixture was pipetted into quartz cuvettes and analysed every 15 minutes; acquired spectra were run against a reference of H_2O (18.2 MΩ cm). UV-Vis spectra were recorded using a Shimadzu UV-1800 spectrophotometer.

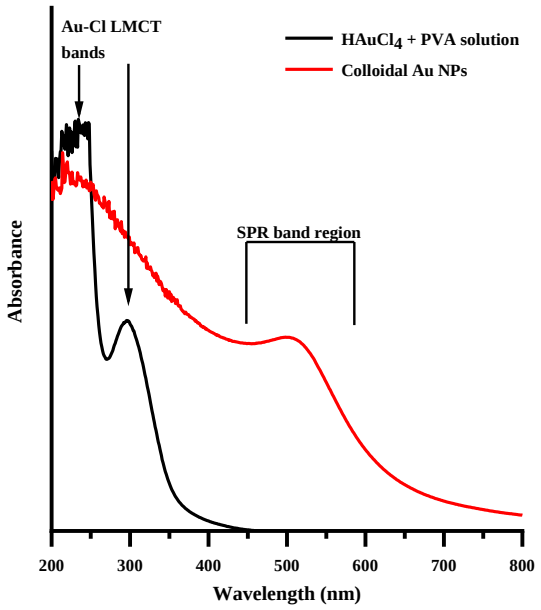

Figure 5-1. *UV-Vis spectra displaying the position of the ligand-metal charge transfer bands present in the $HAuCl_4$ precursor (black), and the evolution of the SPR band following reduction of the precursor salt (red).*

5.2.2.2 Electron Microscopy

Imaging of the colloidal and supported Au NPs was acquired *via* STEM and TEM, respectively. Colloidal Au solutions of varying [Au] were prepared for imaging by pipetting a drop of the colloid onto a holey carbon TEM grid, and drying in air at room temperature. HAADF imaging of the Au NPs was performed by Dr. Briceno de Gutierrez using a JEOL JEM-2800 (200 kV) scanning transmission electron microscope equipped with an off-axis annular detector at JMTC, Sonning Common, U.K.

The TiO_2 supported Au NPs were prepared for imaging by sonicating a small amount of the sample in EtOH. A small aliquot of the supernatant was pipetted onto a 300 mesh Cu TEM grid. Images were acquired by the author using a JEOL JEM-2100 EM (120 kV) at the Research Complex at Harwell, Didcot, U.K.

5.2.2.3 X-ray Absorption Fine Structure Measurements of Colloidal and TiO_2 supported Au

XAFS measurements of both colloidal and TiO_2 supported Au NPs at the Au L_3-edge were performed on the I20-Scanning beamline, DLS, U.K. Colloidal Au NPs were studied in a continuous flow using an adapted stainless steel gas cell with polyimide windows; PTFE tubing (OD = 0.16 cm) and a peristaltic pump were used to continuously move the solution through the cell (*Figure 5-2*). A low flow rate of 1 mL min^{-1} was applied to limit beam damage to the Au NPs and also to limit the evolution of H_2 gas from excess $NaBH_4$ reacting along the tubing walls.[38]

1 wt. % Au/TiO_2 powder catalysts were pressed into 8 mm pellets and studied *ex situ* in an X-ray transparent cell. Static XAFS measurements of the colloidal Au NPs were made in fluorescence mode using a Si(111) four-bounce monochromator, data was collected through a 64 element Ge fluorescence detector with the Xpress2 digital pulse processor.[39] Scans were performed at a time resolution of 43 min $spectrum^{-1}$ (k_{max} = 18), with 6 scans collected for the colloidal solutions and 3 for the powder catalysts. Processing and normalisation of the absorption spectra and analysis of the extended X-ray absorption fine-structure (EXAFS) were accomplished using IFEFFIT with the Horae package (Athena and Artemis).[40,41] Experimental determination of the amplitude reduction factor, S_0^2, was performed through fitting of the Au^0 reference foil EXAFS with an FCC Au (CN = 12) *.cif* file (ICSD collection code = 52249), giving the fixed parameter of 0.83. EXAFS data fittings were made with an *R*-space of $1.74 < R < 3.37$ Å for both the colloidal and TiO_2 supported Au NPs, and a *k*-space of $3 < k < 11.5$ for the colloidal Au NPs and $3 < k < 14$ for the TiO_2 supported Au NPs.

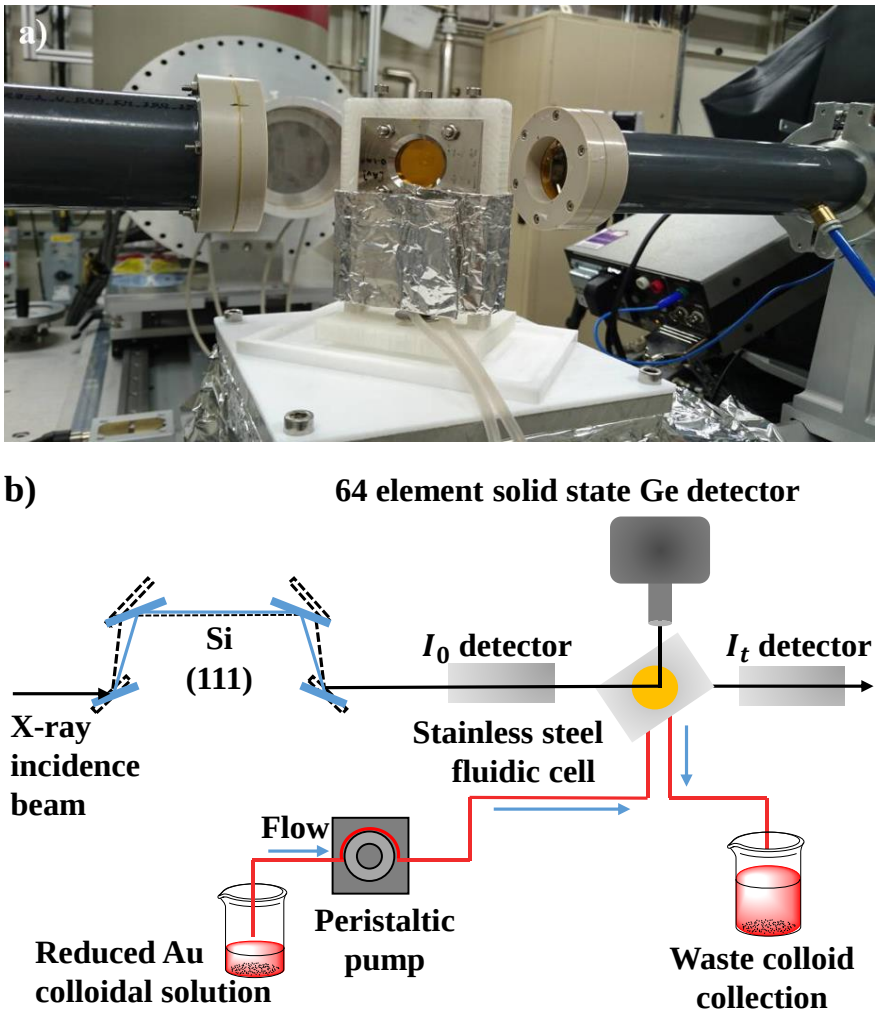

Figure 5-2. *Experimental set-up for the colloidal Au XAFS measurements collected on I20-Scanning beamline, DLS, Didcot, U.K.: a) Photograph of the in situ cell used, and b) experimental schematic detailing the data acquisition; a continuous flow of preformed colloid was pumped through PTFE tubing and XAFS data was acquired in fluorescence mode by a solid state Ge detector.*[39,42]

5.3 Results and Discussion

5.3.1 Influence of Systematic Synthesis Variations on Colloidal Au

5.3.1.1 Ultraviolet-Visible Spectroscopy

UV-Vis has been used to study both the Au precursor solution (reduction rate) and the formation of Au NPs through the appearance of an SPR band prior to NP immobilisation.[43–45] The position of the SPR peak, λ_{max}, is related to the particle size and shape of the NP: blue and red shifting of the wavelength is indicative of decreases and increases to Au particle size, respectively (*Figure 5-3*).[43] In addition, the intensity of the band can also give a rationalisation of particle size, as larger particles give rise to more intense peaks.[2,46] Correlation of TiO_2 supported Au NP size with systematic increases in the synthesis temperature is known to influence the immobilised Au NP size.[43–45] This was replicated in this study, displaying a red shift of the SPR band position as temperature increased from 1 to 75 °C (1 °C = 492 nm, 75 °C = 538 nm)(*Figure 5-3*a), corresponding to the similar trends reported in literature (*Table 5-2*).[4,47,48] Conversely, the [Au] showed only slight shifting of the SPR band peak when increasing 20-fold (50 µM = 492 nm, 1000 µM = 498 nm) (*Figure 5-3*b).

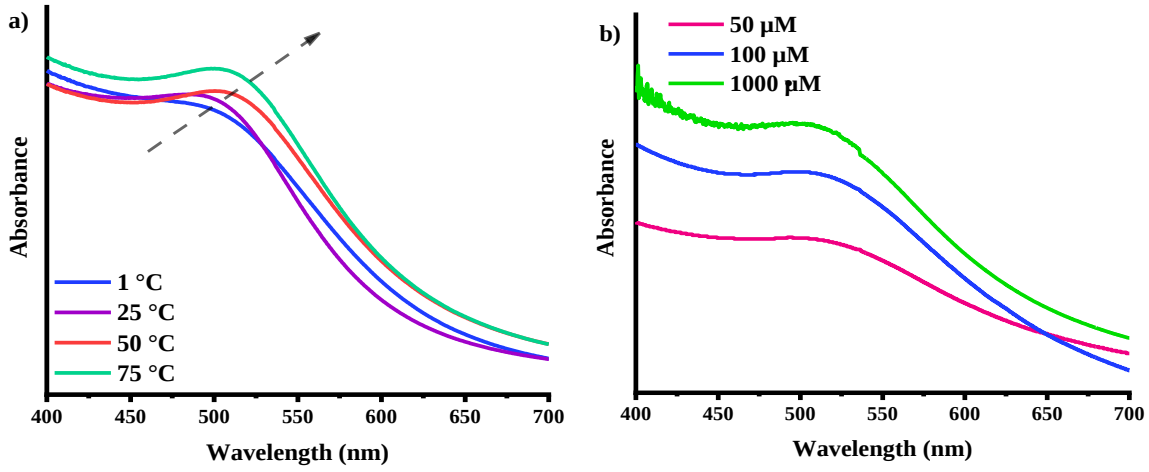

Figure 5-3. *UV-Vis spectra showing the formed Au SPR bands following reduction of the $HAuCl_4$ precursor under various systematic synthesis parameter changes: a) temperature of reduction ([Au] = 100 µM), and b) increased [Au] (reduced at 1 °C). The dashed arrow highlights both the increase in intensity and shift in λ_{max} position, indicating an increase in particle size.*

Table 5-2. *Position of the Au SPR bands (nm) acquired for the temperature and concentration varied colloidal Au series; values here are extrapolated from* ***Figure 5-1.***

Colloidal sample	UV-Vis λ_{max} (nm)
100 µM / 1 °C	492
100 µM / 25 °C	493
100 µM / 50 °C	500-510
100 µM / 75 °C	538
50 µM / 1 °C	495
1000 µM / 1 °C	498

5.3.1.2 Scanning Transmission Electron Microscopy

Characterisation of the textural properties of the prepared Au colloids was first attempted using electron microscopy. Here, the use of conventional transmission electron microscopes cannot offer sufficient magnification to analyse the small Au particles formed. Instead, the use of annular dark-field imaging available in STEM imaging is more suited to differentiate the Au clusters on the TEM grid (*Figure 5-4*). The increased clarity afforded by STEM imaging allowed the formation of small Au clusters in the 50 µM Au colloid to be distinguished. However, an inadequate quantity of Au NPs meant that an accurate representation of NP size could not be determined (*Figure 5-4*a). Imaging of the colloidal solutions prepared at [Au] = 100 and 1000 µM provided sufficient NPs to calculate average sizes (*Figure 5-4*b-c). Au colloids prepared at 100 µM were found to have an average NP size of 3.0 ± 0.9 nm; nonuniformity of these supported Au NPs is explained by coalescence of neighbouring clusters in close proximity. Aggregation of the NPs is observed to a greater extent for the 1000 µM colloid, giving an average Au NP size of 4.6 ± 1.5 nm, alongside decreased NP dispersion. This growth in NP size observed from 100 to 1000 µM [Au] is therefore contradictory to the SPR band positions acquired *via* UV-Vis. To accurately probe colloidal NP size, a bulk characterisation technique should be employed that can encompass a reproducible average without dampening smaller particles in solution.

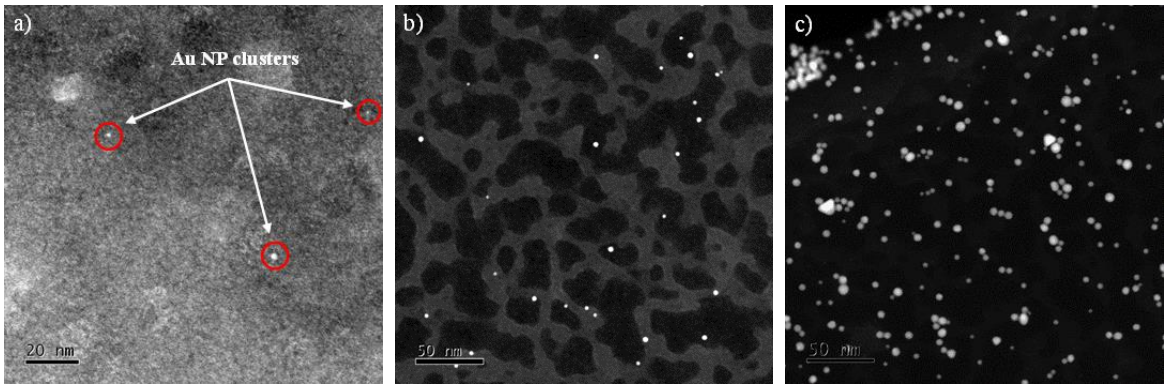

Figure 5-4. *STEM HAADF images of Au colloids prepared at increasing concentrations of Au at 1 °C: a) 50 µm, b) 100 µm and c) 1000 µM pipetted onto a holey carbon TEM grid.*

The assessment of NP size in colloidal solutions has been limited to quantifying data acquired from small angle X-ray scattering studies.[22] The increased ease in performing SAXS experiments on laboratory bench tops makes this technique an attractive route to study NP size.[23] Collection of data through these methods has been reported previously for experiments with [Au] ≥ 250 µM and for NPs that are > 1 nm, therefore they would not have been suitable for identification of colloidal NPs prepared at 50 and 100 µM. For this reason, a bulk technique like XAFS is used for this study as trace concentrations can be measured, which gives a per atom average of the Au species.

5.3.2 Investigating Artificial Colloidal NP Agglomeration *via* XAFS Beam Damage

Recent advances in the increased flux of modern insertion device-based beamlines, and improvements in the design of multi-element fluorescence detectors, has made XAFS a suitable tool to study both colloidal and supported NPs. The high energy, stability and brilliance of the I20-Scanning beamline at DLS, U.K., was utilised to acquire reliable Au L_3-edge XAFS of the fresh colloidal solutions and Au/TiO_2 samples (I20-Scanning flux at 10 KeV = > 10^{12}).[39,49] However, due to the high energy of the X-ray source beam, potential aggregation of the colloidal Au had to be inspected prior to acquiring measurements concerning synthesis variations. The stainless steel cell was filled with the 100 µM Au colloid (prepared at 1 °C) and sealed. The colloidal solution was then placed in the beam path and a XAFS spectrum (k_{max} = 12) was collected over 48 minutes (*Figure 5-5*). If Au cluster size had been impacted by the X-ray source beam during the colloidal dwell time, an increase in intensity would have been observed across the XAFS spectrum as a function of

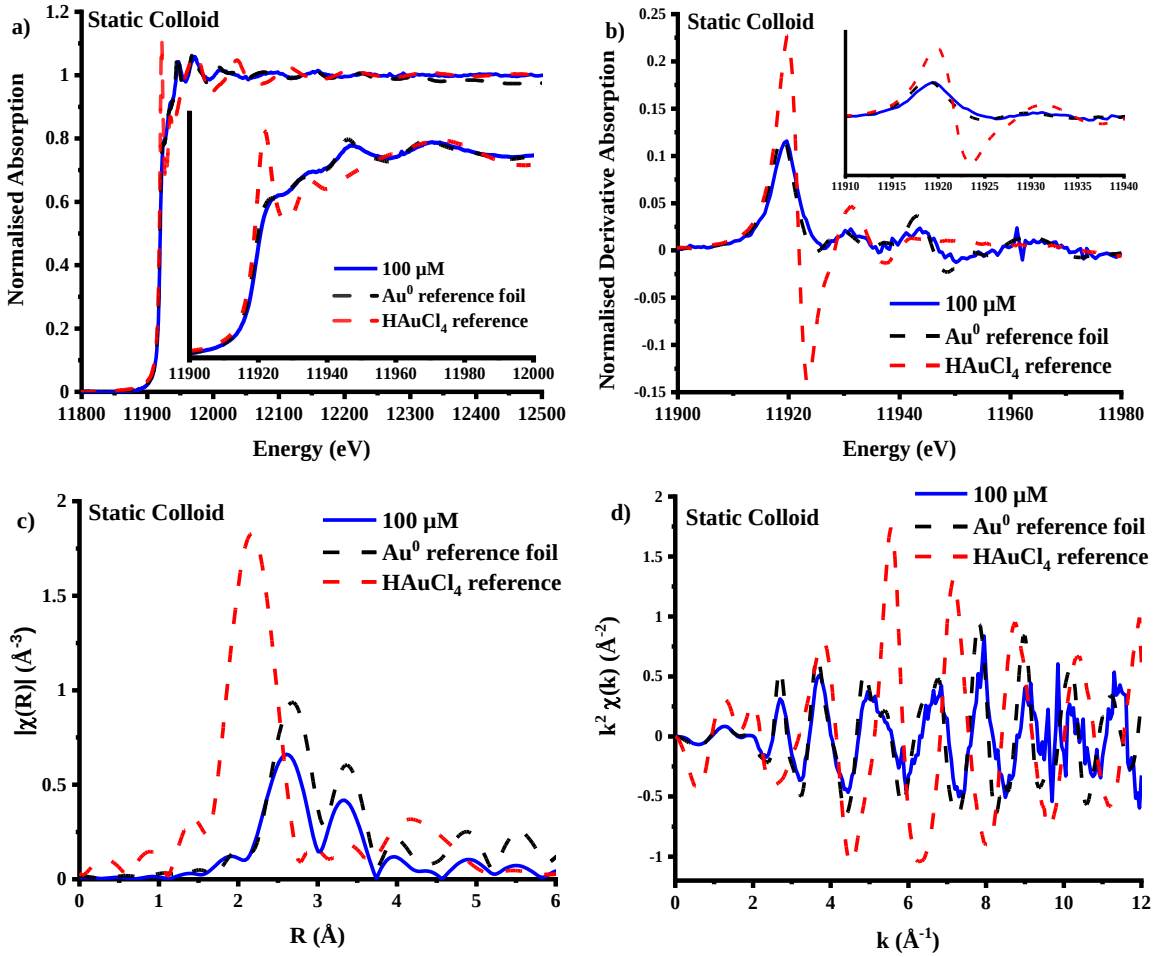

Figure 5-5. *Acquired Au L_3-edge XAFS data of colloidal Au (1 °C and 100 µM [Au]) collected after leaving the colloid in the X-ray source beam path for a full scan (~ 48 minutes), displaying a) a comparison of the normalised 1st derivative of µ(E) for the references and static colloid, b) the XANES spectra of the Au references and static colloid, c) the FT of the k data detailing the nearest neighbouring atomic species to the absorbing atom, and d) the k-space data of A_1 compared to both Au reference materials. All data was acquired at DLS, Didcot, U.K.; both the A_1 static colloid and Au reference datasets were acquired on the I20-Scanning beamline during the course of the experiment, and the $HAuCl_4$ reference was supplied by G. Malta et al., Science, 2019, 355, 1399-1403.*[50]

photon energy. Instead, full reduction of the Au precursor salt to Au^0 clusters is observed in the normalised XANES and the 1st derivative *via* an absence of the absorption edge and the lowered intensity of the first feature at 11919 eV, respectively (*Figure 5-5*a-b). In the FT EXAFS and χ space data, the formation of Au NPs with smaller CN_{Au-Au} than the bulk

reference foil is observed (*Figure 5-5*c-d). Glitches at k = ~9.5-10 are resultant from the monochromator on the beamline.

5.3.3 Colloidal Au L_3-edge X-ray Absorption Fine Structure

In the limited number of colloidal XAFS measurements, the [Au] have typically been > 3 mM.[15,51–53] Therefore, applying their findings to the growth mechanisms observed for colloids prepared in this body of work would be inappropriate given the dilute metal concentrations ([M] ≤ 150 μM) used in the conventional sol-immobilisation procedure.[2,4,47] To elucidate how colloidal growth can be influenced during synthesis, systematic changes to the synthesis temperature (1, 25, 50 and 75 °C) and the [Au] (50, 100 and 1000 μM) were investigated for preformed and immobilised colloidal NPs.

5.3.3.1 X-ray Absorption Near-Edge Structure

The Au L_3-edge XANES spectra of the temperature and concentration varied colloids series are presented below with the Au^0 reference foil for comparison (*Figure 5-6*). Complete reduction of the Au species is observed for all samples due to the absence of an intense edge peak at ~ 11915 eV, which corresponds to the dipole allowed $2p \rightarrow 5d$ transition being forbidden by the full Au 5*d* valence in Au^0.[20,22,52] Analysis of the Au NPs prepared as a function of synthesis temperature (1-75 °C) displayed no noticeable difference in the intensity or energy of the rising edge for both the XANES and its 1st derivative (*Figure 5-6*a-b). However, as the synthesis temperature increased, the intensity of the multiple scattering component in the post-edge at ~ 11946 eV was observed to increase in both the normalised and 1st derivative data. This feature is indicative of the formation of more bulk Au like particles, i.e. Au NPs with 12 nearest Au neighbours.[20,53,54] The influence of the Au concentration on the colloidal NPs is less pronounced in the XANES (*Figure 5-6*c-d); a trend in the multiple scattering component is not present, and so, similar colloidal NP sizes can be rationalised for clusters prepared using 50-1000 μM [Au], and could be caused by either the low synthesis temperature (1 °C), or the PVA stabiliser repelling like charges from other capped Au.[20,53,54]

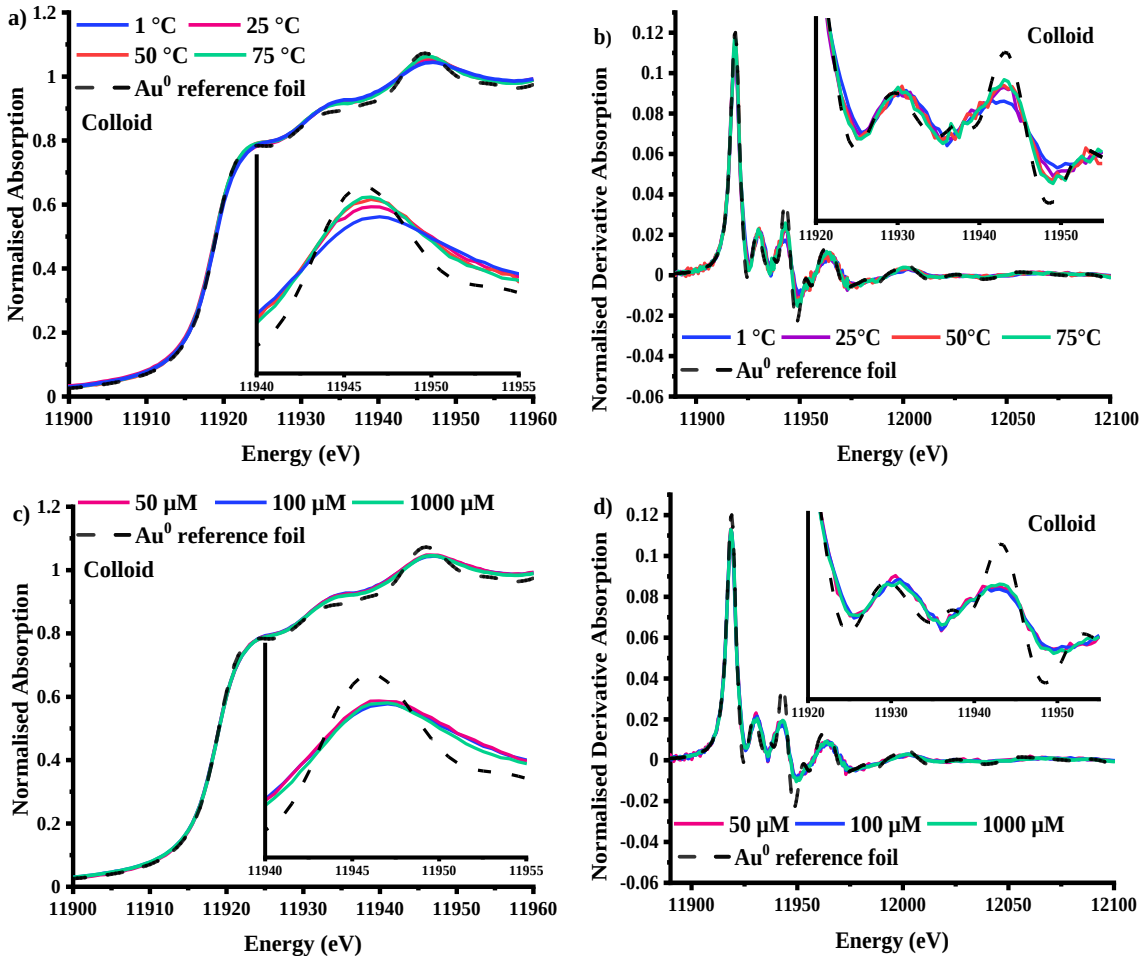

Figure 5-6. *XAFS spectra taken at the Au L_3-edge of the colloidal Au samples; where a) & c) are the XANES spectra detailing change as a function of increasing synthesis temperature and [Au], respectively, and b) & d) are the normalised 1st derivative of the absorption of a) & c), respectively.*

5.3.3.2 Extended X-ray Absorption Fine Structure

Accurate depictions of any trends in NP size are easier to interpret through comparisons and fitting of the EXAFS oscillations in *k* space and as the Fourier transformed EXAFS spectra solutions (*Figure 5-7*a and c, and *Figure 5-7*b and d, respectively). The suggested size trend seen in the temperature controlled XANES data is in agreement with the oscillatory data. Increasing magnitude of the 1st shell Au-Au scattering path at ~ 2.8 Å is also expected for this temperature controlled series.[4] The low magnitude of scattering present for the 1 °C colloid is caused by smaller Au NPs having higher surface fractions, and so, a greater proportion of under coordinated surface Au.[55] Preparation of Au colloids with increasing metal concentration, however, display no change to the magnitude of Au-Au scattering, thus

no trend in NP size is observed; this confirms that colloidal NP size is irrespective of the precursor concentration used.

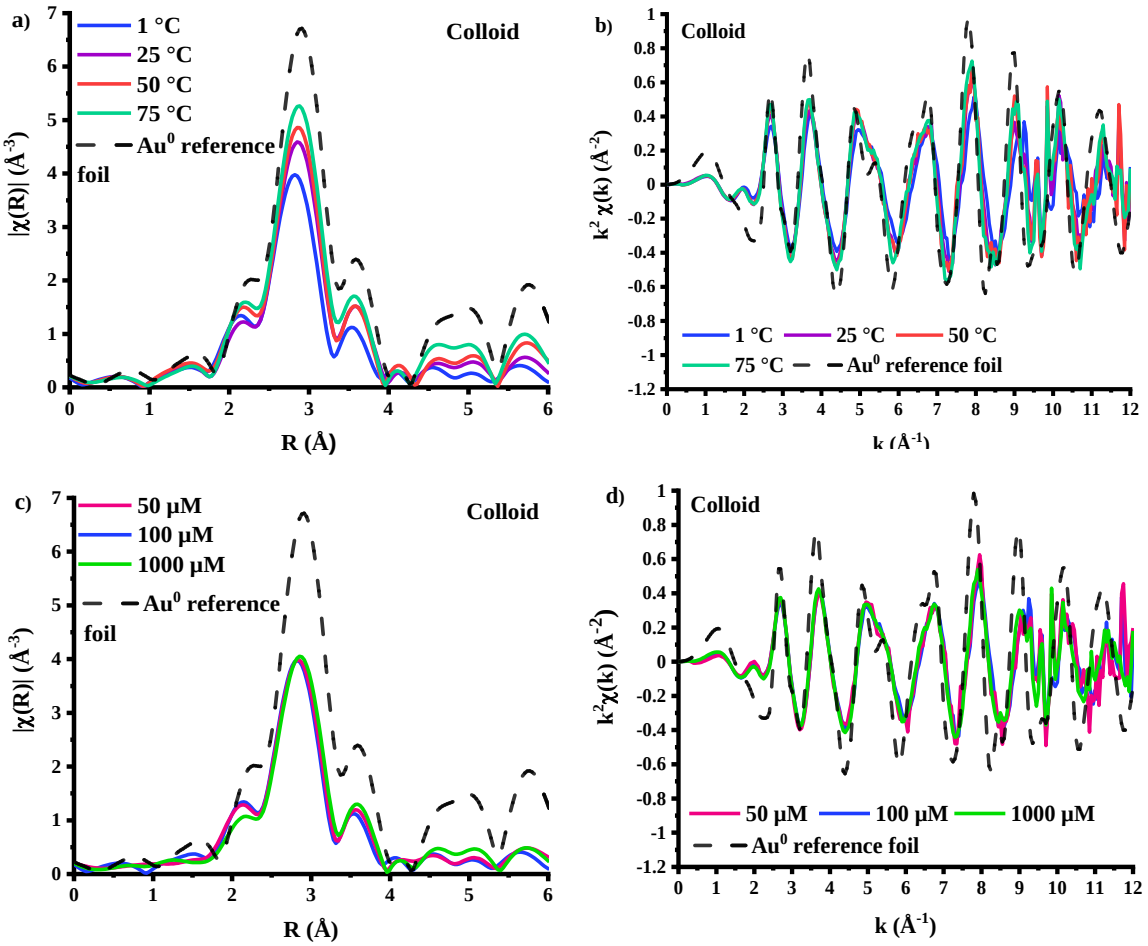

Figure 5-7. *XAFS spectra taken at the Au L_3-edge of the colloidal Au samples; where a) & c) are k^2 EXAFS data for the colloidal Au detailing change as a result of increasing synthesis temperature and [Au], respectively, and b) & d) are experimental FT χ(k) data of the corresponding EXAFS signals showing the influence of temperature and [Au].*

5.3.4 Characterisation of Supported Au Nanoparticles

5.3.4.1 Transmission Electron Microscopy

Supported NP properties can be easily assessed by observing the sample using electron microscopy. TEM imaging was used to investigate the influence of both temperature and [Au] on the supported NP diameters, morphologies and distributions (*Figure 5-8* and *Figure 5-11*). The catalysts prepared under increasing temperatures of synthesis showed an overall trend of increasing NP size, which is expected as temperature is a widely known contributing

factor to NP size.[4,56,57] However, the average TEM NP sizes calculated were all within error of one another, particularly the samples prepared between 1 and 50 °C (1 °C: 2.7 ± 0.7 nm, 25 °C: 2.9 ± 0.9 nm, 50 °C: 2.8 ± 0.8 nm), which is contrary to the trend observed in the colloidal EXAFS of the same samples. Imaging of the increasing [Au] supported NPs provided easier distinction of their respective sizes than found for the temperature series. As one would expect, a linear trend in the immobilised NP size was observed from 50 to 1000 µM (50 µM: 2.3 ± 0.9 nm, 100 µM: 2.7 ± 0.7 nm, 1000 µM: 3.9 ± 1.7 nm), with the greatest increase in NP size occurring as the [Au] increased 10-fold.[47] Nevertheless, the NP sizes measured for Au/TiO_2 prepared at 50 and 100 µM suggest the growth phase of the colloids is only mildly impacted at ultra-dilute [Au] concentration. To depict the changes in NP size without operator bias, *ex situ* XAFS were performed on pellets of each sample.

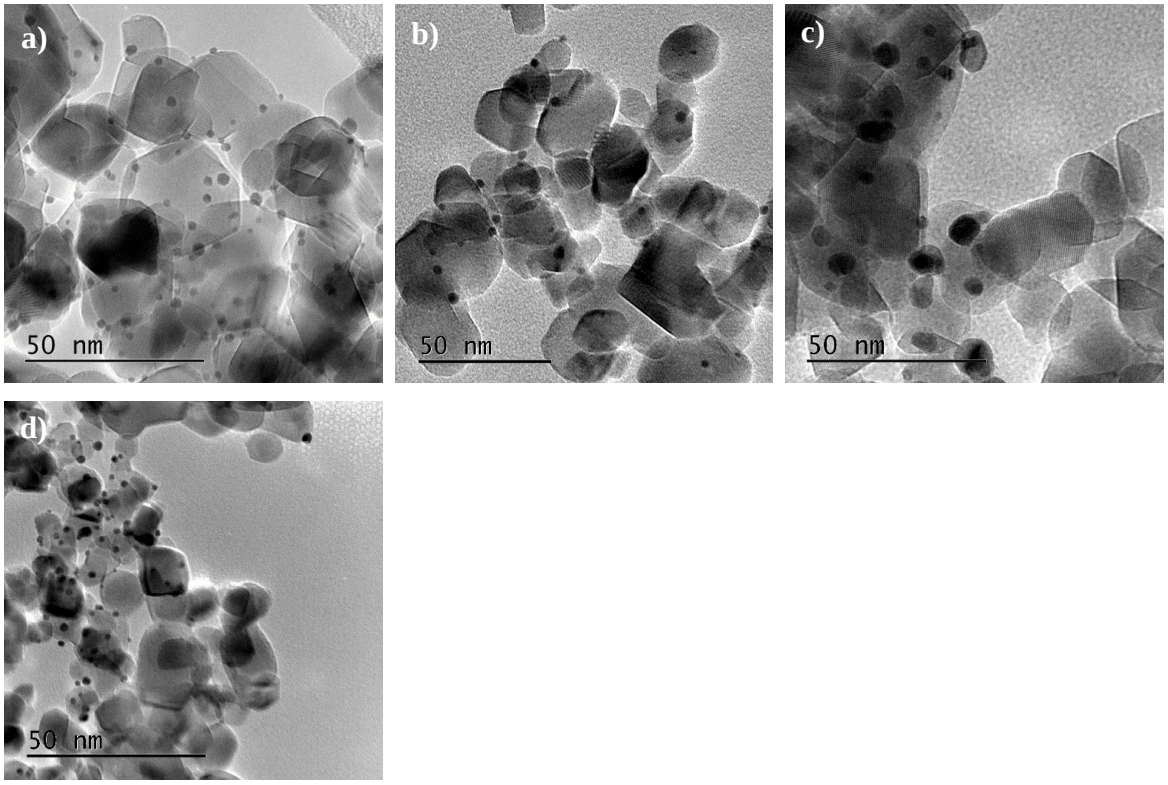

Figure 5-8. *TEM images of the TiO_2 supported Au NPs synthesised under varied synthesis temperature: a) 1 °C, b) 25 °C, c) 50 °C, and d) 75 °C.*

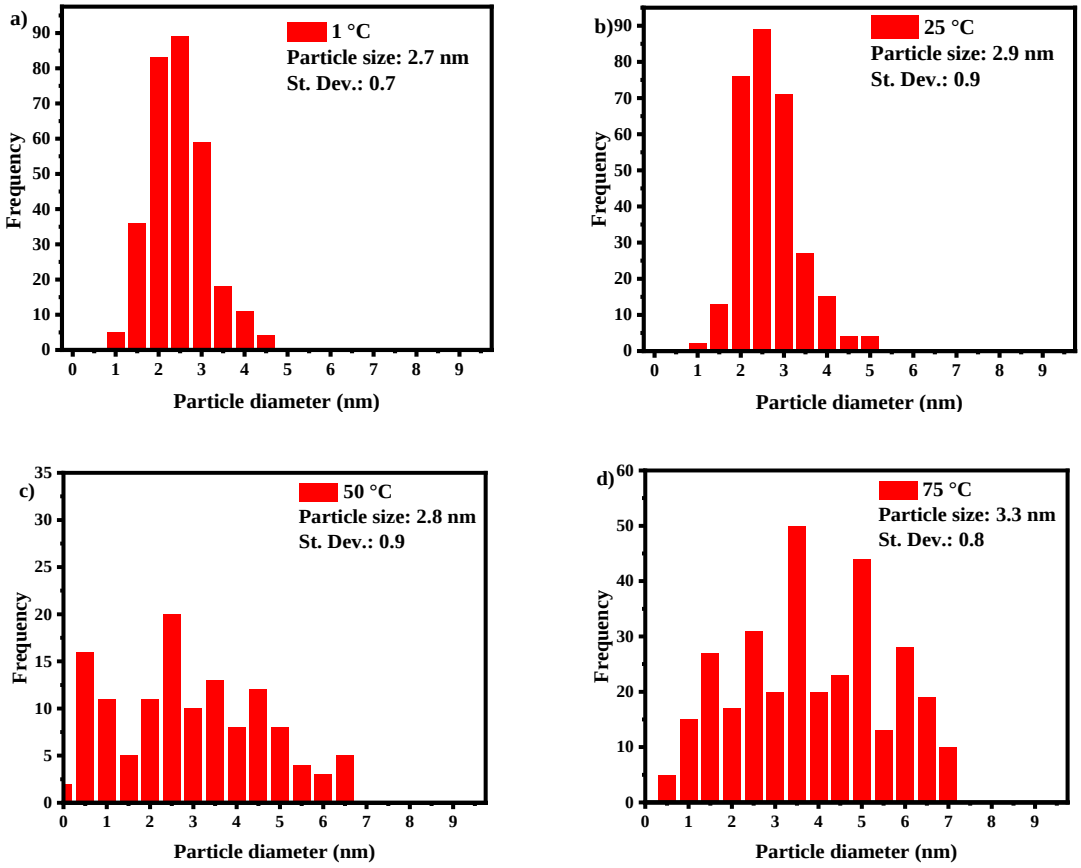

Figure 5-9. *Au particle size histograms for the Au/TiO_2 catalysts prepared under varied synthesis temperatures: a) 1 °C, b) 25 °C, c) 50 °C, and d) 75 °C. All Au particle sizes are calculated from 200-300 Au NPs.*

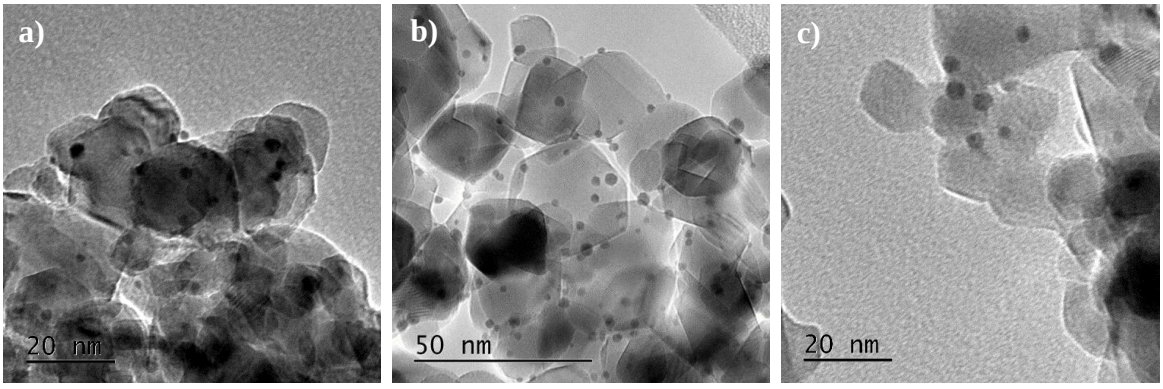

Figure 5-10. *TEM images of the TiO_2 supported Au NPs synthesised with differing [Au]: a) 50 µM, b) 100 µM, and c) 1000 µM.*

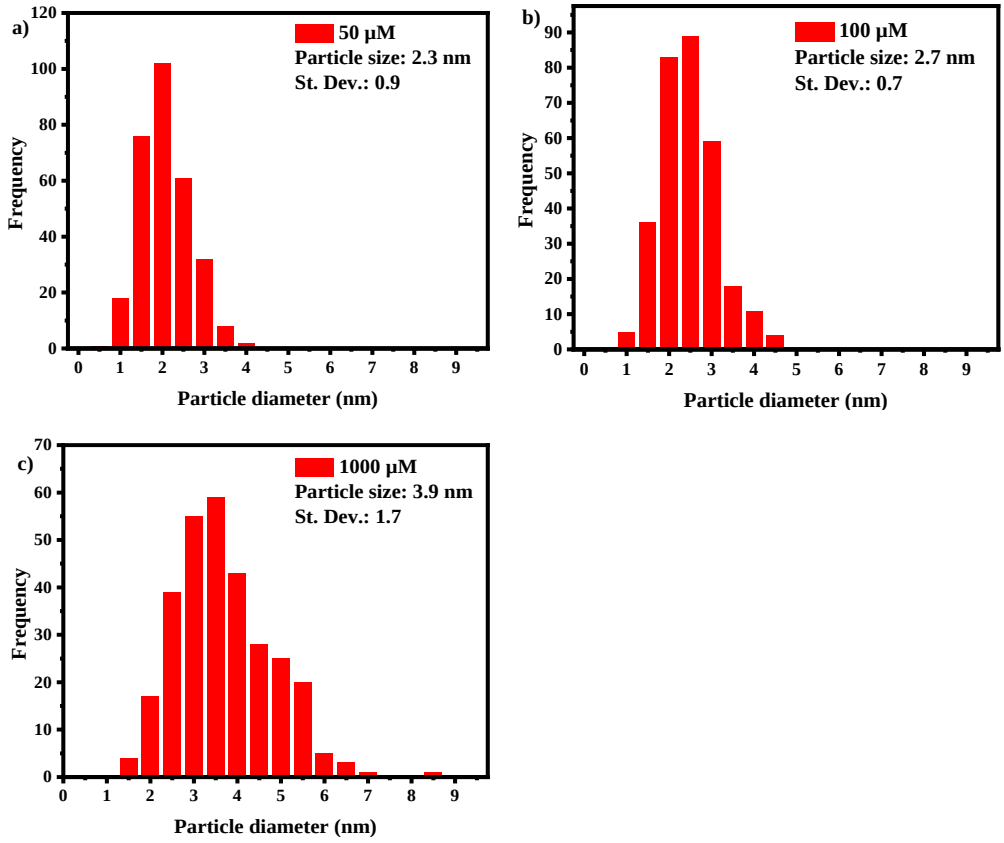

Figure 5-11. *Au particle size histograms for the Au/TiO_2 catalysts prepared with differing [Au]: a) 50 µM, b) 100 µM and c) 1000 µM. All Au particles sizes are calculated from 200-300 Au NPs.*

5.3.4.2 X-ray Absorption Near-Edge Structure

Post immobilisation, there is no evident shift in the rising energy nor any increase in the intensity of the white line peak for all samples, confirming that no change to the metal oxidation state occurs during immobilisation (*Figure 5-12*). The influence of the synthesis temperature on the supported NPs displays the same trend as the colloid, with an increase in intensity of the post edge feature witnessed as the temperature rises (~ 11946 eV).[20,53,54] Au/TiO_2 prepared with increasing [Au] again showed no difference in their XANES spectra, which at first glance suggests the NPs grow in a uniform manner during immobilisation..

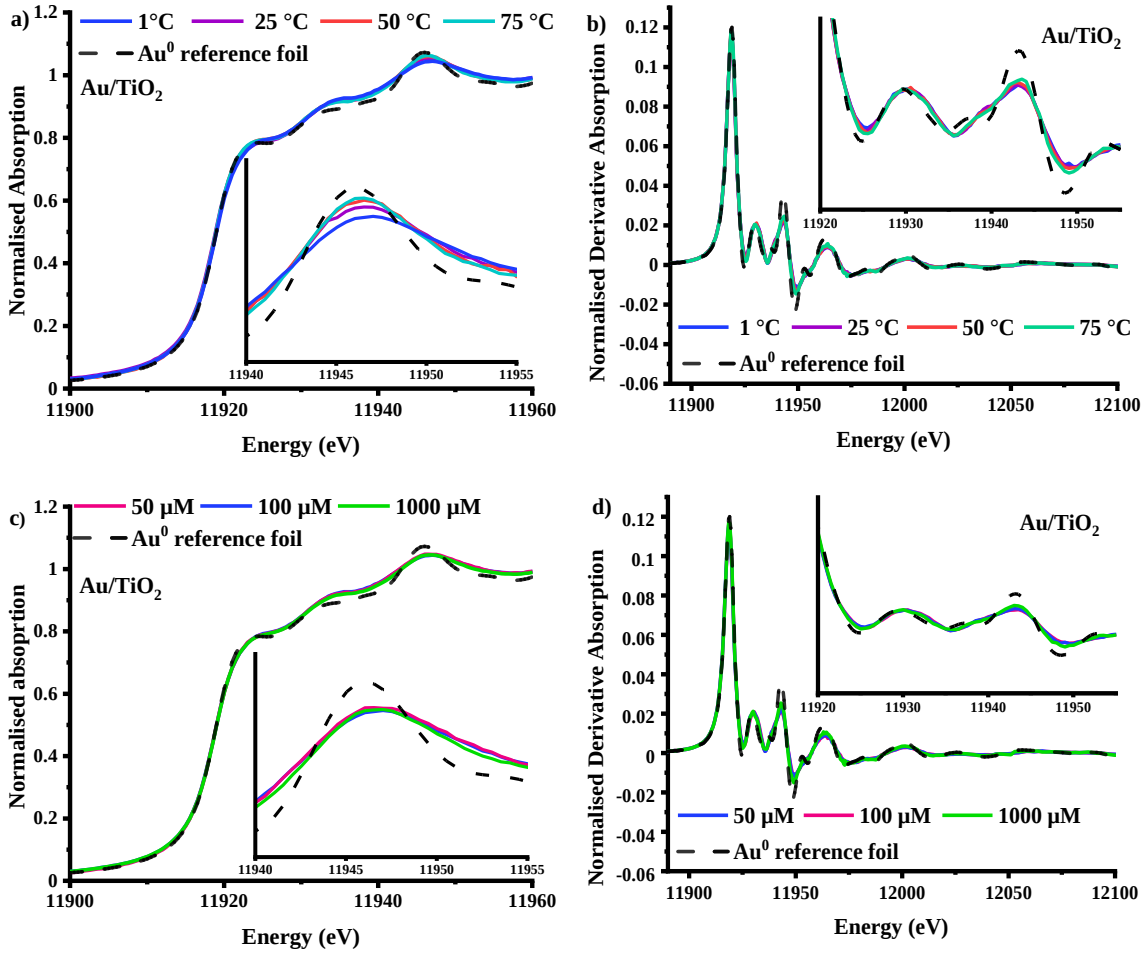

Figure 5-12. *XAFS spectra taken at the Au L_3-edge of the prepared Au/TiO_2 samples; where a) & c) are the XANES spectra of Au/TiO_2 detailing change as a result of increasing synthesis temperature and [Au], respectively, and b) & d) are the normalised 1st derivative of the absorption, respectively.*

5.3.4.3 Extended X-ray Absorption Fine Structure

Immobilisation of the colloidal NPs prepared at increasing synthesis temperature, yielded the same trend in Au-Au scattering observed for the pre-immobilised colloid (1 < 25 < 50 < 75 °C) (*Figure 5-13*a-b); this is consistent with similar synthesis conditions reported in literature.[4] EXAFS analysis of the Au/TiO_2 samples prepared at increasing [Au] display a trend in the Au-Au scattering magnitude that is complementary to that observed *via* TEM, where the abundance of scattering increased from 50→1000 µM [Au] (*Figure 5-13*c-d). The evolution of this trend suggests that the immobilisation procedure plays a larger role in determining NP growth than previously reported for the sol-immobilisation synthesis process.

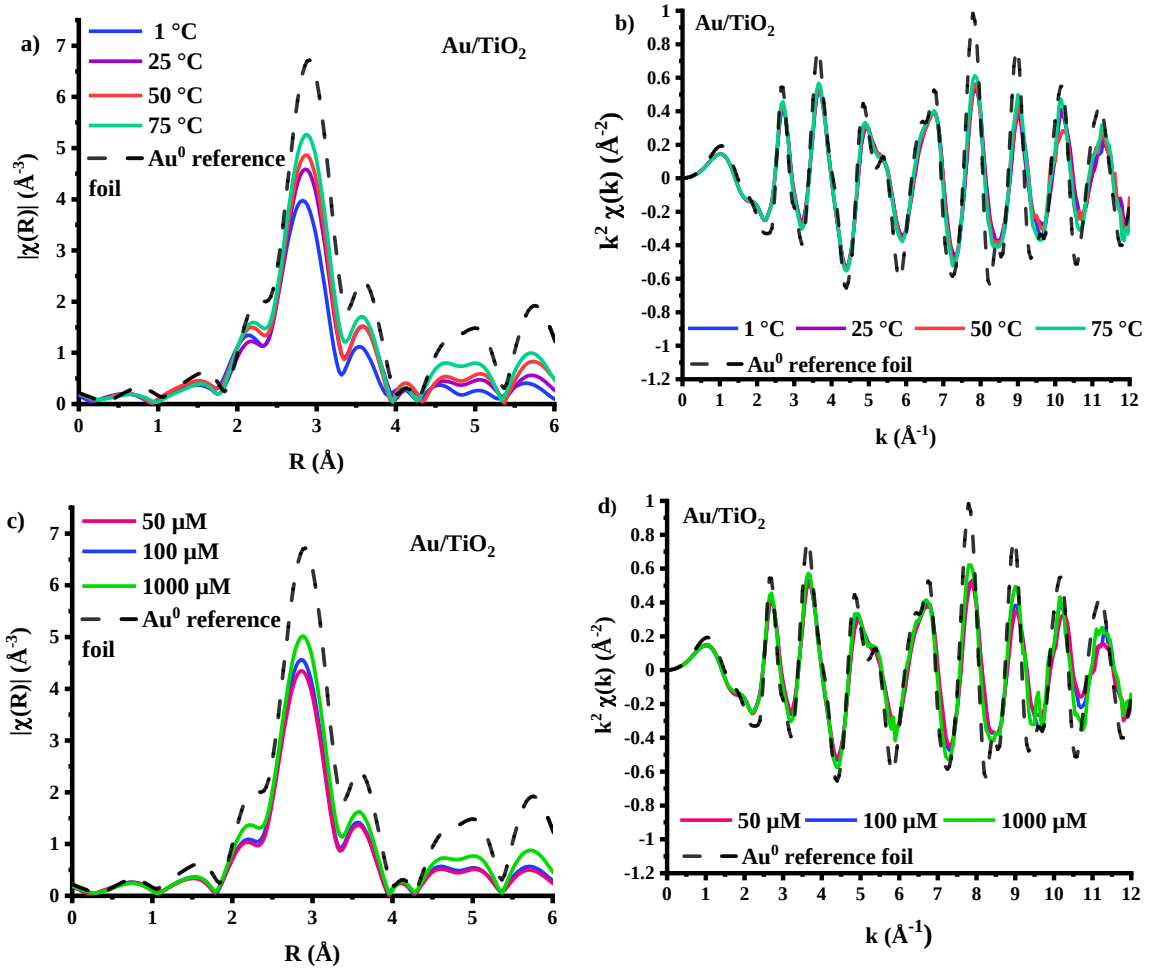

Figure 5-13. *XAFS spectra taken at the Au L_3-edge of the prepared Au/TiO_2 samples; where a) & c) are k^2 EXAFS data for the TiO_2 supported Au detailing change as a result of increasing synthesis temperature and [Au], and b) & d) are the experimental FT χ(k) data of the corresponding EXAFS signals for colloidal Au showing the influence of temperature and [Au].*

5.3.5 Modelling Au NP size from EXAFS coordination numbers

Modelling of the EXAFS data was performed using the 1st shell Au-Au scattering pathway, with full colloidal formation, Au-Cl scattering paths are not present and therefore not used in modelling the EXAFS data. Initial fitting of the Au reference foil with a database *.cif* file for metallic Au (FCC structure, Au CN = 12) gave the amplitude reduction factor (S_0^2) as 0.83. This value was then applied during the fitting of the data in the Artemis software package.[41] Fitting of the experimental EXAFS data gives a quantified interpretation of the average CN structure around the Au absorber (*Figure 5-14*-*Figure 5-16*).

The observed trend in the temperature varied colloidal EXAFS is translated to CN_{Au-Au} increasing from 9.3 ± 0.6 (1 °C) to 10.3 ± 0.7 (75 °C) (*Figure 5-14*). It is apparent that there is no difference in the magnitude of the Au-Au scattering path in the colloidal solutions, which is reflected in the fitting of the EXAFS as the CN are all within error of one another: 50 µM = 9.2 ± 0.9, 100 µM = 9.3 ± 0.6, 1000 µM = 9.4 ± 0.4 (*Figure 5-15*).

Table 5-3. *Au L_3-edge EXAFS first shell fitting parameters for the Au L_3-edge for spectra collected for synthesised colloidal and TiO_2 supported Au NPs. $S_0^2 = 0.83$, was determined by the fitting of an Au foil standard; fit range: colloids $3 < k < 11.5$, $1.74 < R < 3.37$. TiO_2 supported NPs $3 < k < 14$, $1.74 < R < 3.37$. The accuracy of the fit is described by an R_{factor} value, where the confidence of the fit is represented by the smallest value above zero.*

	CN_{Au-Au}	**E_0 (eV)**	**σ^2 (Å^2)**	**R_{factor}**	**R_{Au-Au} (Å)**
Au foil	12 (Fixed)	4.3 ± 0.2	0.008	0.0057	2.85
Colloidal Au Nanoparticles					
100 µM / 1 °C	9.3 ± 0.6	3.6 ± 0.5	0.0108 ± 0.0006	0.0084	2.806 ± 0.005
100 µM / 25 °C	9.8 ± 0.5	4.3 ± 0.4	0.0096 ± 0.0005	0.0061	2.833 ± 0.004
100 µM / 50 °C	10.2 ± 0.7	4.2 ± 0.5	0.0096 ± 0.0006	0.0090	2.839 ± 0.004
100 µM / 75 °C	10.3 ± 0.7	4.4 ± 0.5	0.0090 ± 0.0006	0.0100	2.843 ± 0.004
50 µM / 1 °C	9.2 ± 0.9	3.6 ± 0.6	0.0100 ± 0.0090	0.0180	2.812 ± 0.006
1000 µM / 1 °C	9.4 ± 0.4	4.7 ± 0.4	0.0109 ± 0.0006	0.0006	2.828 ± 0.004
TiO_2 supported Au Nanoparticles					
100 µM / 1 °C	10.0 ± 0.7	4.1 ± 0.5	0.01024 ± 0.0007	0.026	2.836 ± 0.004
50 µM / 1 °C	9.5 ± 0.8	4.2 ± 0.5	0.0104 ± 0.0008	0.0024	2.836 ± 0.005
1000 µM / 1 °C	11.2 ± 0.4	4.6 ± 0.3	0.0095 ± 0.0005	0.0008	2.848 ± 0.003

The relationship between colloidal synthesis temperature and NP size has already been established for different metal NP systems and is thus not considered further.[4,5,58] An increase in the fitted EXAFS CN from the colloidal values is observed as a function of [Au]: 50 µM = 9.5 ± 0.8, 100 µM = 10.0 ± 0.7, 1000 µM = 11.2 ± 0.4 (*Figure 5-16*). Interestingly, the difference between the colloidal and supported CNs also increases as a function of [Au], suggesting that NP growth is affected by the immobilisation process.

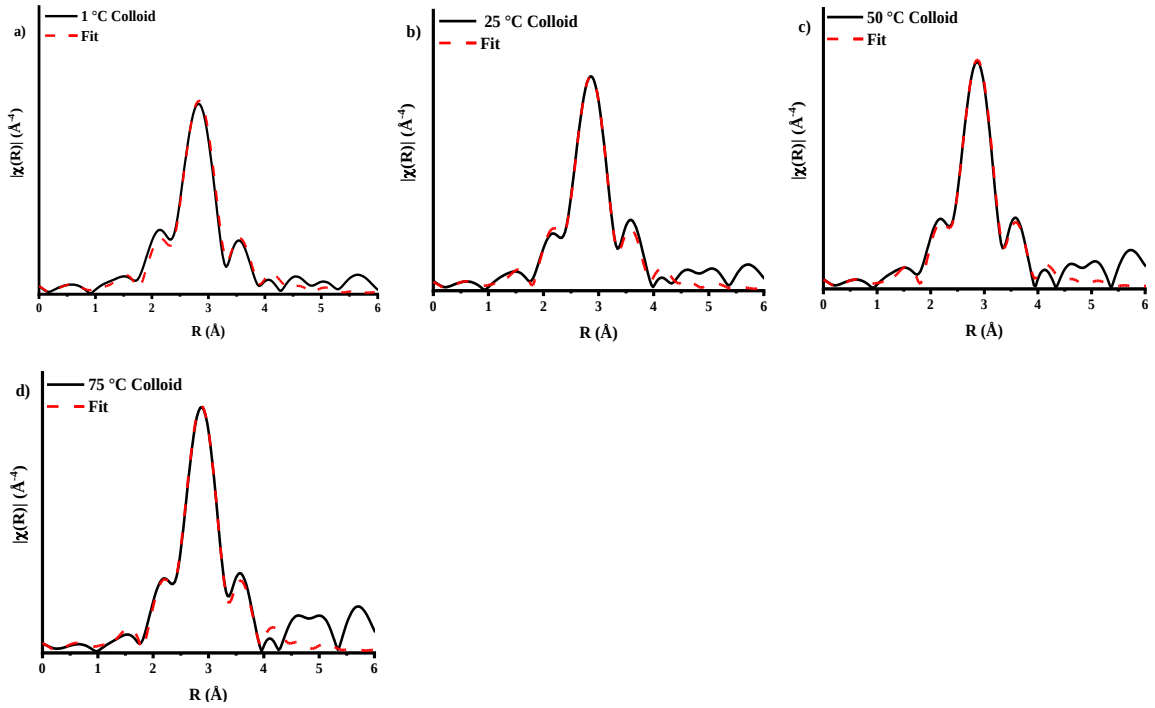

Figure 5-14. *Fitted experimental Fourier transform χ data of the corresponding EXAFS signals for colloidal Au (100 µM) prepared under increasing temperature: a) 1 °C, b) 25 °C, c) 50 °C and d) 75 °C.*

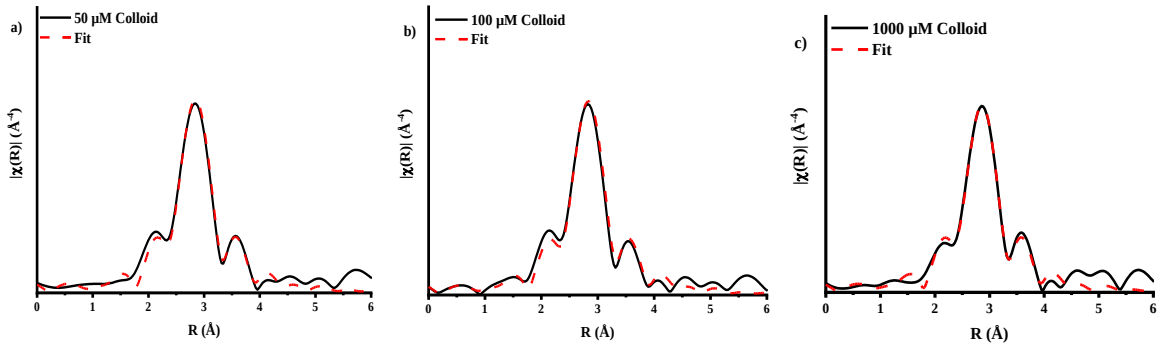

Figure 5-15. *Fitted experimental Fourier transform χ data of the corresponding EXAFS signals for colloidal Au prepared under increasing temperature: a) 50 µM, b) 100 µM, c) 1000 µM).*

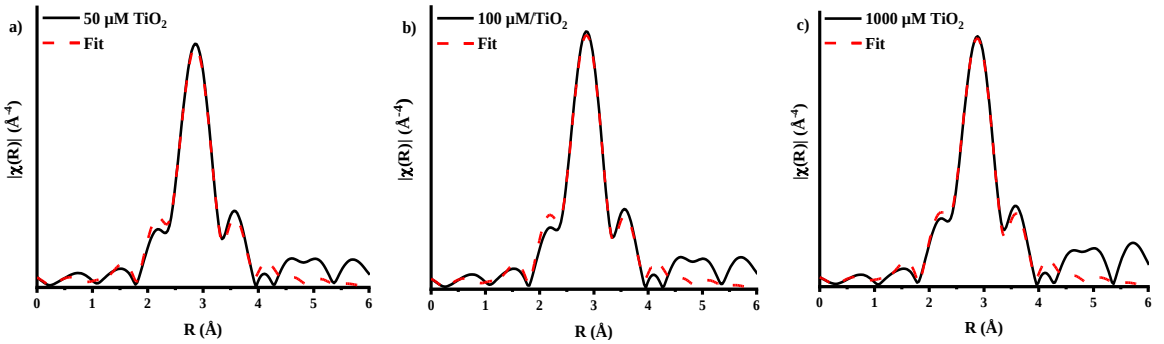

Figure 5-16. *Fitted experimental FT χ data of the corresponding EXAFS signals for TiO_2 supported Au NPs prepared under increasing temperature: a) 50 µM, b) 100 µM, c) 1000 µM.*

The acquired average $CN_{Au\text{-}Au}$ for the colloidal and supported samples was further used to calculate the average Au NP size with greater accuracy than found through TEM measurements alone.[59] Average NP sizes were thus calculated following methods reported by Beale and Weckhuysen.[60] XAFS spectra were modelled based on different particle sizes assuming all Au NPs were; (1) spherical in shape, (2) FFC in packing and (3) smaller than 3 nm in diameter. The equations used in the determination of nanoparticle size and number of atoms within the particle are given below (*Equation 5-1*), calculated NP size values can be found in *Table 5-4* and *Table 5-5*. Fitting of the associated errors in the CN gives an error of ± 0.1 that was applied for all samples.

(i) $$y = \frac{V_{\max} \times x^n}{k^n + x^n}$$

(ii) $$x = \sqrt[n]{\frac{y\,k^n}{V_{\max} - y}}$$

Equation 5-1. *(i) Hill function used to simulate the Au nanoparticle size of the prepared colloidal and TiO_2 supported Au, and (ii) is the equation to determine the number of atoms in a spherical particle; where y is the Au CN calculated from the EXAFS data, x is the number of atoms in a spherical particle with FCC packing structure, V_{max} is the maximum coordination number in the packing structure (FCC = 12), k and n are fixed constants (16.74737 and 0.48934, respectively) for spherical FCC structured NPs with a coordination sphere of < 12.*[60]

Table 5-4. *Calculation of the average Au NP size from the fitted EXAFS colloidal CN_{Au-Au} using the Hill function described by Beale and Weckhuysen.*[60]

	Au Colloids					
	100 µM / 1 ºC	100 µM / 25 ºC	100 µM / 50 °C	100 µM / 75 °C	50 µM / 1 ºC	1000 µM / 1 ºC
y	9.3	9.8	10.2	10.3	9.2	9.4
x^n	13.7	17.7	22.5	24.1	13.05	4
x	209.7	354.7	580.0	665.0	190.4	231.5
Volume[a] (cm^3)	1.9E-21	3.2E-21	5.3E-21	6.1E-21	1.7E-21	2.1E-21
Radius (cm)	7.7E-08	9.2E-08	1.1E-07	1.1E-07	7.5E-08	8.0E-08
Diameter (nm)	1.5 ± 0.1	1.8 ± 0.1	2.2 ± 0.1	2.3± 0.1	1.5 ± 0.1	1.6 ± 0.1

a: Volume was calculated using the density of Au, 19.32 g cm^{-3}

Table 5-5. *Calculation of the average Au NP size from the fitted supported Au EXAFS CN_{Au-Au} using the Hill function described by Beale and Weckhuysen.*[60]

	Au/TiO_2		
	100 µM / 1 ºC	50 µM / 1 ºC	1000 µM / 1 ºC
y	10	9.5	11.2
x^n	19.9	15.1	55.6
x	449.1	256.3	3682.5
Volume[a] (cm^3)	4.1E-21	2.3E-21	3.4E-20
Radius (cm)	9.9E-08	8.2E-08	2.0E-07
Diameter (nm)	2.0 ± 0.1	1.6 ± 0.1	4.0 ± 0.1

a: Volume was calculated using the density of Au, 19.32 g cm^{-3}

Particle sizes obtained from the fits confirmed that, within error of the measurement, adjusting the concentration of the Au, between 50-1000 µM, precursor does not alter the size of the colloidal NPs produced (*Table 5-6*). This is an important observation as it is already known that for sol-immobilisation, increasing the concentration of initial precursor solutions manifests itself as an increase of supported Au NP sizes,[47] where even the smallest increase in the average CN_{Au-Au} expresses itself as a noticeable increase in NP size (*Figure 5-17*). However, it is confirmed by this study that this effect occurs during the immobilisation phase and not in the preformed colloidal NPs.

Table 5-6. *Au SPR band maximum and average NP diameters calculated through TEM and EXAFS analysis.*

Sample notation	Colloidal Au NPs			Au/TiO_2	
	UV-Vis λ_{max} (nm)	Ave. TEM NP Size (nm)	Ave. EXAFS NP Size (nm)	Ave. TEM NP Size (nm)	Ave. EXAFS NP Size (nm)
100 µM / 1 °C	498	3.0 ± 0.9	1.6 ± 0.1	2.7 ± 0.7	2.0 ± 0.1
100 µM / 25 °C	493	-	1.9 ± 0.1	2.9 ± 0.9	-
100 µM / 50 °C	500-510	-	2.2 ± 0.1	2.8 ± 0.9	-
100 µM / 75 °C	538	-	2.3 ± 0.1	3.3 ± 0.8	-
50 µM / 1 °C	492	-	1.5 ± 0.1	2.3 ± 0.6	1.6 ± 0.1
1000 µM / 1 °C	495	4.6 ± 1.5	1.6 ± 0.1	4.0 ± 1.0	2.3 ± 0.1

One possible explanation for this behaviour could be attributed to the mobility of NPs on the support surface. As the synthesis temperature reaches the Hüttig ($T_H = 0.3T_{melting}$ [K]) and Tamman temperatures ($T_T = 0.5T_{melting}$ [K]), the surface atoms and bulk atoms become mobile,[61] constituting a mechanism of particle mobility.[62] For NPs ~ 2 nm in size, as observed in the colloidal solutions, the $T_{melting}$ can be as low as ~ 330 °C,[63] yielding T_H ~ -93 °C and T_T ~ 25 °C.[64] From this, it can be suggested that higher concentration of the

Au precursor ,and subsequent increase in surface NP density, coupled with slow migration of the mobile surface atoms, yields NP growth through Ostwald ripening.[65] Contrary to this, when preparing the colloid with lower [Au precursor], NPs are dispersed with larger interparticle distances, revealing negligible changes to NP size pre- and post-immobilisation.

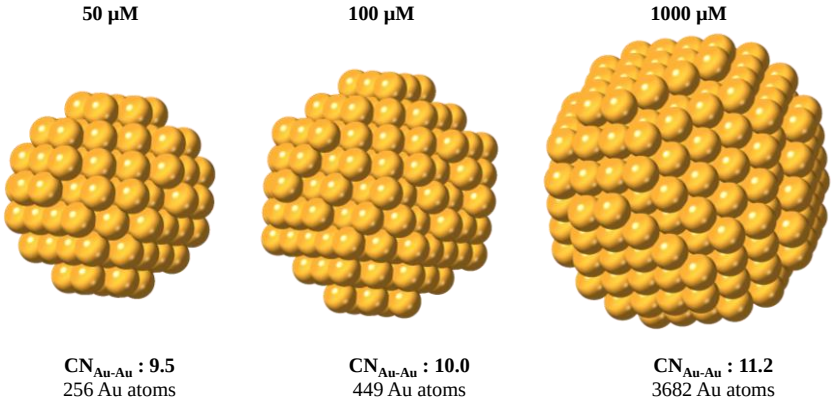

Figure 5-17. *Visualisation of the average supported Au NP sizes for the investigated [Au], calculated using the fitted 1st shell CN$_{Au-Au}$ and modelled based on the methods discussed previously.[37] Images were produced using the CrystalMaker® software package.*

A comprehensive explanation for this behaviour has yet to be given in the literature, but a plausible reason could be associated with a saturation of anchoring sites on the surface of the support, which, in turn, force the coalescence of non-anchored NPs. In the case presented, the general Au wt. % does not change amongst the samples; however, a possible change in local particle density during the immobilisation phase may be what causes the growth in the particles, similar to the phenomenon seen by changing the metal loading.[25] Regardless of the cause for the increase in NP size, it is clear that in order to fully design and optimise supported NPs it is crucial to understand the relatively underexplored immobilisation process; this is a key point in directing the resultant NP properties.

5.4 Conclusions

The work presented in this chapter demonstrates that XAFS is a suitable method to extract quantifiable structural data for ultra-dilute solutions of colloidal Au NPs (50 μM). These studies have revealed several key findings:

(1) Colloidal Au particle size is dependent on the temperature of reduction, with lower temperatures generating smaller particles,

(2) [Au] does not influence the size of the formed colloidal NPs within the range of 50 to 1000 μM,

(3) The immobilisation stage of synthesis primarily influences the Au particle size growth process (*Figure 5-18*).

Therefore, controlling and optimising the immobilisation step is of paramount importance for the use of dilute metal colloidal solutions to synthesise supported metal NPs with uniform size/shape. Furthermore, it is the first study to the author's knowledge which has successfully measured XAFS of colloidal solutions with [Au] < 3 mM. This work acts as a proof of concept for Chapter 6, where the *in situ* generation of colloidal Au is investigated using XAFS spectroscopy.

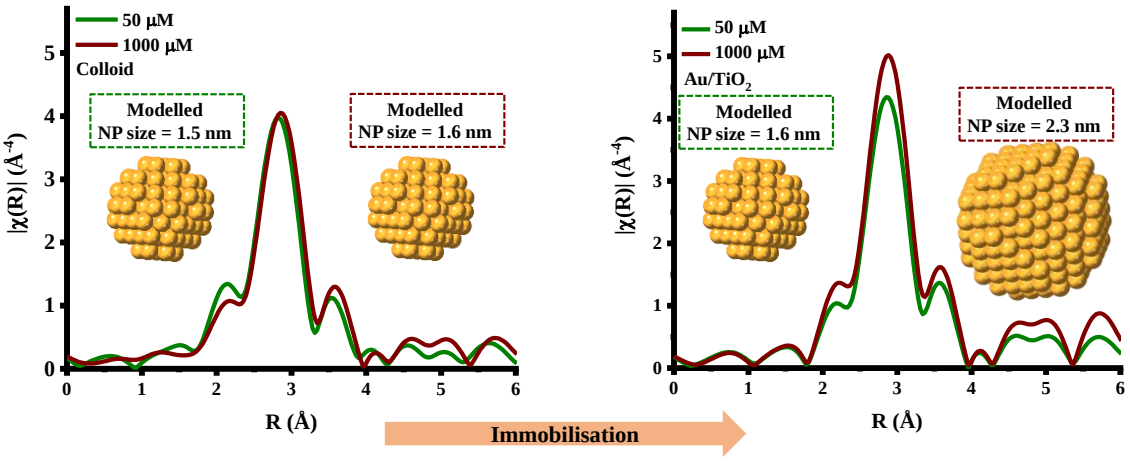

Figure 5-18. *Illustration of the key finding of Chapter 5; the modelled EXAFS Au NP size shows that [Au] does not influence colloidal NP size (left), and the immobilisation process plays a significant role in the growth of supported Au NPs (right).*

5.5 References

1 A. Villa, D. Wang, G. M. Veith, F. Vindigni and L. Prati, *Catal. Sci. Technol.*, 2013, **3**, 3036–3041.

2 L. Prati and A. Villa, *Acc. Chem. Res.*, 2014, **47**, 855–863.

3 J. A. Lopez-Sanchez, N. Dimitratos, P. Miedziak, E. Ntainjua, J. K. Edwards, D. Morgan, A. F. Carley, R. Tiruvalam, C. J. Kiely and G. J. Hutchings, *Phys. Chem. Chem. Phys.*, 2008, **10**, 1921–1930.

4 S. M. Rogers, C. R. A. Catlow, C. E. Chan-Thaw, D. Gianolio, E. K. Gibson, A. L. Gould, N. Jian, A. J. Logsdail, R. E. Palmer, L. Prati, N. Dimitratos, A. Villa and P. P. Wells, *ACS Catal.*, 2015, **5**, 4377–4384.

5 S. M. Rogers, C. R. A. Catlow, C. E. Chan-Thaw, A. Chutia, N. Jian, R. E. Palmer, M. Perdjon, A. Thetford, N. Dimitratos, A. Villa and P. P. Wells, *ACS Catal.*, 2017, **7**, 2266–2274.

6 T. Teranishi and M. Miyake, *Chem. Mater.*, 1998, **4756**, 594–600.

7 A. R. Tao, S. Habas and P. Yang, *Small*, 2008, **4**, 310–325.

8 S. D. Perrault and W. C. W. Chan, *Proc. Natl. Acad. Sci. U. S. A.*, 2010, **107**, 11194–11199.

9 D. Huang, F. Liao, S. Molesa, D. Redinger and V. Subramanian, *J. Electrochem. Soc.*, 2003, **150**, G412.

10 S. D. Brown, P. Nativo, J.-A. Smith, D. Stirling, P. R. Edwards, B. Venugopal, D. J. Flint, J. A. Plumb, D. Graham and N. J. Wheate, *J. Am. Chem. Soc.*, 2010, **132**, 4678–4684.

11 S. Al-Sayari, A. F. Carley, S. H. Taylor and G. J. Hutchings, *Top. Catal.*, 2007, **44**, 123–128.

12 J. Polte, T. T. Ahner, F. Delissen, S. Sokolov, F. Emmerling, A. F. Thünemann and R. Kraehnert, *J. Am. Chem. Soc.*, 2010, **132**, 1296–1301.

13 J. Ohyama, K. Teramura, T. Shishido, Y. Hitomi, K. Kato, H. Tanida, T. Uruga and T. Tanaka, *Chem. Phys. Lett.*, 2011, **507**, 105–110.

14 T. Sakai and P. Alexandridis, *J. Phys. Chem. B*, 2005, **109**, 7766–7777.

15 B. Abécassis, F. Testard, Q. Kong, B. Francois and O. Spalla, *Langmuir*, 2010, **26**, 13847–13854.

16 L. Yang, H. Cheng, Y. Jiang, T. Huang, J. Bao, Z. Sun, Z. Jiang, J. Ma, F. Sun, Q. Liu, T. Yao, H. Deng, S. Wang, M. Zhu and S. Wei, *Nanoscale*, 2015, **7**, 14452–

14459.

17 M. Harada and S. Kizaki, *Cryst. Growth Des.*, 2016, **16**, 1200–1212.

18 T. Shibata, H. Tostmann, B. Bunker, A. Henglein, D. Meisel, S. Cheong and M. Boyanov, *J. Synchrotron Radiat.*, 2004, **8**, 545–547.

19 J. Ohyama, K. Teramura, Y. Higuchi, T. Shishido, Y. Hitomi, K. Kato, H. Tanida, T. Uruga and T. Tanaka, *ChemPhysChem*, 2011, **12**, 127–131.

20 T. Yao, Z. Sun, Y. Li, Z. Pan, H. Wei, Y. Xie, M. Nomura, Y. Niwa, W. Yan, Z. Wu, Y. Jiang, Q. Liu and S. Wei, *J. Am. Chem. Soc.*, 2010, **132**, 7696–7701.

21 M. Harada, K. Saijo and N. Sakamoto, *Colloids Surfaces A Physicochem. Eng. Asp.*, 2009, **349**, 176–188.

22 M. Giorgetti, G. Aquilanti, B. Ballarin, M. Berrettoni, M. C. Cassani, S. Fazzini, D. Nanni and D. Tonelli, *Anal. Chem.*, 2016, **88**, 6873–6880.

23 F. Hubert, F. Testard, A. Thill, Q. Kong, O. Tache and O. Spalla, *Cryst. Growth Des.*, 2012, **12**, 1548–1555.

24 S. Skou, R. E. Gillilan and N. Ando, *Nat. Protoc.*, 2014, **9**, 1727.

25 J. Kennedy, W. Jones, D. J. Morgan, M. Bowker, L. Lu, C. J. Kiely, P. P. Wells and N. Dimitratos, *Catal. Struct. React.*, 2015, **1**, 35–43.

26 B. G. Trewyn, I. I. Slowing, S. Giri, H.-T. Chen and V. S. Lin, *Acc. Chem. Res.*, 2007, **40**, 846–853.

27 S. Ayyappan, R. Srinivasa Gopalan, G. N. Subbanna and C. N. R. Rao, *J. Mater. Res.*, 1997, **12**, 398–401.

28 J. A. Trindell, J. Clausmeyer and R. M. Crooks, *J. Am. Chem. Soc.*, 2017, **139**, 16161–16167.

29 M. Bowker, C. Morton, J. Kennedy, H. Bahruji, J. Greves, W. Jones, P. R. Davies, C. Brookes, P. P. Wells and N. Dimitratos, *J. Catal.*, 2014, **310**, 10–15.

30 M. M. Maye, J. Luo, I.-I. S. Lim, L. Han, N. N. Kariuki, D. Rabinovich, Liu and C.-J. Zhong, *J. Am. Chem. Soc.*, 2003, **125**, 9906–9907.

31 K. R. Brown and M. J. Natan, *Langmuir*, 1998, **14**, 726–728.

32 X.-M. Li, M. R. de Jong, K. Inoue, S. Shinkai, J. Huskens and D. N. Reinhoudt, *J. Mater. Chem.*, 2001, **11**, 1919–1923.

33 M. Boronat and A. Corma, *Langmuir*, 2010, **26**, 16607–16614.

34 B. Roldan Cuenya, M. Alcántara Ortigoza, L. K. Ono, F. Behafarid, S. Mostafa, J. R. Croy, K. Paredis, G. Shafai, T. S. Rahman, L. Li, Z. Zhang and J. C. Yang, *Phys. Rev. B - Condens. Matter Mater. Phys.*, 2011, **84**, 245438.

35 M. Comotti, W. Li, B. Spliethoff and F. Schu, *J. Am. Chem. Soc.*, 2006, 917–924.

36 B. R. Cuenya, *Thin Solid Films*, 2010, **518**, 3127–3150.

37 B. S. Lee, Y. S. Chi, J. K. Lee, I. S. Choi, C. E. Song, S. K. Namgoong and S. Lee, *J. Am. Chem. Soc.*, 2004, **126**, 480–481.

38 J. G. Mesu, A. M. Beale, F. M. F. De Groot and B. M. Weckhuysen, *J. Phys. Chem. B*, 2006, **110**, 17671–17677.

39 S. Hayama, G. Duller, J. P. Sutter, M. Amboage, R. Boada, A. Freeman, L. Keenan, B. Nutter, L. Cahill, P. Leicester, B. Kemp, N. Rubies and S. Diaz-moreno, *J. Synchrotron Radiat.*, 2018, **25**, 1556–1564.

40 M. Newville, *J. Synchrotron Radiat.*, 2001, **8**, 96–100.

41 B. Ravel, in *X-ray Absorption and X-ray Emission Spectroscopy. Theory and Applications*, eds. J. A. van Bokhoven and C. Lamerbiti, Wiley, 2016, p. 283.

42 S. Diaz-Moreno, M. Amboage, M. Basham, R. Boada, N. E. Bricknell, G. Cibin, T. M. Cobb, J. Filik, A. Freeman, K. Geraki, D. Gianolio, S. Hayama, K. Ignatyev, L. Keenan, I. Mikulska, J. Frederick, W. Mosselmans, J. J. Mudd and S. A. Parry, *J. Synchrotron Rad*, 2018, 1–12.

43 V. Amendola, R. Pilot, M. Frasconi, O. M. Maragò and A. M. Iatì, *J. Phys. Condens. Matter*, 2017, **29**, 203002.

44 X. Zhou, G. Liu, J. Yu and W. Fan, *J. Mater. Chem.*, 2012, **22**, 21337.

45 L. Xu, J. Peng, C. Srinivasakannan, L. Zhang, D. Zhang, C. Liu, S. Wang and A. Q. Shen, *RSC Adv.*, 2014, **4**, 25155.

46 T. Hendel, M. Wuithschick, F. Kettemann, A. Birnbaum, K. Rademann and J. Polte, *Anal. Chem.*, 2014, **86**, 11115–11124.

47 N. Dimitratos, A. Villa, L. Prati, C. Hammond, C. E. Chan-Thaw, J. Cookson and P. T. Bishop, *Appl. Catal. A Gen.*, 2016, **514**, 267–275.

48 J. Piella, N. G. Bastús and V. Puntes, *Chem. Mater.*, 2016, **28**, 1066–1075.

49 Diamond Light Source, I20-scanning, https://www.diamond.ac.uk/Instruments/Spectroscopy/I20/XAS_XES_Branchline.html, (accessed 28 April 2021).

50 G. Malta, S. A. Kondrat, S. J. Freakley, C. J. Davies, L. Lu, S. Dawson, A. Thetford, E. K. Gibson, D. J. Morgan, W. Jones, P. P. Wells, P. Johnston, C. R. A. Catlow, C. J. Kiely and G. J. Hutchings, *Science*, 2017, **355**, 1399–1403.

51 X. Liang, Z. Wang and C. Liu, *Nanoscale Res. Lett.*, 2010, **5**, 124–129.

52 Z. Song, J. P. L. Kenney, J. B. Fein and B. A. Bunker, *Geochim. Cosmochim. Acta*,

2012, **86**, 103–117.

53 M. Harada and H. Einaga, *Langmuir*, 2007, **23**, 6536–6543.

54 Y. M. Yiu, P. Zhang and T. K. Sham, *Nanotechnology*, 2003, **3**, 183–186.

55 W. Szczerba, H. Riesemeier and A. F. Thünemann, *Anal. Bioanal. Chem.*, 2010, **398**, 1967–1972.

56 G. Mountrichas, S. Pispas and E. I. Kamitsos, *J. Phys. Chem. C*, 2014, **118**, 22754–22759.

57 S. Hong, H. Hwang and J. W. Kim, *ECS Trans.*, 2018, **85**, 149–158.

58 H. Bahruji, M. Bowker, G. Hutchings, N. Dimitratos, P. P. Wells, E. Gibson, W. Jones, C. Brookes, D. Morgan and G. Lalev, *J. Catal.*, 2016, **343**, 133–146.

59 N. S. Marinkovic, K. Sasaki and R. R. Adzic, *Zast. Mater.*, 2016, **57**, 101–109.

60 A. M. Beale and B. M. Weckhuysen, *Phys. Chem. Chem. Phys.*, 2010, **12**, 5562–5574.

61 J. A. Moulijn, A. E. van Diepen and F. Kapteijn, *Appl. Catal. A Gen.*, 2001, **212**, 3–16.

62 T. W. Hansen, A. T. DeLaRiva, S. R. Challa and A. K. Datye, *Acc. Chem. Res.*, 2013, **46**, 1720–1730.

63 G. Guenther and O. Guillon, *J. Mater. Sci.*, 2014, **49**, 7915–7932.

64 D. James Martin, D. Decarolis, Y. I. Odarchenko, J. J. Herbert, T. Arnold, J. Rawle, C. Nicklin, H.-G. Boyen and A. M. Beale, *Chem. Commun.*, 2017, **53**, 5159–5162.

65 W. Z. Ostwald, *Zeitschrift für Phys. Chemie*, 1900, **34**, 495–503.

Chapter 6 *In situ* Colloidal Au Formation: Monitoring Nanoparticle Growth *via* X-ray Absorption Fine Structure Spectroscopy

Reactor vessels utilised in the sol-immobilisation synthesis of heterogeneous catalysts are predominantly on the macroscale (i.e. round bottom flasks or beakers) and are used for batch synthesis, as performed for the Pd catalysts prepared in Chapters 3 and 4. The preparation of NP catalysts *via* smaller systems (i.e. microfluidic) has become much more prevalent in the search to continuously prepare NP catalysts with greater optimisation of properties than those achievable through batch methods.[1–4] Synthesis using microsized systems is of great benefit in the desire to understand the formation of NPs, in particular the nucleation step(s). Whereby, a process that occurs on a time scale of a few hundred seconds in batch, can be observed much more readily on a microfluidic scale at static time points along a mixing channel.[5]

6.1 Introduction

The continuous synthesis of nanoparticles in microflow devices has been employed largely for both industrial and biomedical research.[6,7] However, the design and implementation of a microfluidic cell is not as straight forward as using laboratory equipment for batch synthesis. The design of the reactor, as well as various process parameters, must be contemplated as they exude the same influence on microfluidic results, similar to the nature of the stabilising and reducing agents in macroscale syntheses (*Figure 6-1*).

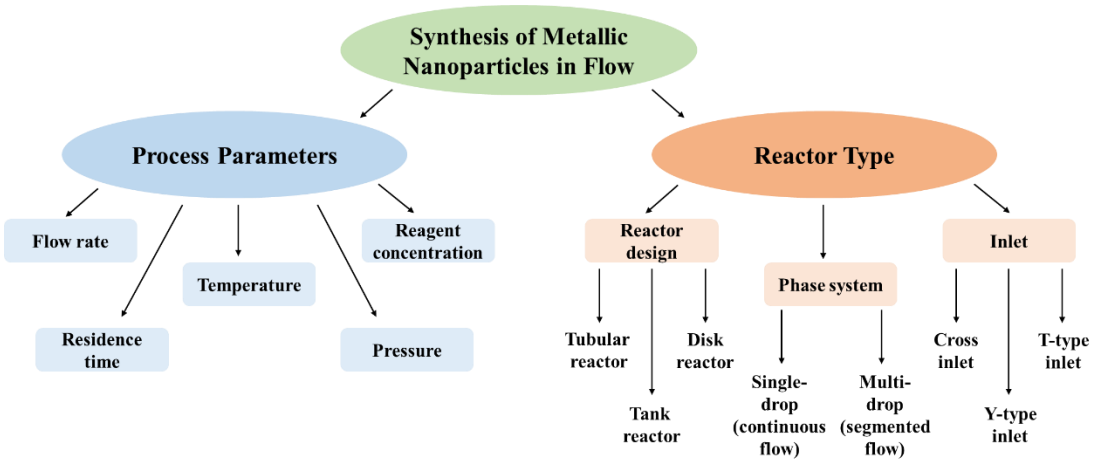

Figure 6-1. *Factors affecting the properties of nanoparticles prepared using flow methods; image modified from Długosz et al., React. Chem. Eng., 2020,* ***5****, 1620.*[8]

6.1.1 Phase System

Manipulation of the flow pattern used in microfluidic systems is one of the most commonly used methods to control the degree of mixing or interaction of the reagent streams; it has been reported that, through systematic changes in the flow pattern, smaller NPs can be formed.[9] Modifications to the property of the flow pattern are referred to as passive mixing and can be separated into two distinct flow regimes: single-drop (continuous flow)[10] and multi-drop (segmented flow).[11] In a single-drop system, the reagent stream(s) flow through microchannels where nucleation and nanoparticle growth occur continuously, ensuring the reaction is as homogenous as possible. In this process, the flow of liquid phases run parallel to one another, drastically reducing the mixing inside the channels, leading to longer residence times, varied NP size distributions and axial dispersions. Fluctuations in the flow rate, resultant of the continuous flow, have been reported to cause variations in the parabolic flow regime which influences the rate of NP growth within the reactor channels. The effect on the growth of NPs is heterogeneous in nature, with the faster inner flow reducing NP residence time and the outer slower flow having the opposite effect (*Figure 6-2*a).[2,10,12] Multi-drop synthesis of nanoparticles involves the use of two or more immiscible fluids in segregated phases, usually comprised of either liquid-liquid flows (e.g. water in oil or oil in water), or liquid-gas flows. The insertion of a secondary phase leads to the formation of immiscible segments within the flow, which act as individual mixing environments (*Figure 6-2*b). The use of a segmented flow system affords greater mixing of the reagents (axial dispersion) as well as reducing fluctuations to the fluid velocity inside of the mixing channel.

Furthermore, the use of a multi-drop system affords narrower residence times for the reaction solution along the mixing channel, reproducibly yielding nanoparticles with uniform, small particle diameters, and reducing the likelihood of contamination and/or fouling.[1,2,9,11]

Both single- and multi-drop flow regimes have significant disadvantageous factors to account for when preparing nanoparticles; however, multi-systems do not offer the same flexibility as continuous flow systems when used for *in situ* measurements. The inserted liquid or gas phase slugs will lead to consistent drops in signal as they pass through the X-ray beam path, imp-acting the success of any *in situ* XAFS measurements.

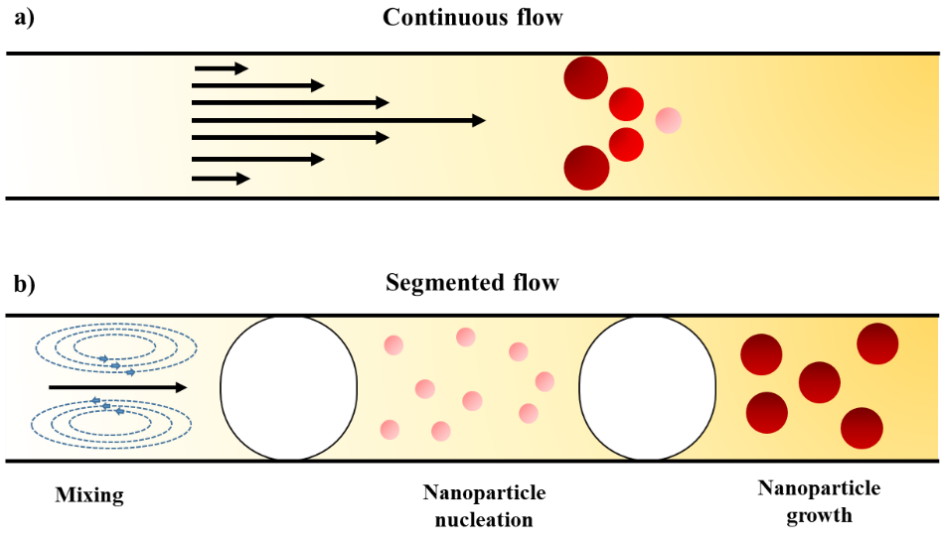

Figure 6-2. *Illustration of the different flow regimes used in the preparation of nanoparticles in microfluidic systems: a) velocity profile of a continuous flow (single-drop) regime inside of a straight reactor channel; the flow rates are shown to increase toward the centre of the reactor channel, b) gas-liquid segmented flow (multi-drop) preparation of nanoparticles, where pockets of reagent mixing are separated by the insertion of a non-miscible phase (i.e. gas), the recirculation phenomena is observable in this method. Time-resolved nucleation and growth of nanoparticles occurs within the liquid slugs along the length of the reactor channel; image adapted from Yen et al., Angew. Chem., 2005,* ***117****, 5583-5587.*[13]

6.1.2 Inlet Design

One of the more important aspects in reactor design is the design chosen for the reactant inlets. Mixing that occurs resultant of the inlet immediately impacts the nucleation process of NPs. Of the available types of inlets, passive mixers offer a cost effective way of

regulating NP size and uniformity by controlling the degree of mixing between the reactant solutions, as well as aiding in minimising the deposition or fouling of solid particles.[14,15] The three types of inlets commonly used are: a) Y-type, b) T-type, where the inlets allow the fluids to come in contact with one another and diffuse, with a single solution outlet, and c) cross connector, where one solution is confined into a thin jet by a second solution perpendicular to the path of the first solution (*Figure 6-3*). Rapid diffusion of one solution into the other is again the cause of mixing, generating movement from the second solution into the thin stream.[16] Hongyu *et al*. reported the production of Ag NPs with narrower size distributions by implementing a T-type inlet over a Y-type. They described this as a consequence of the better mixing profile achieved by the T-type junction.[17] Further to this, the modification of a T-type inlet has been reported by Ameloot *et al*. wherein the highly controlled segmented flow synthesis of metal organic frameworks (MOFs) was achieved by inserting a syringe tip through the inlet, along the longest wall. This syringe tip allowed a metal-ion-containing phase to flow through the centred capillary needle into a mixing zone outside of the inlet. A secondary ligand-containing solution was pumped through the bottom of the junction, once capsules of the first solution came into contact with the second, formation of the MOF occurred.[18]

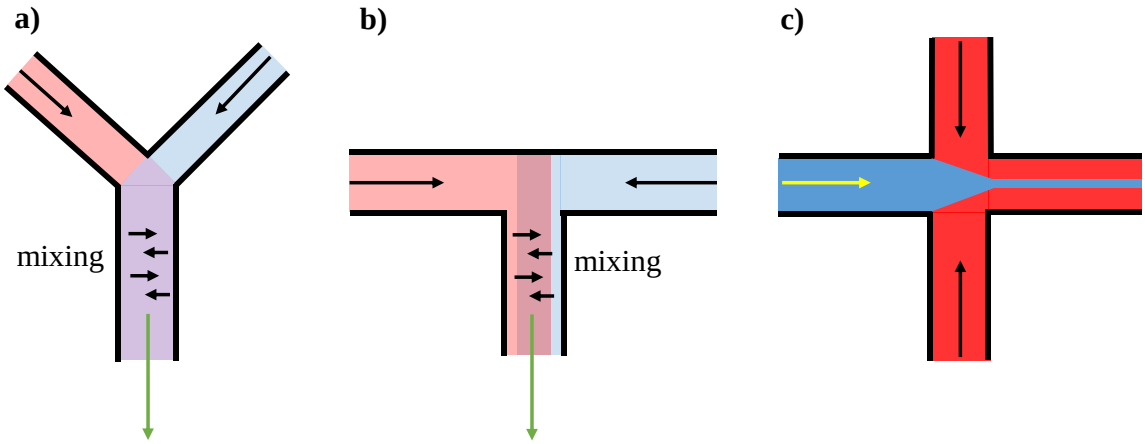

Figure 6-3. *Flow reactor inlet designs used in the preparation of nanoparticles: a) Y-type, b) T-type, and c) cross inlet; image adapted from Długosz et al., React. Chem. Eng., 2020,* ***5****, 1625.*[8]

6.1.3 Reactor Design

Whilst the initial interaction and diffusion of reagent solutions within the inlet is an important factor in nucleating NPs in flow, the subsequent growth of NP clusters can also

be influenced by the design implemented between the inlet junction and the outlet. In much of the literature, the choice of reactor design has focussed on increasing the mixing of the system without external influence, i.e. passive mixing. Passive mixing is implemented by changes to the mixing channel geometry (bending radius, turning angle and channel diameter), and by introducing ridges, grooves and bends into the microreactor channels of the microfluidic device.[6,11,14,17,19–24] Introduction of bends into the reactor channel flow path have resulted in microreactors with shorter mixing channels. Crucially, the extent of mixing is seen to increase from straight to bending channels due to the asymmetrical velocity profile along the channel bend.[24–26] Similarly, the inner diameter of the microreactor channel can be manipulated to control nanoparticle nucleation and growth.[23] Another well utilised strategy to increase reagent mixing is to vary the "smoothness" of the mixing channel by introducing patterned grooves and ridges along its floor and walls, respectively, leading to a constant shift in the velocity profile and enhancing the mixing further.[27]

The ratio of the reactor wall surface area to its volume thus increases as the inner diameter decreases, making an increase in mixing through faster mass and energy exchange in the reactor expected.[28] However, this is not the case, with various groups reporting that constriction of the inner diameter has greater influence on the dispersion of the formed NPs.[8,17,29] Here, it is thought that the greater polydispersity results from a decrease in the interfacial forces between the reagent solutions, impacting transfer of mass and energy. Therefore, for channels with larger diameters, nucleation events occur along the entire reactor volume, whereas on decreasing the inner diameter, there are more instances of precursor solutions coming into contact with the channel surface, thus reducing the number of nucleation and growth processes across the reactor as a whole.[29] It should be taken into account that this decrease in channel diameter can lead to increased instances of fouling on the reactor walls, potentially clogging the microreactor.

6.1.4 Process Parameters

As for batch methods, process parameters (e.g. temperature, pressure, reagent concentrations, flow rates and residence times) exert influence on the size, shape and physical descriptors of the prepared nanoparticles, as well as control process efficiency.[17,19,29] These parameters are discussed in more detail below.

6.1.4.1 Temperature

The relationship of increased colloidal NP size with greater temperatures of synthesis is well established for macroscale processes.[30–34] Similarly, at the microscale, variations in temperature play much the same role in altering NP size.[35–37] An increase in the energy supplied into the system causes larger particles in solution (greater energy stability) to assimilate smaller, less energetically stable particles *via* Ostwald ripening, causing an increase in their size.[38] Furthermore, when higher temperatures are employed, the nucleation rate increases and the formed monomers/ions can diffuse more freely within the solution, influencing the uniformity of NP growth, i.e. NP dispersion.[39] Ahrberg *et al*. described how iron oxide NP size decreases with increasing temperature, however, this was explained as a result of shortened residence times (see section 6.1.4.4).[40] In the synthesis of large NP structures, where constant temperatures are necessary, microfluidic devices offer much greater control of temperature than batch methods. This can be a tricky pursuit due to the excellent heat dissipation of microscale devices with larger surface-to-volume ratios.[28] Control and uniformity of temperature within microfluidic systems is achievable, either by submerging the mixing channel into oil baths at constant temperatures, or by subjecting specific points or regions along the mixing path to different temperatures.[26,36,41]

6.1.4.2 Pressure

Exerting external pressure onto microscale systems to monitor and adapt the flow profile within a microfluidic device is one of the more commonly utilised methods to influence NP size. Three main types of pressure controller are used:[6]

(1) Compressed air is used to pressurise a reagent reservoir connected to the mixing channel through various tubes, and moves through the cell into the channel *via* a pressure gradient.

(2) Non-mechanical energy based controllers manipulate pressure *via* passive methods which are quite simple to implement and, as no external pumps are used, pulse-free low flow rates can be achieved;[28] however, this method does not afford quantitative control over the flow rate. One example of this is capillary action, where the interplay between the surface tension of a liquid and the geometry and surface chemistry of the solid cause a pressure difference in the channel to induce flow from the inlet to the outlet.[42] Therefore, as the diameter of the channel decreases, an increase in the capillary induced pressure is observed.[43,44]

(3) Mechanical energy based controllers use mechanical pumps (peristaltic and syringe pumps) to dispense the desired volume of solution into the microreactor channels. For peristaltic pumps, the creation of a vacuum by compressing the tube as it passes over a roller, draws liquid through the tube and towards the cell. Unfortunately, it can cause pulsing of the solution through the system which can be problematic in continuous flow synthesis.[28] Syringe pumps offer a more user friendly approach to liquid dispensing than peristaltic pumps, with many models monitoring the flow rate accurately by modulating the volume and dispensing speed of a syringe with the power of the internal motor,[6,28] and, importantly, they can be used in conjunction with multiple syringe pumps if required.[18]

6.1.4.3 Reagent Concentration

Synthesis of nanoparticles under varied reagent concentrations is one area of microfluidics that is lacking in literature. In the limited studies, increase in the metal precursor salt concentration appears to have negligible impact on formed nanoparticle size. Zhang *et al*. reported the preparation of Cu NPs in a continuous flow reactor and reasoned that "…*insensitivity of particle size and size distribution to the reactants concentration may be interpreted as a result of the very fast and efficient mass diffusion of reactants in the microfluidic reactor"*.[45] Furthermore, with faster and more efficient mixing, the radial concentration of gradients is minimised and the nucleated metal atoms have similar opportunities to aggregate, regardless of the metal concentration.[45,46] This is also reported by Hossain *et al*. in the controlled production of Pt NPs, wherein they showed that no change in the average Pt NP size occurred on increasing the [H_2PtCl_6] from 1 to 4 mM, but at 10 mM, larger NPs were observed; they rationalised that this was due to incomplete reduction of the metal salt solution by the reducing agent.[38] Contrary to this, the lower mixing efficiency in batch vessels is understood to be a contributing factor in NP growth at elevated [metal].[47,48] For segmented flow reactors, the literature suggests that NP size can be influenced by the concentration of the metal precursor in solution: an increase in more than one order of magnitude causes fast precipitation of large amounts of NPs, which can aggregate and block the reactor channels.[40]

6.1.4.4 Flow Rate and Residence Times

Fine-tuning of the flow rates used in microreactors can be utilised to influence NP growth, and impacts both the time taken for the synthesis solution to move through the microreactor

(residence time), and the mixing profile inside of the reactor walls (i.e. laminar or turbulent flow). Simply put, the residence time increases as the flow rate decreases (*Figure 6-4*), meaning NP size and shape can change to a greater extent under prolonged mixing.[19,36] Conversely, in segmented flow systems, the efficient mixing within isolated pockets reduces the residence time of the process.[13,49,50]

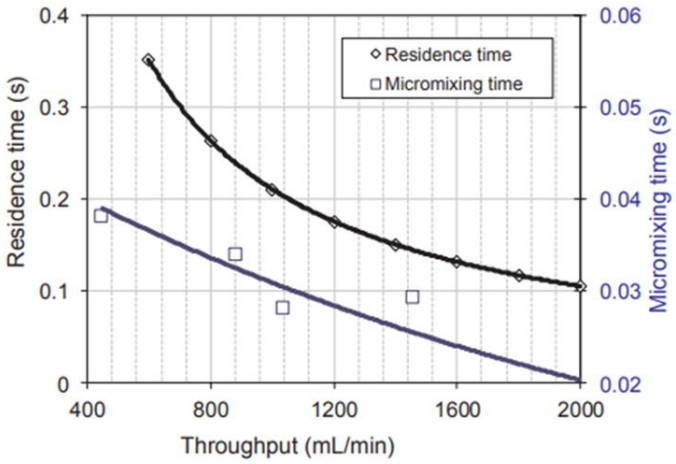

Figure 6-4. *The correlation between residence time and micromixing time in a static microreactor; image taken from X. Guo et al., Exp. Therm. Fluid Sci., 2018,* ***99****, 407-419.*[51]

Another key aspect with respect to flow rates is the mixing pattern inside the reactor walls. This is described by the Reynolds number, Re, which offers a dimensionless description of the ratio of inertial forces to viscous forces within a fluid (*Equation 6-1*); laminar flows have a Re < 2100, turbulent flow have a Re > 2100.[52,53]

$$\mathrm{Re} = \frac{\rho\, v\, L}{\mu}$$

Equation 6-1. *Mathematical expression for the Reynolds number, where ρ is the fluid density, μ is the dynamic viscosity, v is the flow velocity, and L is the length of the channel.*

In laminar flows, diffusion is the driving force behind mixing, producing non-uniform flow profiles, i.e. slower at the reactor walls and faster at the centre of the channel (*Figure 6-5*a). For turbulent mixing, non-uniform velocity profiles are again present, however, they result in stretching and thinning of the fluid lamellae, reducing diffusion distances and increasing the extent and speed of mixing (*Figure 6-5*b). The flow velocity with a cylinder is defined as the volume of fluid passing through a set area during a period of time, and is described as

$v = V / t$, where V is the volume and t is the elapsed time. The relationship between the flow velocity and the flow rate is defined as $v = A\,\bar{v}$, where A is the cross-sectional area within the mixing channel cylinder and $\bar{v}$ is the average velocity of the liquid. Within the flow velocity equation, A can be further substituted for πr^2 (*Equation 6-2*).

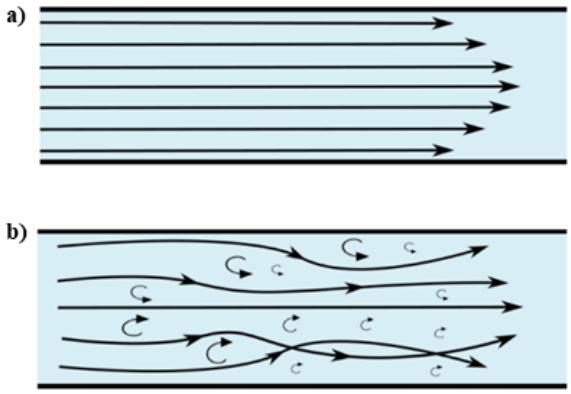

Figure 6-5. *Diagram showing the flow profile within a tubular channel when under a) laminar and b) turbulent mixing; image taken from CFDsupport.*[54]

$$v = \frac{\bar{v}}{\pi r^2}$$

Equation 6-2. *Relationship between the flow velocity and the average flow rate within a cylinder, where v is the flow velocity, $\bar{v}$ is the average velocity of the liquid (flow rate) and r is the radius of the cylinder.*

In microreactors, the small channel diameters generally produce low Reynolds numbers making the flow profile mainly laminar with mixing *via* diffusion. Diffusional transport in mixing channels is described by Fick's Law (*Equation 6-3*); it can be used to find the mixing time of the reaction, which is the time taken to reach homogeneity between the reagent solutions along the mixing channel. From Fick's Law, mixing time is found to be related to the distance that one solution has to diffuse to interact and mix with a second solution. Improved mixing is thus achievable by decreasing the diffusion distance.[55]

$$t \propto \frac{d_t^2}{D}$$

Equation 6-3. *Fick's Law, where t is the mixing time, d_t is the lamella width and D is the diffusion coefficient.*

6.1.5 *In situ* Investigations of Nanoparticle Formation

Utilisation of non-destructive X-ray based techniques has become a very beneficial tool in mapping the initial processes that occur in NP formation, namely small angle X-ray scattering (SAXS) and X-ray absorption fine structure (XAFS).[5,56–61] SAXS is a very useful technique to employ in the characterisation of colloidal NPs and has been combined with *in situ* XAFS in multiple studies.[56,57,62,63] SAXS, much like dynamic light scattering, is seen as a straight forward and easy to use analytical method, and is commonly employed in the determination of monodispersed NPs. However, to analyse polydisperse solutions, additional methods are required; these methods are dependent on several factors such as the ease of implementation prior knowledge of size and shape variance within the solution and the concentration of particles.[64] In many cases, analysis is performed when particle sizes or shapes are assumed to be fixed.[56,65,66] Nonetheless, Polte *et al*., used a combined SAXS/XAFS experiment to observe the formation of Au NPs using a citric acid method *in situ*.[56] This work allowed the mechanism of NP formation to be presented with greater clarity, by describing different steps for NP growth *via* both nuclei coalescence and further monomer attachment. However, due to the size limitations previously discussed for scattering techniques, the spectral analysis could not adequately reveal information pertaining to nuclei formation.

The energy region surrounding the edge jump of the XAFS spectrum, XANES, has been used in time-resolved experiments to observe the reduction and growth of colloidal NPs for various metal systems.[65–70] The elegant experiments presented in the referenced studies describe reduction through changes to the oxidation state of the metal absorber *via* alterations in the element specific absorption edge intensity and scattering features after the white line in XANES. To truly understand the fundamental processes involved in NP formation, the change undergone to the nearest neighbours of a single metal atom must also be determined. For this, the higher energy XAFS region, EXAFS, has been interrogated for aqueous NPs, albeit in limited instances.[65–67,71] These beneficial studies have focussed on the formation of NPs using mild reducing agents and metal concentrations > 3 mM,[72,73] and so are measured over long periods of reduction (up to 90 minutes).[69] The limited number of beamlines capable of giving the time resolution necessary to follow the kinetics of reduction using strong reducing agents, i.e. $NaBH_4$, means that accurate *in situ* measurements of sol-immobilisation synthesis using $NaBH_4$ are severely limited due to its high reducing

efficiency; the [Au] investigated was 4.6 mM,[74] far from typical [Au] used in commercially relevant syntheses, e.g. 0.1 mM.[75]

Alongside the choice of characterisation techniques, the materials and flow regime used in fluidic reactor systems must be considered. Firstly, the incorporation of materials with high surface energies increase the likelihood of interaction, detrimentally increasing instances of nucleation and NP growth. In many cases, this can lead to metal deposition on the walls of the fluidic reactor. For *in sit*u XAFS measurements, the deposition of formed NPs can be mitigated through the use of an optimal flow regime, moving the formed colloid at a constant speed through the cell and path of the X-ray source beam. This is especially prevalent as the high sensitivity needed to measure NP nucleation requires high intensity X-rays from synchrotron sources, which can cause beam damage and artificial agglomeration of the NP species.[76]

The work presented in this chapter continues from the work published in Chapter 5.[30] Here, the ability to measure ultra-dilute colloidal solutions ([Au] $\leq$ 100 μM) was established in order to measure the *in situ* reduction of a $HAuCl_4$ precursor solution using dimethylamine borane. The experiment performed followed the same Au NP synthesis outlined in the previous chapter, however, the nature and conditions of the reducing agent were altered to ensure a more mild reduction than that achieved using $NaBH_4$. SPR band positions in different colloidal Au solutions were characterised using UV-Vis spectroscopy. XRF measurements were used to analyse the potential fouling of Au on the mixing channel following colloidal synthesis. XAFS measurements were performed *in situ* to measure the reduction of the Au precursor salt solution at distinct points along a mixing channel.

6.2 Experimental

6.2.1 Colloidal Au Nanoparticle Synthesis

Colloidal Au nanoparticles were synthesised in this chapter following the same primary procedure as described for the batch colloids (Chapters 3, 4, and 5). However, the focus of the *in situ* measurements was not on how alterations to the synthetic protocol influences NP size, but instead focussed on the formation of Au colloids *in situ*. For this, a dual syringe pump system was employed (comprised of one Aladdin AL-1000 single syringe pump and one AL-4000 dual syringe pump). The single syringe pump contained the PVA capped precursor salt, $HAuCl_4$, in solution ([Au] = 100 μM, PVA:Au (wt/wt) = 0.65, 0.01 g mL). The second syringe pump was used to control the flow of the reducing agent solution (either $NaBH_4$ (0.1 M) or DMAB (0.1 M)). Both syringes were kept at room temperature for the experiments. Optimal flow rates were calculated to produce an annular flow regime, with the inner flow comprised of the capped precursor solution and the outer flow composed of the aqueous reducing agent.

Fouling was prevalent during the initial microfluidic synthesis of the colloidal NPs, so two different routes were employed to limit the deposition of Au NPs onto the lining of the tubing: (1) mixing the reducing agent with NaOH (0.15 M) to suppress the rate of $NaBH_4$ or DMAB decomposition, and (2) coating the reactor walls and mixing channel with a pre-prepared fluorinated oil composed of 1*H*,1*H*,2*H*,2*H*-perfluoro-1-octanol (PO) and octadecafluorodecahydronaphthalene (PFD) 10 % v/v PO in PFD (*Figure 6-6*).[4]

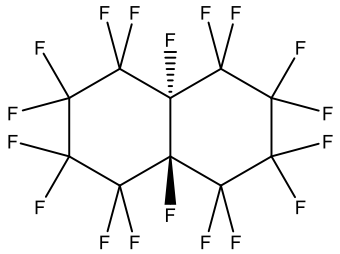

Octadecafluorodecahydronaphthalene (PFD)

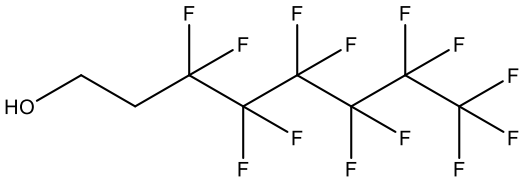

1*H*,1*H*,2*H*,2*H*-perfluoro-1-octanol (PO)

Figure 6-6. *Component chemicals for the fluorinated oil (10 % v/v PO in PFD) used to coat the walls of the microfluidic cell to prevent deposition of Au NPs onto the wall surface during measurements.*

6.2.2 UV-Visible Spectroscopy

UV-Vis spectroscopy was used to give an indication of colloidal Au nanoparticle sizes *via* the position of the SPR band relative to other colloidal Au catalysts prepared (λ_{max}).[72,77,78] The position and broadness of the SPR bands were dependent on the various parameters applied during synthesis.[30,72] Briefly, changes made to the reducing agent employed, the solvation of the reducing agent in varying [$NaOH_{(aq)}$]. Reduction of $HAuCl_4$ and formation of colloidal Au SPR bands were recorded using a Shimadzu UV-1800 spectrometer. Samples were analysed in a quartz cuvette post mixing of the syringe solutions within the cell's mixing channel.

6.2.3 X-ray Fluorescence Measurements

XRF analysis was employed to measure the polyimide tubing used in the design of the microfluidic cell for *in situ* measurement of Au NPs. Samples were prepared by cutting the tubing (inner diameters (ID): 0.64, 0.32 and 0.16 cm) into five distinct sections, each 2 cm in length, and then slicing these small pieces of tubing in half lengthways. These were then placed into holders with Mylar polyester thin film windows (Chemplex Industries Inc.), where trace impurities of Ca, P, Fe, Zn, Cu, Zr, Ti and Al are present. The sample holders were then loaded into a PANalytical Epsilon3-XL X-ray fluorescence spectrometer, and elemental analysis of Au deposition was performed. The measurements were acquired at the ISIS Materials Characterisation laboratory at ISIS Neutron and Muon Source, Didcot, U.K.

6.2.4 Hydrolysis Measurements of Sodium Borohydride

The evolution of hydrogen during $NaBH_4$ hydrolysis was monitored in solutions of H_2O and NaOH (Supelco). These measurements were performed by preparing solutions of $NaBH_4$ (0.1 M, granular, Merck), using either deionised water (18.2 MΩ cm) or $NaOH_{(aq)}$, where [$NaOH_{(aq)}$] = 0.05, 0.1, 0.15 and 0.2 M, in 100 mL plastic syringes (BD Plastipak). The syringes were capped using PTFE stoppers and left for 50 minutes, the average length of one fluorescence scan on I20-Scanning, DLS, Didcot, U.K. The extent of decomposition for each solution was determined by reading the fluid level markers on the syringe.

6.2.5 X-ray Absorption Fine Structure Measurements

In situ XAFS measurements of colloidal Au NP formation were acquired on the I20-Scanning beamline at DLS, Didcot, UK. Samples were measured in fluorescence mode using a Si(111) four-bounce monochromator and the data were collected through a 64 element Ge fluorescence detector with the Xspress2 digital pulse processor.[79] Scans were performed at a time resolution of 18 min spectrum^{-1} (XANES only), with 4 scans performed at each position. Processing of the absorption spectra was accomplished using the Demeter software package (Athena), where the acquired datasets at each point where merged and aligned using a Au^0 reference foil.[80]

6.2.5.1 I20-Scanning Experimental Set-up

XAFS measurements of colloidal Au NPs at the Au L_3-edge were performed on the scanning branch of the I20-Scanning beamline at DLS, Didcot, U.K. A dual syringe system was employed, where syringe 1 dosed $HAuCl_4$ ([Au] = 100 µM) and PVA, flow rate = 0.4 mL min^{-1} (1 × 30 mL syringe), and syringe 2 delivered DMAB ([DMAB] = 500 µM) dissolved in $NaOH_{(aq)}$ ([NaOH] = 0.15 M), flow rate = 1.6 mL min^{-1}, dual syringe pump using 2 × 60 mL syringes (*Figure 6-7*). The solvation of the mild reducing agent in NaOH was performed to further suppress any undesired H_2 evolution, mitigating any signal loss resultant from bubbling along the data acquisition region. Prior to XAFS acquisition the issue of fouling was addressed, here the mixing zone and cell tubing were purged with the aforementioned fluorinated oil.[4] Both solutions were pumped toward the mixing zone through 0.16 cm (ID) PTFE tubing; the mixing channel was comprised of polyimide tubing (ID = 0.16 cm, wall thickness = 0.005 cm, length = 10 cm).

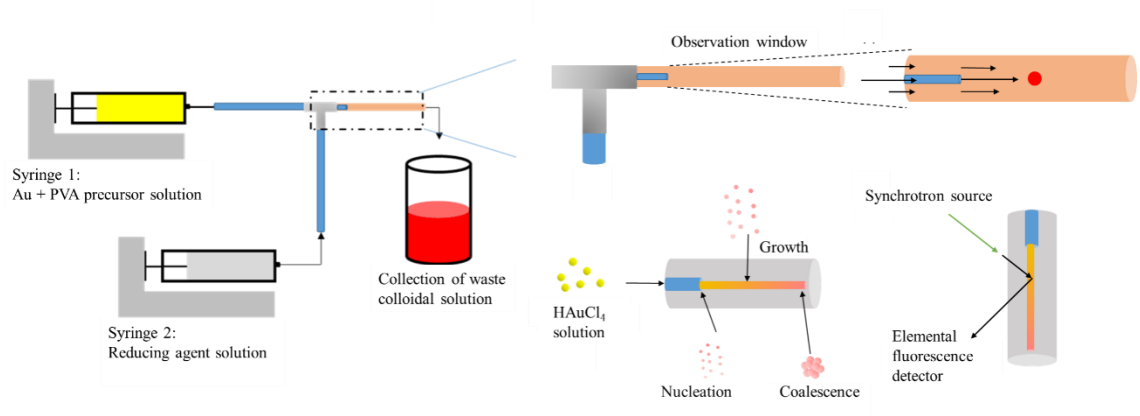

Figure 6-7. *Graphical representation of the in situ XAFS experiment performed on the I20-Scanning beamline at DLS, Didcot, U.K. Both the precursor salt and reducing agent solutions are delivered via syringe pumps to a T-junction, where the formation of the colloid takes place.*

XAFS data were acquired by measuring three points along the mixing channel, each separated by 3 cm (*Figure 6-8*): the beginning (Position 1), the middle (Position 2), and the end (Position 3). To prevent fouling of the mixing channel outlet, 0.16 cm ID PTFE tubing was attached to the outlet using a 0.20 cm ID PTFE connector, which moved the prepared colloids toward a waste beaker. After each measurement, the system was flushed with water through both syringe pumps and the polyimide tubing was replaced. Before the next XAFS measurement was collected, the prepared fluorinated oil was purged through the system *via* syringe pump 1 (i.e. coating the tubing used to cycle the Au precursor solutions).

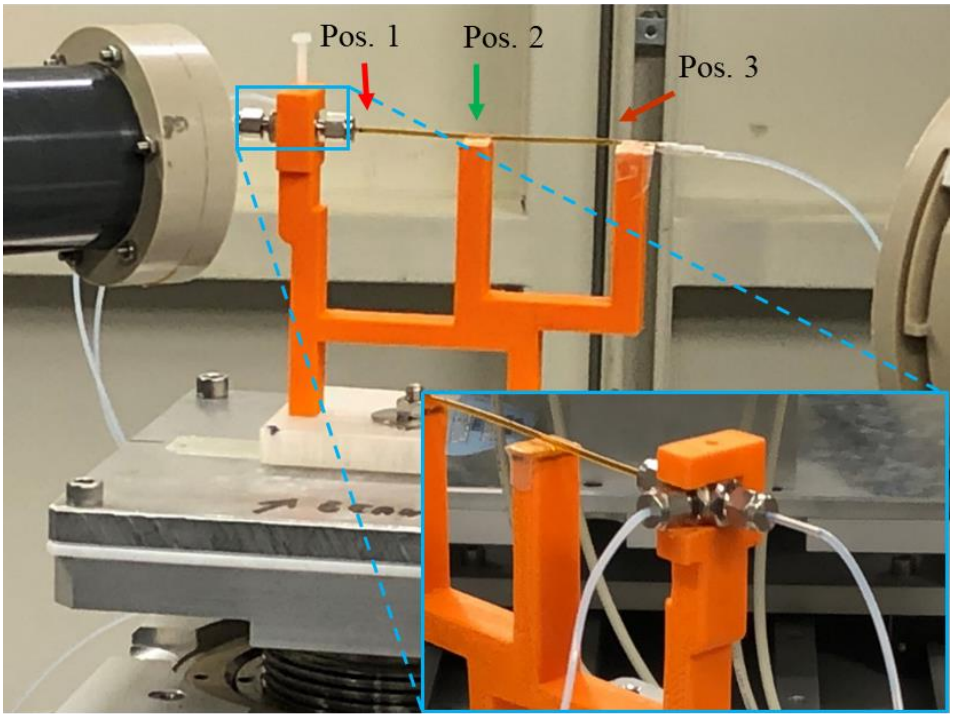

Figure 6-8. *Image depicting the static positions for XAFS acquisition at the beginning (Pos. 1), middle (Pos. 2) and end (Pos. 3) of the mixing zone. A front view of the T-junction in the 3D printed holder is also shown.*

6.3 Results and Discussion

Understanding the primary nucleation and growth steps involved in NP formation is crucial in the mass production of tailored NP catalysts on industrial scales.[4] In particular, the ability to control the large-scale synthesis of metallic NPs according to the desired properties and linked activities can be achieved *via* simplistic changes to the protocol, e.g. increasing precursor flow rates or altering the solution pH.[78,81] The work presented in this chapter is a continuation of the work presented in Chapter 5, where the ability to measure colloidal solutions at [Au] = 100 μM was established.[30] XAFS measurements of colloidal Au formation are presented in this work; however, to adequately measure these phenomena, a cell with the capacity to monitor NP formation had to be designed and constructed.

6.3.1 Cell Design for *In Situ* X-ray Absorption Fine Structure Measurements

6.3.1.1 Flow Regime Calculation for Laminar Flow

The flow regime employed in a microfluidic system is known to have an influence over the nucleation and growth processes of NPs, whether it is *via* the use of a segmented flow to increase distinct instances of nucleation, or the use of laminar flows to reduce mixing within the reactor channels.[29,50] Therefore, the type of flow regime is highly important. For this study, the interaction and mixing of the precursor salt and reducing agent solutions is monitored. To successfully perform this, a flow regime with low mixing and reduced metal deposition on the reactor walls was required. The use of a continuous phase is optimal in preventing loss of the XAFS signal, as previously discussed, slugs of non-metal containing phases uninterruptedly travel through the X-ray path.[56] Furthermore, as a system without high levels of mixing is preferable, the amount of mixing within a system can be suppressed either *via* reactor design, or by using a laminar flow regime where the characteristic Reynolds number is < 2100.[20] Calculations of Re are performed using *Equation 6-1* and *Equation 6-2* (Reynolds number calculations are presented in *section* 8.2). Based on the total volume of solution used across the two syringe pumps and the time per one successful XANES scan (18 min spectrum^{-1}), the theoretical maximum flow rate is 8.3 mL min^{-1}. However, to ensure the volume of either solution did not reach zero during data acquisition, a much lower total flow rate was used; a combined flow rate (syringe pump 1 and syringe pump 2) of 2 mL min^{-1} (0.02 m s^{-1}) was chosen for this work which gives a Re value of 1857.2 for the fluid along the mixing channel (laminar).[20,50] Whilst lower flow rates could have been employed, a sufficiently high enough flow rate was required to ensure reliable pumping of the dual syringe pump (reducing agent solutions) toward the mixing cell.

Further to this, movement of the multiple liquid phases with respect to one another must be factored into the cell design. Due to the use of a continuous flow system, the choice of flow regime is limited to either annular or parallel flow profiles (*Figure 6-9*). For this work, the interaction and/or deposition of the Au containing phase with the reactor walls was not desirable, therefore, the cell was designed to operate utilising an annular flow profile.

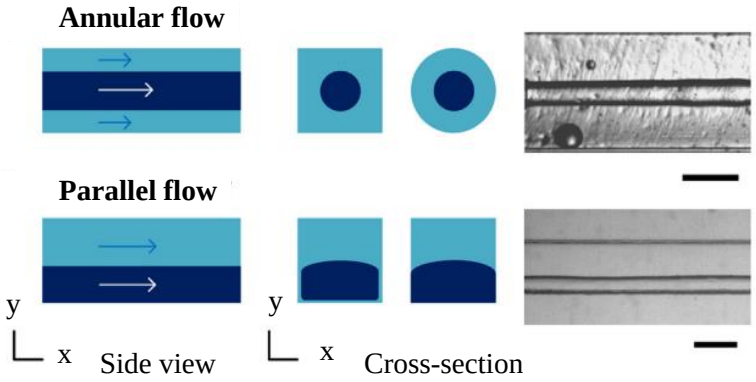

Figure 6-9. *Flow patterns in continuous phase systems illustrating annular and parallel flow regimes as side views, cross sections and as real-time images of the flow regime; image taken from Wang et al., Chem. Eng. Sci., 2017,* ***169****, 18-33.*[82]

6.3.1.2 *In situ* X-ray Absorption Fine Structure Cell Design

To achieve an annular flow profile, the design of the reactor had to ensure that the encasing of one flow within the other was possible. The use of commercially available products allowed for preparation and refinement of the cell without the need to reprint and etch mixing channels in an X-ray transparent material, as is the case for many *in situ* microfluidic processes.[27,83] The reactor was designed so that the inner flow (Au precursor solution) would be pumped into the middle of the reducing agent flow at the beginning of the mixing channel (*Figure 6-10*). Here, the Au precursor solution is pumped through a modified 28 G needle (BD PrecisionGlide®) inserted through a Swagelok® stainless steel T-junction connector. The reducing agent flow is pumped through the base of the connector and, once it reaches the mixing channel, an annular flow profile is achieved.

In addition to this, the length and flow path of the reagents within the mixing channel were chosen to afford complete reduction of the precursor salt and to also prevent additional instances of reagent mixing. The length of the mixing channel is important; firstly, a longer mixing channel will have a greater probability of complete reduction and subsequent NP growth occurring. Secondly, the length of the mixing channel is intrinsically linked to the reagent mixing *via* the Reynold's number, and so, if the length is too long or too short, the mixing within the channel can change from laminar to turbulent, which would require further refinement of parameters elsewhere.[20,27,84] For many *in situ* studies of this nature, a long mixing channel with bends etched into the cell are common; however, the presence of these bends increases the likelihood of mixing and so can artificially influence the growth process of the NPs.[85] As the study presented in this chapter is concerned with investigating the initial

nucleation and growth steps, a straight mixing channel was attached to the end of the T-junction (*Figure 6-10*).

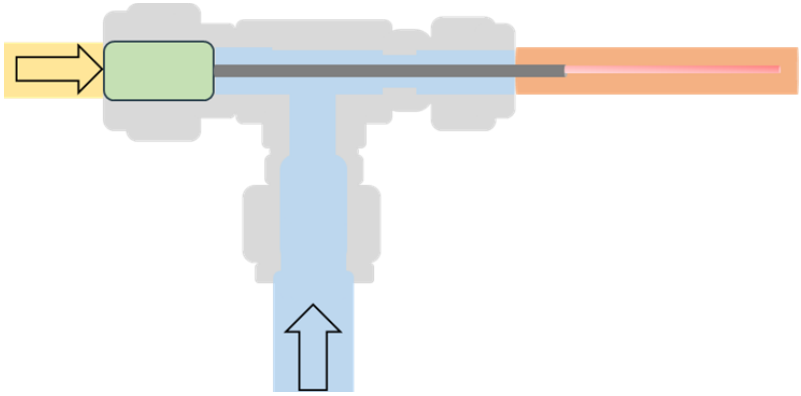

Figure 6-10. *Cut-away view of the T-junction showing how the modified needle tip was inserted to establish the encapsulated flow. The PVA capped precursor solution (yellow) flows through a modified needle tip centred in the tubing (needle is 28 G), and the reducing agent solution (blue) flows around it, as the two solutions interact colloidal Au form and increase in size along the mixing channel (red stream). An optimised flow ratio of precursor and reducing solutions gives a constant stream of colloid along the length of the mixing zone.*

Review of the limited literature concerning the preparation and characterization of colloidal solutions detailed a similar system employed by Ameloot *et al*. in the production of hollow MOFs.[18] Briefly, the cell designed by Ameloot *et al*. was used to prepare Cu based MOFs by constantly forming droplets of aqueous solution within a surrounding continuous organic phase; this was achieved by using two separate syringe pumps supplying liquid toward a T-junction, with the aqueous phase moving through an inserted capillary (needle tip) within the T-junction and interacting with the organic phase.

6.3.2 Suppression of H_2 Evolution *via* Reducing Agent Decomposition

The use of a strong reducing agent in the batch synthesis of colloidal metal NPs is necessary to produce NPs with controllably small sizes.[86,87] However, due to its very reactive nature, hydrolysis of $NaBH_4$ leads to the spontaneous generation of $H_{2(g)}$,[88–91] even at low sol-immobilisation temperatures (Chapters 3, 4), and can, in theory, produce 4 mol H_2 from 1 mol $NaBH_4$ (*Equation 6-4*).[92]

$$NaBH_4 + 2H_2O \rightarrow NaBO_2 + 4H_2$$

Equation 6-4. *Hydrolysis reaction of $NaBH_4$ under standard conditions (25 °C, 1 atm. pressure).*[88,92]

Production of vast quantities of $H_{2(g)}$ (bubbling), is detrimental for *in situ* reduction measurements. Although the beneficial use of a segmented flow regime has been reported in nanoparticle synthesis[2,4,11], its use for X-ray absorption studies is not optimal. This is due to the constant loss of signal as the phase interacting with the beam is constantly changing from one of high metal loading, to the inserted gaseous or liquid phase, more commonly referred to as a 'slug'.

A widely used method to slow the rate of NaBH4 decomposition is to prepare the solution in the presence of NaOH; increasing the pH of the solution, increases the activation energy of $NaBH_4$ hydrolysis.[93] Measurements of the decomposition of $NaBH_4$ under increasing molarity of NaOH were performed as close to the *in situ* experiment as possible. To achieve this, $NaBH_4$ (0.1 M) was prepared in solutions of increasing [$NaOH_{(aq)}$] (0.05, 0.10, 0.15 and 0.20 M) within a plastic syringe. After 50 minutes (the approximate length of one fluorescence scan performed in the static colloid measurements), the movement of the syringe plunger due to the production of H_2 allowed for monitoring of $NaBH_4$ decomposition (*Figure 6-11*).

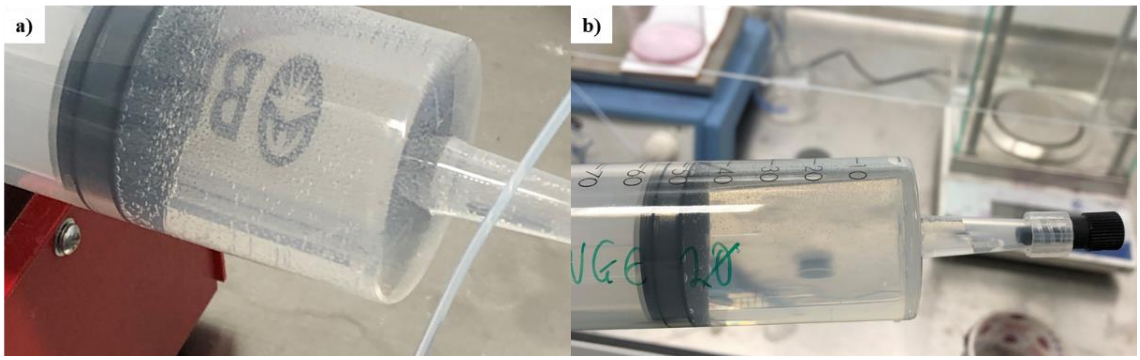

Figure 6-11. *Close up images of $H_{2(g)}$ evolution from the decomposition of a) $NaBH_4$ in H_2O, and b) $NaBH_4$ in 0.1 M NaOH.*

As expected, the quantity of H_2 gas produced was greatest when no NaOH was added (4.5 mL of $H_{2(g)}$). When using the lower [$NaOH_{(aq)}$] (0.05 M or 0.10 M), 1 mL of $H_{2(g)}$ was observed, whilst moving to harsher concentrations (0.15 and 0.20 M) stopped the production of $H_{2(g)}$ altogether (*Table 6-1*). UV-Vis of the formed colloids can also elucidate how varying

the basicity of the solution influences average colloidal NP size *via* assessment of the position of the SPR band (λ_{max}).[94] A shift in its position to higher wavelength is consistent with an increase to the average NP size, which is in agreement with the literature (*Figure 6-12* and *Table 6-1*).[72,87]

Table 6-1. *Quantity of $H_{2(g)}$ evolved during the reduction of $HAuCl_4$ using $NaBH_4$ (0.1 M) prepared in solutions of increasing NaOH molarity. The associated change in the position of the UV-Vis SPR band with increasing basicity is also described.*

0.1 M $NaBH_4$ dissolved in X, where X =	**$H_{2(g)}$ Production (mL)**	**UV-Vis SPR band Position (nm)**
H_2O	4.5	492
0.05 M NaOH	1.0	503
0.10 M NaOH	1.0	520
0.15 M NaOH	0.0	520
0.20 M NaOH	0.0	520

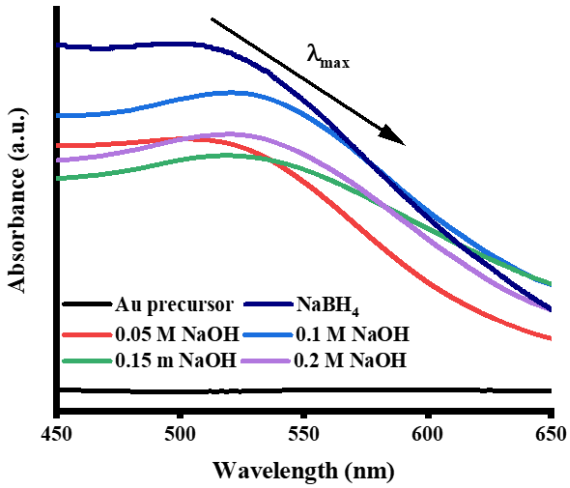

Figure 6-12. *UV-Vis spectra of the SPR band (λ_{max}) region for the colloidal Au NPs ([Au] = 100 µM) prepared in increasing [NaOH], the spectrum of the Au precursor salt solution ($HAuCl_4$) is also included for reference.*

6.3.2.1 Au Reduction using $NaBH_4$ and DMAB

Whilst the use of $NaBH_4$ prepared in solutions with high [NaOH] has been shown to aid in the suppression of H_2 production, the increase in pH as the [NaOH] rises has also been found

to influence not only the size, but the shape of colloidal Au. Interestingly, a slightly basic solution is considered optimal for the formation of spheres and rod-like NPs.[95] The reaction of $NaBH_4$ with water has already been stated to theoretically produce 4 mol H_2 per mol $NaBH_4$ (*Equation 6-4*).[92] In reality, the amount of H_2 produced is much lower for the reduction of a metal precursor,[38] and so the formation of H_2 bubbles in the beam path may be limited (*Equation 6-5*).

$$H_2PtCl_6 + NaBH_4 + 3H_2O \rightarrow Pt + H_3BO_3 + 5HCl + NaCl + 2H_2$$

Equation 6-5. *Reduction of a Pt^{2+} precursor salt by $NaBH_4$ in water.*[38]

The use of boron-based reagents (e.g. $NaBH_4$, DMAB ($BH_3.NH(CH_3)_2$), *etc.*) in the *in situ* generation of hydrogen has been reported widely in the preparation of metallic nanoparticles, whereby dehydrogenation of the B-H bonds produces H_2 that sequentially reduces metal precursor complexes.[31,32,47,96–98] It should be noted that the dehydrogenation of DMAB (without the presence of a metal precursor) theoretically yields one mole less H_2 than $NaBH_4$ (*Equation 6-6*).[96,99]

$$(CH_3)_2NHBH_3 + 2H_2O \rightarrow (CH_3)_2NH_2BO_2 + 3H_2$$

Equation 6-6. *Hydrolysis reaction of dimethylamine-borane (25 °C, 1 atm.).*[99]

Reduction of the Au precursor salt with the milder reducing agent generates larger clusters of Au in the synthesis solution, and is noticeable by the evolution of a dark purple sol in the DMAB colloid. The UV-Vis spectra of the colloids confirms the formation of smaller Au NPs in $NaBH_4$ due to the broadening of the SPR band, indicative of Au NPs < 10 nm (*Figure 6-13*).[100] A slow reduction, though not beneficial for controlling the final NP size and dispersion, is optimal for this study as the production of H_2 is limited. Therefore, the likelihood of signal loss during *in situ* XAFS measurements is greatly reduced when DMAB is employed as the reducing agent.

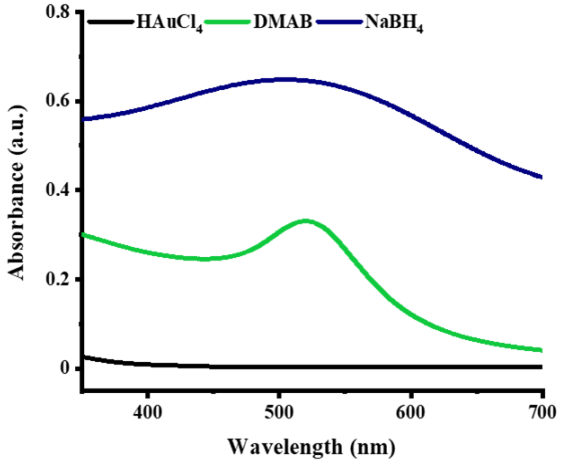

Figure 6-13. *UV-Vis spectra showing the SPR band formation for a fresh $HAuCl_4$ salt solution, as well as $HAuCl_4$ salt solutions reduced in DMAB, and $NaBH_4$.*

6.3.2.2 X-ray Fluorescence Analysis of Au Deposition

The potential deposition of Au nanoparticles onto the surface inside of the mixing channel is an important aspect that must be addressed when designing microfluidic experiments. For the system prepared, two main types of NP fouling can occur: (1) chemical reaction fouling, where solids formed through chemical reactions attach to the surface, and (2) particulate fouling, where fine particles in the reactant streams interact with the surface.[101] These processes can therefore artificially influence NP growth and make the *in situ* experiment unusable. The extent of Au nanoparticle fouling was measured using XRF analysis (*Table 6-2*). A fresh polyimide tube was initially measured to ascertain that no trace Au metal was detectable on the inner wall. XRF analysis of the fouled tubing measured the [Au] in five equal length segments of the mixing channel (*Figure 6-14*). The extent of Au deposition was investigated for tubing with increasing internal diameter: 0.16, 0.32 and 0.64 cm (IDs of tubing are compatible with stainless steel Swagelok® T-junction sizes).

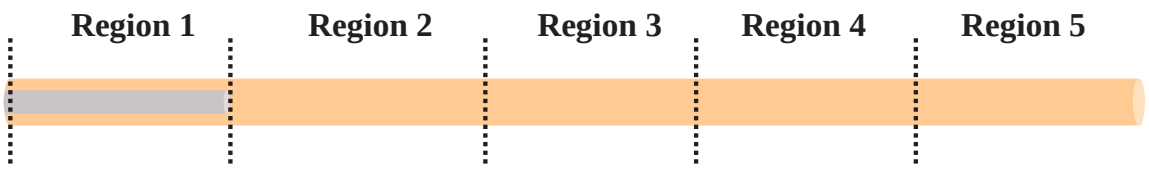

Figure 6-14. *Schematic of the sections of the used polyimide tubing measured during XRF analysis. Region 1 encompasses the capillary tip inserted into the beginning of the mixing channel.*

Table 6-2. *Au deposition on the inner walls of the tubing as determined via XRF. Colloid formation within the mixing channel was performed using flow rates of 0.4 mL min^{-1} ($HAuCl_4$ and PVA) and 1.6 mL min^{-1} (DMAB and 0.15 M NaOH).*

Tubing Material (ID)	**Au XRF Signal (ppm)**				
	Region 1	**Region 2**	**Region 3**	**Region 4**	**Region 5**
Polyimide (0.16 cm)	2.6	0.0	20.6	221.0	1.5
Polyimide (0.32 cm)	109.6	720.8	100.6	162.4	197.1
Polyimide (0.64 cm)	4.0	31.3	25.3	41.6	14.7

The presence of Au deposited on the inner walls of the mixing channel was observed for all used tubing. Fouling of the metal solution on the reactor walls can provide a lower energy surface for particle nucleation to occur, subsequently stimulating uncontrolled cluster growth.[102] The undesired deposition coupled with the high energy X-ray beam probing the reactor could lead to further beam related particle aggregation, thus making the measurement unreliable to assess for NP growth. The most fouling of Au is observed within the 0.32 cm ID tubing, with the majority of the deposition occurring in the region post-capillary (Region 2), wherein the precursor salt solution and reducing agent streams have first contact. Deposition of Au is also noted in the first region of the tubing and can be attributed to either backflow of the Au solution, or human error during sample preparation.

The smallest average amount of Au measured corresponds to the largest ID tubing; this is due to the larger volume of the reducing agent solution encasing the precursor solution, providing a longer path from the centre of the tubing to the wall. With the larger diameter, the Au falling toward the wall is more likely to travel the length of the tube instead of depositing in an earlier region. From XRF measurements, the tubing that would be most suited for the experiment is the 0.64 cm ID polyimide, however, the much greater volume of liquid within a 0.64 cm ID mixing channel (where channel length = 10 cm) would result in

a volume of 3.0 cm^3 within the channel, for 0.16 cm and 0.32 cm ID calculated volumes are 0.2 cm^3 and 0.8 cm^3, respectively. As the intention is to monitor NP growth *via* XAFS, this larger volume within the channel will result in greater photon loss from the source beam, before and after interaction with the inner Au stream, compared to the 0.16 cm ID. Therefore, it was concluded that the use of a smaller ID tube would better aid in limiting undesired photon loss (explored further in section *6.3.2.3*).

The issue of deposition was dealt with by coating the inner walls of the reactor with an inert, pre-prepared fluorinated oil mixture; this was composed of 1*H*,1*H*,2*H*,2*H*-perfluoro-1-octanol and octadecafluorodecahydronaphthalene mixed in a 10 % v/v ratio (PO:PFD) and was used for the continuous preparation of colloidal Pd.[4] The fluorinated oil ensured complete wetting of the reactor walls, preventing the Au (precursor salt and NPs) from adhering to the inner channel surface, and inhibiting artificial NP growth.

6.3.2.3 Photon Loss through the Mixing Channel

The loss of photons during *in situ* experiments is another concern that has to be addressed before attempting XAFS measurements. To ensure minimal loss of photons, a high flux beamline should be used, and so, for this experiment, an insertion device beamline (i.e. I20-Scanning, DLS, Didcot, U.K.) was preferable. X-ray transparent and low energy materials are also essential to consider when designing a microfluidic device to acquire accurate nucleation and growth data; in particular, low energy materials limit undesirable artificial deposition and growth of NPs from occurring. Stainless steel,[103] and Si-based oxides and glasses[52,53] are commonly used materials for the creation of XAFS fluidic cells intended to be interrogated by soft X-rays (< 8 KeV), where the X-ray transparent windows are comprised of polydimethylsiloxane (PDMS) or polyimide.[25]

Photon loss through various mixing channel materials and wall thicknesses are presented here and calculated using *Equations 2-5* and *2-6*, where the photon energy range is 11600-12400 eV (*Figure 6-15*).[104,105] Mixing channel materials were chosen from commercially available 1/16th inch ID (0.16 cm ID) tubing that was rigid enough to prevent bending of the channel in the event that product accumulated at the outlet; smooth polyimide tubing with wall thicknesses ranging from 300-700 μm were investigated. The tubing sizes chosen were also compatible with the stainless steel T-junction used in the reactor. Furthermore, photon loss through the aqueous solutions proved to be negligible due to the same ID being used for all tested tubing, making deviations in the calculated X-ray

transmission a result of the increasing wall thickness. For this reason, the mixing channel was prepared from 0.16 cm ID smooth polyimide tubing with a wall thickness of 300 µm.

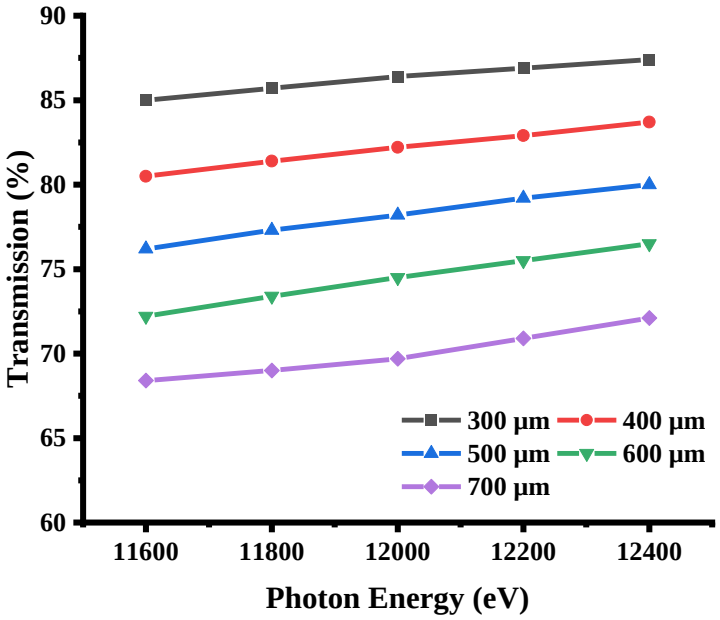

Figure 6-15. *X-ray transmission around the Au L_3 edge energy of polyimide tubing with increasing wall thicknesses (300-700 µm).*

6.3.3 *In situ* X-ray Absorption Fine Structure Acquisition

6.3.3.1 Oscillatory Issues with the Syringe Pump

The stability of the precursor solution under the beam path was initially investigated prior to the *in situ* reduction studies, the materials and flow rates are listed in *Table 6-3*. Photoreduction of the precursor solution ([Au] = 100 µM) was not observed. During data acquisition, the edge jump of the XANES region was recorded successfully, but issues arose in the EXAFS region. The unexpected increase in oscillations past the white line peak can be explained by minute movements of the syringe pump being detected by the fluorescence detector and I_0 chamber. Doubling the flow rate increased the frequency of these oscillations, confirming that EXAFS acquisition was not feasible using this set-up (*Figure 6-16*a). Notwithstanding this, the absorption edge for Au^{3+} is still visible, and so, the nature of the experiment was modified to measure the absorption energy as a function of Au reduction. In place of Au^{3+} and Au^{+} references being measured on the beamline, they were acquired from work performed by G. Malta *et al*. and reflect the oxidation states of Au that can form during chemical reduction (*Figure 6-16*b).[106]

Table 6-3. *Materials and syringe flow rates utilised during the preparation of the microfluidic system utilised to measure colloidal Au formation via in situ XAFS.*

Material	**Description**
Precursor solution	$HAuCl_4$ ([Au] = 100 µM) capped using PVA (0.01 g mL^{-1} solution)
Reducing agent solution	DMAB (500 µM) in $NaOH_{(aq)}$ (0.15 M)
Cell tubing	PTFE, 0.16 cm (ID)
Mixing channel	Polyimide tubing, 0.16 cm (ID), 0.005 cm (wall thickness), 10 cm (length)
Fluorinated oil	1*H*,1*H*,2*H*,2*H*-perfluoro-1-octanol (PO) 10 % v/v in Octadecafluorodecahydronaphthalene (PFD)
Inserted capillary	28 G needle
Syringe Solution	**Flow Rate**
Precursor solution flow rate	0.4 mL min^{-1}
Reducing agent solution flow rate	1.6 mL min^{-1}

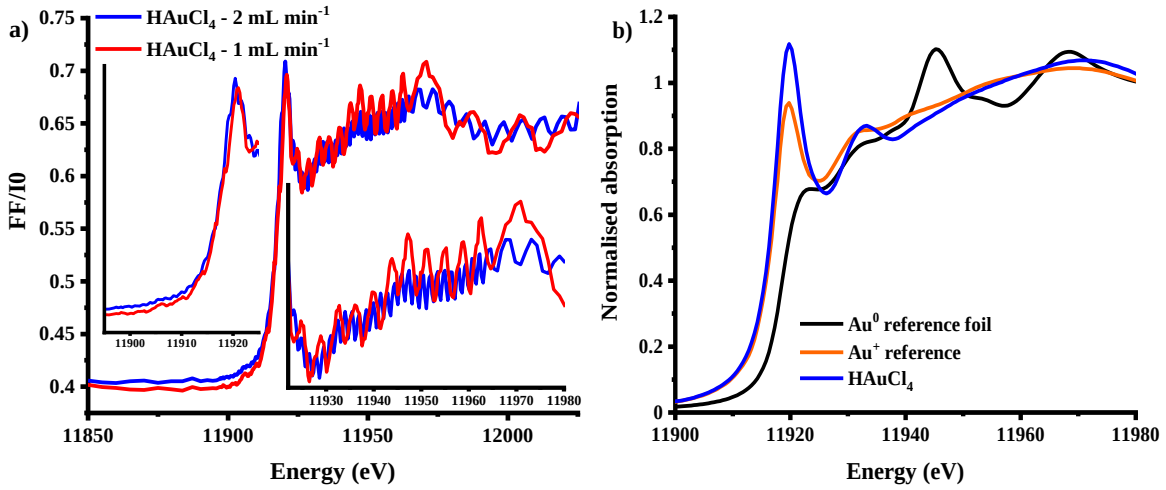

Figure 6-16. *Au L_3-edge XANES acquired on the I20-Scanning beamline at DLS, Didcot, U.K. showing the a) fluorescence mode XANES spectra for $HAuCl_4$ solutions pumped at flow rates of 1 and 2 mL min^{-1}, and the b) transmission mode XANES spectra for the different Au reference compounds; Au^+ and Au^{3+} references acquired from G. Malta et al., Science, 2017,* ***355****, 1399–1403.*[106]

6.3.3.2 Static Point Measurements of Au Reducing *via In situ* XANES

XANES data were collected *in situ* to monitor the reduction of Au along three positions of the mixing channel; the dilute metal concentration studied is a continuation from the work presented in Chapter 5, [Au] = 100 µM.[30] Formation of Au clusters was monitored *via* reductions in intensity of the white line peak at 11919 eV, indicative of the $2p_{3/2} \rightarrow 5d$ electronic transition. An increase in the intensities of two post-edge features can also elucidate changes in the local Au structure *in lieu* of EXAFS. ~ 13 eV above the absorption edge a feature is observed that is characteristic of multiple scattering phenomena in the square planar geometry of the $[AuCl_4]^-$ complex.[107,108] The second feature is present at ~ 11946 eV and is only observed for the Au^0 reference foil.[65,109,110] The intensity of this feature corresponds to the formation of clusters resembling a bulk-like Au structure, e.g. FCC, where the local environment surrounding the absorbing Au atom is composed of 12 neighbouring Au atoms. The acquisition of spatially-resolved XANES was made easier using the milder reducing agent DMAB, which is reflected in the small decrease in intensity and shift in position (~ 5 eV) of the white line peak as the solution progresses along the mixing channel (*Figure 6-17*a-c). The reduction route of the Au species in DMAB suggests that Au^{3+} undergoes reduction directly to Au^0, without forming Au^+ as an intermediate. XANES acquired at Position 1 clearly shows that the reduction process begins

instantaneously, even in milder reducing conditions (DMAB and 0.15 M NaOH), with this first position corresponding to 500 ms post solution interaction. To clarify, complete reduction is not yet achieved, with only a slight decrease in the intensity of the absorbing edge observed. The post-edge features show slight changes, particularly to the feature at 11946 eV beginning to appear.[65,109,110] At this first point, the formation of some Au clusters has occurred (*Figure 6-17*a). Two seconds after the initial point of chemical reduction, a more prominent shift in the absorption energy can be seen (*Figure 6-17*b). At Position 2, mixed Au^{3+} and Au^{0} scattering features are observed, suggesting that the precursor salt is still in solution, even in minor quantities. The final point measurement acquired along the reactor channel (Position 3) shows the white line peak disappear 3.5 seconds after the initial point of reduction; the accompanied shift in absorption edge position also proposes that reduction of all Au^{3+} species has taken place. Nevertheless, the intensity of the post-edge features do not align with the Au^{0} reference foil, therefore it is evident that in this system, small Au^{0} clusters are formed after 3.5 seconds of reaction. Without EXAFS analysis, however, quantification of these Au NPs is challenging. That being said, the data acquired is novel in and of itself. To the best of the author's knowledge, no other studies have reported the ability to successfully acquire *in situ* XANES data at the dilute concentration presented ([Au] = 100 µM) using a microfluidic system, the closest being [Au] = 300 µM.[56,69]

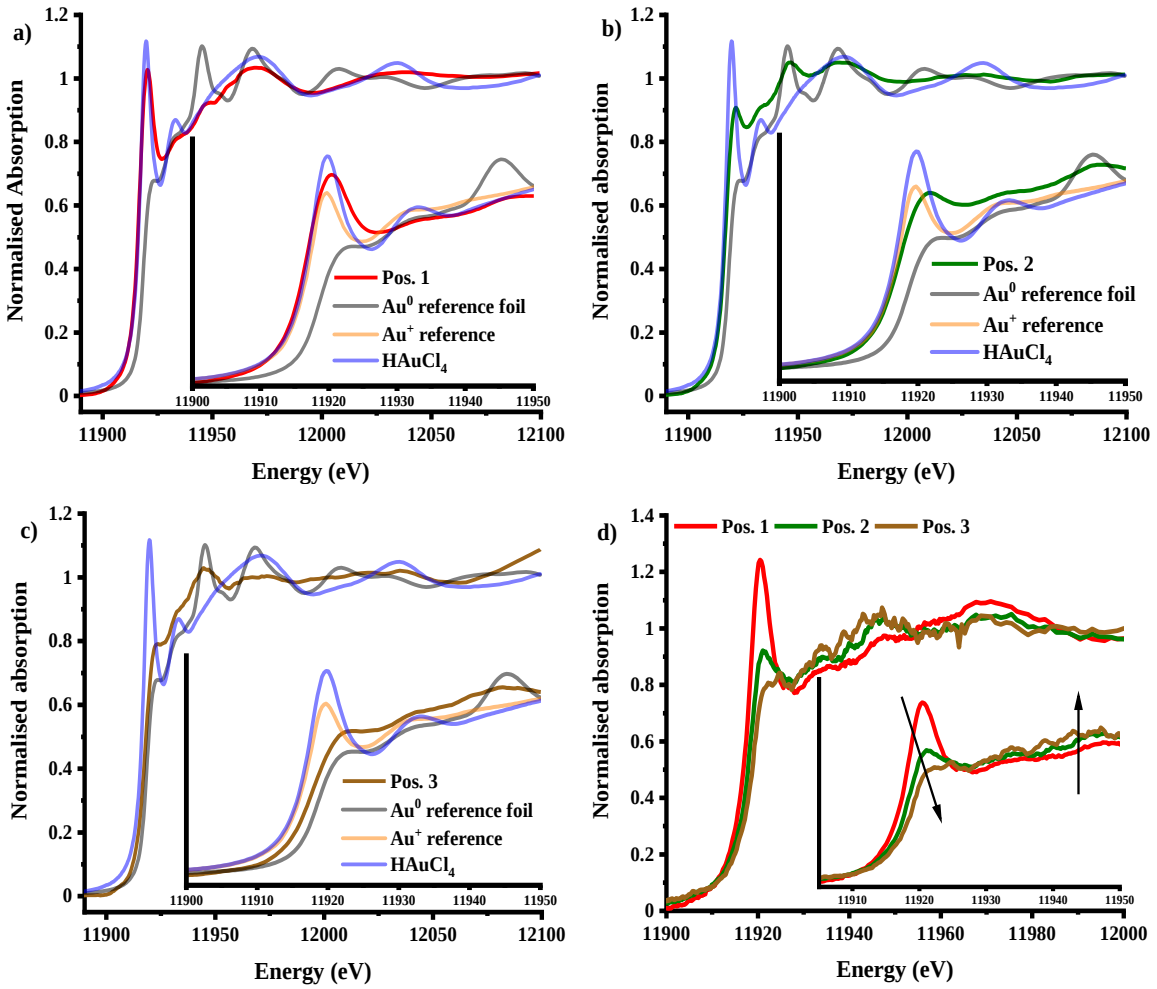

Figure 6-17. *XANES spectra acquired during the in situ reduction of $HAuCl_4$ using DMAB in 0.15 M NaOH solution, measured on the I20-Scanning beamline at DLS, Didcot, U.K. Au L_3-edge XANES are shown at different positions along the mixing channel: a) Position 1, b) Position 2, c) Position 3, and d) comparison of the Au species along the mixing channel. (a-c) include the XANES spectra of the reference Au^0 and $HAuCl_4$.*

6.4 Conclusions

In conclusion, the pursuit to monitor Au nanoparticle formation *in situ* at [Au] = 100 µm was, in part, successful. The major obstacle was to design a microfluidic device that would:
(1) Establish a continuous laminar flow that is present as an annular stream.
(2) Prevent Au fouling on the walls of the reactor, and any subsequent artificial growth in NP size.
(3) Allow for high energy X-ray analysis.

The desired flow regime was attained by using low flow rates of the reagent solutions to give a laminar flow (Re = 1857.2), an annular flow was achieved using modified T-junction with a capillary inserted through the long edge. Furthermore, a continuous flow through the mixing channel was achieved by using basic synthesis conditions ($[NaOH_{(aq)}]$ = 0.15 M) and a mild reducing agent (DMAB), suppressing $H_{2(g)}$ evolution as a result of DMAB decomposition. Au deposition was prevented in the cell by coating the inner walls with a fluorinated oil, and was confirmed during solution stability measurements. XAFS analysis was made possible using polyimide, an X-ray transparent material, as the mixing channel. The flow rate chosen afforded constant movement of the solution through the X-ray beam path, preventing photoreduction as a result of prolonged beam exposure.

XANES measurements at distinct time points along the mixing channel clearly showed the progression of chemical reduction, with Au^{3+} reducing to Au^0 without forming Au^+ as an intermediate. Furthermore, colloidal Au formation was observed in under 4 s, 500 times faster than the macroscale NP preparation presented in Chapter 5. Unfortunately, EXAFS data could not be acquired due to minute movements of the syringe pump motors being detected by the sensitive equipment on the beamline; this was an unforeseen issue. Though it was not trialled during this project, it is the author's opinion that a smoother pump (such as the Tacmina Smoothflow Pump Q) would be beneficial for this endeavour.

Nevertheless, the data acquired is novel in and of itself, as, to the best of the author's knowledge, no other studies have reported the successful acquisition of *in situ* XANES data at the dilute concentration presented ([Au] = 100 µM), the closest being [Au] = 300 µM.[56,69] The work in this chapter provides an essential building block for further investigations into monitoring nucleation events on a microscale.

6.5 References

1 J. M. Köhler, L. Abahmane, J. Wagner, J. Albert and G. Mayer, *Chem. Eng. Sci.*, 2008, **63**, 5048–5055.

2 C.-X. Zhao, L. He, S. Z. Qiao and A. P. J. Middelberg, *Chem. Eng. Sci.*, 2011, **66**, 1463–1479.

3 A. Jahn, J. E. Reiner, W. N. Vreeland, D. L. DeVoe, L. E. Locascio and M. Gaitan, *J. Nanoparticle Res.*, 2008, **10**, 925–934.

4 W. K. Wong, S. K. Yap, Y. C. Lim, S. A. Khan, F. Pelletier and E. C. Corbos, *React. Chem. Eng.*, 2017, **2**, 636–641.

5 J. Polte, *CrystEngComm*, 2015, **17**, 6809–6830.

6 K. Amreen and S. Goel, *ECS J. Solid State Sci. Technol.*, 2021, **10**, 017002.

7 J. M. Lim, A. Swami, L. M. Gilson, S. Chopra, S. Choi, J. Wu, R. Langer, R. Karnik and O. C. Farokhzad, *ACS Nano*, 2014, **8**, 6056–6065.

8 O. Długosz and M. Banach, *React. Chem. Eng.*, 2020, **5**, 1619–1641.

9 K. F. Jensen, *MRS Bull.*, 2006, **31**, 101–107.

10 H. R. Sahoo, J. G. Kralj and K. F. Jensen, 2007, 5806–5810.

11 V. S. Cabeza, S. Kuhn, A. A. Kulkarni and K. F. Jensen, *Langmuir*, 2012, **28**, 7007–7013.

12 S. Badilescu and M. Packirisamy, *Polymers*, 2012, **4**, 1278–1310.

13 B. K. H. Yen, A. Günther, M. A. Schmidt, K. F. Jensen and M. G. Bawendi, *Angew. Chemie*, 2005, **117**, 5583–5587.

14 K.-J. Wu, G. M. de Varine Bohan and L. Torrente-Murciano, *React. Chem. Eng.*, 2017, **2**, 116–128.

15 V. Narayanamurthy, Z. E. Jeroish, K. S. Bhuvaneshwari, P. Bayat, R. Premkumar, F. Samsuri and M. M. Yusoff, *RSC Adv.*, 2020, **10**, 11652–11680.

16 D. E. Hertzog, X. Michalet, M. Jäger, X. Kong, J. G. Santiago, S. Weiss and O. Bakajin, *Anal. Chem.*, 2004, **76**, 7169–7178.

17 H. Liu, J. Huang, D. Sun, L. Lin, W. Lin, J. Li, X. Jiang, W. Wu and Q. Li, *Chem. Eng. J.*, 2012, **209**, 568–576.

18 R. Ameloot, F. Vermoortele, W. Vanhove, M. B. J. Roeffaers, B. F. Sels and D. E. de Vos, *Nat. Chem.*, 2011, **3**, 382–387.

19 M. Jiao, J. Zeng, L. Jing, C. Liu and M. Gao, *Chem. Mater.*, 2015, **27**, 1299–1305.

20 K. Ward and Z. H. Fan, *J. Micromechanics Microengineering*, 2015, **25**, 094001.

21 Y. Song, J. Hormes and C. S. S. R. Kumar, *Small*, 2008, **4**, 698–711.

22 M. B. Kulkarni and S. Goel, *Nano Express*, 2020, **1**, 1–30.

23 C. J. Denis, C. J. Tighe, R. I. Gruar, N. M. Makwana and J. A. Darr, *Cryst. Growth Des.*, 2015, **15**, 4256–4265.

24 D. M. Fries and P. R. von Rohr, *Chem. Eng. Sci.*, 2009, **64**, 1326–1335.

25 A. Ghazal, J. P. Lafleur, K. Mortensen, J. P. Kutter, L. Arleth and G. V. Jensen, *Lab Chip*, 2016, **16**, 4263–4295.

26 E. Y. Erdem, J. C. Cheng, F. M. Doyle and A. P. Pisano, *Small*, 2014, **10**, 1076–1080.

27 A. D. Stroock, S. K. W. Dertinger, A. Ajdari, I. Mezić, H. A. Stone and G. M. Whitesides, *Science*, 2002, **295**, 647–651.

28 P. Watts and C. Wiles, *Chem. Commun.*, 2007, 443–467.

29 H. Huang, H. du Toit, M. O. Besenhard, S. Ben-Jaber, P. Dobson, I. P. Parkin and A. Gavriilidis, *Chem. Eng. Sci.*, 2018, **189**, 422–430.

30 G. F. Tierney, D. Decarolis, N. Abdullah, S. M. Rogers, S. Hayama, B. de Gutierrez, A. Villa, C. R. A. Catlow, P. Collier, N. Dimitratos and P. P. Wells, *Nanoscale Adv.*, 2019, **1**, 2546–2552.

31 S. M. Rogers, C. R. A. Catlow, C. E. Chan-Thaw, D. Gianolio, E. K. Gibson, A. L. Gould, N. Jian, A. J. Logsdail, R. E. Palmer, L. Prati, N. Dimitratos, A. Villa and P. P. Wells, *ACS Catal.*, 2015, **5**, 4377–4384.

32 S. M. Rogers, C. R. A. Catlow, C. E. Chan-Thaw, A. Chutia, N. Jian, R. E. Palmer, M. Perdjon, A. Thetford, N. Dimitratos, A. Villa and P. P. Wells, *ACS Catal.*, 2017, **7**, 2266–2274.

33 A. Villa, D. Wang, G. M. Veith, F. Vindigni and L. Prati, *Catal. Sci. Technol.*, 2013, **3**, 3036–3041.

34 S. Link and M. A. El-Sayed, *J. Phys. Chem. B*, 1999, **103**, 4212–4217.

35 J. Boleininger, A. Kurz, V. Reuss and C. Sönnichsen, *Phys. Chem. Chem. Phys.*, 2006, **8**, 3824–3827.

36 E. Shahbazali, V. Hessel, T. Noël and Q. Wang, *Phys. Sci. Rev.*, 2019, **1**, 1–21.

37 K. Shibuki, M. Takesue, T. M. Aida, M. Watanabe, H. Hayashi and R. L. Smith, *J. Supercrit. Fluids*, 2010, **54**, 266–271.

38 M. J. Hossain, M. S. Rahman, M. S. Rahman, M. A. Ali, N. C. Nandi, P. Noor, K. N. Ahmed and S. Akhter, *J. Nanostructure Chem.*, 2016, **6**, 49–56.

39 M. James, R. A. Revia, Z. Stephen and M. Zhang, *Nanomaterials*, 2020, **10**, 1–19.

40 C. D. Ahrberg, J. W. Choi and B. G. Chung, *Beilstein J. Nanotechnol.*, 2018, **9**, 2413–2420.

41 L. H. Hung and A. P. Lee, *J. Med. Biol. Eng.*, 2007, **27**, 1–6.

42 P. J. Resto, B. Mogen, F. Wu, E. Berthier, D. Beebe and J. Williams, *J. Vis. Exp.*, 2009, 3–7.

43 A. Olanrewaju, M. Beaugrand, M. Yafia and D. Juncker, *Lab Chip*, 2018, **18**, 2323.

44 J. C. T. Eijkel and A. van den Berg, *Lab Chip*, 2006, **6**, 1405–1408.

45 Y. Zhang, W. Jiang and L. Wang, *Microfluid. Nanofluidics*, 2010, **9**, 727–735.

46 L. Uson, V. Sebastian, M. Arruebo and J. Santamaria, *Chem. Eng. J.*, 2016, **285**, 286–292.

47 N. Dimitratos, A. Villa, L. Prati, C. Hammond, C. E. Chan-Thaw, J. Cookson and P. T. Bishop, *Appl. Catal. A Gen.*, 2016, **514**, 267–275.

48 Z. S. Pillai and P. V. Kamat, *J. Phys. Chem. B*, 2004, **108**, 945–951.

49 B. K. H. Yen, N. E. Stott, K. F. Jensen and M. G. Bawendi, *Adv. Mater.*, 2003, **15**, 1858–1862.

50 R. Baber, *Synthesis of inorganic nanoparticles using microfluidic devices*, UCL, 2017.

51 X. Guo, Y. Fan and L. Luo, *Exp. Therm. Fluid Sci.*, 2018, **99**, 407–419.

52 G. Hofmann, G. Tofighi, G. Rinke, S. Baier, A. Ewinger, A. Urban, A. Wenka, S. Heideker, A. Jahn, R. Dittmeyer and J.-D. D. Grunwaldt, *J. Phys. Conf. Ser.*, 2016, **712**, 012072.

53 E. M. Chan, M. A. Marcus, S. Fakra, M. ElNaggar, R. A. Mathies and A. P. Alivisatos, *J. Phys. Chem. A*, 2007, **111**, 12210–12215.

54 CFDsupport, Laminar vs. Turbulent Flow, https://www.cfdsupport.com/OpenFOAM-Training-by-CFD-Support/node334.html, (accessed 17 May 2021).

55 W. Ehrfeld, V. Hessel and H. Löwe, in *Microreactors - New Technology for Modern Chemisty*, eds. W. Ehrfeld, V. Hessel and H. Löwe, Wiley-VCH, Mainz, 1st edn., 2000, pp. 41–85.

56 J. Polte, R. Erler, A. F. Thünemann, S. Sokolov, T. T. Ahner, K. Rademann, F. Emmerling and R. Kraehnert, *ACS Nano*, 2010, **4**, 1076–1082.

57 J. Feng, M. Kriechbaum and L. E. Liu, *Nanotechnol. Rev.*, 2019, **8**, 352–369.

58 B. L. Caetano, C. V. Santilli, S. H. Pulcinelli and V. Briois, *Phase Transitions*, 2011, **84**, 714–725.

59 P. R. A. F. Garcia, O. Prymak, V. Grasmik, K. Pappert, W. Wlysses, L. Otubo, M. Epple and C. L. P. Oliveira, *Nanoscale Adv.*, 2020, **2**, 225–238.

60 N. Steinfeldt, *Langmuir*, 2012, **28**, 13072–13079.

61 T. Hendel, M. Wuithschick, F. Kettemann, A. Birnbaum, K. Rademann and J. Polte, *Anal. Chem.*, 2014, **86**, 11115–11124.

62 W. Szczerba, H. Riesemeier and A. F. Thünemann, *Anal. Bioanal. Chem.*, 2010, **398**, 1967–1972.

63 B. R. Pauw, C. Kästner and A. F. Thünemann, *J. Appl. Cryst*, 2017, **50**, 1280–1288.

64 A. Agbabiaka, M. Wiltfong and C. Park, *J. Nanoparticles*, 2013, 1–11.

65 M. Harada and H. Einaga, *Langmuir*, 2007, **23**, 6536–6543.

66 M. Harada and S. Kizaki, *Cryst. Growth Des.*, 2016, **16**, 1200–1212.

67 M. Harada and Y. Inada, *Langmuir*, 2009, **25**, 6049–6061.

68 M. Honda, Y. Baba, I. Shimoyama and T. Sekiguchi, *Rev. Sci. Instrum.*, 2015, **86**, 1–6.

69 J. Polte, T. T. Ahner, F. Delissen, S. Sokolov, F. Emmerling, A. F. Thünemann and R. Kraehnert, *J. Am. Chem. Soc.*, 2010, **132**, 1296–1301.

70 I. J. Godfrey, A. J. Dent, I. P. Parkin, S. Maenosono and G. Sankar, *ACS Omega*, 2020, **5**, 13664–13671.

71 T. Shibata, H. Tostmann, B. Bunker, A. Henglein, D. Meisel, S. Cheong and M. Boyanov, *J. Synchrotron Radiat.*, 2001, **8**, 545–547.

72 V. Amendola, R. Pilot, M. Frasconi, O. M. Maragò and A. M. Iatì, *J. Phys. Condens. Matter*, 2017, **29**, 203002.

73 X. Liang, Z. Wang and C. Liu, *Nanoscale Res. Lett.*, 2010, **5**, 124–129.

74 J. Ohyama, K. Teramura, Y. Higuchi, T. Shishido, Y. Hitomi, K. Kato, H. Tanida, T. Uruga and T. Tanaka, *ChemPhysChem*, 2011, **12**, 127–131.

75 L. Prati and A. Villa, *Catalysts*, 2012, **2**, 24–37.

76 L. C. McKenzie, P. M. Haben, S. D. Kevan and J. E. Hutchison, *J. Phys. Chem. C*, 2010, **114**, 22055–22063.

77 X. Zhou, G. Liu, J. Yu and W. Fan, *J. Mater. Chem.*, 2012, **22**, 21337.

78 L. Xu, J. Peng, C. Srinivasakannan, L. Zhang, D. Zhang, C. Liu, S. Wang and A. Q. Shen, *RSC Adv.*, 2014, **4**, 25155.

79 S. Hayama, G. Duller, J. P. Sutter, M. Amboage, R. Boada, A. Freeman, L. Keenan, B. Nutter, L. Cahill, P. Leicester, B. Kemp, N. Rubies and S. Diaz-moreno, *J. Synchrotron Radiat.*, 2018, **25**, 1556–1564.

80 B. Ravel and M. Newville, *J. Synchrotron Radiat.*, 2005, **12**, 537–541.

81 B. G. Ershov, E. V. Abkhalimov, R. D. Solovov and V. I. Roldughin, *Phys. Chem. Chem. Phys.*, 2016, **18**, 13459–13466.

82 K. Wang and G. Luo, *Chem. Eng. Sci.*, 2017, **169**, 18–33.

83 A. M. Karim, N. Al Hasan, S. Ivanov, S. Siefert, R. T. Kelly, N. G. Hallfors, A. Benavidez, L. Kovarik, A. Jenkins, R. E. Winans and A. K. Datye, *J. Phys. Chem. C*, 2015, **119**, 13257–13267.

84 K. Robertson, *Chem. Cent. J.*, 2017, **11**, 4.

85 D. Di Carlo, *Lab Chip*, 2009, **9**, 3038–3046.

86 F. Porta, L. Prati, M. Rossi, S. Coluccia and G. Martra, *Catal. Today*, 2000, **61**, 165–172.

87 L. Prati and A. Villa, *Acc. Chem. Res.*, 2014, **47**, 855–863.

88 U. B. Demirci, O. Akdim, J. Andrieux, J. Hannauer, R. Chamoun and P. Miele, *Fuel Cells*, 2010, **10**, 335–350.

89 J.-H. Wee, K.-Y. Lee and S. H. Kim, *Fuel Process. Technol.*, 2006, **87**, 811–819.

90 V. G. Minkina, S. I. Shabunya, V. I. Kalinin, V. V. Martynenko and A. L. Smirnova, *Int. J. Hydrogen Energy*, 2012, **37**, 3313–3318.

91 V. G. Minkina, S. I. Shabunya, V. I. Kalinin, V. V. Martynenko and A. L. Smirnova, *Int. J. Hydrogen Energy*, 2008, **33**, 5629–5635.

92 J. Zhang, T. S. Fisher, J. P. Gore, D. Hazra and P. V. Ramachandran, *Int. J. Hydrogen Energy*, 2006, **31**, 2292–2298.

93 Q. Wang, L. F. Zhang and Z. G. Zhao, *IOP Conf. Ser. Mater. Sci. Eng.*, 2018, **292**, 012031.

94 V. Amendola and M. Meneghetti, *J. Phys. Chem. C*, 2009, **113**, 4277–4285.

95 J. Piella, N. G. Bastús and V. Puntes, *Chem. Mater.*, 2016, **28**, 1066–1075.

96 O. Lidor-Shalev and D. Zitoun, *RSC Adv.*, 2014, **4**, 63603–63610.

97 M. Wojnicki, T. Tokarski, V. Hessel, K. Fitzner and M. Luty-Błocho, *J. Flow Chem.*, 2019, **9**, 1–7.

98 M. Wojnicki, K. Pacławski, E. Rudnik and K. Fitzner, *Hydrometallurgy*, 2011, **110**, 56–61.

99 H. Cai, L. Liu, Q. Chen, P. Lu and J. Dong, *Energy*, 2016, **99**, 129–135.

100 W. Haiss, N. T. K. Thnah, J. Aveyard and D. G. Fernig, *Anal. Chem.*, 2008, **79**, 4215–4221.

101 M. Schoenitz, L. Grundemann, W. Augustin and S. Scholl, *Chem. Commun.*, 2015,

51, 8213–8228.

102 L. Panariello, S. Damilos, H. du Toit, G. Wu, A. N. P. Radhakrishnan, I. P. Parkin and A. Gavriilidis, *React. Chem. Eng.*, 2020, **5**, 663–676.

103 R. Dootz, A. Otten, S. Köster, B. Struth and T. Pfohl, *J. Phys. Condens. Matter*, 2006, **18**, S639–S652.

104 E. Gullikson, Filter Transmission, https://henke.lbl.gov/optical_constants/filter2.html, (accessed 20 May 2021).

105 B. L. Henke, E. M. Gullikson and J. C. Davis, *At. Data Nucl. Data Tables*, 1993, **54**, 181–342.

106 G. Malta, S. A. Kondrat, S. J. Freakley, C. J. Davies, L. Lu, S. Dawson, A. Thetford, E. K. Gibson, D. J. Morgan, W. Jones, P. P. Wells, P. Johnston, C. R. A. Catlow, C. J. Kiely and G. J. Hutchings, *Science*, 2017, **355**, 1399–1403.

107 F. Farges, J. A. Sharps and G. E. Brown Jr., *Geochim. Cosmochim. Acta*, 1993, **57**, 1243–1252.

108 M. Giorgetti, G. Aquilanti, B. Ballarin, M. Berrettoni, M. C. Cassani, S. Fazzini, D. Nanni and D. Tonelli, *Anal. Chem.*, 2016, **88**, 6873–6880.

109 T. Yao, Z. Sun, Y. Li, Z. Pan, H. Wei, Y. Xie, M. Nomura, Y. Niwa, W. Yan, Z. Wu, Y. Jiang, Q. Liu and S. Wei, *J. Am. Chem. Soc.*, 2010, **132**, 7696–7701.

110 Y. M. Yiu, P. Zhang and T. K. Sham, *Nanotechnology*, 2003, **3**, 183–186.

Chapter 7 Conclusions and Future Works

The work presented in this thesis has focussed on elucidating how variations to the synthesis procedure can affect change in sol-immobilisation prepared NP catalysts (supported and unsupported). The themes of this thesis can be divided into two sections: (1) optimising the sol-immobilisation synthesis procedure for Pd/TiO_2 *via* changes to the colloidal synthesis solvent, and (2) understanding how the synthesis procedure influences NP nucleation and growth of colloidal Au NPs. To achieve these, a wide range of laboratory-based characterisation techniques, such as UV-Vis, STEM, MP-AES, FTIR, TPD/TPR, and TGA, were employed. Additionally, synchrotron radiation was utilised to study the effect of synthesis parameters both *in situ* and *ex situ.*

Optimisation of the sol-immobilisation synthesis protocol was investigated in Chapters 3 and 4, where PVA-capped colloidal Pd NPs were prepared and immobilised during an acidification step onto TiO_2 at a reduction temperature of 1 °C and in altered synthesis solvents. The use of different linear and branched short chain alcohols (C_1-C_4) in the synthesis solvent was first explored using equal vol. % ratios of $XOH:H_2O$ (XOH = MeOH, EtOH, PrOH, IPA and *t*BuOH). It was established that the smallest Pd NPs were formed in synthesis solvents composed of 50 vol. % MeOH, the alcohol with the shortest chain length (Pd NP size = 1.1 ± 0.6 nm); however it should be noted that all alcohol-prepared NPs, bar PrOH, displayed smaller average NP sizes than those prepared in a 100 vol. % H_2O system (Pd NP size = 2.6 ± 1.4 nm). The achieved Pd loading and accessibility of NP surface sites displayed no trend with increasing alcohol chain length or sterics. Further understanding of how MeOH influenced colloidal preparation was sought by preparing Pd NPs in solvents with increasing $[MeOH_{(aq)}]$. Equal $MeOH:H_2O$ mixtures were again found to yield the smallest Pd NPs, however, increasing the MeOH concentration above 50 vol. % led to an increase in NP size as well as drastically reduced the achieved Pd loading. In addition to this, the inclusion of MeOH in the synthesis solvent had a detrimental impact on the accessibility of Pd NP surface sites, with the H_2O based synthesis producing far greater populations of bridged and linear surface adsorption sites.

The decreased surface site availability with inclusion of MeOH, and the reduced Pd loading as $[MeOH_{(aq)}] > 50$ vol. %, is hypothesised to either be caused by insufficient solvation of PVA and the precursor salt in increasing $[MeOH_{(aq)}]$, or be a consequence of interactions between the colloidal Pd nanoparticle surface and the stabiliser inhibiting access to surface

sites. This could be confirmed by further investigation into the use of incremental concentrations of the remaining C_2-C_4 alcohols to determine how slight changes to the synthesis solvent can ultimately impact the final catalyst.

In Chapter 4 the use of MeOH in the synthesis solvent was further examined, with the focus to streamline the synthesis process. The issues observed in Chapter 3 regarding low Pd loadings at high [$MeOH_{(aq)}$] were explored by forming Pd colloids in MeOH:H_2O synthesis solvents of varying vol. % ratios: 0:100, 50:50, 100:0. Removal of the stabilisation and acidification processes in each of these syntheses showed an expected increase in NP size for all three reaction solvents, but the immobilisation of Pd onto the support surface was improved for 50 and 100 vol. % MeOH systems as compared to the analogous stabilised and acidified catalysts prepared in Chapter 3.

Changes to the catalyst surface were elucidated by testing the Pd catalysts activity in the hydrogenation of the α,β-unsaturated aldehyde, furfural. The selectivity of the reaction is known to be consequential of the available surface sites and how furfural associates to them, i.e. both the aldehyde C=O and the furan ring C=C can be hydrogenated through adsorption adjacent or parallel to the metal surface; this results in the production of the primary hydrogenation product, furfuryl alcohol (*via* C=O adsorption) and secondary product, tetrahydrofurfuryl alcohol (*via* C=O and C=C adsorption). Without the acidification step present, the PVA-capped Pd NPs prepared in MeOH displayed a much larger abundance of accessible surface sites (particularly linear C=O) than the acidified H_2O prepared Pd-PVA NPs. However, this did not translate to an increased PdMeP TOF for furfural hydrogenation. Instead, it was discovered that using Pd-PVA NPs prepared in the H_2O only solvent systems had the highest furfural TOF. This higher activity was discovered to be a consequence of the over hydrogenation of furfural to ethers, and the acid catalysation of furfural to acetals - the latter of which did not occur on the MeOH synthesised catalyst. Acid catalysation of furfural is a process that occurs over Brønsted acid sites on the support material; by using MeOH as the synthesis solvent, this pathway was switched off *via* the suppression of H_2 spillover. This phenomenon occurred due to increased quantities of the stabilising polymer clustering around the Pd NPs, support surfaces, and their interfaces, which was confirmed using HRTEM and H_2-TPR. To further support the hypothesised suppression of H_2 spillover for PVA-capped Pd catalysts prepared in MeOH, additional characterisation could be performed, though suitable techniques to measure the extent of H_2 spillover under *operando* conditions are few and far between. One promising approach would be to monitor the H_2 environment before and after H_2 pre-treatment (5 bar) using *in situ* H^1- or D^2-NMR.

Elucidating the growth processes of colloidal solutions as a function of synthesis temperature (1, 25, 50 and 75 °C) and [Au] (50, 100 and 1000 μM) was presented in Chapter 5. Sol-immobilisation of PVA-capped Au NPs were performed in H_2O only solvent systems, and an acidification step was employed during the immobilisation phase. By using Au, initial assessments of the synthesis conditions on colloidal NP growth were made *via* comparisons of the UV-Vis SPR bands. However, this does not give a true indication of NP size as dampening of smaller Au NPs can occur. In addition, acquired STEM imaging of the colloidal solutions yielded inaccurate representations of NP size, either through insufficient sample NP population, limitations of the instrument, or human error. XAFS was successful in minimising these associated errors as it is element specific and does not require long range order within the sample. Beam damage was avoided by using an adapted stainless steel cell with X-ray transparent windows, which the preformed colloids were pumped through. Fitting of the EXAFS data with an appropriate crystallographic information file (*cif*) enabled the average coordination number of the absorbing Au atoms to be found; this was then translated to average Au NP size *via* an established literature method.[1,2] As expected, increased colloidal NP size was correlated with greater temperatures of reduction (1 °C = 1.5 ± 0.1 nm, 25 °C = 1.8 ± 0.1 nm, 50 °C = 2.2 ± 0.1 nm and 75 °C = 2.3 ± 0.1 nm). Conversely, the synthesis of colloidal Au at increasing [Au] displayed no definitive increase in NP size, even with a 20-fold increase in [Au] from 50→1000 μM (50 μM = 1.5 ± 0.1 nm, 1000 μM = 1.6 ± 0.1 nm). The influence of the immobilisation procedure was then elucidated, where the varied [Au] colloids were anchored onto TiO_2. Following characterisation of the solid samples, growth in NP size is evidently dependent on the initial [Au] (50 μM = 1.6 ± 0.1 nm, 1000 μM = 4.0 ± 0.1 nm). The immobilisation phase is therefore a significant parameter that should be considered when preparing NPs *via* sol-immobilisation. The contribution of NP anchoring toward NP growth could be further elucidated using synchrotron techniques coupled with microjet mixing systems, with one such system available on the Phoenix beamline at the Swiss Light Source. Nevertheless, this is the first work, to the author's knowledge, that reports the successful acquisition of colloidal XAFS at [Au] ≤ 300 μM.[3–6]

Chapter 6 pursued understanding of the primary nucleation and growth events in colloidal PVA-capped Au nanoparticle synthesis at 100 μM [Au]. Building on the work presented in Chapter 5, *in situ* XAFS was utilised to measure colloidal nanoparticle formation. Unlike Chapters 3, 4 and 5, synthesis in Chapter 6 was performed in a purpose-built microfluidic cell, and was not without its own obstacles. The flow regime, Au deposition on the reactor

walls, evolution of H_2 during reducing agent decomposition, and the cell materials compatibility with XAFS experiments all had to be addressed when designing an appropriate microfluidic device. A continuous laminar flow regime, with a Reynolds number < 2100, was achieved by using optimal reagent flow rates and short mixing channel lengths. The desired annular flow, where the precursor salt stream was encapsulated in the reducing agent stream, was attained by inserting a modified 28 G needle tip along the long edge of a stainless steel T-junction and increasing the reducing agent flow rate in comparison to the precursor salt. Fouling of the metal species on the mixing channel walls was avoided by pre-treating the inner walls of the microfluidic cell with a premade fluorinated oil. The production of $H_{2(g)}$ during synthesis, and potential interruption of the XAFS measurement, was negated by altering the reducing agent and the solution used to solvate it. In the previous chapters, $NaBH_4$ (0.1 M) was employed due to its fast reduction capabilities, however, 4 mol $H_{2(g)}$ are produced for 1 mol hydrolysed $NaBH_4$. Instead, DMAB (0.1 M) was prepared in $NaOH_{(aq)}$ (0.15 M) to ensure slow decomposition of the reducing agent, thus suppressing unwanted gas evolution. Photon loss was kept to a minimum by constructing the mixing channel from smooth 0.16 cm (ID) polyimide tubing, an X-ray transparent material, with a wall thickness of 300 μm (photon loss = < 15 %). It should be noted that photoreduction of the Au in the path of the beam was not observed.

In situ XANES data was acquired along the length of the mixing channel, describing the change in oxidation state between 500 milliseconds and 3.5 seconds of reaction time. Reduction of the precursor salt was observed to begin < 500 milliseconds, despite milder reduction conditions being employed. Reduction of the precursor salt was complete after 3.5 s, with the XANES spectra detailing reduction from $Au^{3+} \rightarrow Au^0$ without forming Au^+ as an intermediate oxidation state. Moreover, colloidal Au formation was achieved *via* the microfluidic system 500 times faster than in the batch conditions used in Chapter 5. An unforeseen issue arose from the movements of the syringe pump motors detected by the sensitive equipment on the beamline. Consequentially, EXAFS measurements were not acquired due to overlapping oscillations after the absorption edge. Nevertheless, the successful monitoring of Au reduction *via in situ* XAFS measurements presented in Chapter 6 is, to the best of the author's knowledge, the first achieved at dilute metal concentrations ([Au] = 100 μM).

The sourcing of a smoothflow pump would be advised for further attempts at measuring the formation of colloidal nanoparticles using *in situ* XAFS, to ensure that the oscillatory region of the spectrum is not dampened. By monitoring the change in the local environment of the

metal species during reduction, an accurate per atom interpretation of NP reduction and growth could be acquired, with wide-reaching benefits for industrial preparations of NP catalysts, as well as affording characterisation of bi-metallic NP nucleation and growth processes.

In conclusion, the work presented in this thesis provides new insight into how variations to the synthesis solvent and immobilisation steps can not only control Pd NP size, but also contribute to improved catalytic selectivity. Moreover, a method was established capable of measuring colloidal NP formation using *in situ* synchrotron methods. The applications of understanding nucleation and growth of colloidal NPs are wide reaching, allowing for the mass production of tailored metallic NPs.

7.1 References

1 A. M. Beale and B. M. Weckhuysen, *Phys. Chem. Chem. Phys.*, 2010, **12**, 5562–5574.

2 A. Jentys, *Phys. Chem. Chem. Phys.*, 1999, **1**, 4059–4063.

3 M. Harada and R. Ikegami, *Cryst. Growth Des.*, 2016, **16**, 2860–2873.

4 M. Harada, Y. Inada and M. Nomura, *J. Colloid Interface Sci.*, 2009, **337**, 427–438.

5 I. J. Godfrey, A. J. Dent, I. P. Parkin, S. Maenosono and G. Sankar, *ACS Omega*, 2020, **5**, 13664–13671.

6 J. Polte, T. T. Ahner, F. Delissen, S. Sokolov, F. Emmerling, A. F. Thünemann and R. Kraehnert, *J. Am. Chem. Soc.*, 2010, **132**, 1296–1301.

Chapter 8 Appendix

8.1 Chapter 4–Supplementary Information

8.1.1 Conversion and Yield Tables for Furfural Hydrogenation over Pd/TiO_2 catalysts

Table 8-1. *Conversion and product yields for all prepared catalysts and fresh TiO_2 support used in the hydrogenation of furfural, conversion and yields were calculated after 15 minutes reaction time; conditions: 50 °C, 5 bar H_2, furfural 0.3 M furfural/metal ratio 500 mol/mol, solvent IPA.*

Sample	Furfural Conversion (%)	Yield (%)							
		FA	THFA	Acetal	THF-ME	THFIE	FIE	2-MF	2-MTHF
PdWPA	14	7	1	3	0	2	1	0	0
PdWP	5	2	0	3	0	0	0	0	0
Pd50MeP	8	5	1	1	0	1	0	0	0
PdMeP	8	5	2	0	0	0	1	0	0
PdW	3	0	0	0	0	0	3	0	0
Pd50Me	6	1	0	3	0	0	2	0	0
PdMe	6	3	1	2	0	0	0	0	0

Table 8-2. *Conversion and product yields for all prepared catalysts and fresh TiO_2 support used in the hydrogenation of furfural, conversion and yields were calculated after 5 hrs reaction time; conditions: 50 °C, 5 bar H_2, furfural 0.3 M furfural/metal ratio 500 mol/mol, solvent 2-propanol.*

Sample	Furfural Conv. (%)	Yield (%)								Mass Balance (%)
		FA	THFA	Acetal	THF-ME	THFIE	FIE	2-MF	2-MTHF	
PdWPA	74	2	47	1	6	15	1	1	1	99
PdWP	21	12	3	5	0	1	0	0	0	100
Pd50MeP	54	20	27	3	0	4	0	0	0	100
PdMeP	53	24	23	0	0	3	3	0	0	100
PdW	15	3	0	0	0	0	12	0	0	99
Pd50Me	49	9	22	5	1	7	5	0	0	100
PdMe	37	10	18	4	0	5	0	0	0	100
TiO_2	25	0	0	25	0	0	0	0	0	100

8.1.2 Time on line profile for Acetal formation over PdWPA and PdMeP

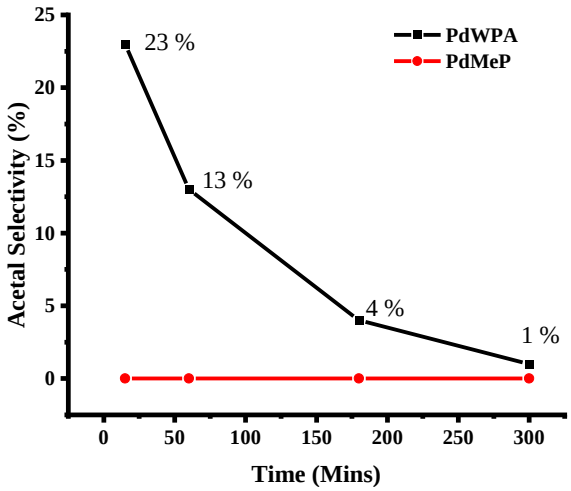

Figure 8-1. *Time online selectivity profile for acetal production over fresh 1 wt. % Pd/TiO_2 catalysts; PdWPA (black), and PdMeP (red).*

8.1.3 Recycling data for Furfural Hydrogenation over Pd/TiO_2 catalysts

Table 8-3. *Conversion and product yields for six successive hydrogenation cycles over the prepared PdWPA catalyst. Data was collected after 3 hrs of reaction time. Conditions: 50 °C, 5 bar $H_{2,}$, furfural 0.3 M; furfural/metal ratio 500 mol/mol, solvent 2-propanol.*

Cycle	Furfural Conv. (%)	Yield (%)								Mass Balance (%)
		FA	THFA	Acetal	THF-ME	THFIE	FIE	2-MF	2-MTHF	
1	72	5	48	1	3	9	0	2	2	99
2	70	7	48	0	2	6	2	1	0	97
3	67	13	40	2	1	4	7	0	0	100
4	53	8	30	1	1	4	9	0	0	100
5	36	6	16	1	0	0	13	0	0	100
6	22	5	1	1	0	0	15	0	0	100

Table 8-4. *Conversion and product yields for six successive hydrogenation cycles over the prepared PdMeP catalyst. Data was collected after 3 hrs of reaction time. Conditions: 50 °C, 5 bar $H_{2,}$ furfural 0.3 M; furfural/metal ratio 500 mol/mol, solvent 2-propanol.*

Cycle	Furfural Conv. (%)	Yield (%)								Mass Balance (%)
		FA	THFA	Acetal	THF-ME	THFIE	FIE	2-MF	2-MTHF	
1	56	21	23	0	0	7	7	0	0	102
2	55	21	22	0	1	6	7	0	0	102
3	50	18	15	1	1	5	12	0	0	102
4	44	15	11	3	0	4	13	0	0	101
5	31	10	5	1	0	4	13	0	0	101
6	21	6	2	1	1	3	10	0	0	100

Table 8-5. *Conversion and product yields for six successive hydrogenation cycles over the prepared PdMe catalyst. Data was collected after 3 hrs of reaction time. Conditions: 50 °C, 5 bar H_2, furfural 0.3 M; furfural/metal ratio 500 mol/mol, solvent 2-propanol.*

Cycle	Furfural Conv. (%)	Yield (%)								Mass Balance (%)
		FA	THFA	Acetal	THF-ME	THFIE	FIE	2-MF	2-MTHF	
1	26	10	8	0	0	3	4	0	0	99
2	18	2	0	0	0	0	15	0	0	99
3	16	2	0	0	0	0	14	0	0	100
4	9	1	0	0	0	0	8	0	0	100
5	2	1	0	0	0	0	1	0	0	100
6	0	0	0	0	0	0	0	0	0	100

8.2 Chapter 6-Supplimentary Information

The flow profile achieved in the *in situ* cell mixing channel is described by the unit-less Reynolds number (Re), where Re > 2100 and Re < 2100 describe turbulent and laminar flows, respectively. Re was calculated by:

$$\mathrm{Re} = \frac{v\,\mathrm{L}}{\eta}$$

Where, v is the fluid velocity, L is the mixing channel length (10 cm) and η is the fluid viscosity.

The fluid velocity is calculated by:

$$v = \frac{\bar{v}}{\pi r^2} = 0.0165784 \text{ m s}^{-1}$$

Where, $\bar{v}$ is the flow rate (2 mL min^{-1}) and r is the mixing channel radius (0.08 cm).

The fluid viscosity is determined using the dynamic viscosity and density of the fluid being pumped through the cell (H_2O).

$$\eta = \frac{\mu}{\rho} = 8.927 \times 10^{-7} \text{ m}^2\text{s}^{-1}$$

Where, μ is the dynamic viscosity (0.00089 kg m^{-1} s^{-1}) and ρ is the fluid density (997 kg m^{-3}).

Re will thus be calculated by:

$$\mathrm{Re} = \frac{v\,\mathrm{L}}{\eta} = \frac{0.0165784 \times 0.1}{8.927 \times 10^{-7}}$$

$$\mathrm{Re} = 1857.18$$

Therefore the flow profile used in the *in situ* mixing channel is laminar (Re < 2100).